



University of Kentucky
UKnowledge

University of Kentucky Master's Theses

Graduate School

2008

INTEGRATED GEOPHYSICAL IMAGING OF SUBSURFACE GEOLOGIC CONDITIONS ACROSS A CONTAMINANT PLUME, MCCRACKEN COUNTY, KENTUCKY

Cora A. Blits

University of Kentucky, ceande5@gmail.com

[Right click to open a feedback form in a new tab to let us know how this document benefits you.](#)

Recommended Citation

Blits, Cora A., "INTEGRATED GEOPHYSICAL IMAGING OF SUBSURFACE GEOLOGIC CONDITIONS ACROSS A CONTAMINANT PLUME, MCCRACKEN COUNTY, KENTUCKY" (2008). *University of Kentucky Master's Theses*. 560.

https://uknowledge.uky.edu/gradschool_theses/560

This Thesis is brought to you for free and open access by the Graduate School at UKnowledge. It has been accepted for inclusion in University of Kentucky Master's Theses by an authorized administrator of UKnowledge. For more information, please contact UKnowledge@lsv.uky.edu.

ABSTRACT OF THESIS

INTEGRATED GEOPHYSICAL IMAGING OF SUBSURFACE GEOLOGIC CONDITIONS ACROSS A CONTAMINANT PLUME, MCCRACKEN COUNTY, KENTUCKY

Over 7.8 km of seismic reflection data and 2 km of electrical resistivity data were acquired, processed, and interpreted during this multi-method geophysical study. Objectives included the definition of geologic conditions underlying a contaminant plume in McCracken County, western Kentucky, and the determination of the potential for structural control on the rate and direction of plume migration. Both geophysical methods indicate the presence of multiple high-angle normal faults outlining a series of asymmetric grabens ranging in width from 160 m to almost 300 m and striking between N40°E and N45°E. There was agreement between the two methods on fault location and degree of near-surface offset, with offsets of 1 to 2 m observed at 10 to 20 m below ground surface and 3 to 8 m observed at 20 to 30 m depth. Bedrock displacement was generally 2 to 3 times larger, with offsets of 10 to 26 m observed. The faults appear to have originated in the Paleozoic with predominantly normal reactivation occurring as recently as the Pleistocene. The fault strikes generally approximate the orientation of the northwestern contaminant plume. Observed offset of the Regional Gravel Aquifer may form a preferential flow path for contaminant migration.

KEYWORDS: Mississippi Embayment, Contaminant Plume, Neotectonics, SH-Wave Seismic Reflection, Electrical Resistivity Imaging

Cora A. Blits

November 14, 2008

INTEGRATED GEOPHYSICAL IMAGING OF SUBSURFACE GEOLOGIC
CONDITIONS ACROSS A CONTAMINANT PLUME, MCCRACKEN COUNTY,
KENTUCKY

By

Cora Anderson Blits

Dr. Edward W. Woolery

Director of Thesis

Dr. Dhananjay Ravat

Director of Graduate Studies

November 14, 2008

RULES FOR USE OF THESES

Unpublished theses submitted for the Master's degree and deposited in the University of Kentucky Library are as a rule open for inspection, but are to be used only with due regard to the rights of the authors. Bibliographical references may be noted, but quotations or summaries of parts may be published only with the permission of the author, and with the usual scholarly acknowledgements.

Extensive copying or publication of the thesis in whole or in part also requires the consent of the Dean of the Graduate School of the University of Kentucky,

A library that borrows this thesis for use by its patrons is expected to secure the signature of each user.

Name

Date

THESIS

Cora Anderson Blits

The Graduate School
University of Kentucky

2008

INTEGRATED GEOPHYSICAL IMAGING OF SUBSURFACE GEOLOGIC
CONITIONS ACROSS A CONTAMINANT PLUME, MCCRACKEN COUNTY,
KENTUCKY

THESIS

A thesis submitted in partial fulfillment of the
requirements for the degree of Master of Science in the
College of Arts and Sciences
at the University of Kentucky

By

Cora Anderson Blits

Lexington, Kentucky

Director: Dr. Edward W. Woolery, Associate Professor of Geology

Lexington, Kentucky

2008

Copyright © Cora Anderson Blits 2008

ACKNOWLEDGEMENTS

I would like to thank the Kentucky Research Consortium for Energy and the Environment, the Department of Energy, and the Kentucky Geological Survey for their support of this project.

TABLE OF CONTENTS

Acknowledgements.....	iii
List of Tables	vii
List of Figures.....	viii
List of Files	x
Chapter One: Introduction	
1.1 Background.....	1
1.2 Study Objective.....	3
1.3 Regional Geology	3
1.3.1 Structural Framework	3
1.3.2 Regional Stratigraphy and Depositional History	5
1.4 Study Area Geology.....	7
1.4.1 Location of Study Area.....	7
1.4.2 Site Structure.....	7
1.4.3 Site Stratigraphy.....	8
1.5 Related Studies.....	11
Chapter Two: Methodology	
2.1 Multi-Method Geophysical Studies	20
2.2 SH-Wave Seismic Reflection	20
2.2.1 Method Justification.....	20
2.2.2 Data Acquisition	21
2.2.3 Data Processing.....	22
2.2.4 Resolution	23
2.3 Electrical Resistivity Imaging.....	24
2.3.1 Method Justification.....	24
2.3.2 Data Acquisition	26
2.3.3 Data Processing.....	27
2.3.4 Resolution	29
Chapter Three: Interpretation	
3.1 Seismic Reflection Background.....	43
3.1.1 General.....	43
3.1.2 Vertical Exaggeration	44
3.1.3 Resolution	45
3.1.4 Identification of Reflectors	46
3.2 Seismic Line Interpretation.....	47
3.2.1 Line UK-A3	47
3.2.1.1 Deformation Zone 1	48
3.2.1.2 Deformation Zone 2.....	49
3.2.1.3 Deformation Zone 3.....	49
3.2.2 Line UK-B	50

3.2.2.2	Deformation Zone 5.....	52
3.2.2.3	Deformation Zone 6.....	52
3.2.3	Line UK-G1	53
3.2.3.1	Deformation Zone 7.....	54
3.2.3.2	Deformation Zone 8.....	55
3.2.3.3	Deformation Zone 9.....	55
3.2.4	Line UK-G2	56
3.2.4.1	Deformation Zone 10.....	56
3.2.5	Line UK-H.....	57
3.2.5.1	Deformation Zone 11.....	57
3.2.5.2	Deformation Zone 12.....	58
3.2.6	Line UK-I.....	59
3.2.6.1	Deformation Zone 13.....	59
3.2.6.2	Deformation Zone 14.....	60
3.2.7	Line UK-J.....	61
3.2.7.1	Deformation Zone 15.....	62
3.2.7.2	Deformation Zone 16.....	63
3.3	Electrical Resistivity Background.....	64
3.3.1	General.....	64
3.3.2	Resolution	65
3.4	Electrical Resistivity Section Interpretation	65
3.4.1	Line UK-001	65
3.4.2	Line UK-002	68
3.4.3	Line UK-003	70
3.4.4	Line UK-004	71

Chapter Four: Discussion

4.1	Correlation between Seismic and Electrical Methods	118
4.2	Structural Style of Deformation.....	119
4.3	Implications for Groundwater Movement	122

Chapter Five: Conclusions..... 130

Appendices

Appendix A:	Seismic Reflection Data.....	132
Section 1:	Uninterpreted Seismic Profiles	133
Section 2:	Detailed Processing Procedure	188
Section 3:	Field Files	203
Appendix B:	Electrical Resistivity Imaging Data.....	219
Section 1:	Uninterpreted Electrical Resistivity Profiles	220
Section 2:	Convergence Curves.....	232
Section 3:	Cross-Plots.....	244
Section 4:	Relative Model Sensitivities	256
Section 5:	Normalized Resistivity Sections.....	268
Section 6:	Alternate Processing Techniques.....	273

Appendix C: Depths to Stratigraphic Units	290
References.....	295
Vita.....	300

LIST OF TABLES

Table 2.1, Seismic Survey Acquisition Parameters	30
Table 2.2, SH-Wave Seismic Reflection Processing Procedures	31
Table 2.3, Electrical Resistivity Survey Acquisition Parameters	32
Table 2.4, Electrical Resistivity Imaging Inversion Settings.....	33
Table 2.5, Electrical Resistivity Imaging Processing Settings	34
Table 3.1, Resolution Limits for Near-Surface Reflectors	74
Table 3.2, Resolution Limits for Bedrock Reflectors	75
Table 3.3, Resolution Limits for Electrical Resistivity Imaging Profiles.....	76

LIST OF FIGURES

Figure 1.1, Map of Contaminant Plume Locations.....	14
Figure 1.2, Structure of the Central Mississippi Valley.....	15
Figure 1.3, Study Area Location.....	16
Figure 1.4, Map of Previously Interpreted Structural Features	17
Figure 1.5, Stratigraphic Section Showing Local Units	18
Figure 1.6, Stratigraphic Cross-Section	19
Figure 2.1, Site Map with Locations of Seismic Reflection Survey Lines.....	35
Figure 2.2, Examples of Seismic Reflection Field Files.....	36
Figure 2.3, Schematic Layout of a 4-Electrode Dipole-Dipole Array	37
Figure 2.4, Site Map with Locations of Electrical Resistivity Survey Lines.....	38
Figure 2.5, Example of Measured and Calculated Apparent Resistivity Pseudosections and the Resulting Inverted Resistivity Section.....	39
Figure 2.6, Example of Predicted vs. Measured Apparent Resistivity Cross-Plot	40
Figure 2.7, Example of Resistivity Inversion Convergence Curve	41
Figure 2.8, Example of a Resistivity Model Sensitivity Section	42
Figure 3.1, Amplitude vs. Frequency Plot for Line UK-H.....	77
Figure 3.2, Map of Boring Locations with the Study Area	78
Figure 3.3, Section UK-A3 with Deformation Zone 1 through 3.....	79
Figure 3.4, Section UK-B with Deformation Zones 4 through 6.....	80
Figure 3.5, First Section of UK-G1with Deformation Zone 7 and 8.....	81
Figure 3.6, Second Section of UK-G1 with Deformation Zone 9	82
Figure 3.7, Section UK-G2 with Deformation Zone 10	83
Figure 3.8, Section UK-H with Deformation Zone 11	84
Figure 3.9, Section UK-I with Deformation Zones 12 and 13.....	85
Figure 3.10, Section UK-J with Deformation Zones 14 and 15	86
Figure 3.11, First Interpreted Section of Line UK-A3.....	87
Figure 3.12, Second Interpreted Section of Line UK-A3	88
Figure 3.13, Third Interpreted Section of Line UK-A3	89
Figure 3.14, Fourth Interpreted Section of Line UK-A3	90
Figure 3.15, Fifth Interpreted Section of Line UK-A3	91
Figure 3.16, First Interpreted Section of Line UK-B.....	92
Figure 3.17, Second Interpreted Section of Line UK-B	93
Figure 3.18, Third Interpreted Section of Line UK-B	94
Figure 3.19, Fourth Interpreted Section of Line UK-B	95
Figure 3.20, First Interpreted Section of Line UK-G1.....	96
Figure 3.21, Second Interpreted Section of Line UK-G1	97
Figure 3.22, Third Interpreted Section of Line UK-G1	98
Figure 3.23, Fourth Interpreted Section of Line UK-G1	99
Figure 3.24, Fifth Interpreted Section of Line UK-G1	100
Figure 3.25, Sixth Interpreted Section of Line UK-G1	101
Figure 3.26, Seventh Interpreted Section of Line UK-G1	102
Figure 3.27, First Interpreted Section of Line UK-G2.....	103

Figure 3.28, Second Interpreted Section of Line UK-G2	104
Figure 3.29, First Interpreted Section of Line UK-H.....	105
Figure 3.30, Second Interpreted Section of Line UK-H	106
Figure 3.31, Third Interpreted Section of Line UK-H.....	107
Figure 3.32, First Interpreted Section of Line UK-I.....	108
Figure 3.33, Second Interpreted Section of Line UK-I.....	109
Figure 3.34, First Interpreted Section of Line UK-J.....	110
Figure 3.35, Second Interpreted Section of Line UK-J	111
Figure 3.36, Third Interpreted Section of Line UK-J	112
Figure 3.37, Fourth Interpreted Section of Line UK-J.....	113
Figure 3.38, Interpreted Electrical Resistivity Section UK-001	114
Figure 3.39, Interpreted Electrical Resistivity Section UK-002	115
Figure 3.40, Interpreted Electrical Resistivity Section UK-003	116
Figure 3.41, Interpreted Electrical Resistivity Section UK-004	117
Figure 4.1, Correlation of Seismic Section UK-H to Electrical Resistivity Profile UK-001	123
Figure 4.2, Correlation of Seismic Section UK-I to Electrical Resistivity Profile UK-002	124
Figure 4.3, Expanded View of Lines UK-I and UK-002.....	125
Figure 4.4, Correlation of Seismic Section UK-J to Electrical Resistivity Profile UK-003	126
Figure 4.5, Map of Major Zones of Deformation	127
Figure 4.6, Map of Fault Locations with Regard to the Location of Structural Features Interpreted in Past Studies	128
Figure 4.7, Map of Faulting and Contaminant Plume Location	129

LIST OF FILES

File 1, Thesis.pdf (76.02 mb)

CHAPTER ONE

INTRODUCTION

1.1 BACKGROUND

The Paducah Gaseous Diffusion Plant (PGDP), located in the Jackson Purchase region of western Kentucky, was constructed by the U.S. Atomic Energy Commission between 1951 and 1955 (Clausen et al., 1992). The plant began producing enriched uranium through the gaseous diffusion of uranium hexafluoride in 1952 (Garner et al., 1995). Today the plant is owned by the U. S. Department of Energy and operated by United States Environmental Corporation (USEC), Inc.

In August of 1988 trichloroethylene (TCE) and technetium-99 (Tc-99) were found in several privately-owned offsite wells located approximately one mile north of the plant (Clausen et al., 1992). In November of 1988 the Department of Energy acknowledged PGDP as the source of contamination and entered into an Administrative Consent Order with the U. S. Environmental Protection Agency. This has produced a series of comprehensive site investigations designed to determine the source and extent of groundwater contamination both on and off site. PGDP was designated a Superfund site in 1994, making it a priority for remediation (Jacobs, 1997).

TCE, a common chlorinated solvent, was primarily used at PGDP as a cleaning agent in degreasing facilities (Clausen et al., 1992). It is believed that over extended periods of time the consumption of drinking water containing concentrations of TCE over the Maximum Contaminant Level (MCL) of 5 parts per billion (ppb) can cause damage to

the liver, kidneys, immune and endocrine systems, and contribute to an increased cancer risk (US EPA, 2000). Tc-99, a fission byproduct, is believed to have been introduced through the reprocessing of nuclear reactor tails (Clausen et al., 1992). Tc-99 is assigned a MCL of 4 millirem per year, the general level associated with manmade radionuclides (US EPA, 2007). The ingestion of drinking water with levels of Tc-99 exceeding this concentration can lead to an increased risk of cancer and other adverse radiation-related health effects (US EPA, 2007).

Past studies have identified a TCE plume extending from the PGDP industrial area approximately 4-km to the northeast and a plume containing both TCE and Tc-99 extending almost 5 km northwest (Clausen et al., 1992) (Figure 1.1). The migration rate and direction of these plumes within the regional shallow gravel aquifer is of particular significance because of the proximities of the northeastern plume to multiple residences along Metropolis Lake Road (McCracken Co., KY) and the northwestern plume to Little Bayou Creek and the Ohio River (Clausen et al., 1992).

The proposed adverse health effects of TCE and Tc-99 coupled with the increasing probability of human contact, predominantly through the consumption of contaminated drinking water, have prompted the consideration of various remediation strategies. Previous undertakings have included the supply of potable water to impacted areas, restriction of public access to areas of known surface contamination (including portions of Little Bayou Creek), the construction of silt fences around above-ground disposal areas, and the remediation of certain identified Areas of Concern and Solid Waste Management Units. It is generally agreed that remediation will continue within the area through the use of established techniques as well as developing technologies.

1.2 STUDY OBJECTIVES

In order for realistic, high-resolution groundwater contamination assessment and/or mitigation strategies to be formulated for PGDP and surrounding areas, an accurate understanding of the subsurface geologic framework influencing contaminant plume migration must be defined. The environmentally sensitive nature of the PDGP remedial projects and the lack of broad outcrop or surface exposure for the majority of geologic units make high-resolution geophysical methods ideal for characterizing significant subsurface features that potentially correlate with the preferred groundwater flow path.

A non-invasive, high-resolution, integrated geophysical study was undertaken to understand the configuration of post-Paleozoic geologic features across the northwest contaminant plume. Specifically, this study utilized seismic and electrical geophysical techniques via multiple subsurface profiles of varying scale and resolution.

1.3 REGIONAL GEOLOGY

1.3.1 Structural Framework

The Jackson Purchase region is located within the northern Mississippi embayment of the central United States. The embayment, a 200,000 km² southward-dipping depression, was first proposed by Burke and Dewey as a failed arm of a triple rift junction created through the opening of the Gulf of Mexico (1973). Subsequent geological and geophysical investigations found that the embayment formed through the Mesozoic reactivation of a late Precambrian to early Cambrian rift, termed the Reelfoot rift (Ervin and McGinnis, 1975; Mooney et al., 1983; Braile et al., 1986; Sexton, 1988;

Hildenbrand and Hendricks, 1995; Kolata and Hildenbrand, 1997). Further geophysical investigations found a 70 km-wide northeast trending graben with approximately 2 km of structural offset coincident with the Reelfoot rift under portions of the northern Mississippi embayment (Kane et al., 1981; Hildenbrand et al., 1982). The Reelfoot rift is the host geologic and tectonic crustal structure for the New Madrid seismic zone, with the most intense present day seismicity located within the central graben (Braile et al., 1986; Kane et al., 1981; Johnston and Shedlock, 1992).

The Jackson Purchase region lies at the juncture of the Reelfoot rift and the equivalent aged Rough Creek graben (Figure 1.2). This juncture is one of the most intensely faulted areas in the central United States (Kolata and Hildenbrand, 1997). The Rough Creek graben is bounded to the north by the Rough Creek-Shawneetown fault system and to the south by a series of faults, including the Pennyriple fault system (Kolata and Nelson, 1991). The Rough Creek-Shawneetown fault system continues to the north where it abruptly bends, joining the Lusk Creek and Raum fault zones to form the northwestern boundary of the Fluorspar Area fault complex (Goldhaber, et al., 1992; Nelson et al., 1997). While the Reelfoot rift hosts “the most seismically active area of the central and eastern United States” (Sexton and Jones, 1986), the Rough Creek graben is relatively aseismic (Wheeler, 1997). There is currently a lack of consensus regarding the seismotectonic relationship between these two structures (Goldhaber et al., 1992; Braile et al., 1997; Potter et al., 1997; Wheeler, 1997).

Directly to the north of the Jackson Purchase region is the exposed, heavily faulted Fluorspar Area fault complex (FAFC). The FAFC is described by Nelson et al. (1997; 1999) as a series of predominantly high angle (>60°) faults striking between

N20°E and N40°E and outlining a series of horsts and grabens. The faults generally display normal offset, although reverse and oblique-slip offsets are present as well, reflecting multiple episodes of fault movement (Nelson et al., 1999). The FAFC is thought to have originated in the Cambrian along with the formation of the Reelfoot rift, with faulting continuing into the Quaternary (Potter et al., 1997; Nelson et al., 1997, 1999; McBride et al., 2002, 2003; Woolery and Street, 2002). The FAFC extends at least as far south as the northern bank of the Ohio River (Nelson et al., 1999; McBride et al., 2002) and into the Jackson Purchase region under the sedimentary cover of the Mississippi embayment (Kolata and Nelson, 1991; Nelson et al., 1997; Wheeler, 1997; Woolery and Street, 2002). McBride et al. (2002) have noted that several FAFC fault zones become wider and more complex from the bedrock uplands of Illinois southward into the Mississippi embayment portion of southern Illinois. Studies conducted north of the Jackson Purchase region in Massac and Pulaski counties, Illinois show faulting into Pleistocene sediments, with most recent known faulting appearing to predate Wisconsinan glaciation (Nelson et al., 1999; McBride et al., 2002).

1.3.2 Regional Stratigraphy and Depositional History

The stratigraphy of the Jackson Purchase region has been significantly influenced by the structural histories of the Reelfoot rift and Rough Creek graben and by its location within the northern reaches of the Mississippi embayment. Regional stratigraphy consists of northwest-dipping Paleozoic strata unconformably overlain by south-dipping unconsolidated to semi-consolidated clastic sedimentary deposits from the Cretaceous through the Quaternary (Nelson et al., 1999). Sediments thin northward, thus several

formations found in Tennessee and Alabama are absent within the northern Mississippi embayment (VanArsdale and TenBrink, 2000).

The sedimentary record of the region reveals a complex tectonic history. Cretaceous sediments rest in an angular unconformity on middle Mississippian limestone, and late Mississippian and Devonian shale locally. These are thought to represent a valley alluviation event following regional uplift and erosion associated with the emergence of the Pascola arch during the Late Paleozoic (Kolata and Nelson, 1991). A marine transgression marks the late Cretaceous, with regional deposition occurring in a fluvial deltaic environment (Clausen et al., 1992). Through the Paleocene the transgression of the Mississippi Embayment Sea continued with its maximum advance into the embayment occurring during this time (McBride et al., 2003). The extent of this transgression is demonstrated through the presence of clay sediment deposited under low energy, brackish conditions and the presence of deltaic sediment along what are thought to have been sea margins (Clausen et al., 1992).

During the Eocene renewed regional uplift led to a marine regression and the alluviation of stream courses, with deposition occurring in low gradient meandering streams that cut the planar deposits of the Paleocene (Olive, 1980). Several periods of uplift produced the multiple erosional surfaces that separate Pliocene deposits from underlying Eocene to Cretaceous sediments (Olive, 1980). During the Pliocene sedimentary deposition continued with the ancestral Tennessee River partially filling its course and an alluvial fan that began forming during the late Eocene and Oligocene increased in size until it covered most of the Jackson Purchase region (Olive, 1980).

Pleistocene glaciation events produced fluctuations in sea level which alternately

led to the erosion of underlying formations and the deposition of reworked alluvial sediments (Olive, 1980). Near the end of the Wisconsinan the Ohio River began to flow in its present course (Clausen et al., 1992) with loess deposits formed in upland regions from the extensive glaciation and deglaciation that occurred during the Quaternary generally found covering terraces adjacent to the river (Harris and Street, 1997). During the Holocene, rivers and tributaries slowly incised into underlying sediment, lowering their courses below the level of Wisconsinan flow. Holocene alluvial deposits are found adjacent to the Ohio River and in tributary stream valleys (Harris and Street, 1997).

1.4 STUDY AREA GEOLOGY

1.4.1 Location of Study Area

The study area is located approximately 16 km west of the city of Paducah in McCracken County, western Kentucky (Figure 1.3). It begins immediately north of the Paducah Gaseous Diffusion Plant and continues to within 1 km of the Ohio River. The study area extends to the west into the 1125-hectare (ha) West Kentucky Wildlife Management Area. The area also contains portions of Little Bayou Creek, an 11 km perennial stream which joins Bayou Creek 4.8 km north of the plant before entering the Ohio River.

1.4.2 Site Structure

Several past studies suggest that the Fluorspar Area fault complex extends beneath the study area (Drahovzal and Hendricks, 1996; Langston and Street, 1998; Woolery and Street, 2002). Faulting 8-km northwest of PGDP was originally mapped by

Olive (1980) with faults observed to extend into Tertiary and Quaternary sediments. The features were based on indirect evidence and could also be interpreted as resulting from non-tectonic forces. Previous integrated geophysical site studies near PGDP have identified several northeast oriented anomalies within the study area (Drahovzal and Hendricks, 1996; Langston et al., 1998). Langston et al. (1998) identified a large graben with strike of N50°E to N60°E intersecting the northwestern contaminant plume (Figure 1.4). Drahovzal and Hendricks (1996) provided an alternate interpretation of these seismic sections, instead identifying two faults with strikes of approximately N45°E. They also identified a lineament from SLAR imagery, with strike parallel to that of the faults (Figure 1.4).

1.4.3 Site Stratigraphy

Late Cretaceous through Tertiary sediments within the region show extensive lateral and vertical variation resulting from their complex depositional histories. In close proximity to the study area, middle Mississippian limestone is unconformably overlain by 92 to 101 m of south to southwesterly dipping sedimentary deposits (Olive, 1980) (Figure 1.5).

In many locations of the study area, limestone considered to be bedrock is unconformably overlain by the Tuscaloosa formation. The Upper Cretaceous Tuscaloosa formation, also known as the Post Creek formation, consists of rounded to subrounded chert gravel in a matrix of siliceous clay (Clausen et al., 1992).

Unconformably overlying the Tuscaloosa formation is the Upper Cretaceous McNairy formation consisting of interbedded and interlensing sand, silt and clay (Olive,

1980) (Figures 1.5 and 1.6). The McNairy formation, in the study area, is commonly divided into a lower sand-dominated member, a middle member of silty and clayey fine sand and an upper member of interbedded sands, silts, clays and sparse gravels (SAIC, 2002). The lower member is most commonly encountered in the southern portion of the Jackson Purchase region, with the middle member most prevalent near the study area (Clausen et al., 1992). The overlying Paleocene Clayton formation cannot be distinguished from the McNairy deposits without the study of palynological evidence and is undifferentiated with the McNairy for the purposes of this study. The total thickness of the Clayton-McNairy in the study area is approximately 60 m, although thicknesses of up to 90-m have been encountered to the south (SAIC, 2002).

South of the study area the Porters Creek Clay conformably overlies the McNairy formation. This Paleocene formation consists of massive montmorillonitic clay with varying amounts of silt and fine sand, but becomes sandier to the south (Clausen et al., 1992). Within the study area the Porters Creek Clay has been removed by the ancestral Tennessee River with only thin, isolated remnants remaining (Woolery and Street, 2002).

Unconformably overlying the Porters Creek Clay in the region are the Eocene Wilcox, Claiborne and Jackson formations, collectively known as the Eocene sediments (Clausen et al., 1992). These undifferentiated sand, silt and clay deposits are generally absent within the study area, but thicken to over 30 m to the south.

Within the study area the McNairy formation is unconformably overlain by the Continental Deposits, dating from the Pleistocene, Pliocene and possibly Miocene (Clausen et al., 1992) (Figure 1.5). The oldest deposits consist of lobes of poorly sorted silt, sand and gravel that begin under the southern end of the study area and extend north

beyond the Ohio River (SAIC, 2002) (Figure 1.6). Pleistocene sediments are commonly divided into the Lower Continental Deposits (i.e. Mounds Gravel or the Lafayette Gravel) and the Upper Continental Deposits (i.e. Metropolis formation). The Lower Continental Deposits consist of sand and gravel and follow the regional trend of southward thickening (SAIC, 2002). Upper Continental Deposits consist of a basal sand unit that fines upward to a fine sand or coarse silt covered by a silty clay or clayey silt and a layer of sand and gravel (SAIC, 2002). Textural features are generally gradational, with no recognizable bedding features apart from broad sand and gravel lenses (SAIC, 2002). The sandy and gravelly lower portions of the Continental Deposits are thought to provide a preferential flow path for groundwater in the area and are collectively known as the Regional Gravel Aquifer (RGA).

At least three late Pleistocene loesses unconformably cap earlier sediments (i.e. Loveland Silt, Roxana Silt and Peoria Loess in ascending age), but are all grouped as Pleistocene loess through the course of this study (Lettis and Associates, 2006). These deposits, consisting of unstratified clayey silt, have been found to have a relatively constant thickness of 3 to 4.5 m south of the study area and are believed to maintain this thickness until they approach the erosional surfaces of the Ohio River (SAIC, 2002).

Valley alluvial deposits, dating from the Pleistocene through the present, consist of sandy and silty clay or clayey silt with occasional sand and gravel (Clausen et al., 1992). They are found within the floodplain of the Ohio River, which has incised 6 to 9 m into underlying sedimentary deposits. Within the study area these deposits are found adjacent to Little Bayou Creek.

1.5 RELATED STUDIES

Numerous studies aimed at the identification and characterization of subsurface structure have been undertaken since the identification of TCE and Tc-99 in groundwater offsite of PGDP facilities. Research has been complicated by the scarcity of geologic outcrops, vegetation density, the presence of thick unconsolidated and semi-consolidated sediment incapable of transforming near-surface structure into identifiable geomorphic features, the long recurrence interval for large earthquakes and the environmentally sensitive nature of the study area (Drahovzal and Hendricks, 1997; Woolery and Street, 2002). As a result, the majority of past structural studies have utilized remote sensing and geophysical methods.

The first published study to propose structural control on groundwater flow and contaminant dispersal at PGDP was conducted by Drahovzal and Hendricks (1997). Proprietary seismic reflection data, U. S. Army Corps of Engineers “sparker” reflection data and lineaments inferred from Side-Looking Airborne Radar (SLAR) imagery were compiled in this study. Interpretation of these data was compared with the findings of Nelson et al. (1997) collected north of the Ohio River. Drahovzal and Hendricks (1997) found a strong northeast trend in lineaments as likely evidence of the continuation of the Fluorspar Area fault complex beneath the sedimentary infill of the Mississippi embayment. More specifically, they listed the Barnes Creek-Massac structure identified in southern Illinois as a likely source of observed faulting in the study area. In addition to their anomalous findings, the authors identified similarity in strike of the two major contaminant plumes to the structural trend of the area. These interpretations, along with the identification of a northeast trending fault zone coincident with the northwestern

contaminant plume, suggested that groundwater movement was likely affected by local faulting and fracturing.

The relationship between subsurface structure and groundwater flow in the study area was further examined by Langston et al. (1998). Over 17 km of near-surface SH-wave reflection and refraction data were collected to characterize the shallow subsurface in the vicinity of PGDP. Seismic reflection profiles revealed displacements in the bedrock reflector that propagated into the Lower Continental Deposits. Three fault zones coincident with the edges of the contaminant plumes and parallel to their directions of migration were identified and interpreted as preferential flow paths for TCE and Tc-99. Langston et al. (1998) also correlated their findings to the work of Nelson et al. (1997), providing further evidence for the continuation of the FAFC into western Kentucky.

Woolery and Street (2002) collected a 400 m high-resolution SH-wave CDP profile in the study area. This line was interpreted and correlated with a 710 m line collected by Langston and Street (1998). Both were found to demonstrate faulting and apparent fold propagation into the Quaternary section less than 10 m below the ground surface. The data also demonstrated structural styles associated with episodic movement. Major structural characteristics of these faults were consistent with those of the FAFC in southern Illinois. The surveys suggested structural continuation of the FAFC Raum Fault zone beneath the study area.

A localized fault study was conducted southeast of the study area at the location of a potential CERCLA waste disposal facility (SAIC Engineering, Inc., 2002). This study utilized P-wave and S-wave seismic investigation techniques. The seismic sections revealed 6 to 11 northeast-striking normal faults. The faults were interpreted to form

narrow horsts and grabens or to represent a series of rotated blocks. Quaternary faulting was found within 6.1 m of the surface. There was no attempt to extend the fault investigation outside the site. As with previous studies, no Holocene age faulting was identified.

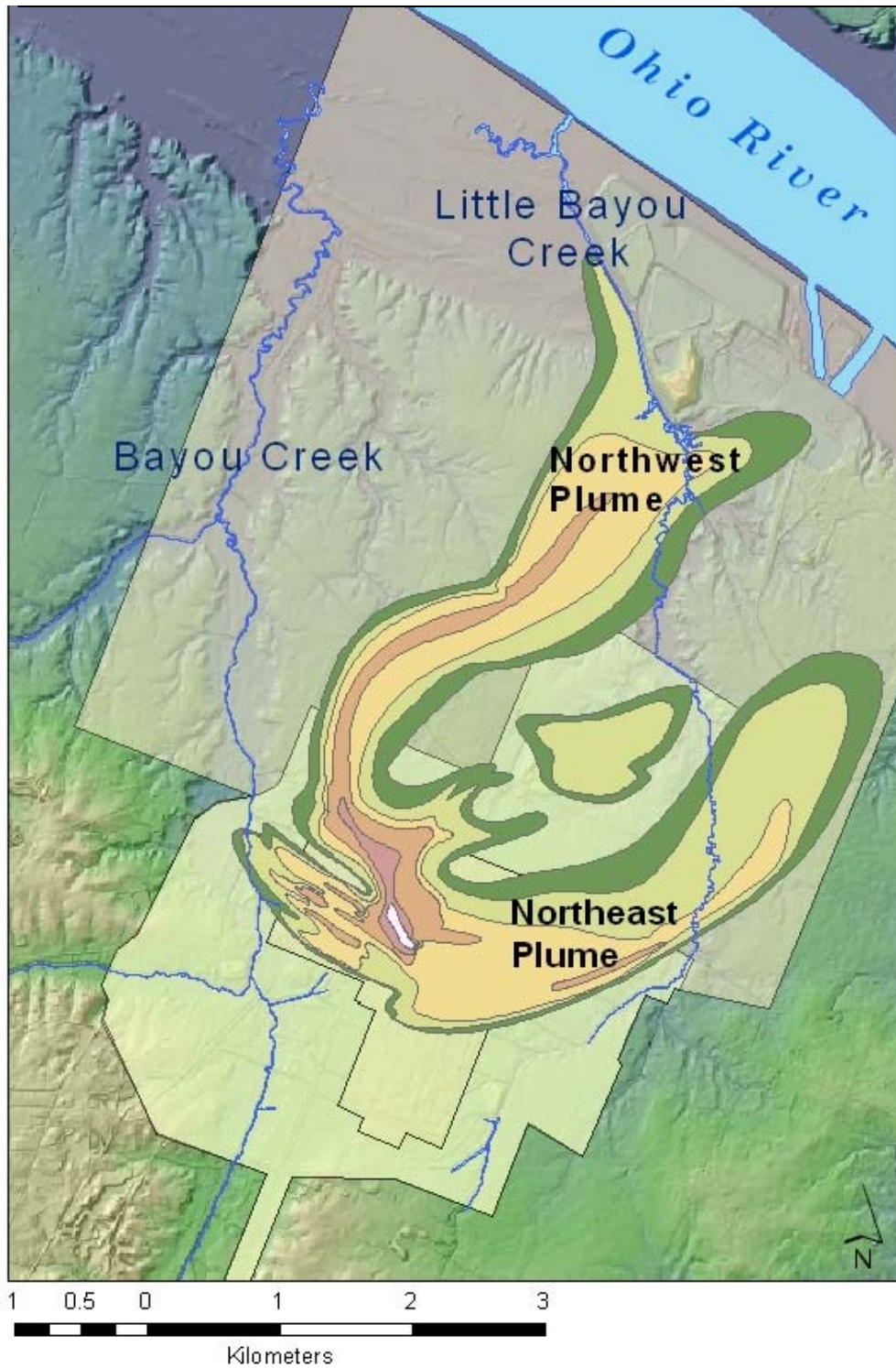


Figure 1.1: Location of TCE contaminant plumes north of the Paducah Gaseous Diffusion Plant, McCracken County, Kentucky.

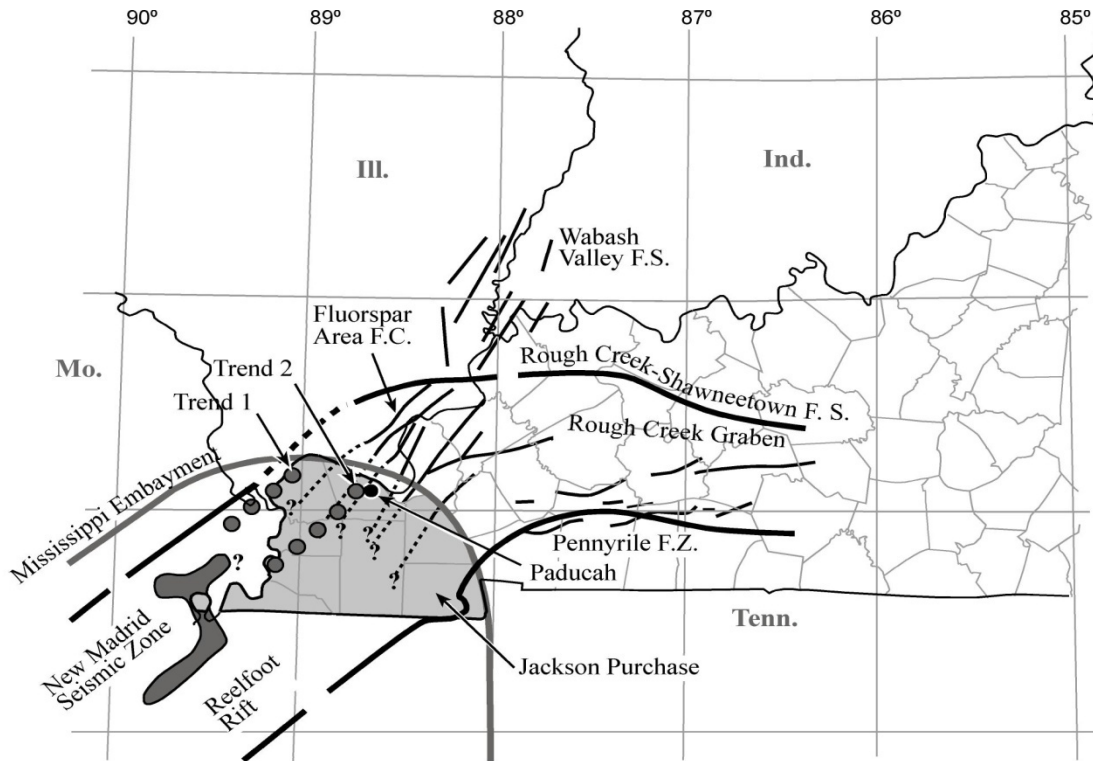


Figure 1.2: Structure of the central Mississippi Valley modified from Kolata and Nelson, 1997. Trends 1 and 2 indicate trends of seismicity identified by Wheeler (1997). The Jackson Purchase region is shown as the shaded portion of western Kentucky, within the Mississippi embayment.

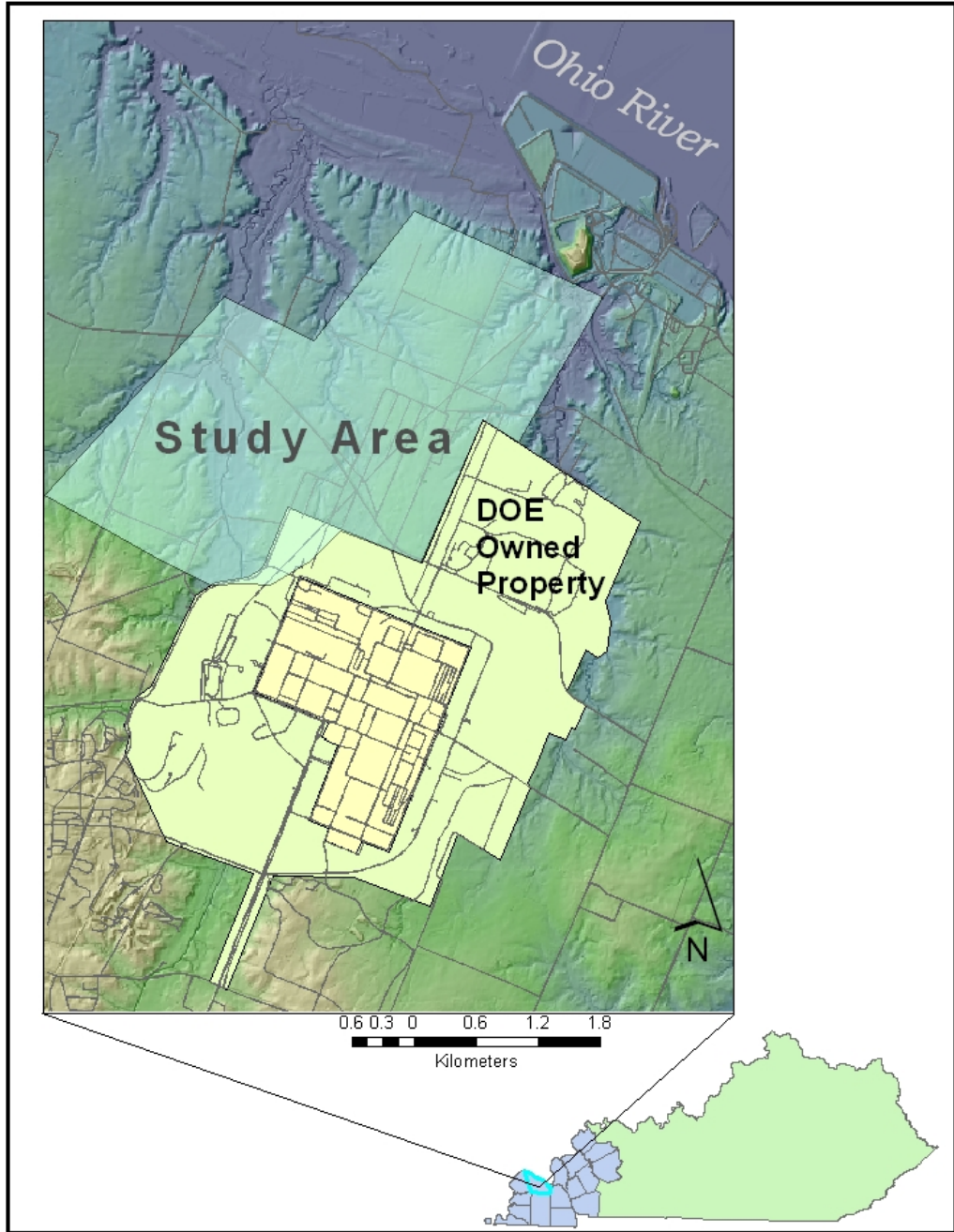


Figure 1.3: Location of the study area in McCracken County, western Kentucky.

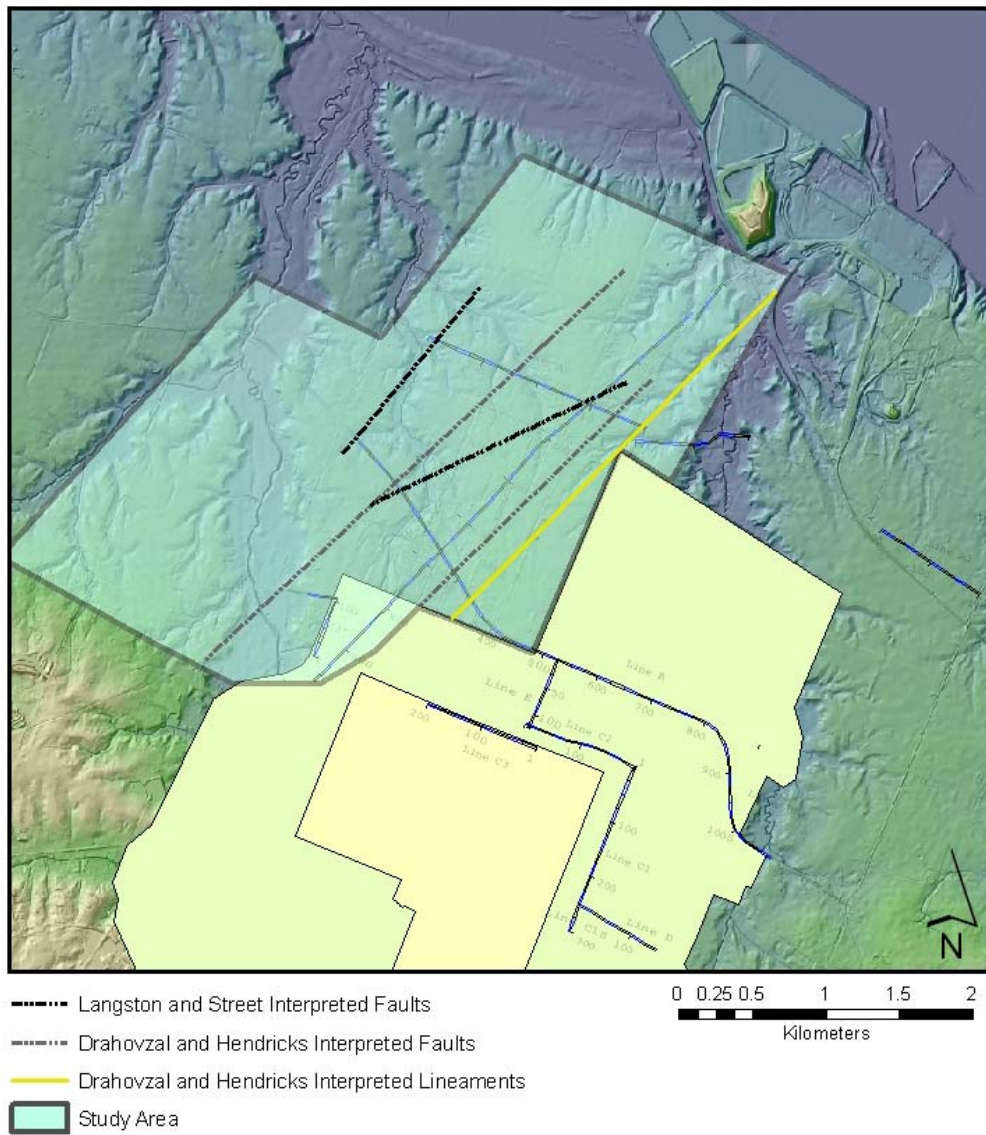


Figure 1.4: Locations of interpreted lineaments and faults within the study area, north of PGDP. Also shown are the locations of seismic lines collected by Langston and Street (1998).





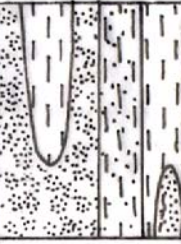


System	Series	Formation	Lithology	Approximate Thickness (m)	Description
Q u a t e r n a r y	Pliocene and Holocene	ALLUVIUM		0-2	Brown or gray sand and silty clay or clayey silt. Formed from recent floodplain deposits in the Ohio River valley
	Pleistocene	LOESS		3-4.5	Brown or yellowish-brown to tan or gray unstratified silty clay. Eolian sediments deposited in upland areas and sloping sides of stream valleys.
	Pleistocene	CONTINENTAL DEPOSITS		25-35	Orange to brown clayey silt with some very fine sand and traces of fine to medium sand; occasional layers of light gray clay and lenses of gravel. Deposited in a deltaic environment.
	Pliocene-Miocene (?)	CLAYTON FORMATION			Brown to reddish-brown silty and sandy chert gravel with beds of gray sandy gravel, silt, and clay. Deposited in a high-energy braided stream environment.
Cretaceous	Paleocene	McNAIRY FORMATION		58-65	Grayish-white to dark gray to black clay, often silty, micaceous, and lignitic. Interbedded with light gray to yellowish-brown very fine to medium grained sand. Mostly clay in upper part; sand and clay alternate throughout the middle; micaceous fine basal sand with possible lenses of gravel. Deposited in a deltaic environment.
		TUSCALOOSA FORMATION		unknown	White, well-rounded or broken chert gravel in clay matrix. Discontinuous stream-laid deposits.
Mississippian		MISSISSIPPIAN CARBONATES		150+	Dark gray limestone and interbedded chert with some shale. Deposited in a shallow marine environment.

Figure 1.5: Stratigraphic section of the study area. Modified from Clausen et al., 1992. Descriptions from Ch2M Hill (1989).

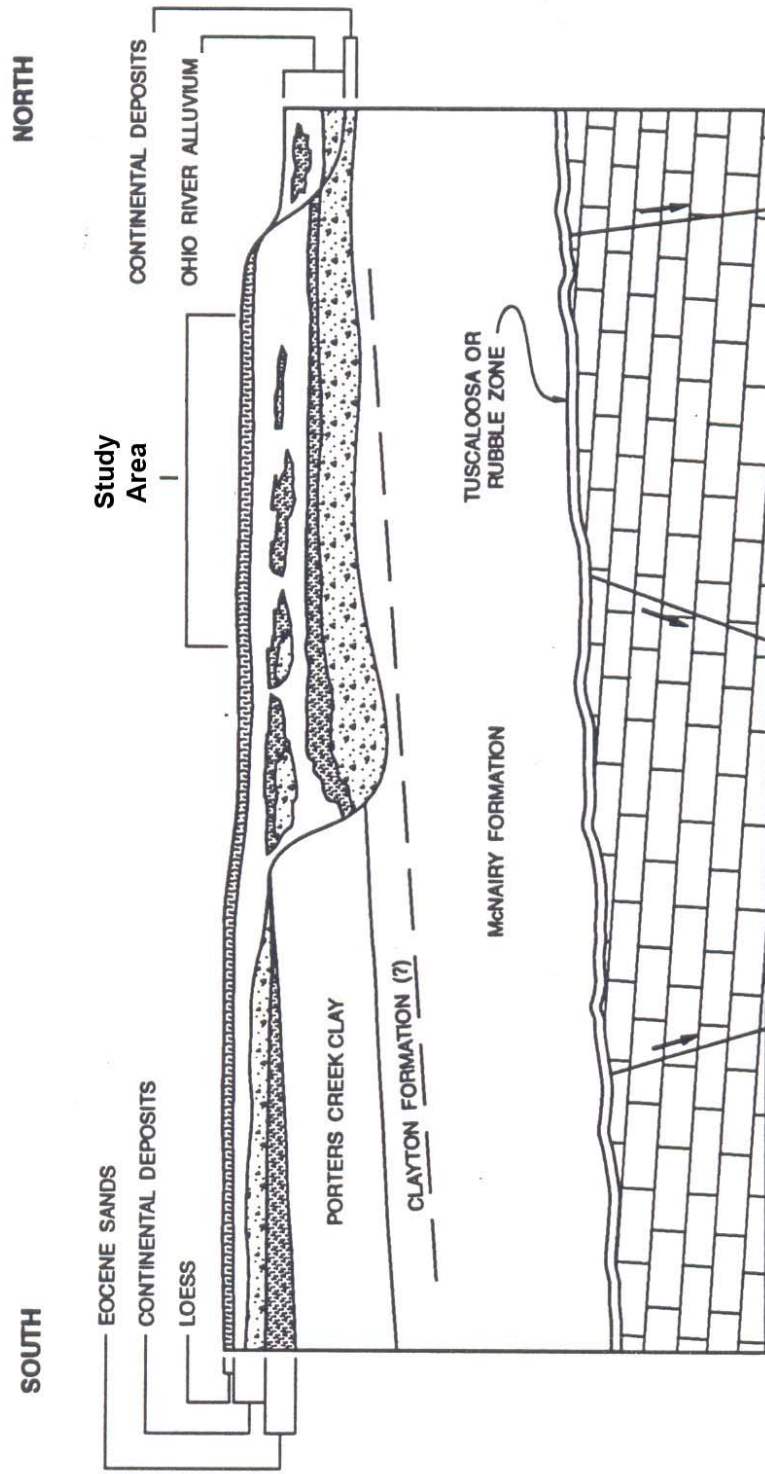


Figure 1.6: Schematic cross-section of the area modified from Clausen et al., 1992. Porters Creek Clay and Eocene Sediments are generally absent north of the terrace. Within the study area the McNairy formation is unconformably overlain by the Continental Deposits.

CHAPTER TWO

METHODOLOGY

2.1 MULTI-METHOD GEOPHYSICAL STUDIES

Site studies employing multiple near-surface geophysical surveys have increased in recent years. Decreased acquisition and processing times have made it economically viable to collect complementary data that depict varying physical properties at differing depths and resolutions. The joint interpretation of multiple data sets have been successfully used in a variety of environmental (Matis et al., 1994; Clement et al., 1997), structural, and paleoseismic investigations (Demagnet, 2001).

2.2 SH-WAVE SEISMIC REFLECTION

2.2.1 Method Justification

P-wave seismic reflection profiles have traditionally been used in near-surface imaging of areas of unconsolidated, water-saturated, sediment (Sexton and Jones, 1986; Sexton, 1988; Sexton et al., 1992; Schweig et al., 1992; VanArsdale et al., 1992; Williams et al., 1995; McBride and Nelson, 2001; Odum et al., 2002). This method contains inherent drawbacks, however. P-waves are fluid sensitive, traveling with the water rather than the lower velocity sediment matrix. As a result, stratigraphic changes may be masked by the saturation. In addition, the small temporal window associated with P-waves makes it difficult to identify reflecting boundaries because of the decreased separation of signal and coherent noise.

Although using S-waves for subsurface imaging may not be state-of-the-practice,

some researchers have found success using horizontally polarized shear waves in near-surface (<100 m) seismic investigations (Woolery et al., 1993, 1996; Woolery and Street, 2002; Harris, 1996; Harris et al., 1998). S-waves can reduce the associated problems of P-wave surveys. Shear waves are “framework waves” and are not affected by water. Also, S-waves have velocities five to ten times lower than those of P-waves, increasing the sizes of the optimal windows. The associated temporal and spatial separations aid in the interpretation of reflecting boundaries and the application of increased fold without the introduction of adverse wide-angle reflection effects. More importantly, lower velocities mean that resolution can be increased by a factor of two to three times through the use of S-waves. This increased resolution is of particular importance in imaging small displacements in near surface sediments. The horizontal SH-mode is preferable to vertically polarized SV-waves as SH-waves are more easily identified due to the lack of mode conversion at impedance boundaries.

2.2.2 Data Acquisition

The locations of the SH-wave seismic reflection surveys were selected using the mapped location of the northwest plume, existing seismic reflection profiles and, in the case of line UK-I, by the results of electrical resistivity profiling. Logistical concerns were also taken into consideration; thus surveys were conducted coincident with paved roads. Two seismic reflection profiles totaling 1.18 kilometers (km) were collected in the study area. An additional 5 seismic reflection profiles collected by Langston and Street (1997) and Wood, McDowell, Woolery and Wang (2000-2001) were processed to yield an additional 6.6 km of data (Figure 2.1).

UK-H data were collected using a 48-channel Geometrics NX StrataVisor seismograph with an internal hard drive and an instantaneous dynamic range of 115 dB. UK-I data were collected using two 24-channel Geometrics Geodes with an instantaneous dynamic range of 110 dB. Both recording systems used 24 Mark Products 30 hertz (Hz), horizontally-polarized geophones with 7.5 cm spikes laid out in two inline spreads. The geophones and shot interval were spaced at 2 m for line UK-H. The geophone spacing for UK-I was 4 m with a shot interval and near offset of 4 m. Seismic data were collected at a sample interval of 0.25 ms with a record length of 1.024 s. A 15 Hz low cut filter was used with the high-cut filter out. A 60 Hz notch filter was not required at either location.

The seismic energy source used in the surveys was provided by striking a horizontal steel H-pile with a 1.4 kilogram (kg) engineer's hammer. The hold-down weight of the H-pile, consisting of the weight of the H-pile section and the hammer swinger, was approximately 80 to 90 kg. The H-pile was coupled to the ground by embedding the edges in slit trenches. The SH-wave was generated by placing the H-pile anvil flanges orthogonal to the profile direction, but coincident with the horizontal hammer swing, thus generating a SH-mode wave. The H-pile was struck on both sides to produce oppositely polarized waves. Polarity reversals were used to enhance identification of the SH-wave signal. Records were generally vertically stacked six times at each shot point. Table 2.1 contains acquisition parameters for all seismic lines.

2.2.3 Data Processing

Seismic data were processed using VISTA 7.0 (Seismic Image Software, 1995)

running on a Pentium 4 computer. Although some variation was noted from line to line, a similar general processing procedure was followed in all seismic lines (Table 2.2).

During preprocessing, data field files were converted to standard SEG-Y format. 24- and 12-channel files were extracted from the 48-channel field files, providing 12- and 6-fold stacked data sets, respectively (Figure 2.2a).

Exponential gain recovery and mean amplitude scaling were applied followed by band-pass filtering and automatic gain control (Figure 2.2b). A geometry header was constructed for each line and applied to the combined and filtered files. Insignificant topographic changes along the survey transects required no elevation statics. Bad traces resulting from poorly coupled geophones, disconnected geophones, etc., were nulled and muting of coherent noise (i.e., refraction, etc.) was applied (Figure 2.2c). Offset sorting and stacking for semblance analysis was used to derive the velocity model. The normal moveout (NMO) correction was applied as a function of the velocity model. The data were CDP sorted and stacked to produce a “brute” stack image.

Post-stack operations consisted of frequency-wave number (F-K) filtering applied to the CDP stack and additional AGC applied when needed. In order to minimize artifact generation (e.g., Gibbs effect) gentle filter slopes were applied. Residual statics were also applied to increase signal coherency. Detailed processing procedures for each line are given in section 2 of Appendix A.

2.2.4 Resolution

Vertical resolution is defined by the ability to distinguish reflections from the top and bottom of the layer (Geldart and Sheriff, 2004). At minimum there must be a half-

cycle separation between the reflections (Geldart and Sheriff, 2004). This corresponds to a minimum thickness of one-quarter wavelength, termed the resolvable limit. A layer in which the top and bottom are not distinguishable may still be detectable as a single seismic reflection (Sheriff and Geldart, 1989). The detectable limit corresponds to a minimum thickness of approximately one-eighth of the wavelength (Sheriff and Geldart, 1989).

The horizontal resolution is determined by the radius of the first Fresnel zone, the portion of the reflector from which reflected energy arrives approximately in phase (Geldart and Sheriff, 2004). Wave energy within the first Fresnel zone interferes constructively, with the contributions of successive pairs of zones effectively canceling each other (Geldart and Sheriff, 2004). The radius of the first Fresnel zone (R_1) is defined by the relationship:

$$R_1 = \left(\frac{V}{2}\right)\left(\frac{t}{f}\right)^{1/2}$$

Where, V = velocity, t = two-way travel time, and f = frequency.

2.3 ELECTRICAL RESISTIVITY IMAGING

2.3.1 Method Justification

Electrical resistivity imaging (ERI), also referred to as electrical resistivity ground imaging (ERGI) and electrical resistivity tomography (ERT), utilizes an array of electrodes placed on the ground surface with any two electrodes used to introduce electrical current and another two electrodes used to measure the associated potential (i.e., voltage) at a specified distance. Because electrical flow is assumed to disperse

throughout the subsurface, values recorded at the surface provide information on the resistivities of near-surface materials (Baines et al., 2002). Electrical resistivity surveying performed through the measurement of a series of constant separation traverses, with electrode separation increasing for successive traverses, provides horizontal and vertical variation in resistivity that can be transformed into a vertical cross section through inversion (Griffith and Barker, 1993). If information on local lithology is available, the inverted resistivity section can be converted to a geologic cross-section.

Although tables depicting common ranges of resistivity values for many earth materials are available (AGI, 2007a), resistivity is largely controlled by site-specific geologic and hydrologic conditions. The largest influence on resistivity in the shallow subsurface is the electrolytic conduction of aqueous fluids distributed across grain boundaries or contained in pores, fractures and faults (Ward, 1990). A secondary factor influencing resistivity is grain size, with resistivity increasing in proportion to grain size (Chambers et al., 1997). As a result of these properties electrical resistivity has been used successfully in groundwater prospecting, groundwater and soil remediation efforts (Matis et al., 1994; Clement et al., 1997; Chambers et al., 2006), in the study of subsurface sedimentary structures (Baines et al., 2002), and in the study of subsurface faulting (Hawley, 1943; Rayner et al., 2007).

Two-dimensional (2D) resistivity surveys have been shown to provide an efficient and economical method of obtaining near-surface stratigraphy and structure information when it can be assumed that subsurface features are essentially 2D and strike perpendicular to the measured profile (Griffith and Barker, 1993). If these conditions are not met, three-dimensional (3D) structures may be misrepresented and significant noise

can be introduced, reducing the resolution of the profile. In areas of complex geology, 3D imaging should be used for accurate subsurface characterization.

2.3.2 Data Acquisition

A dipole-dipole array was selected for use in all surveys (Figure 2.3). This configuration provides better horizontal resolution and better depth coverage at the ends of the survey lines than other traditional arrays and also avoids electromagnetic coupling (Dahlin and Bing, 2003). The dipole-dipole array is sensitive to in-line spacing error and three-dimensional geologic variations that produce a lower signal-to-noise ratio than other array types, however. This limits depth penetration and often requires greater care in data processing and interpretation as the noise can lead to artifacts and distortions in the inverted resistivity section (Dahlin and Bing, 2003).

The locations of the 2D electrical resistivity surveys were located with regard to the locations of SH-wave seismic reflection profiles, the northwestern plume and logistical considerations. Four 2D resistivity profiles totaling 2.024 km were collected for the study (Figure 2.4).

Data were collected using a single-channel SuperSting earth resistivity meter with internal memory and switching for 56 electrodes. 45 centimeter (cm) stainless steel electrodes were driven 28 to 32 cm into the ground and coupled to four inline passive cables. Roll-along was performed as needed. Electrode spacing was between 2 and 6 m (Table 2.3). AGI “smart-electrode” internal switching used 4 electrodes for each measurement with electrodes selected from a command file created by the administrative (SSAdmin) software. The maximum dipole separation was set at 6-times the current-

electrode spacing and the maximum n-value was set at 8. Values above these generally produce unacceptable levels of noise (AGI, 2007b).

The SuperSting unit serves as both the receiver of measured data and the source for electrical current, with power supplied by a 12 volt deep-cycle battery. Two cycles of current injection lasting 1.2 seconds each were used for every electrode configuration. A maximum error of 2% between any two readings was selected with 1 repeat measurement when the maximum error was exceeded. Maximum injected current was set at 2000 milliamps (mA). A contact resistance test was performed on all lines before measurements were taken to ensure proper operating conditions.

2.3.3 Data Processing

An iterative inversion method using average apparent resistivity was applied to produce the final resistivity sections. Although smooth model inversion was used in preliminary trials, robust least squares inversion was used because its minimization of the absolute values of data misfit (L_1 -norm) was better constrained compared with the minimization of the squares of misfit data (L_2 -norm) (Dahlin and Bing, 2003). As a result this method is more adept at handling noisy data and resolving lateral resistivity boundaries (AGI, 2006).

EarthImager 2D version 2.2.0 resistivity inversion software (AGI, 2006) was used to process the collected data and produce inverted subsurface resistivity profiles by minimizing the disagreement between measured and predicted resistivity values (Figures 2.5, 2.6). Data with minimum voltage below 0.2 millivolts (mV), absolute V/I below 0.0005 ohms (Ohm), apparent resistivity below 1 Ohm·m and above 10000 Ohm·m, and

data with repeat error above 3% were removed from the data set before beginning the inversion. A finite element forward modeling method with the Cholesky decomposition forward equation solver and the Dirichlet boundary condition was applied to the data. Two mesh divisions were used between successive electrodes. A thickness incremental factor of 1.1 was applied in an attempt to account for the decrease in model resolution with depth.

For the inversion, stabilizing and damping factors of 10 were selected. Reciprocal surveys were not conducted due to time constraints; therefore a default of 3% estimated noise was used. A robust data conditioner and robust model conditioner of 1 were used with a resolution factor of 0.2 (Table 2.4). Because the surveys were designed to image both vertical stratigraphic change and lateral discontinuities, the horizontal/vertical roughness ratio was set between 0.5 and 2.0. Although topographic information was collected for all lines, elevation change was not considered to produce an appreciable effect on any inverted resistivity section with the exception of UK-004. Therefore, this is the only line where a terrain correction was applied. Continuous resistivity profiling (CRP) was used in the inversion of line UK-002 due to the large number of data collected.

The objective of inversion is to find a model whose response fits most closely to the measured data, with the root mean square (RMS) error indicating the quality of the fit. In order to reduce RMS error and prevent the introduction of artifacts, data with a relative misfit above a defined percentage was removed from the data set and the set was inverted again (Table 2.5). While preferable to retain as much of the original data as possible, it has been shown that up to 30% of data points can be removed without any

significant decrease in the resolving power of the data set (AGI, 2007b). The last iteration to produce a considerable decrease in RMS error, as shown by the convergence curve, and yielding an acceptable RMS error was selected as the representative model for the data set (Figure 2.7). The relative model sensitivity, equivalent in magnitude to the model vector obtained by multiplying the transposed sensitivity matrix by the sensitivity matrix and extracting the diagonals, was also considered in evaluating the models (Figure 2.8). Model blocks with higher sensitivities, such as those in close proximity to the electrodes, commonly correlate to better model resolutions.

2.3.4 Resolution

The resolution of an electrical resistivity imaging survey is dictated by the geometry of the survey and, to a lesser extent, by subsurface resistivities (Stummer et al., 1994). Features underlying the electrode array can be resolved to as little as one-half the electrode spacing, although caution should be exercised in the interpretation of features with dimensions less than one electrode spacing (AGI, 2007a). While decreasing electrode spacing increases the resolution of small features, it also decreases the depth of penetration. Although the lateral resolution of the dipole-dipole array is superior to most other arrays, its resolution decreases exponentially below depths equivalent to 14-25% of the sum of the lengths of the four inline cables (AGI, 2007a). Because the shallow subsurface in the study area is relatively conductive, which can introduce more noise into the data, a maximum effective depth of 15% of the survey length was used.

Table 2.1: Acquisition parameters for all seismic reflection profiles.

Seismic Reflection Acquisition Parameters										
Line Name	Suvey Type	Near Offset	Shot Interval	Geophone Spacing	Sample Interval (ms)	Record Length (s)	Acq. Filt. - Low Cut (Hz)	Acq. Filt. - Hi Cut (Hz)	Notch Filter (60 Hz)	Geophone (Hz)
UK-A3 ₁	SH-wave	0m	4m	4m	0.5	1.00	10	250	Yes	30
UK-B ₁	SH-wave	0m	4m	4m	0.5	1.00	10	250	Yes	30
UK-G1 ₁	SH-wave	0m	4m	4m	0.5	1.00	10	250	Yes	30
UK-G2 ₁	SH-wave	0m	4m	4m	0.5	1.00	10	250	Yes	30
UK-H	SH-wave	2m	2m	2m	0.25	1.024	15	Out	No	30
UK-I	SH-wave	4m	4m	4m	0.25	1.024	15	Out	No	30
UK-J ₂	SH-wave	2m	2m	2m	0.25	1.024	15	Out	Yes	30

1: Collected by Langston and Street (1997)

2: Collected by Wood, McDowell, Woolery and Wang (2000-2001)

Table 2.2: Generalized processing procedure for SH-wave seismic reflection data.

Generalized Steps for Processing Seismic Reflection Data	
Processing Step	Comment
Reformat Data	Convert from DAT format to standard SEG-Y format
Extract Data	Create file containing data from optimum window
Exponential Gain Recovery	Correct for spherical divergence
Mean Amplitude Scaling	Equalize traces
Bandpass Filter	Attenuate noise outside of a range of frequencies
Automatic Gain Control (AGC)	Normalize data within a given time window
Geometry	Apply acquisition geometry header to traces
Trace Kills	Remove noisy traces
Trace Mutes	Remove refractions, direct waves, and ground roll
Sort by Offset	Reorder data based into common-offset gathers
Stack by Offset	Combine sorted files
Velocity Analysis	Obtain a subsurface velocity model
Normal Moveout (NMO)	Correct for source-receiver travel time differences
Sort by CDP	Reorder data by common subsurface point
Stack by CDP	Vertically sum NMO-corrected CDP gathers
F-K Filter	Attenuate linear coherent noise

Table 2.3: Acquisition parameters for electrical resistivity imaging profiles.

Electrical Resistivity Imaging Acquisition Parameters									
Line Name	Array Type	Electrode Spacing (m)	Maximum n	Maximum Dipole	Measure Time (s)	Cycles	Maximum Error (%)	Maximum Repeat	Maximum Current (mA)
UK-001	Dipole-Dipole	6	8	6	1.2	2	2.0	1	2000
UK-002	Dipole-Dipole	6	8	6	1.2	2	2.0	1	2000
UK-003	Dipole-Dipole	6	8	6	1.2	2	2.0	1	2000
UK-004	Dipole-Dipole	2	8	6	1.2	2	2.0	1	2000

Table 2.4: Standard resistivity inversion settings used on all electrical resistivity imaging profiles.

Resistivity Inversion Settings	
Number of CG iterations	6
Starting iteration of quasi Newtonian method	20
Smoothness factor	10
Damping factor	10
Estimated noise	3%
Robust data conditioner	1
Robust model conditioner	1
Minimum resistivity (Ohm-m)	1
Maximum resistivity (Ohm-m)	100000
Model parameter width	1
Model parameter height	1
Resolution factor	0.2
Stop Criteria:	
Number of iterations	8
Maximum RMS error	3%
Error reduction	5%

Table 2.5: Horizontal/Vertical Roughness Ratio for each profile along with maximum percentage of relative data misfit retained, number of data points removed and the corresponding total percentage of data removed (including that selected for removal through initial settings). Corresponding RMS error is also included for the representative model selected from each trial.

Electrical Resistivity Processing					
Line Name	Horiz/Vert Roughness Ratio	% Relative Data Misfit	Data Points Removed	% Data Removed	RMS Error
UK-001	1.2	NONE 10	NONE 95	0.1 7.2	9.34 4.64
UK-002	1.2	NONE 21 16.5	NONE 247 177	15.3 23.6 29.6	15.41 9.11 7.86
UK-003	1.0	NONE 20 14	NONE 223 61	6.7 23.5 28.0	27.14 7.40 5.90
UK-004	0.5	NONE 17.5 12.5	NONE 63 57	0 13.2 25.1	14.32 9.54 6.14

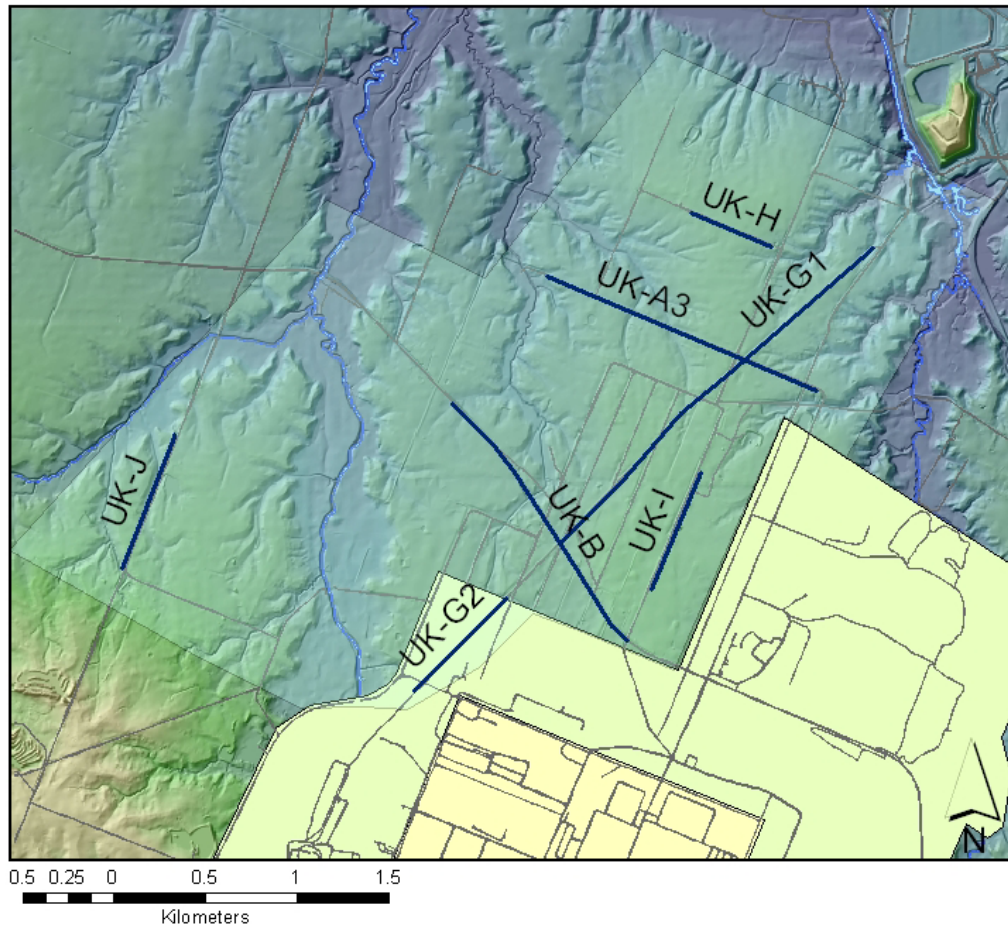


Figure 2.1: Locations of seismic reflection surveys within the study area.

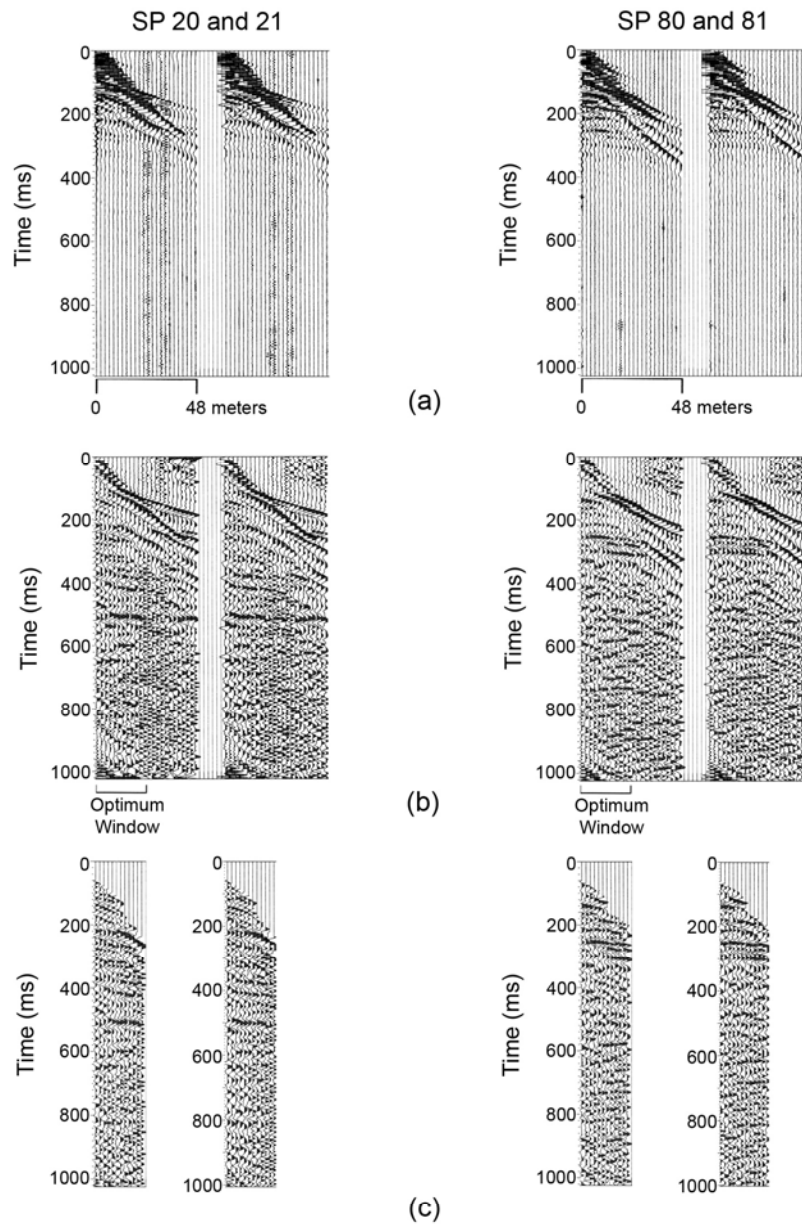


Figure 2.2: Example of field files collected on two sides of a fault. Data are shown as raw (a), bandpass filtered (25/85 Hz) with AGC applied (150 msec) (b), and muted with 500 ms AGC applied (c). Additional field files are provided in Appendix A, section 3

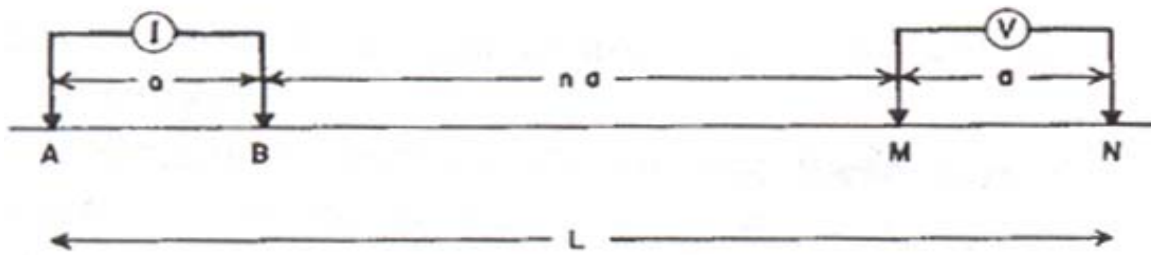


Figure 2.3: Schematic layout of a 4-electrode dipole-dipole array modified from Edwards, 1977. The inter-electrode spacing is represented by “a” while “n” is a scaling factor which determines the distance from the current electrodes to the potential electrodes.

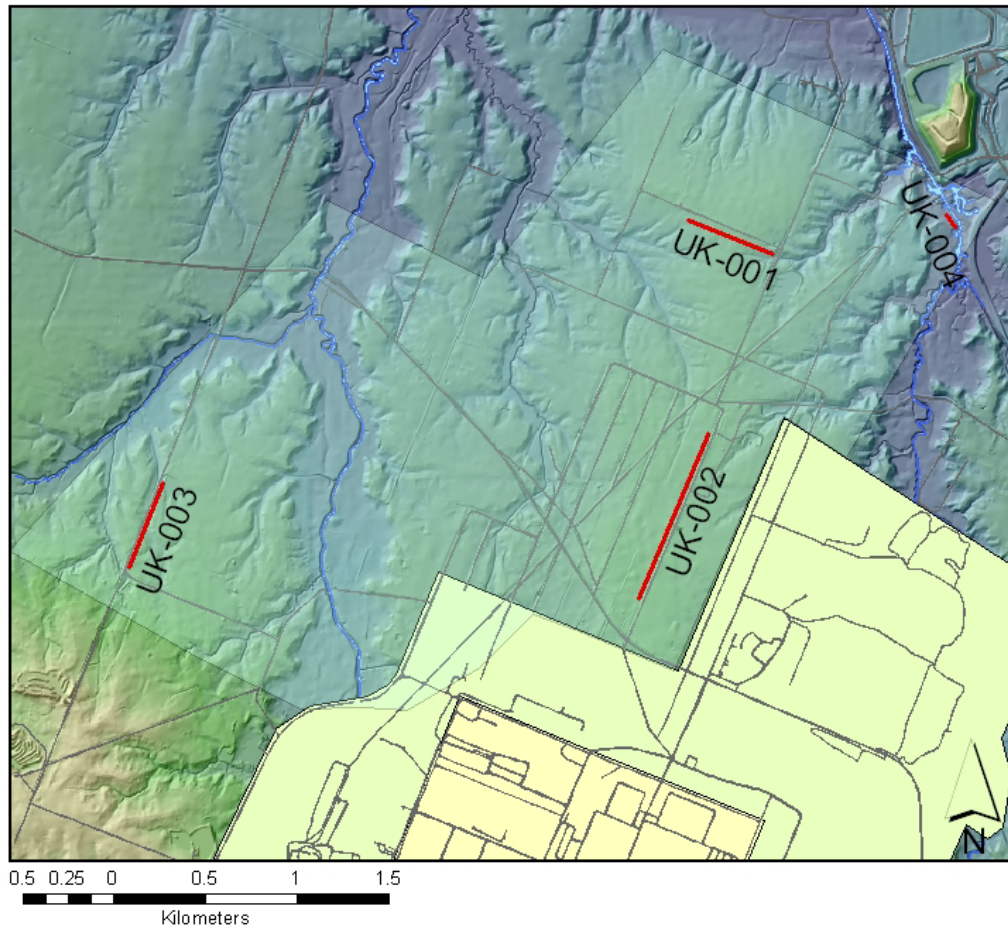


Figure 2.4: Locations of electrical resistivity imaging surveys within the study area.

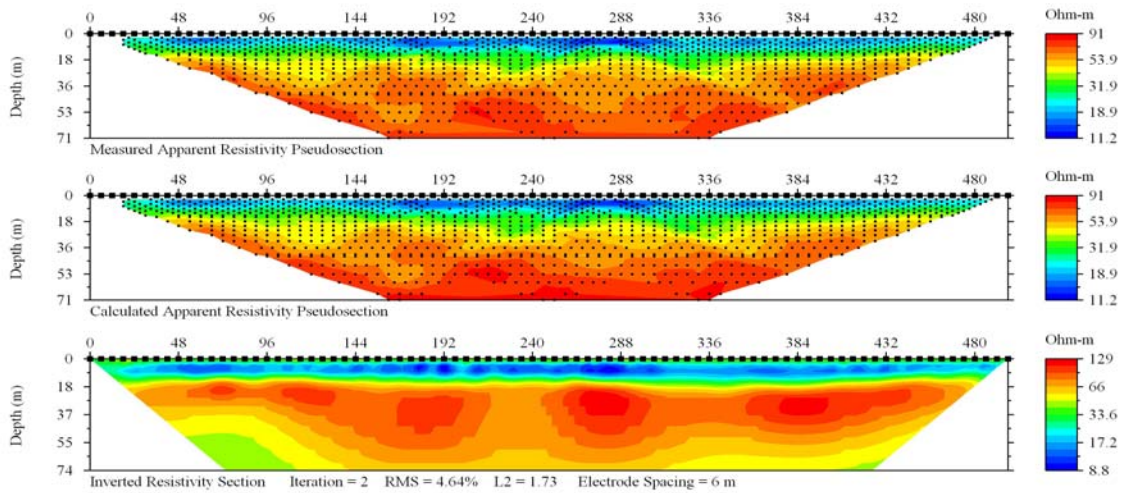


Figure 2.5: Example of a measured apparent resistivity pseudosection (top), a calculated apparent resistivity pseudosection (middle), and an inverted resistivity section (bottom). The pseudosections represent the measured and calculated resistivities of electrically homogeneous and isotropic half-spaces which would result in the recorded resistivity values. The inverted resistivity section attempts to approximate as closely as possible subsurface resistivity conditions. Measured and calculated apparent resistivity pseudosections, along with inverted resistivity sections, are provided for all trials in Appendix B, section 1.

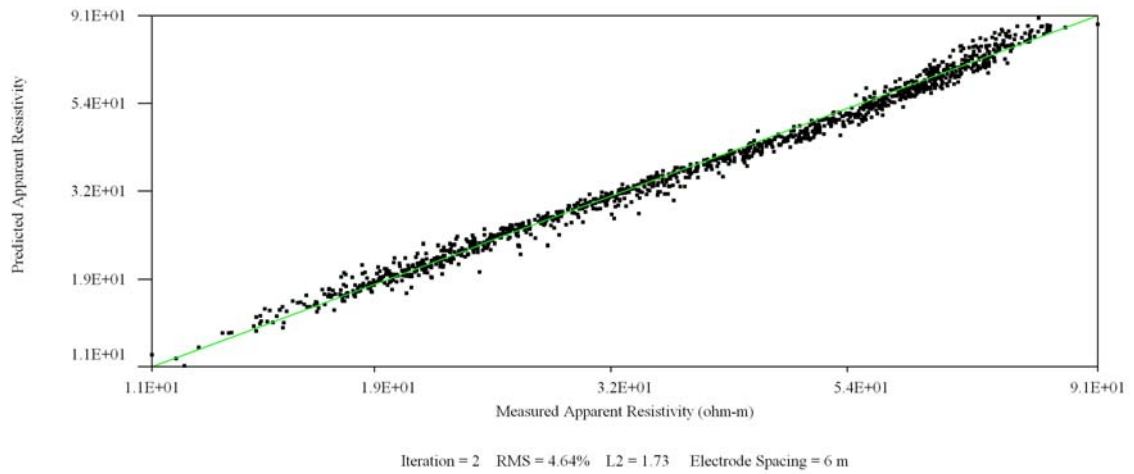


Figure 2.6: Example of a predicted apparent resistivity vs. measured apparent resistivity cross-plot. Cross-plots visually demonstrate the closeness of fit between the predicted and measured pseudosections, providing another means to assess the quality of the model. Cross-plots for all trials are given in Appendix B, section 3.

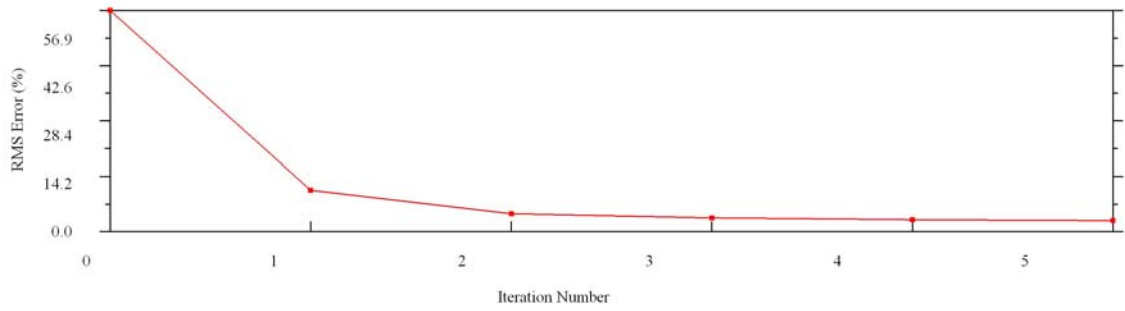


Figure 2.7: Example of a convergence curve of the resistivity inversion. The iteration at which the RMS error begins to converge is generally chosen as the representative model for the data set. Convergence curves for all trials are provided in Appendix B, section 2.

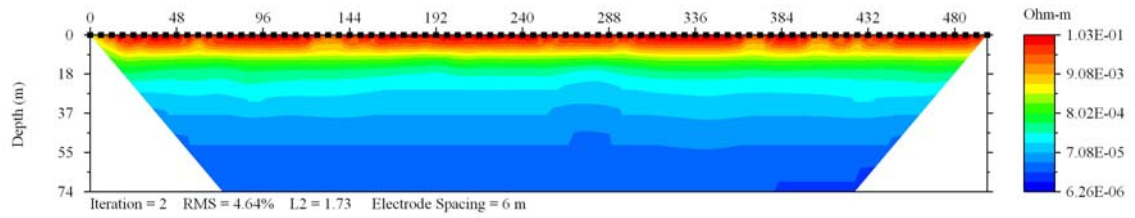


Figure 2.8: Section representing the sensitivity of the model at different locations. Higher sensitivities commonly result in higher model resolutions. Sensitivity sections for all trials are given in Appendix B, section 4.

CHAPTER THREE

INTERPRETATION

3.1 SEISMIC REFLECTION BACKGROUND

3.1.1 General

High-resolution near-surface SH-wave stacked reflection profiles were used to identify structural, stratigraphic and erosional features. All interpretations are shown on the frequency-wave number (F-K) filtered sections. Due to the complex nature of near-surface geology only prominent and coherent features visible in multiple horizons and within the resolvable limits were considered. Interpretations are focused on major deformation zones, with secondary or subtle structural features that occur outside of these zones shown on the interpreted sections, but not discussed. Interpretations of faulting were based on factors such as reflector offset, deformation, thickening and/or changes in apparent dip of reflectors, loss of coherency and the presence of diffractions. Distinct offset on the bedrock reflector was generally more prominent than within the soil horizons. This is most likely attributable to factors such as the lower shear strengths of soils, causing bending of the unconsolidated material rather than sharp offsets, lower impedance contrasts between soil layers and a lower degree of offset higher in the section. In addition, constructive interference caused by spatial sampling less than the horizontal resolution can diminish the ability to image a distinct offset. An example erosional feature is also shown on one section. Other smaller scale sedimentary features are seen in the sections, but were considered to be outside the scope of this study. Uninterpreted sections are presented in Appendix A, section 1.

3.1.2 Vertical Exaggeration

In order to interpret the seismic sections in a meaningful way two-way travel time was converted to depth. This was done through the use of the Dix equations, given as:

$$V_{\text{int}} = \left[\frac{(t_2 \cdot V_{\text{rms}2} - t_1 \cdot V_{\text{rms}1})}{(t_2 - t_1)} \right]^{1/2}$$
$$h = V_{\text{int}} \cdot \frac{(t_2 - t_1)}{2}$$

Where $V_{\text{int},n}$ is interval velocity, $V_{\text{rms},n}$ and $V_{\text{rms},n-1}$ are stacking velocities of the interval, t_n and t_{n-1} are the two-way travel times to the upper and lower reflectors, respectively, and h is equivalent to the thickness of the interval.

The conversion of two-way travel time to depth leads to vertical exaggeration of the profile. Vertical exaggeration changes with depth due to velocity fluctuations within the time section. Therefore, the intervals used in the determination of the vertical exaggeration were confined to the area between the first identifiable reflector and the top of the bedrock reflector. Below this depth velocity increases rapidly. For lines with 4-m spacing vertical exaggeration was determined to be 0.4 within ± 0.05 . Due to velocity contrasts between subsurface sediments underlying lines UK-H and UK-J, UK-H was determined to have a vertical exaggeration of 0.8, while UK-J showed a 1:1 relationship between horizontal distance and depth. It is important to note that on sections where the ratio of the vertical scale to the horizontal scale is less than one, the fault dip angle on the profile appears lower than actual. Reported dip angles were corrected for exaggeration by the comparison of horizontal distance to depth rather than visual inspection.

3.1.3 Resolution

Examination of amplitude vs. frequency graphs for the seismic reflection lines provided two distinct peaks, a lower frequency amplitude spike corresponding to the dominant bedrock frequency and a higher frequency spike corresponding to the near-surface soil layers (Figure 3.1). Bedrock frequency varied within a relatively fixed range of 30-40 Hz while near surface dominant frequencies ranged from 45 to 75 Hz. Higher frequencies are desirable because they produce images with higher horizontal and vertical resolutions. Field acquisition procedures can influence the signal frequencies (e.g. type of source, variations in hammer swing, source-to-ground coupling, variations material attenuation, etc).

The horizontal resolution of features is determined by the radius of the first Fresnel zone. Based on near surface-velocities, two-way travel times and dominant frequencies, near-surface horizontal resolution was determined to range between 6 and 8 m for lines with 4 m spacing, or approximately 1.5 to 2 shotpoints. Lines with 2 m spacing yielded horizontal resolutions of approximately 4 to 6 m, or 2 to 3 shotpoints (Table 3.1). At depth, horizontal resolution generally ranged from 19 to 23-m for 4-m lines, while lines with 2 m spacing yielded a value of approximately 20 m (Table 3.2).

Vertical and detectable resolutions of a reflector are determined by the wavelength. Within the near surface, the resolvable limit for lines with 4 m spacing ranged from 0.8 to 1.1 m, while the detectable limit was between 0.4 and 0.6 m (Table 3.1). Lines with 2 m spacing had lower resolvable and detectable limits of 0.6 to 0.8 m and 0.3 to 0.4 m, respectively. The longer dominant wavelength of the bedrock reflector yielded a resolvable limit of 2.1 to 3.0 m and a detectable limit of 1.0 to 1.5 for lines with

4- m spacing (Table 3.1). Lines with 2 m spacing showed similar values of 2.4 to 2.7 m for the resolvable limit and 1.2 to 1.3 for the detectable limit (Table 3.2).

3.1.4 Identification of Reflectors

Reflections were correlated to lithologic interfaces by comparing the depth calculations with local boring logs. In general, the top-of-bedrock reflector has the highest amplitude. This is due to the high impedance contrast between the lithified limestone bedrock and the overlying semi-consolidated sediments. The top of the Paleozoic bedrock, identified as R3, has the lowest coherency. Interfaces within the sediment section were lower in amplitude, but a few were coherent throughout the profiles and generally between lines. The highest amplitude reflection within the sedimentary section is the interface between the undifferentiated sands and clays of the Cretaceous McNairy formation and the coarser sands and gravels of the Lower Continental Deposits (R2). Another impedance boundary (R1), seen on most profiles, is correlated with the top of the Pleistocene age Lower Continental Deposits, a horizon at which the sands and gravels of this unit transition to the predominantly clayey sands and silts of the Upper Continental Deposits.

With the exception of borings Z-12 and Z-16 which extend to bedrock, borings within the area are generally shallow, reaching depths ranging between 20 and 30 m (Figure 3.2). As a result, confident depth correlations were limited to the top of the Lower Continental Deposits and to the top of the McNairy formation in most cases. The limited borehole data provided local depths to bedrock of 98 and 101 m, while depth calculations yielded lesser values of 82 and 83 m, respectively. This indicates potential

error between 16 and 18%. In the near surface, calculated and measured depths varied between 0 and 12%. These discrepancies may be due to factors such as irresolvable near-surface velocity variations, differences in the classification of soil horizons based on visual sediment classifications versus measured changes in the elastic properties of the soil, and the use of off-line borings. It is believed that the calculated bedrock depths were systematically lower than those provided from the boring logs due to difficulties inherent in the semblance analysis of higher velocity layers. As a result, the stacking velocities for the bedrock reflectors are 20 to 30% lower than expected in this environment. Depths to lithologic units based on boring logs are provided in Appendix C.

3.2 SEISMIC LINE INTERPRETATION

3.2.1 Line UK-A3

Line UK-A3 is a 1652-m ENE–WSW-oriented profile acquire along an unpaved road. This nonproprietary section was originally collected by Langston et al. (1998) as part of general reconnaissance for a related groundwater study. Data quality is good and representative of the entire line. Reflector R3 is strong and generally coherent throughout the section. At locations where there is a loss of bedrock coherency, it is likely due to diffraction interference and intense fracturing associated with the FAFC fault that cross the study area. Near the beginning of the line, R3 appears at 485 milliseconds (ms), or approximately 79 m. At the end of the line this same reflector appears at 535 ms (87 m), with multiple areas of increased offset occurring within fault zones throughout the line. A maximum bedrock depth occurs at 670 ms (108 m) near CDP number 145. Reflector R2 is relatively strong throughout the section, although less continuous than R3. R2 also

demonstrates an increase in depth across the line, appearing at 225 ms (22 m) at the beginning of the line and 310 ms (32 m) where it is last visible at CDP number 80. Depths to R2 determined by velocity analysis are within 4% of the values obtained from boring log 34. Reflector R1 is weak and discontinuous throughout this line, appearing intermittently between CDP numbers 462 and 238 at 220 ms (21 m) to 180 ms (16 m). Three major zones of deformation have been identified within Line UK-A3, and are discussed below.

3.2.1.1 Deformation Zone 1

Deformation Zone 1 (DZ-1) was interpreted between CDP numbers 670 and 560 (Figures 3.11 and 3.12). This zone consists of four distinct faults, identified at depth by sharp reflector offsets, loss of continuity and changes in apparent dip. This deformation zone represents a down-dropped feature bounded to the west by one major fault dipping approximately 76° ESE and to the east by a series of three faults dipping WNW at 78 to 80°. Bedrock is thrown down approximately 65 ms (13 m) across the westernmost fault while total bedrock displacement across the eastern faults is equivalent to 50 ms, or approximately 10 m. R2 is not visible west of DZ-1 making it difficult to determine the magnitude of near-surface offset across the western-bounding fault. Within the deformation zone R2 appears between 230 and 250 ms, with near-surface faulting manifested through bulging reflectors and small changes in apparent dip rather than distinct reflector offsets.

These observations support a series of high-angle normal faults extending from bedrock to within 20 m of the surface. The majority of fault displacement is thought to

have occurred prior to the Cretaceous with probable small-scale reactivation occurring in the post-Cretaceous.

3.2.1.2 Deformation Zone 2

Deformation Zone 2 (DZ-2) was interpreted between CDP numbers 530 and 435 (Figures 3.12 and 3.13). This zone consists of three distinct faults, identified by criteria similar to those used for DZ-1. Within this deformation zone a down-dropped block is bounded to the west by two faults dipping ESE at 78 to 86°. To the east it is bounded by a single fault with a WNW dip of 82°. Bedrock displacement across the two westernmost faults totals 140 ms (26 m), with reflector R2 down-thrown by almost 75 ms (8 m) in this area. Displacement across the eastern fault is smaller in magnitude, with reflector R3 displaced by 80 ms (14 m) and R2 displaced by 50 ms (5 m).

As with DZ-1, DZ-2 represents a series of high-angle normal faults. Where R1 is visible it exhibits both loss of coherency and displacement coincident with interpreted faults, suggesting that displacement may extend to within 14 m of the ground surface. The increase in displacement with depth suggests the reactivation of pre-Cretaceous faults as recently as the Pleistocene.

3.2.1.3 Deformation Zone 3

Deformation Zone 3 (DZ-3) was interpreted between CDP numbers 220 and 65 (Figure 3.14). This zone consists of six distinct faults, outlining a downthrown feature. Unlike DZ-1 and DZ-2, no single fault exists outlining a distinct boundary. The three western faults dip at angles of 79 to 82° to the ESE. Total displacement of R3 totals 145

ms (26 m) with the highest displacement of 85 ms (15 m) occurring across the westernmost fault. Displacements of R2 totaled 65 ms (7 m) with 45 ms (5 m), offset across the westernmost fault. R1 is absent within this deformation zone. The eastern boundary of the feature is defined by three faults dipping to the WNW at angles of 79 to 86°. R3 displacement across these faults totals 80 ms (14 m), with the displacement distributed relatively uniformly across all faults. Offset of reflector R2 is 30 ms (3 m), with the reflection disappearing to the east.

Based on disrupted reflectors early in the time record, the series of high-angle normal faults defining this zone extend to within 20 m of the surface. As with the other two deformation zones, this appears to be an area of pre-Cretaceous normal faulting that was reactivated later.

3.2.2 Line UK-B

Line UK-B is a 1652 m NW–SE-oriented profile acquired along a paved road. This nonproprietary section was collected as part of Langston et al.'s 1998 general area reconnaissance for a related groundwater study. Data quality is good and representative of the entire line. An opaque zone thought to represent an area of intense deformation appears between CDP numbers 20 and 107 (Figure 3.16), however not enough data is available at the beginning of the section to conclusively determine the nature and westward extent of this zone. Near CDP number 110, R3 appears at 455 ms, or approximately 72 m below ground surface, with the reflector appearing at 540 ms (87 m) at the end of the line. Multiple areas of increased offset occur within fault zones throughout the line, with a maximum bedrock depth occurring at 610 ms (99 m) around

CDP number 550. Reflector R2 is relatively strong throughout the section, although less continuous than R3. Although offsets of this reflector occur throughout the line, R2 is found at 285 ms (27 m) where it first appears at CDP number 138 and at the end of the line. The calculated depth to R2 at the end of the line agrees with the value provided from boring J-19 to within one meter. Reflector R1 is weak and relatively discontinuous throughout the section. A buried channel feature is apparent in the section between CDP numbers 360 and 485 (Figures 3.17 and 3.18). Three major zones of deformation have been identified within Line UK-B, and are discussed below.

3.2.2.1 Deformation Zone 4

Deformation Zone 4 (DZ-4) was interpreted between CDP numbers 115 and 260 (Figures 3.16 and 3.17). The zone is defined by four distinct faults, identified at depth by sharp reflector offsets, loss of continuity and changes in apparent dip. DZ-4 is a down-dropped feature, with R1 dipping sharply toward the center. It is bounded to the west by two faults dipping ESE at 79 to 80°. To the east it is bounded by two WNW dipping faults with angles of 77 and 86°. Across the two western faults R3 is displaced downward by a total of 80 ms (12 m). R2 is similarly displaced by 35 ms (3 m). Both reflectors rise in the time section across the two eastern faults, with R3 increasing by 85 ms (13 m) and R2 increasing by 75 ms (7 m). Sixty milliseconds (9 m) of the R3 displacement and 40 ms (4 m) of the R2 displacement occur across the easternmost fault.

These observations indicate an area of high-angle normal faults from the pre-Cretaceous that have been reactivated. Based on the disturbance of reflectors in the near-surface, faults within this zone are thought to extend to within 22 m of the surface.

3.2.2.2 Deformation Zone 5

Deformation Zone 5 (DZ-5), consisting of four distinct faults, occurs between CDP numbers 490 and 605 (Figure 3.18). In addition to the indicators used to identify faulting within DZ-4, strong diffractions are also associated with faulting in this zone. DZ-5 outlines a downdropped feature bounded to the west by two ESE-dipping faults and to the east by two WNW-dipping faults. Dip angles of these faults range between 74 and 86°. From the western edge of the fault zone to the center of the downdropped feature R3 moves down 130 ms in the time section (21 m), with 65 ms (11 m) of this displacement occurring across the westernmost fault. Going east R3 rises 100 ms (18 m) with 75 ms (14 m) of movement on the inner fault. R2 has downward displacement across the zone, varying between 250 ms (26 m) on the west and 300 ms (31 m) on the eastern end.

DZ-5 appears to consist of high-angle normal faults typical to the study area. The degree of offset is greatest on R3, with smaller displacements occurring on R2. R1 is not continuous enough throughout this deformation zone to determine an accurate amount of displacement, although there does appear to be some offset and folding along the reflector. Disturbance of near-surface reflectors indicates that faulting may extend to within 22 m of the surface.

3.2.2.3 Deformation Zone 6

Deformation Zone 6 (DZ-6) was interpreted between CDP numbers 685 and 785 (Figure 3.19). The zone consists of four distinct faults resulting in relatively small reflector offsets. The two western faults dip WNW, with the two eastern faults dipping ESE. Dip angle increases from west-to-east between 80 and 86°. Across the deformation

zone R3 moves down in the time section approximately 10 ms (2 m). The largest single displacement occurs between the two central faults, with R3 moving upward 30 ms (6 m). Across the deformation zone R1 moves upward in the time section 25 ms (2 m). R2 is mostly absent within this zone.

DZ-6 appears to be characterized by high-angle pre-Cretaceous normal faulting. Offsets within the area are relatively small in comparison with other deformation zones throughout the study area. This observation, combined with the opposite sense of displacement between reflectors R3 and R1, as well as central upwarping within reflector R3, may indicate a later period of reverse reactivation of these faults; however, it may also be the result of the seismic line intersecting the fault plane at a more oblique angle as the direction of the line bends more to the NW-SE.

3.2.3 Line UK-G1

Line UK-G1 is a 2744 m SW–NE-oriented profile acquired along an unpaved road. This nonproprietary section was collected as part of Langston et al.'s 1998 general area reconnaissance for a related groundwater study. Data quality is generally poor throughout most of the line. Reflector R3 is strong but discontinuous through the section. R2 and R1 are relatively weak and discontinuous. At the southern end of the line R3 appears at 495 ms (71 m), apparently decreasing to 640 ms (99 m) at CDP number 50. Both R2 and R1 appear to rise through the section, with R2 appearing at 290 ms (26 m) near the beginning of the line and at 185 ms (16 m) near CDP number 50. R1 similarly moves up in the time section from 175 ms (14 m) to 135 ms (10 m). Depth values for R2 obtained through velocity analysis near the beginning of the line agree with depths

encountered in boring Z-12 to within one meter. Line UK-G1 runs approximately parallel to the regional FAFC strike; therefore, it is expected that the angle of intersection between any fault plane and the seismic line will be very small, resulting in decreased apparent offsets and highly distorted structure. Four zone of deformation have been identified in line UK-G1, and are discussed below.

3.2.3.1 Deformation Zone 7

Deformation Zone 7 (DZ-7) was interpreted between CDP numbers 1305 and 985 (Figures 3.20 and 3.21). This interpreted zone is defined by three distinct faults which are identified at depth by sharp reflector offsets, loss of continuity and changes in apparent dip. The southernmost fault dips WNW at 74° . Reflector 3 is displaced downward approximately 35 ms (6 m) within this area. R2 does not experience any apparent displacement throughout this deformation zone, appearing at approximately 290 ms throughout the section. The central fault dips 74° to the ESE with 15 ms (3 m) upward displacement visible in R3. No change in the position of R2 is apparent. The northernmost fault within DZ-7 dips to the WNW at 73° . R3 is displaced downward 10 ms (2 m) across the fault, with R2 absent to the north. Reflector 1 is not identified in this deformation zone.

DZ-7 is characterized by high-angle faulting. Bedrock offset indicates normal faulting in the pre-Cretaceous. No offset is observed along R2 to support later reactivation. Based on the poor near-surface data quality, structure was not interpreted above a depth of 30-m.

3.2.3.2 Deformation Zone 8

Deformation Zone 8 (DZ-8) consists of two inferred WNW-dipping faults and occurs between CDP numbers 700 and 550 (Figure 3.23). Fault dips were determined to be 74° for the southern inferred fault and 79° for the northern inferred fault. Negligible bedrock displacement occurs to the south, with 50 ms (9 m) of downward displacement across the northern fault. R2 is largely absent within DZ-8.

Deformation Zone 8 appears to consist of high-angle pre-Cretaceous normal faults. Although there are indications of near-surface faulting, deformation can not be confirmed in the top 30 m of the section. The absence of R2 in DZ-8 prohibits classification of post-Cretaceous faulting.

3.2.3.3 Deformation Zone 9

Deformation Zone 9 (DZ-9) was interpreted between CDP numbers 340 and 95 (Figures 3.25 and 3.26). The zone consists of one fault and two inferred faults. The two inferred faults dip WNW between 75° and 82°. R3 was not visible in the stacked section, prohibiting the determination of offset. No net change in depth to R1 or R2 is discernable. The northernmost fault dips to the ESE at 83°. A 35 ms (6 m) upward displacement of R3 occurs across this fault. Once again, there is no apparent change in the depth to R1 or R2.

DZ-9 is characterized by high angle pre-Cretaceous normal faults. Poor data quality prevents the interpretation of post-Cretaceous faulting, with the extent of faulting only determined to within 35-m of the surface.

3.2.4 Line UK-G2

Line UK-G2 is a 788-m SW–NE-oriented section collected along an unpaved road. UK-G2 is a continuation of UK-G1, and originally collected as part of Langston et al.'s 1998 general area reconnaissance for a related groundwater study. Data quality is generally poor throughout most of the line. All reflectors are relatively weak and discontinuous, with R3 highly discontinuous from CDP number 150 to 1. Net displacement across the line is downward, with R3 appearing at 495 ms (81 m) to the south and at 595 ms (86 m) near the end of the line. Similarly, R1 appears to be downdropped from 155 ms (11 m) to 220 ms (16 m). R2 appears at 350 ms (20 m) at the beginning of the line, but is absent past CDP number 100. The calculated depth to R2 at the beginning of the line correlates well with the top of the McNairy formation observed in boring J-22 to within 1 m.

3.2.4.1 Deformation Zone 10

Deformation Zone 10 (DZ-10) was interpreted between CDP numbers 370 and 320 (Figure 3.27). The zone consists of one fault and one inferred fault. Both faults dip WNW at 75° to 79°. Across both faults reflector R3 is downdropped from 495 ms (81 m) to 550 ms (84 m). R2 is similarly displaced downward from 245 ms (20 m) to 295 ms (25 m). No change was observed in R1.

DZ-10 appears to be characterized by high-angle pre-Cretaceous normal faults reactivated with the same sense of offset in later reactivation. Fault displacement extending across R2 places fault propagation within 20 m of the surface.

3.2.5 Line UK-H

This 490-m section WSW–ENE-oriented section was collected along a paved road approximately 650-m north of line UK-A3. A decreased sampling interval, tighter acquisition geometry and smaller energy source were employed to increase the resolution, especially in the near surface. Data quality for the line is considered excellent for the area. R3 is strong and coherent throughout the section, with the exception of the area between CDP numbers 380 and 400, interpreted as an area of deformation. At the beginning of the line R3 appears at 410 ms, approximately 71 m below ground surface. This reflector moves down in the time section across the profile with a maximum depth occurring at 560 ms (84 m) near CDP number 490. R2 and R1 are also strong across the section, displaying continuity up to CDP numbers 220 and 240, respectively. These reflectors follow the same general trend evident in R3, with R2 appearing at 220 ms (19 m) at CDP number 1 and 275 ms (26 m) at CDP number 385. R1 appears at 115 ms (9 m) at CDP number 1 and 160 ms (13 m) at CDP number 425. The depth to R2 obtained through velocity analysis is within 4% of the depth recorded at MW201. Two deformation zones were interpreted along UK-H, and are discussed below.

3.2.5.1 Deformation Zone 11

Deformation Zone 11 (DZ-11) occurs between CDP numbers 50 and 250 (Figures 3.29 and 3.30). At depth, faults were interpreted from loss of coherency, reflector offset and change in reflector dip. In the near surface faulting was identified by folding and bulging of R1 and R2. One exception is a distinct displacement of R1 near CDP number 430. The deformation zone consists of 4 distinct faults, with dip angles between 85 and

86°. Three of the faults are believed to dip approximately ESE, with the remaining fault dipping WNW. R3 is displaced downward a total of approximately 70 ms (11 m) across the deformation zone, with the majority of displacement occurring across the two westernmost faults. R2 and R1 also show downward displacements of 40 ms (4 m) and 35 ms (3 m), respectively, across DZ-11.

This deformation zone is characterized by a series of high-angle normal faults believed to propagate through the entire time section. High-resolution imaging of R1 shows deformation extending to within 7 m of ground surface. As with other profiles within the study area, this deformation zone is thought to represent a series of pre-Cretaceous normal faults. The increase in resolution of near-surface sediments shows strong evidence for faulting in what is believed to be the top of the Lower Continental Deposits, supporting reactivation of these faults at least into the Pleistocene.

3.2.5.2 Deformation Zone 12

Deformation Zone 12 (DZ-12) occurs between CDP numbers 360 and 420 (Figures 3.30 and 3.31). At depth and in the near surface faulting was interpreted primarily from loss of coherency, with diffractions evident at depth. Based on these indicators, this deformation zone consists of one interpreted fault dipping approximately 86° to the ESE. Reflectors R1 and R2 are identified within the deformation zone, with R1 displaying the strongest signal and greatest coherency. R3 is absent within DZ-12. No net displacement is observed across any of the reflectors.

This deformation zone is characterized by at least one high-angle fault believed to extend from bedrock to within 8 m of the ground surface. The lack of displacement

within this zone prevents the determination of a sense of offset across the interpreted fault. Similarly, reactivation of the fault can not be determined. Therefore, it can only be stated that this deformation zone represents high-angle faulting with movement occurring as recently as the Pleistocene.

3.2.6 Line UK-I

This 688 m SSW–NNE-oriented section was collected along a paved road, and sited to confirm structural features interpreted from an electrical resistivity profile collected coincidentally at the location. In addition, UK-I was used to intersect features identified in lines UK-A3 and UK-B. Data quality is relatively poor, most likely due to the presence of soft sediments and concrete slab foundations in the vicinity of the line. Both of these factors likely contributed to the “ringy” appearance of the data, especially within the top 300 ms. All three reflectors are relatively weak and discontinuous, with R3 displaying the strongest signal. Net displacements across the section are relatively small. R3 moves up in the time section approximately 25 ms (6 m) from 505 ms (77 m) at the southern end to 480 ms (71 m) at the northern end, while R2 moves down 35 ms (3 m) from 285 ms to 320 ms. R1 appears at 200 ms (17 m) at both the beginning and end of the section. The calculated depth to R2 is within 10% of the depth recorded for boring J-3. Two deformation zones are present within the section, and are discussed below.

3.2.6.1 Deformation Zone 13

Deformation Zone 13 (DZ-13) was interpreted between CDP numbers 50 and 70 (Figure 3.32). At depth and in the near-surface, the presence of faults was determined by

loss of coherency, reflector offset, change in reflector dip and the presence of diffractions. This deformation zone consists of one fault continuous in the time section upward to between 280 and 200 ms, and a splay continuous from approximately 790 ms to 320 ms. The through-going fault has an apparent dip of 82° to the WNW, while the fault splay has an apparent dip of 68° to the ESE. Displacement of the top two reflectors is downward across both faults, with R2 experiencing 15 ms (1 m) offset and R1 experiencing 20 ms (1 m) offset. R3 does not experience any net displacement within the deformation zone, appearing at 505 ms (77 m) at the beginning and end of the zone.

This deformation zone is characterized by a high-angle reverse fault with a mid-angle dog-leg splay. The absence of considerable displacement across R3 indicates that this may have been a normal fault that was reactivated as a reverse fault or, more likely, the fault plane intersects the seismic line at an oblique angle, obscuring displacement and distorting the appearance of structure. Due to difficulties in the resolution of near surface reflections, faults were not extended above the top of R2. Therefore, faults are only definitively found to extend within 30 m of the surface.

3.2.6.2 Deformation Zone 14

Deformation Zone 14 (DZ-14) was interpreted between CDP numbers 175 and 300 (Figures 3.32 and 3.33). The presence of faults within the zone was determined by the same techniques employed for DZ-13. DZ-14 is comprised of four faults, three through-going faults and one splaying from the central fault. Two of the through-going faults have apparent WNW dip angles between 87° and 88° , with the third through-going fault and the fault splay dipping ESE between 77° and 73° , respectively. All three

reflectors are apparent and relatively coherent within the deformation zone, with the exception of the area between the central through-going fault and they splay which is largely opaque. All three reflections are displaced upward in the time section across the profile, with R3 displaced 90 ms (7 m) and R2 displaced 65 ms (2 m). R1 was moved upward 10 ms in the time section across the four faults, however variations in near-surface velocities resulted in no net change in depth.

This deformation zone is characterized by three high-angle normal fault with a mid-angle reverse dog-leg splay. As with DZ-13, the displacement of near surface reflectors with negligible displacement at depth most likely indicates an oblique angle of intersection between the fault planes and the seismic line. Faults are known to extend within 30 m of the surface, although higher resolution near-surface imaging image them at a shallower depth.

3.2.7 Line UK-J

This 782 m SSW–NNE-oriented section was collected along a paved road and was sited to intersect structure seen in proprietary lines to the northeast (Woolery and Street, 2002). As with line UK-H, a decreased sampling interval, tighter acquisition geometry and smaller energy source were used to increase resolution, especially in the near surface. Data quality is considered excellent for the area. All three reflectors are strong and coherent, with R3 exhibiting the greatest coherency. Two seismically opaque zones exist within the line, one between CDP numbers 300 and 360 (Figure 3.35) and the other between CDP numbers 460 and 480 (Figure 3.36), most likely representing localized zones of intense deformation. A net upward displacement of all three reflectors

occurs across the section, with the most significant rise seen in R3, which begins at 565 ms (73 m) and reaches 455 ms (57 m) at the end of the profile. R2 moves up in the time section from 290 ms (24 m) in the south to 225 ms (18 m) at the northern terminus of the section. R1 is absent at the beginning of the line, but appears at 170 ms (13 m) at CDP number 25, moving up to 160 ms (12 m) at the end of the line. Depth calculated to R2 from the velocity analysis of the beginning of the line is within 4% of the depth recorded at boring 22, with depth calculated at the end of the line within 12% of the depth recorded at boring 23. Two major deformation zones are present within the section, and are discussed below.

3.2.7.1 Deformation Zone 15

Deformation zone 15 (DZ-15) was interpreted between CDP numbers 110 and 200 (Figure 3.34). At depth and in the near-surface the presence of structure was determined by loss of coherency, reflector offset, change in reflector dip and the bulging of reflectors. This deformation zone consists of two through-going faults and one fault splay. Both through-going faults are near vertical (apparent dip $>88^\circ$), with the fault splay exhibiting an apparent ESE dip of 80° . Small displacements of reflectors occur across the deformation zone, with the largest displacement of 30 ms (5 m) upward in the time section occurring within R3 where it is last visible before the deformation zone between CDP numbers 60 and 200. R1 moved down in the time section approximately 20 ms (1 m), while R2 remained at the same depth across DZ-14.

DZ-15 is characterized by vertical faults with a high-angle dog-leg splay displaying a normal sense of offset. The absence of considerable displacement and the

vertical nature of the faulting make it difficult to determine a fault mechanism. As with other seismic profiles in the area which strike more strongly south to north, the fault plane intersects the seismic line at an oblique angle, obscuring displacement and distorting the appearance of structure. Due to R1 coherency, deformation was interpreted to extend within 11 m of the surface.

3.2.7.2 Deformation Zone 16

Deformation Zone 16 (DZ-16) occurs between CDP numbers 580 and 675 (Figures 3.36 and 3.37). DZ-16 consists of two faults and an additional inferred fault outlining an upthrown block to the south and a downthrown block to the north. The southern fault has an apparent dip of 85° to the WNW, while the northern fault dips to the ESE at 80° . Not enough is known about the inferred fault to ascribe a dip angle to it, although it appears to be approximately vertical. The general sense of displacement of all reflectors across the deformation zone is upward, with 55 ms (7 m) net displacement of R3, 30 ms (3 m) displacement of R2 and 20 ms (2 m) displacement of R1. Across the southernmost fault R3 is displaced upward 35 ms in the time section (5 m), before being thrown down 25 ms (3 m) across the northern fault. The reflector dips upward across the inferred fault, moving up 50 ms in the time section (6 m) between CDP numbers 650 and 675. R2 and R1 are relatively discontinuous throughout this deformation.

This deformation zone is characterized by two high-angle normal faults believed to extend from bedrock to within 14 m of the surface. As is typical within deformation zones in the study area, pre-Cretaceous normal faulting is believed to have been re-activated in the Pleistocene.

3.3 ELECTRICAL RESISTIVITY BACKGROUND

3.3.1 General

In addition to seismic reflection profiles, inverted resistivity sections were used in the characterization of major subsurface features within the study area. Interpretations were performed on sections with the earth resistivity scaled to best demonstrate variations within each individual section. Profiles normalized to a single resistivity scale are provided in Appendix B, section 5. Since resistivity is based on a weighted volumetric average, discrete contacts between soil horizons were not resolvable. As a result, the inverted sections were examined for relatively large-scale structural features and for horizontal and vertical changes in resistivity. Changing resistivity values generally signal an increase in air or fluid filled pores, fractures and/or faults, changes in grain size, fluctuating electrolytic properties of a fluid, and to a smaller extent, contrasts in mineral conductivity. Areas of distinctly higher or lower resistivity in what are believed to be otherwise laterally continuous layers are referred to as deformation zones. Offset of resistive layers across deformation zones, along with other indicators such as dipping and bulging reflectors, may point to the presence of faulting within that area. No features within approximately 3 m of the ground surface ground surface (1 m for line UK-004) are discussed due to boundary effects and the inability of this method to resolve features less than one-half of the electrode spacing. Where possible, layers exhibiting distinct resistivities are correlated to lithologic units. However, the complex relationship between sediments, pore space and groundwater produces correlations that fluctuate both temporally and spatially.

3.3.2 Resolution

The horizontal and vertical resolution of an electrical resistivity survey is dictated by the electrode spacing. Within reasonable field conditions this method can resolve features as small as one electrode spacing. Where field conditions are optimum, it is possible to image features as small as one-half of the electrode spacing, although great care must be exercised in the interpretation of these features. Since all profiles, with the exception of line UK-001, were collected under moderately noisy conditions, resolution for these lines is considered to be equivalent to one electrode spacing. Resolution for line UK-001 is between one-half and one electrode spacing (Table 3.3).

The depth penetration of a survey is determined by the length of the electrical resistivity line before roll-along. For lines UK-001 through UK-003, this is equivalent to approximately 50 m. For line UK-004 two-meter spacing was used between the 42 electrodes deployed, reducing this value to 12.3 m. Based on these values, lines UK-001 through UK-003 can reliably image the upper McNairy deposits, while line UK-004 does not provide good resolution beneath the base of the Upper Continental Deposits.

3.4 ELECTRICAL RESISTIVITY SECTION INTERPRETATION

3.4.1 Line UK-001

UK-001 is a 498 m-long WSW–ENE-oriented profile that was collected coincident with seismic line UK-H. The line was sited in this location to provide additional information on the subsurface structure in this area and to test the viability of electrical resistivity imaging as a complementary method to seismic reflection. Agreement between the measured resistivity pseudosection and the calculated

pseudosection is excellent with less than 5% RMS error for the second iteration after data with relative misfit above 10% was removed.

Three distinct and continuous resistivity layers are visible within the section. The uppermost layer, L1, is characterized by low resistivities (9 to 18 Ohm·m). The top of this layer is present at a depth of approximately 3 m with the base appearing at 9 m throughout most of the profile. L1 thickens to 8 m between electrodes 37 and 52, with the base of the layer appearing at approximately 11 m. The middle layer, L2, is characterized by moderate resistivities ranging from 25 to 40 Ohm·m with the measured value generally increasing with depth. This layer is approximately 4 m thick to the west, with the top of the layer located at 10 m below ground surface. The layer thins to 2 m in the east, with the depth to the top of the layer remaining relatively consistent. L2 thickens between electrodes 51 and 60, with the base of the layer appearing at a depth of 18 m. Based on boring logs 27 and MW201, these layers correlate with the Upper Continental Deposits. The lowest distinct layer, L3, is characterized by medium to relatively high resistivities (75-90 Ohm·m) surrounding discrete high resistivity (100-125 Ohm·m) zones. This layer appears to dip downward from west to east with the top of the layer found at a depth of 14 m near electrode 3 and a depth of 19 m near the end of the line. Zones of high resistivity appear between 18 and 23 m near electrode 12 before thickening to the east, appearing between depths of 22 and 44 m at electrode 64. Based on depths encountered in boring logs, this layer correlates with the Lower Continental Deposits and the upper McNairy formation.

Areas of lower resistivity separating high resistivity zones are thought to represent fracture zones containing increased amounts of pore water and/or increased percentages

of fine grained sediment. Four such areas are identified in this section and are referred to from west to east as Deformation Zone A (DZ-A) to Deformation Zone D (DZ-D) (Figure 3.38). Although distinct faults cannot be imaged by this method, the relative displacement of identified layers across the deformation zones points to the presence of faulting extending to within 15 m of the surface.

The high resistivity zone of L3 moves down approximately one meter across DZ-A, located between electrodes 13 and 16, with resistivity values decreasing from 95 to 97 Ohm·m on either side of the fracture zone to a low of 83 Ohm·m near electrode 15. Deformation Zone B is located between electrodes 23 and 27. Across DZ-B, the top of the high resistivity surface of L3 drops down an additional 6 m. Resistivities of either side of the zone were measured at 97 Ohm·m, with a value of 81 Ohm·m recorded in the center of the deformation zone. The top of the high resistivity zone of L3 is displaced upward 5 m across DZ-C, with resistivity values decreasing from 96 Ohm·m on either side to approximately 77 Ohm·m at electrode 38. This represents the largest change in resistivity seen within a deformation zone. Four meters of downward displacement occur across DZ-D, located between electrodes 52 and 59. Resistivity values outside of the zone measured approximately 97 Ohm·m. Within DZ-4 they were found to be as low as 87 Ohm·m.

Another feature prominent within this section is the lower resistivity (55-49 Ohm·m) area present at depth near the western end of the line. This decrease in resistivity may represent an increase in hydraulic conductivity or a facies change occurring at depths of 35 to 50 m west of section UK-001.

3.4.2 Line UK-002

UK-002 is a 972 m-long SSW–NNE-oriented profile which was sited to intersect structural features imaged on seismic reflection profiles collected west of the line.

Agreement between the measured resistivity pseudosection and the calculated pseudosection is good, with less than 8% RMS error for the first iteration after data with relative misfit above 16.5% was removed.

Three distinct and relatively continuous resistivity layers are visible within the section. The uppermost layer, L1, is characterized by low resistivities (12 to 25 Ohm·m). Near electrode 14 the top of L1 is identified at a depth of 3 m with the base identified at 12 m. Thickness of this layer varies from 7 m to approximately 10 m. A thin mid-resistivity layer (31-42 Ohm·m), referred to as L2, underlies the upper layer. This layer remains relatively consistent in thickness throughout the section, with the top occurring at a depth of 12 m and the base at a depth of 15 m near the beginning of the line. Near the end of the line this layer is found between depths of 15 and 18 m. The approximate locations of these two layers suggest that they most likely correlate with the Upper Continental Deposits. A discontinuous lower layer, L3, is characterized by medium to relatively high resistivities (66-95 Ohm·m) surrounding discrete high resistivity (100-150 Ohm·m) zones. This layer appears to dip downward toward the center of the survey, with depths to the tops of discrete high resistivity zones ranging from approximately 17 to 19 m at the ends of the line to 27 m between electrodes 32 and 80. This layer roughly correlates with the Lower Continental Deposits and upper McNairy formation boundary.

Four distinct zones of lowered resistivity, labeled DZ-E through DZ-H, are thought to represent zones of fracturing within the section (Figure 3.39). Throughout

several areas of the profile disturbances found at depth are also visible within the base of the uppermost low resistivity layer. This, along with apparent offset across several deformation zones, would seem to suggest the presence of faulting extending to within 13 m of the surface.

Across DZ-E, located between electrodes 24 and 30, the high resistivity zone of L3 moves down approximately 8 m, with L1 appearing to thicken at this location. Resistivity values on either side of the deformation zone range from 57 Ohm·m to 58 Ohm·m, with a slightly lower value of 53 Ohm·m seen within the fracture zone. No offset appears to exist across DZ-F, but resistivity values decrease from 59 Ohm·m to 56 Ohm·m within this narrow deformation zone located between electrodes 34 and 53. Deformation Zone G is placed to the north of a lenticular extension of L3 between electrodes 82 and 100. Resistivity outside of the fracture zone is measured at approximately 58 Ohm·m while inside the zone this value is found to be 36 Ohm·m at 30 m below ground surface, with the resistivity decreasing to approximately 28 Ohm·m near the base of the resolvable section (49 m). This large resistivity contrast is over 220 m wide in some areas and over 49 m deep. This would seem to indicate a large-scale structural feature. A fourth area of faulting, DZ-H, is thought to exist from electrode 137 to the end of the section. This is evidenced by a drop in resistivity from 64 Ohm·m at electrode 137 to 52 Ohm·m at electrode 139, with values continuing to decrease to the north. The presence of faulting is further supported by the thickening and downwarping of L1 at this location.

3.4.3 Line UK-003

UK-003 is a 498 m SSW–NNE-oriented profile which was sited to intersect the structural features shown in line UK-J. Agreement between the measured resistivity pseudosection and the calculated pseudosection is good with less than 6% RMS error for the first iteration after data with relative misfit above 14% was removed.

Three distinct resistivity layers are visible within the section, although all are relatively discontinuous. The uppermost layer, referred to as L1, is characterized by low to moderate resistivity values ranging from 12 to 34 Ohm-m. The top of L1 is located at approximately 3 m below ground surface with the base appearing at depths of 8 to 9 m. From depths encountered in borings 22 and 23 it appears that this layer may represent a horizon within the Upper Continental Deposits. A high resistivity layer, L2, is located between depths of 8 and 23 m to the south, with the layer thinning to 9 m near electrode 32. Resistivity values associated with this layer range from 76 to 163 Ohm-m. From electrode 77 to the end of the line this layer thickens dramatically, with its base found at a depth of 35 m, appearing to displace the underlying layer. L2 is continuous from the beginning of the line to electrode 36 and again between electrodes 61 and 72. This layer is thought to correlate with the remaining Upper Continental Deposits and the Lower Continental Deposits based on depths encountered in borings. The lower layer, referred to as L3, is characterized by moderate resistivity values (24-38 Ohm-m) surrounding discrete zones of low resistivity (12-15 Ohm-m). This layer is thought to correlate with the upper McNairy formation.

Two zones of contrasting resistivity, labeled DZ-I and DZ-J, are defined for this section (Figure 3.40). Within L3 these fracture zones represent areas of increased

resistivity, while at depths where L2 is expected to be found, they represent areas of decreased resistivity. This would suggest possible fracturing infilled by moderate-resistivity sediment.

Deformation Zone I, located between electrodes 34 and 46, shows an increase in resistivity within L3 from 19 Ohm·m at the bordering low resistivity zones to 25 Ohm·m within DZ-I. At approximately 9 m below ground surface L2 becomes discontinuous and lower than expected resistivity values ranging from 16 to 47 Ohm·m are found within the deformation zone. Across DZ-I, the low resistivity zone of L3 moves upward from 28 m to a minimum depth of 19 m. Deformation Zone J occurs between electrodes 57 and 66. Resistivity values associated with L3 increase from 19 Ohm·m to 29 Ohm·m within DZ-J, with these values increasing up to 34 Ohm·m at the base of the resolvable section. Where the deformation zone intersects L2 the resistivity decreases from measured values of 54 to 109 Ohm·m seen to the north of DZ-J to between 53 and 62 Ohm·m. Across the deformation zone the depth to the discrete zone of low resistivity found in L3 increases from 19 m to 23 m. The large amounts of offset across the deformation zones, along with the propagation of distinct resistivity changes through multiple layers, suggest the presence of faulting in the area extending to within 8 m of the surface.

3.4.4 Line UK-004

This 498 m NNW–SSE-oriented profile was sited to intersect a potential structural feature that may exert control on a seep within Little Bayou Creek. The seep is located between electrodes 28 and 29. Agreement between the measured resistivity pseudosection and the calculated pseudosection is good, with approximately 6% RMS

error for the first iteration after data with relative misfit above 12.5% was removed.

This section contains both high and low resistivity deviations from a mostly consistent moderate resistivity range of 115 to 189 Ohm·m. High resistivity values, ranging from 303 to 943 Ohm·m, are seen in the near surface as a 3 to 4 m thick layer continuous from electrode 6 to electrode 10 and between electrodes 21 and 38. Another high resistivity zone, with values ranging from 315 to 444 Ohm·m, is interpreted between electrodes 10 and 23, with the top of the zone located at a depth of 9 m and the base located at 17 m. A low resistivity zone, with values of 32 to 45 Ohm·m, exists within this same area between depths of 1 and 6.5 m. This feature may be the result of standing water noted in the vicinity of the survey line between electrodes 11 and 16 when measurements were taken. Based on depths to lithologic units reported for borings MLS-31, D-14, Z-12 and 36, this section can be correlated with Pleistocene loess and the Upper Continental Deposits.

The decrease in electrode spacing used for this survey resulted in a three-fold increase in resolution. Based on this higher resolution image one zone of deformation, DZ-K, and one zone of interest were identified. DZ-K, located between electrodes 27 and 36, was interpreted based on the relatively large offset seen within the upper high resistivity layer. To the north of DZ-K the top of this layer can be seen at 1 m below the surface, with the base of the layer present at approximately 3.5 m depth. Across the northern edge of the deformation zone the layer is down-dropped approximately 2 m. Inside DZ-K the layer appears to dip upward, appearing at 1 m depth to the south of the deformation zone. Examination of this layer suggests the propagation of structure to within at least 3 m of the ground surface. The zone of interest, characterized by the large

resistivity low and the resistivity high at depth, is located between electrodes 10 and 21. Due to poor field conditions when this data was gathered, it is unclear whether the resistivity values in this area could have been skewed by the presence of saturated sediments in the upper 1 m, or whether they represent a structural feature. The thickness of the highly resistive area within this zone makes it unlikely that it is an extension of the near-surface resistive layer, making it impossible to correlate the features in this zone to anything seen in the rest of the section. In order to gain a clearer understanding of this area another survey should be conducted across the zone of interest under better field conditions. Additionally, the survey should extend farther to the north to gain denser data coverage in the northern section of the zone of interest and to provide a better understanding of local subsurface conditions.

Table 3.1: Vertical and horizontal resolution limits for near-surface reflectors. The resolvable limit is equivalent to one-quarter of the dominant while the detectable limit is equivalent to one-eighth of the dominant wavelength. The horizontal resolution is determined by the radius of the first Fresnel zone. In order to provide more conservative estimates, the lowest dominant frequency provided was used in all calculations.

Seismic Reflection Near Surface Resolutions				
Line Name	Dominant Frequency (Hz)	Vertical Resolution		Horizontal Resolution (m)
		Resolvable Limit (m)	Detectable Limit (m)	
UK-A3	45	1.1	0.6	8
UK-B	50-55	0.9	0.5	7
UK-G1	40-50	1.1	0.6	7
UK-G2	45-50	1.0	0.5	6
UK-H	60	0.8	0.4	6
UK-I	60	0.8	0.4	6
UK-J	75	0.6	0.3	4

Table 3.2: Vertical and horizontal resolution limits for the bedrock reflector. The resolvable limit is equivalent to one-quarter of the dominant while the detectable limit is equivalent to one-eighth of the dominant wavelength. The horizontal resolution is determined by the radius of the first Fresnel zone. In order to provide more conservative estimates, the lowest dominant frequency provided was used in all calculations.

Line Name	Dominant Frequency (Hz)	Vertical Resolution		Horizontal Resolution (m)
		Resolvable Limit (m)	Detectable Limit (m)	
UK-A3	30-35	3.0	1.5	23
UK-B	30-35	2.7	1.4	22
UK-G1	30-35	2.7	1.3	22
UK-G2	30-35	2.6	1.3	22
UK-H	30-35	2.7	1.3	20
UK-I	40	2.1	1.0	19
UK-J	35-40	2.4	1.2	21

Table 3.3: Resolution limits for electrical resistivity profiles. Horizontal and vertical resolution ranges from one-half to one electrode spacing based on site conditions. Maximum depth of penetration is assumed to be 15% of the survey line length before roll-along.

Electrical Resistivity Resolutions					
Line Name	Electrode Spacing (m)	Number of Electrodes	Line Length (m)	Depth of Penetration (m)	Resolution (m)
UK-001	6	56	330	49.5	3 to 6
UK-002	6	56	330	49.5	6
UK-003	6	56	330	49.5	6
UK-004	2	42	82	12.3	2

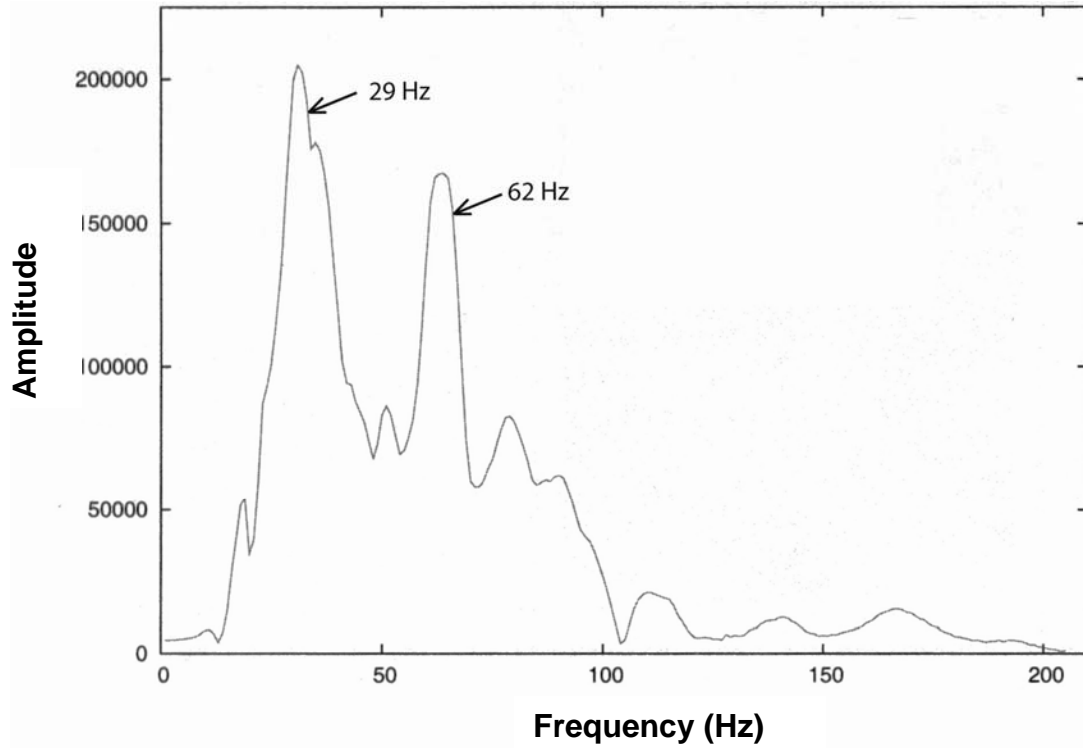


Figure 3.1: Amplitude vs. frequency graph for seismic line UK-H. The first peak, occurring at 29-Hz, corresponds to the bedrock dominant frequency. The second larger peak, occurring at 62-Hz, corresponds to the dominant frequency of unconsolidated near-surface deposits.

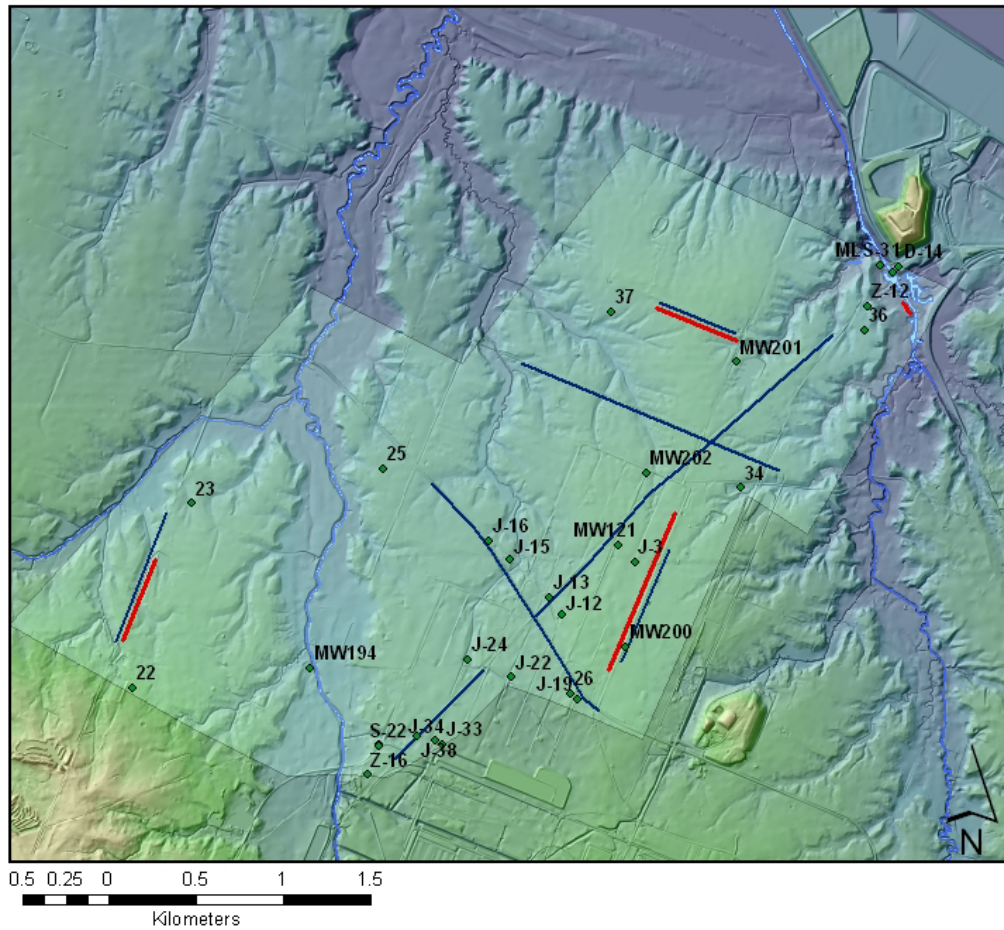


Figure 3.2: Locations of borings within the study area. Borings Z-12 and Z-16 extend to bedrock, while all others extend into the Lower Continental Deposits or McNairy formation.

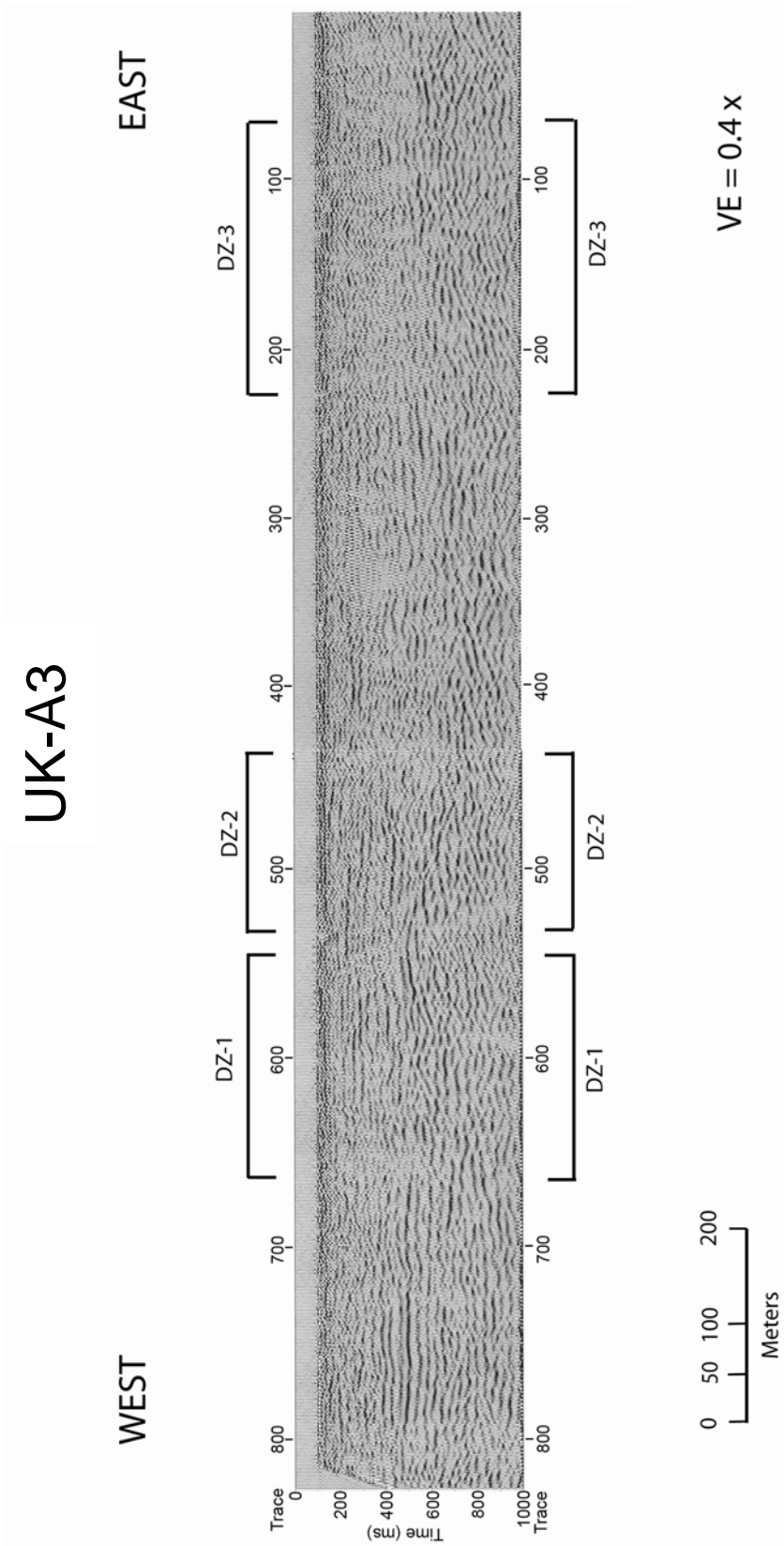


Figure 3.3: Seismic line UK-A3 with interpreted deformation zones shown.

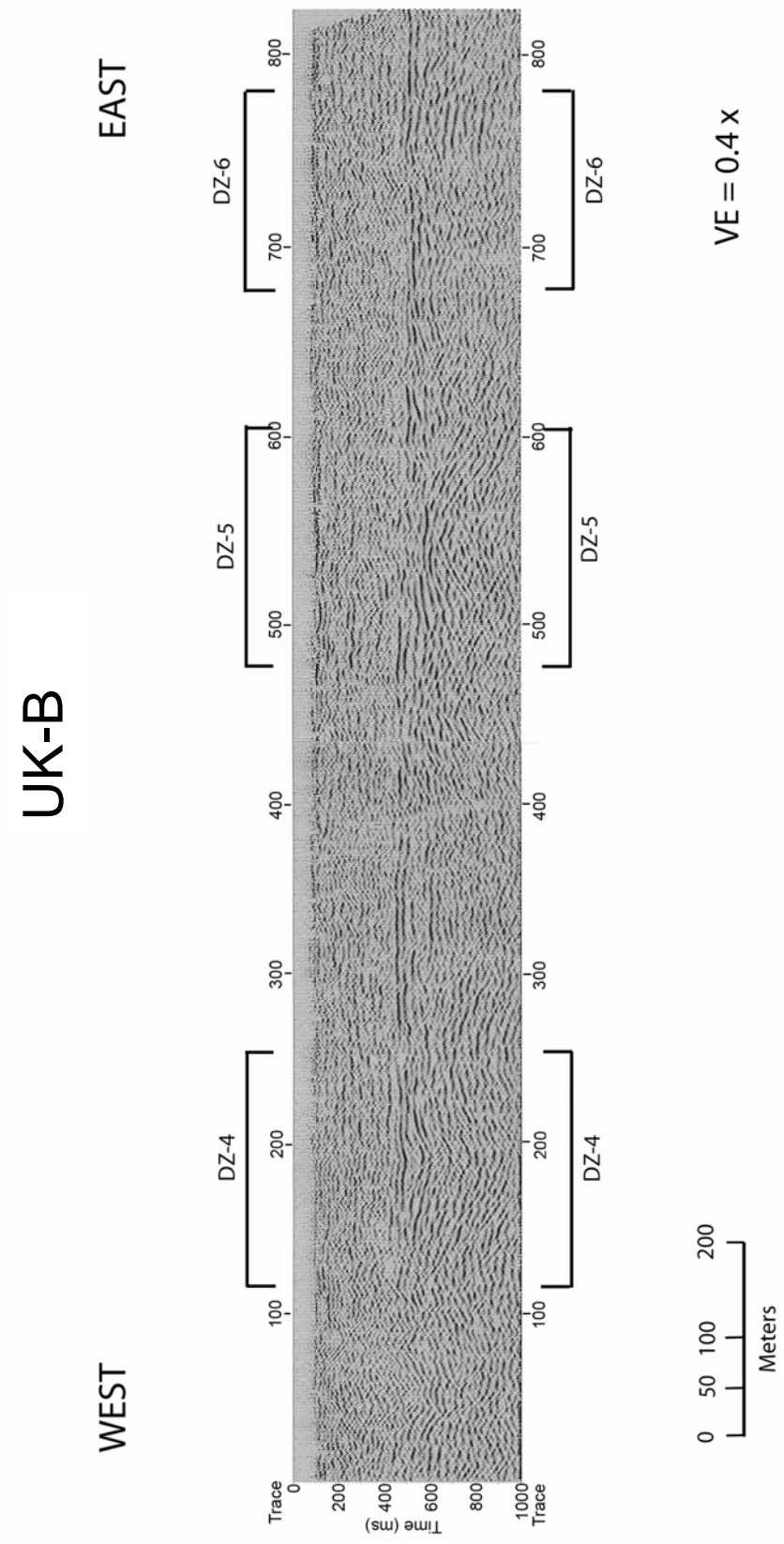


Figure 3.4: Seismic line UK-AB with interpreted deformation zones shown.

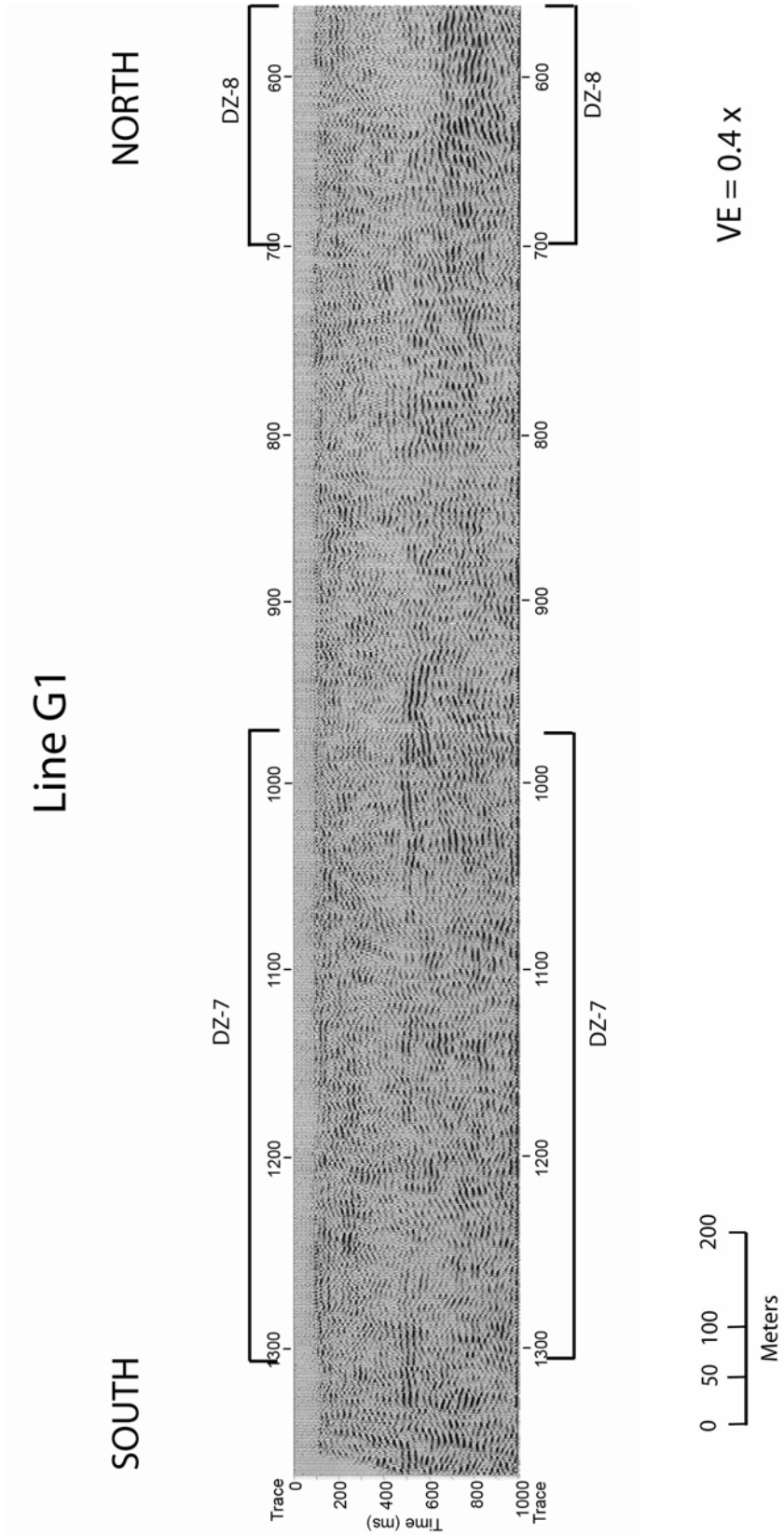


Figure 3.5: Seismic line UK-G1 with interpreted deformation zones.

UK-G1 Continued

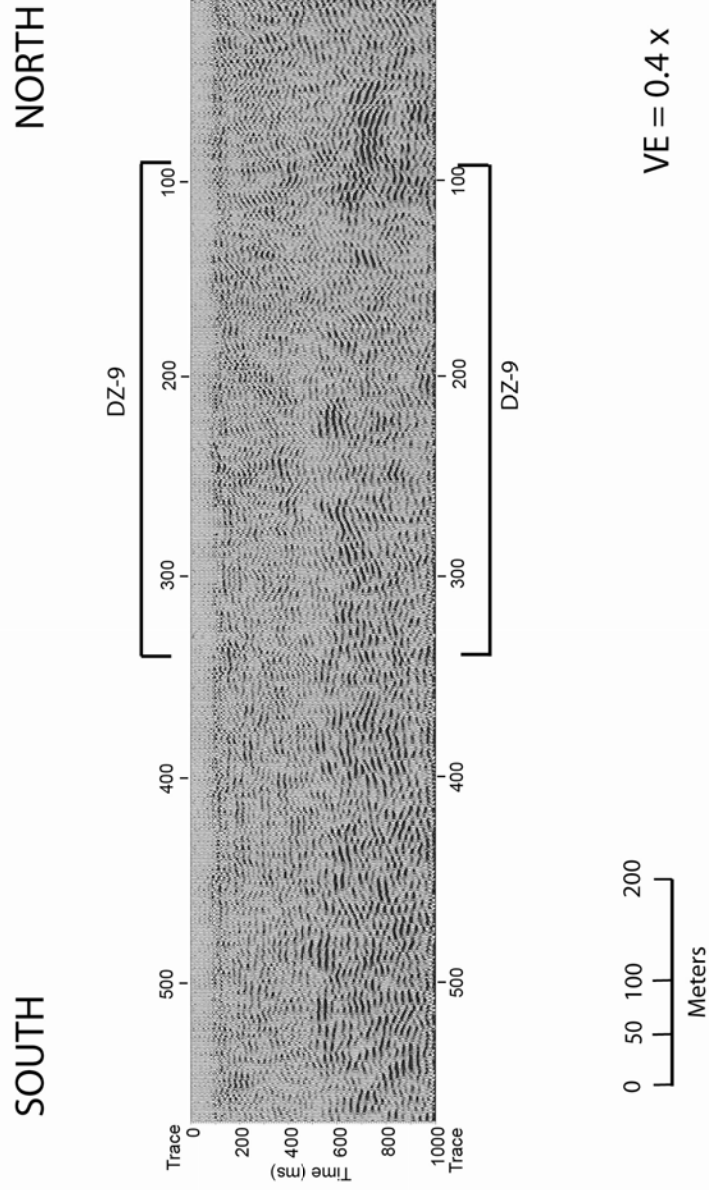


Figure 3.6: Continuation of seismic line UK-G1 with interpreted deformation zone.

UK-G2

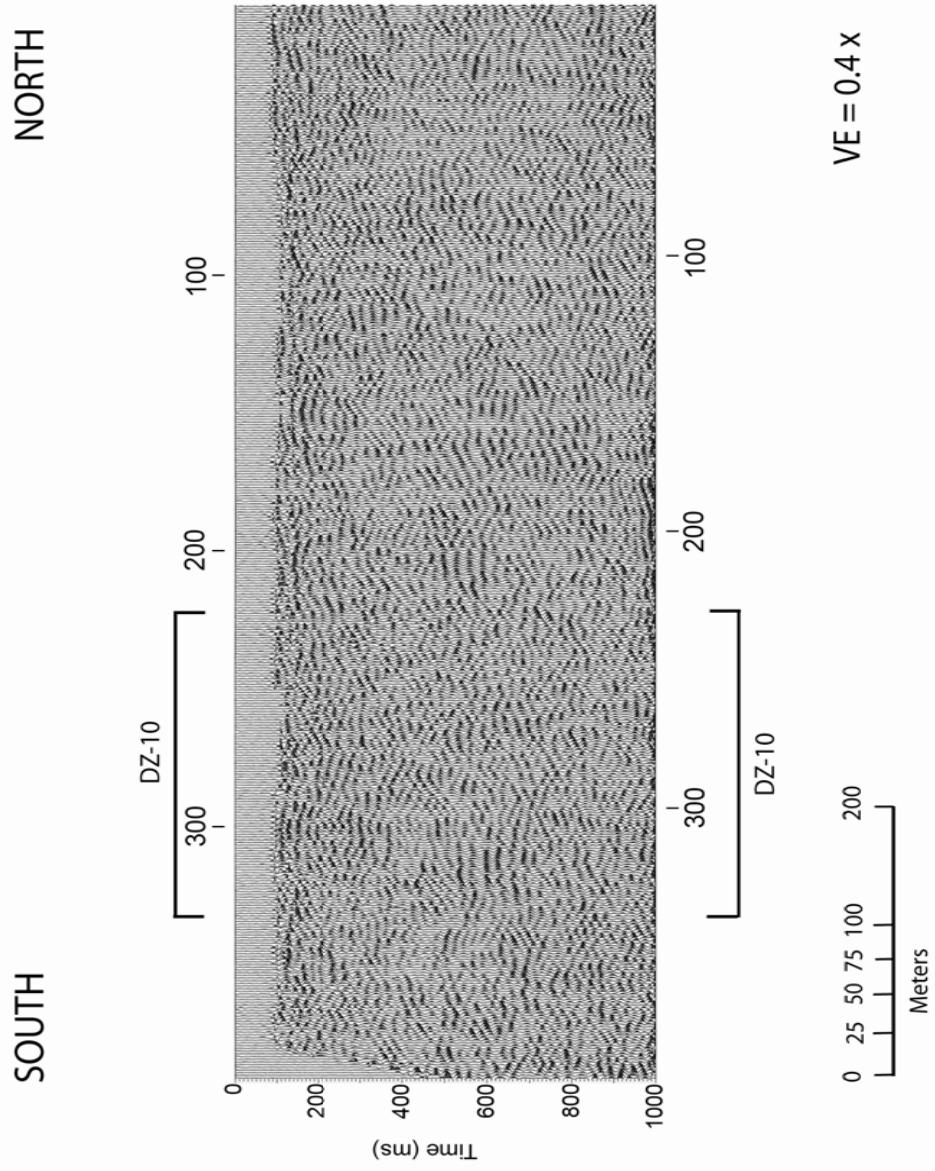


Figure 3.7: Seismic line UK-G2 with interpreted deformation zone.

UK-H

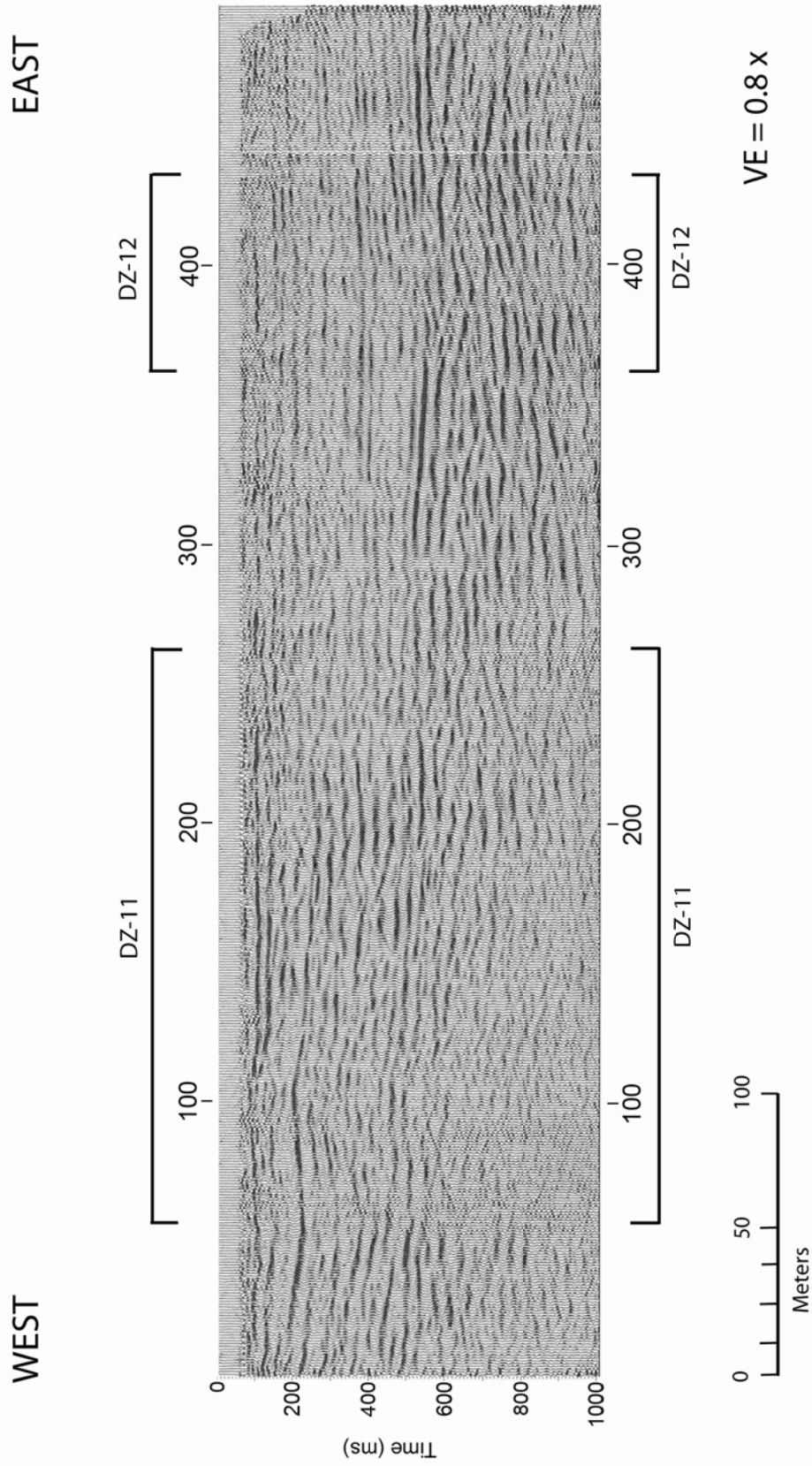


Figure 3.8: Seismic line UK-H with interpreted deformation zone.

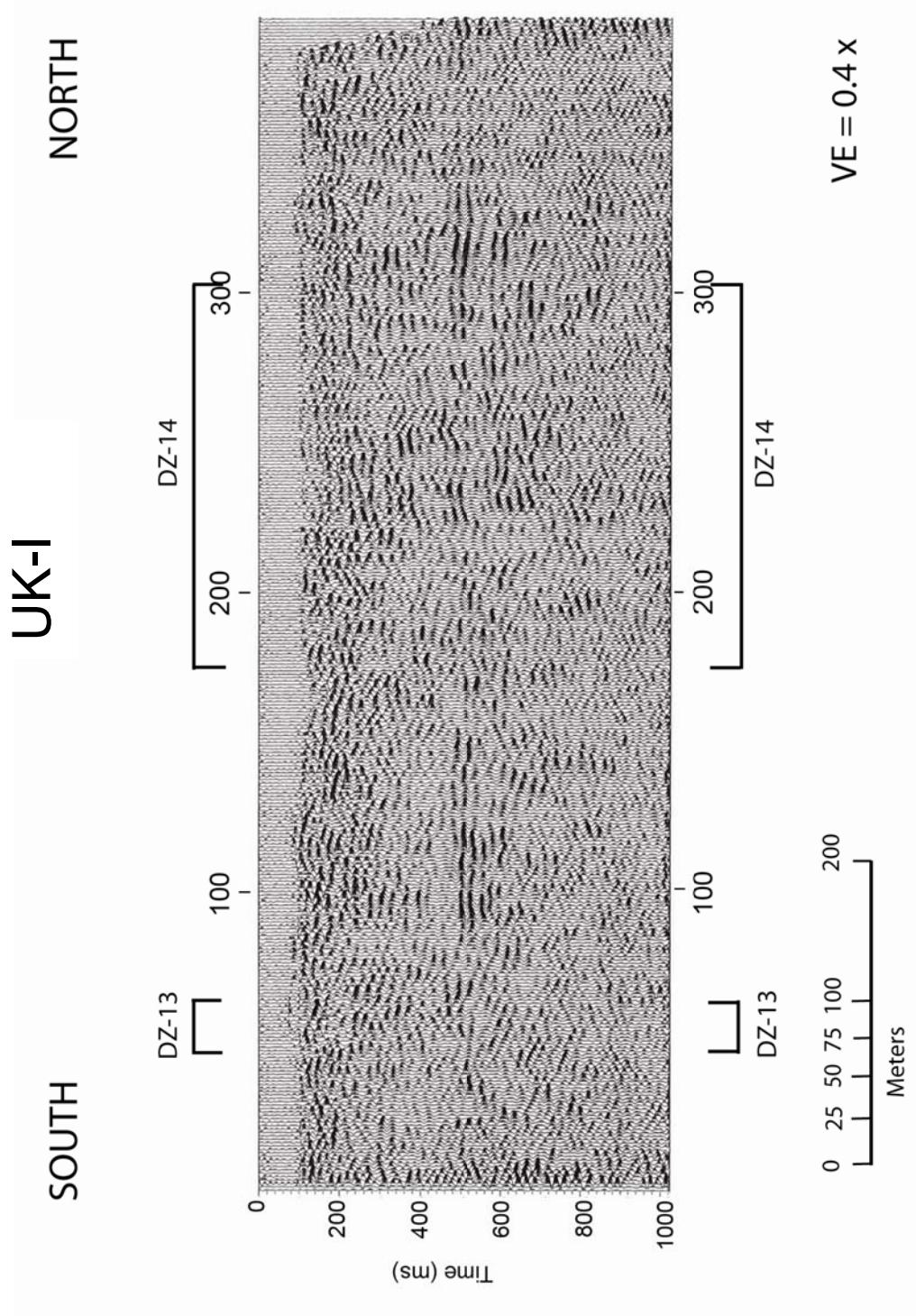


Figure 3.9: Seismic line UK-I with interpreted deformation zones.

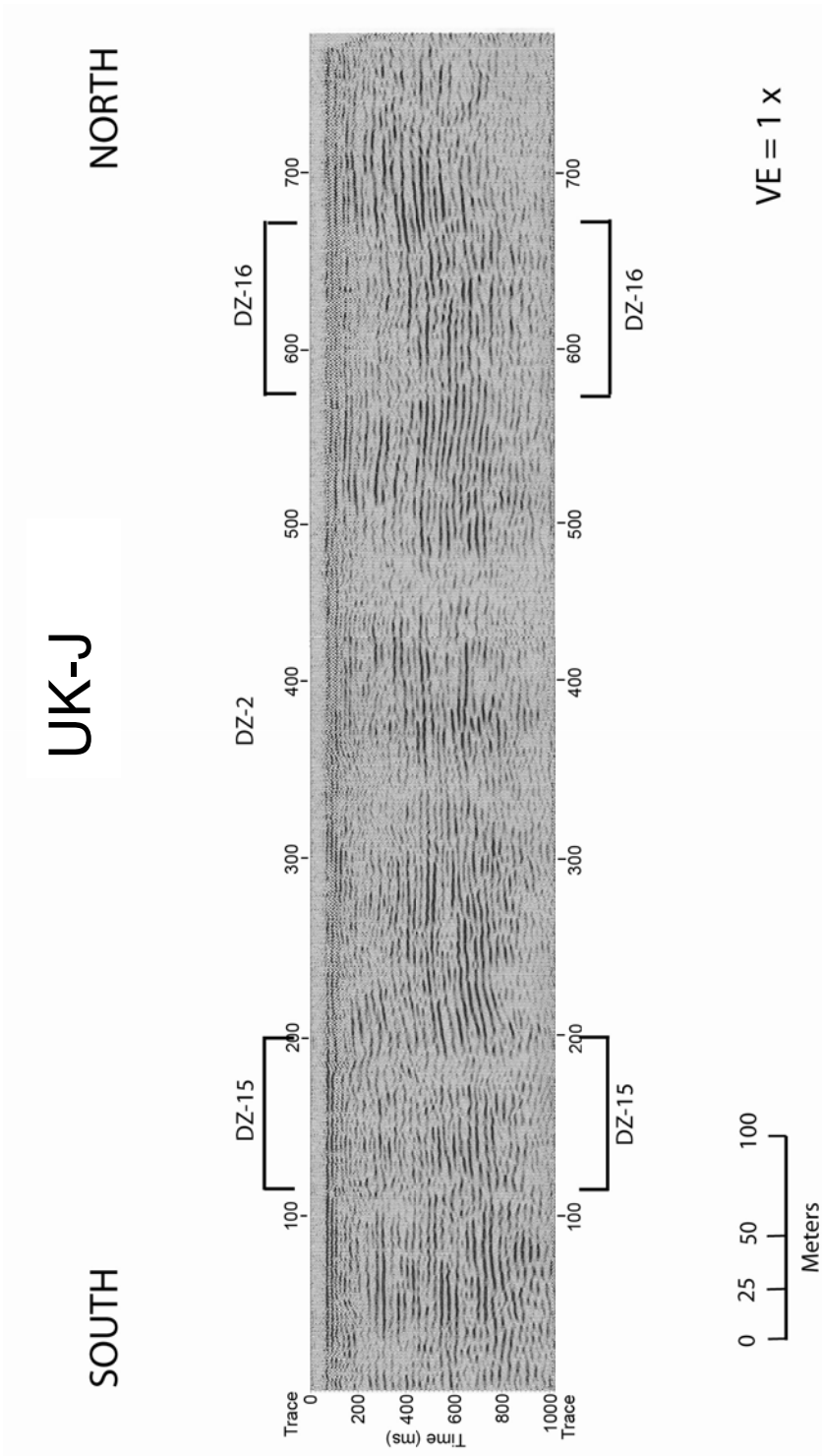


Figure 3.10: Seismic line UK-J with interpreted deformation zones.

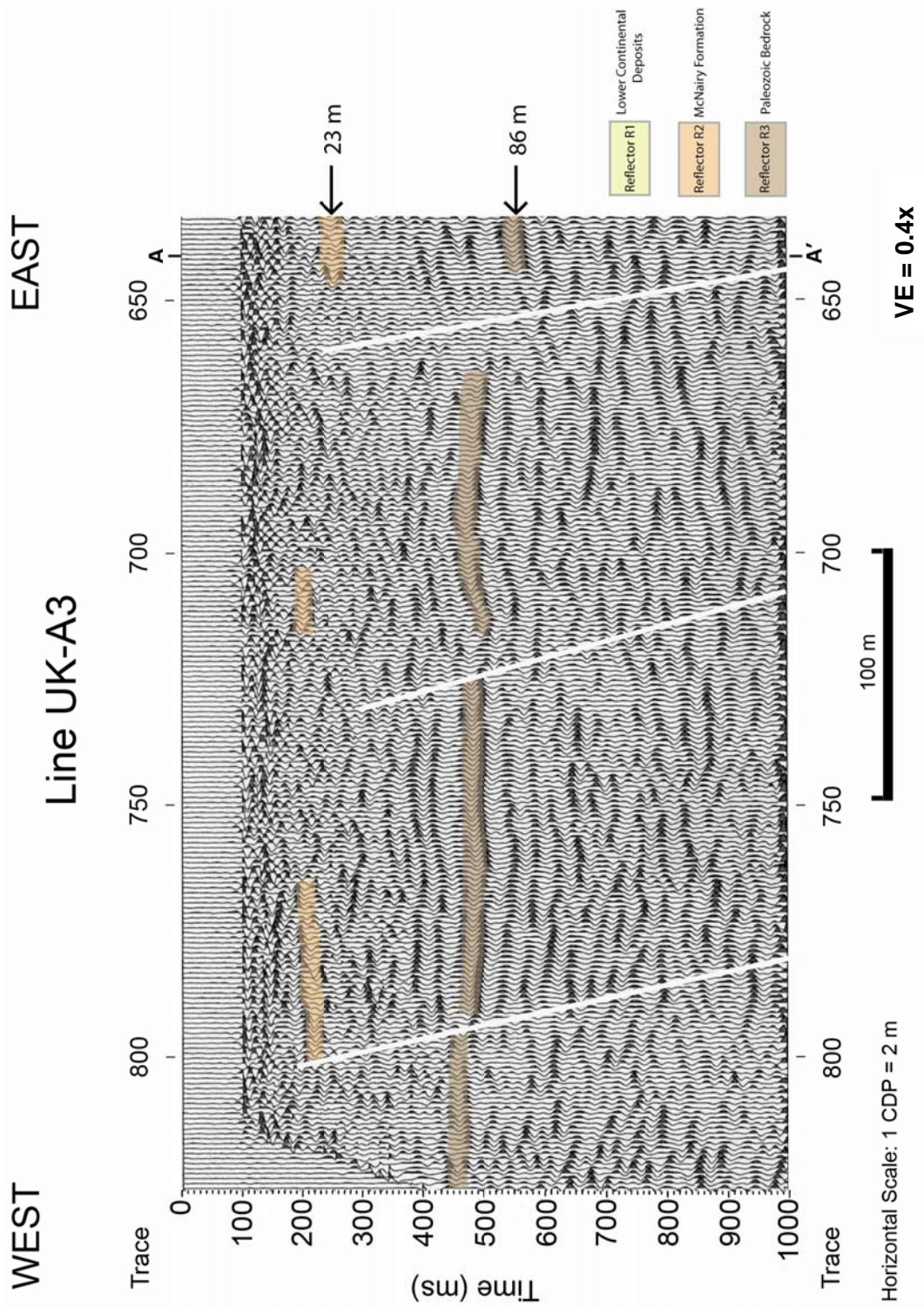


Figure 3.11: Interpreted seismic section UK-A3.

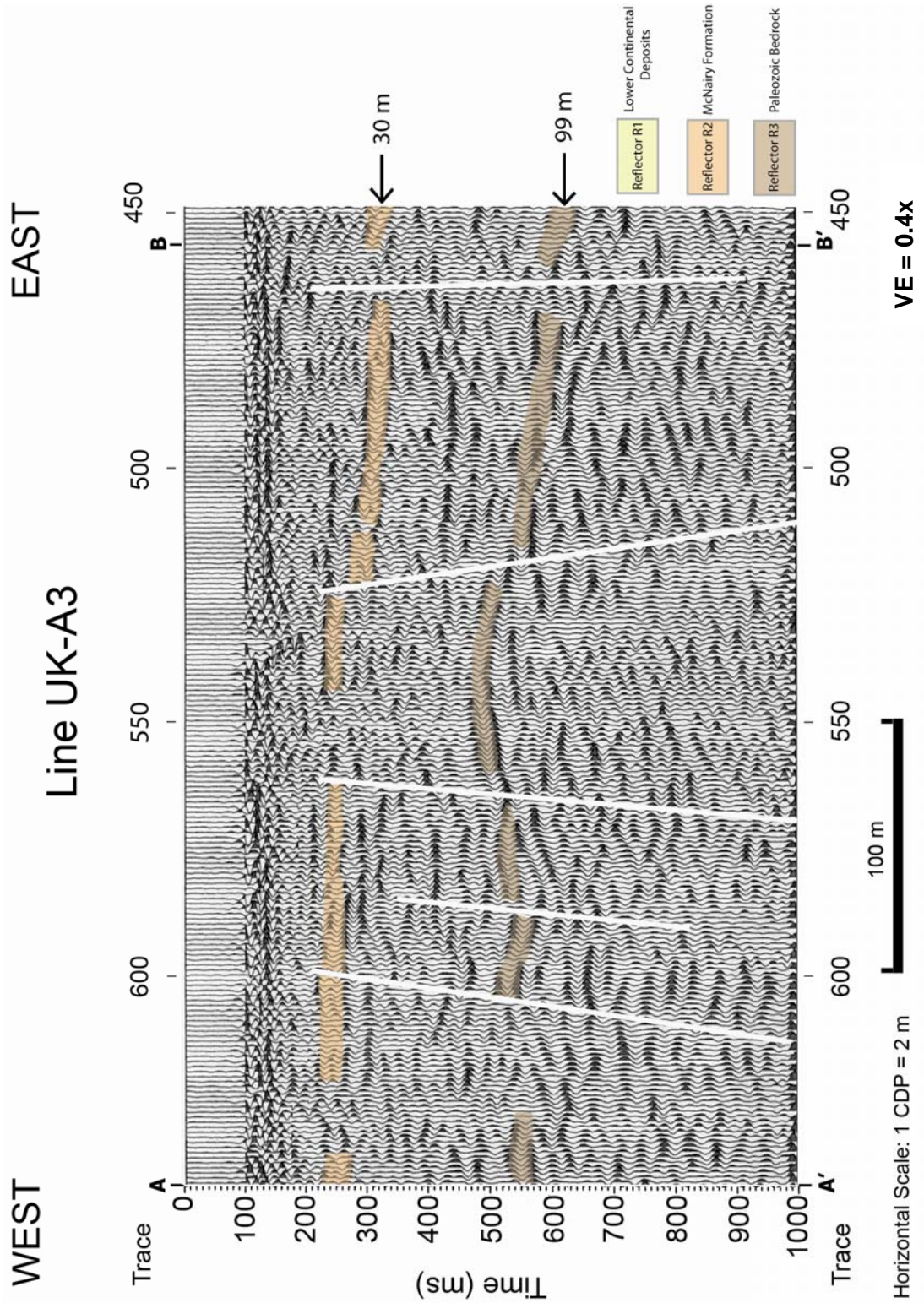


Figure 3.12: Interpreted seismic section UK-A3.

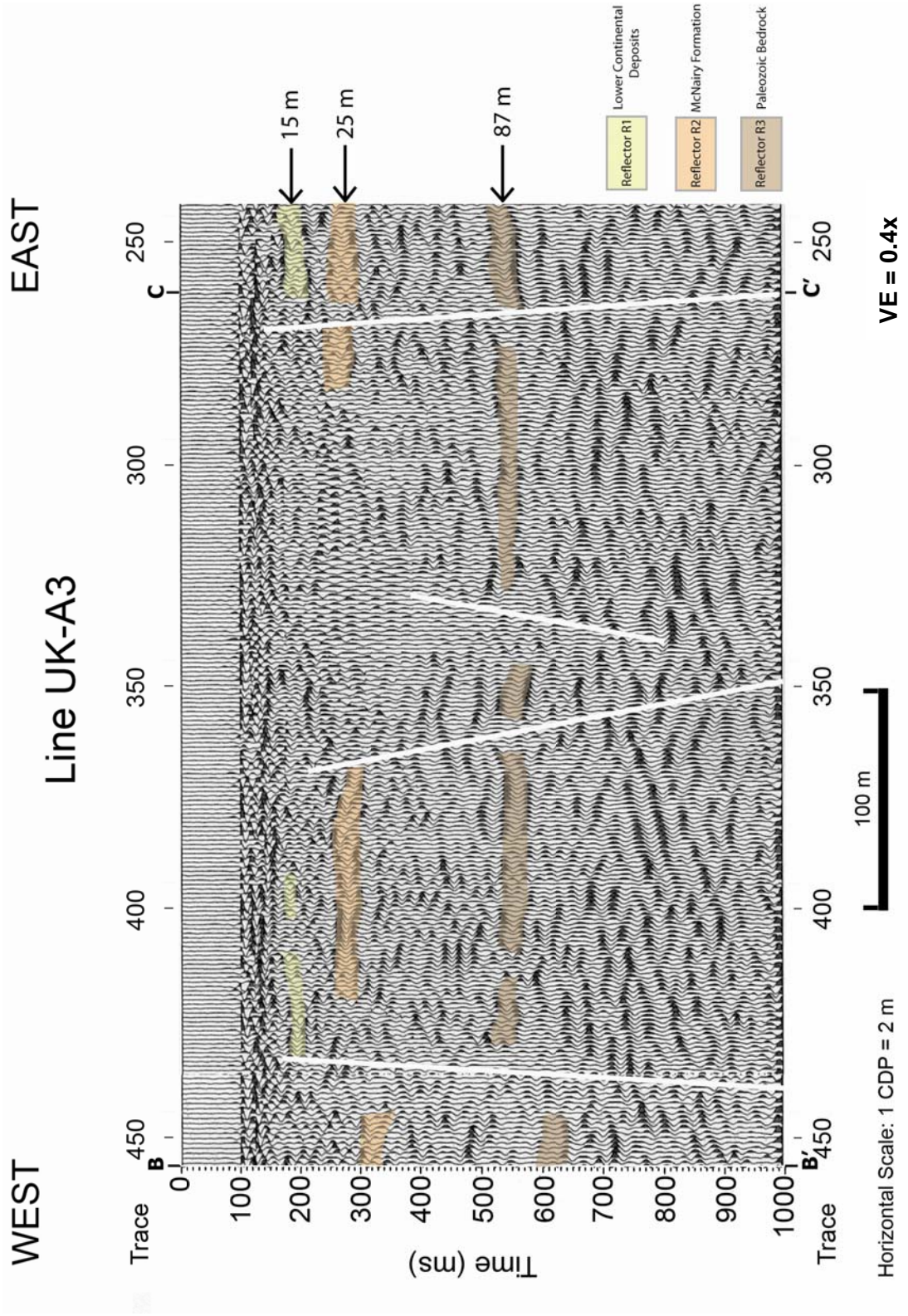


Figure 3.13: Interpreted seismic section UK-A3.

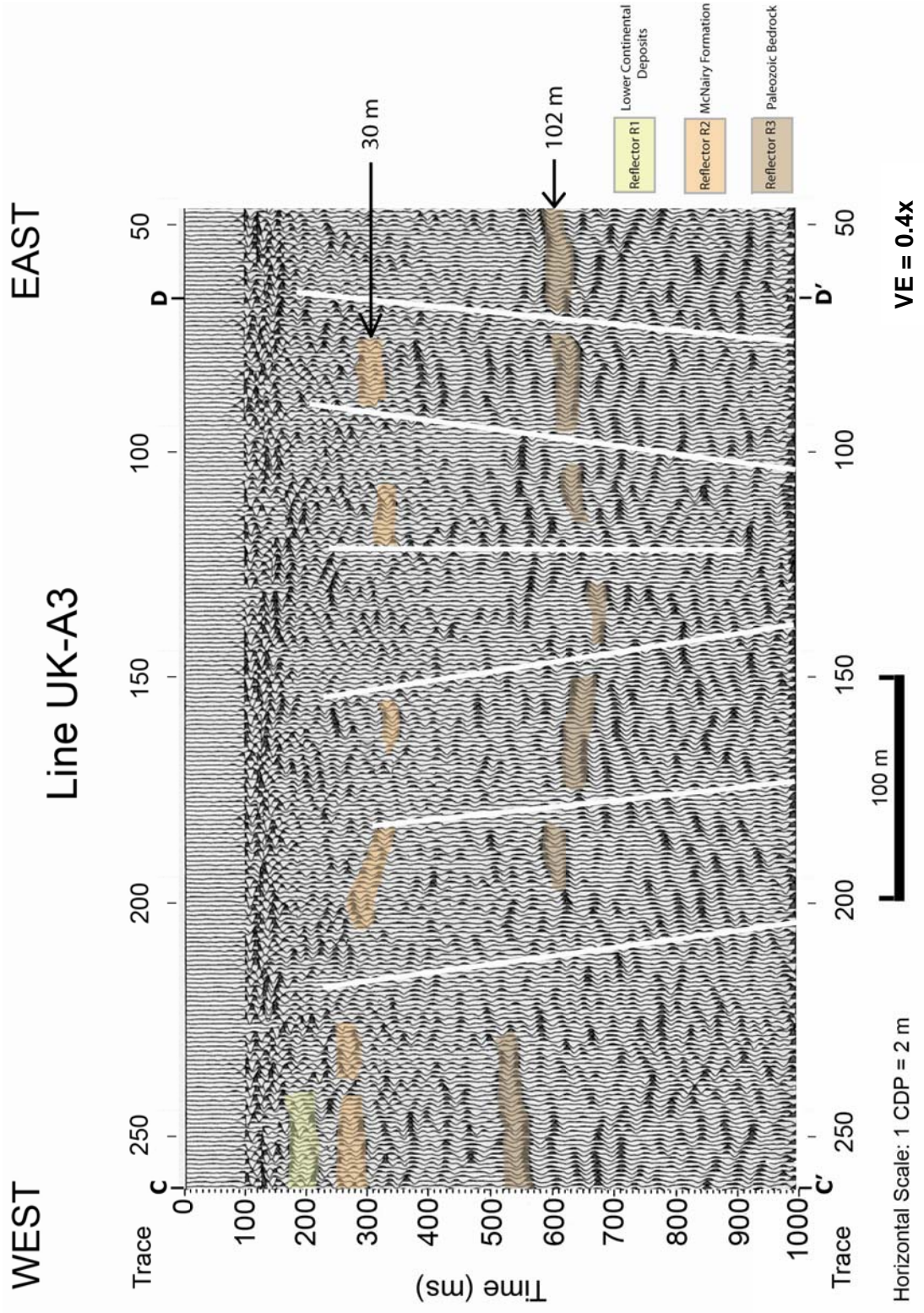


Figure 3.14: Interpreted seismic section UK-A3.

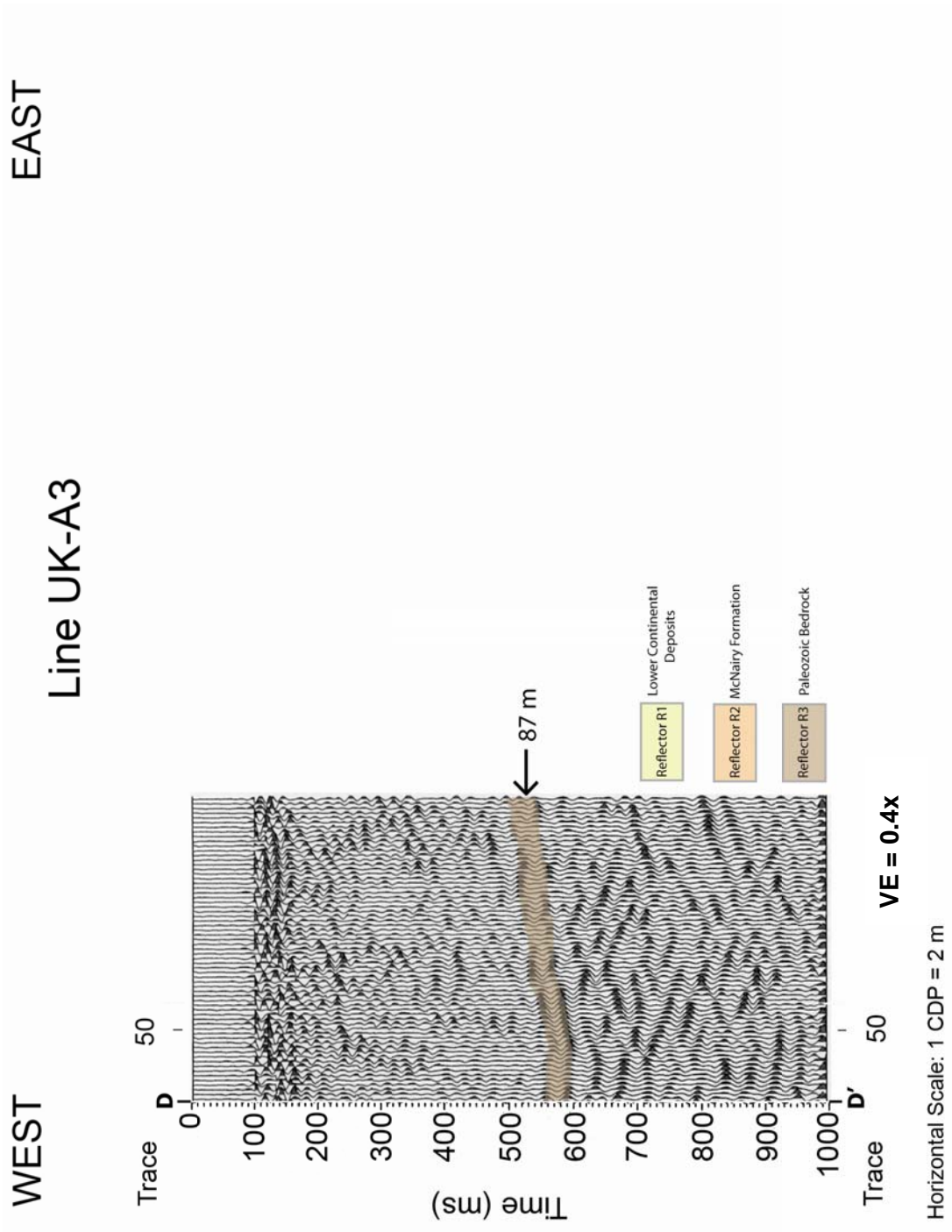


Figure 3.15: Interpreted seismic section UK-A3.

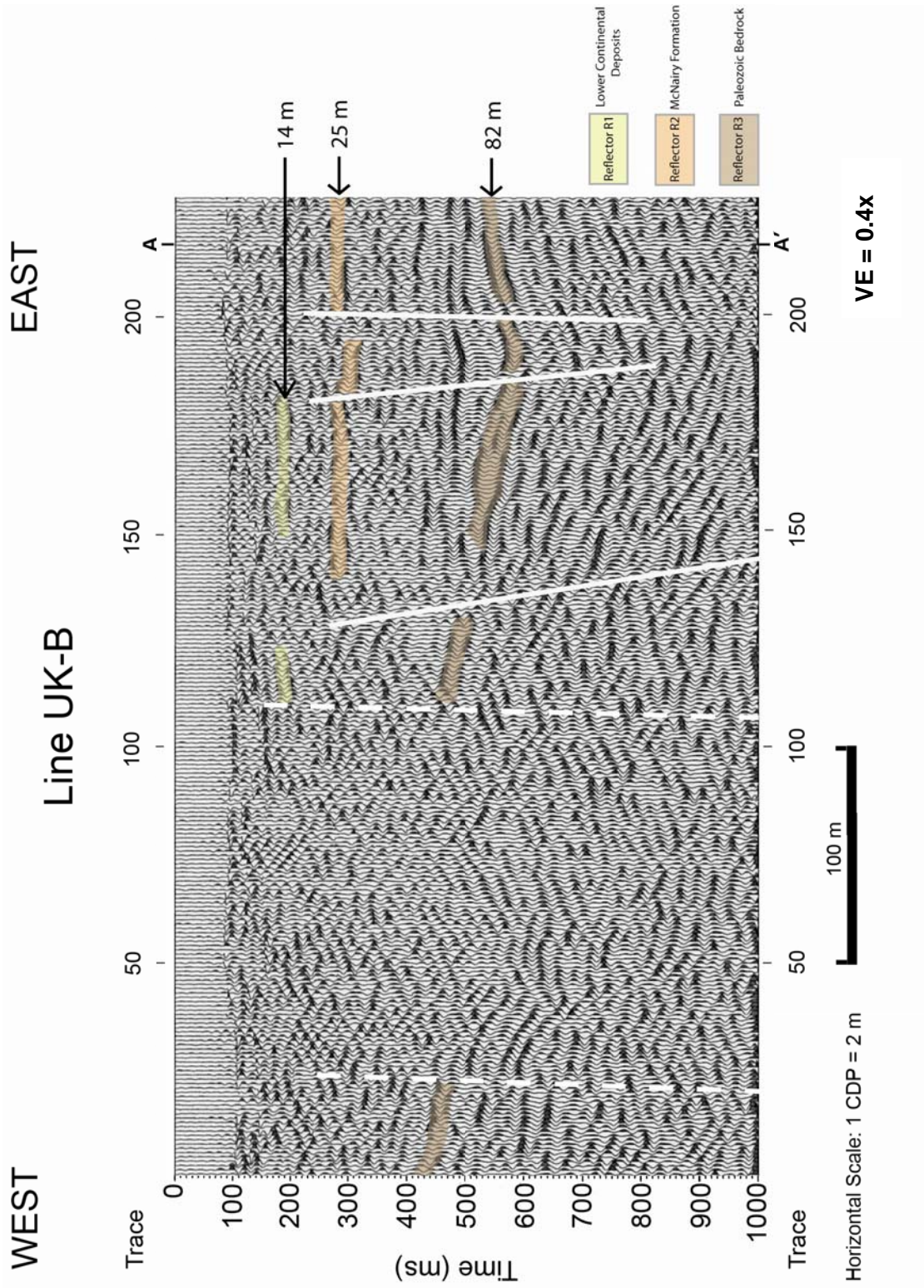


Figure 3.16: Interpreted seismic section UK-B.

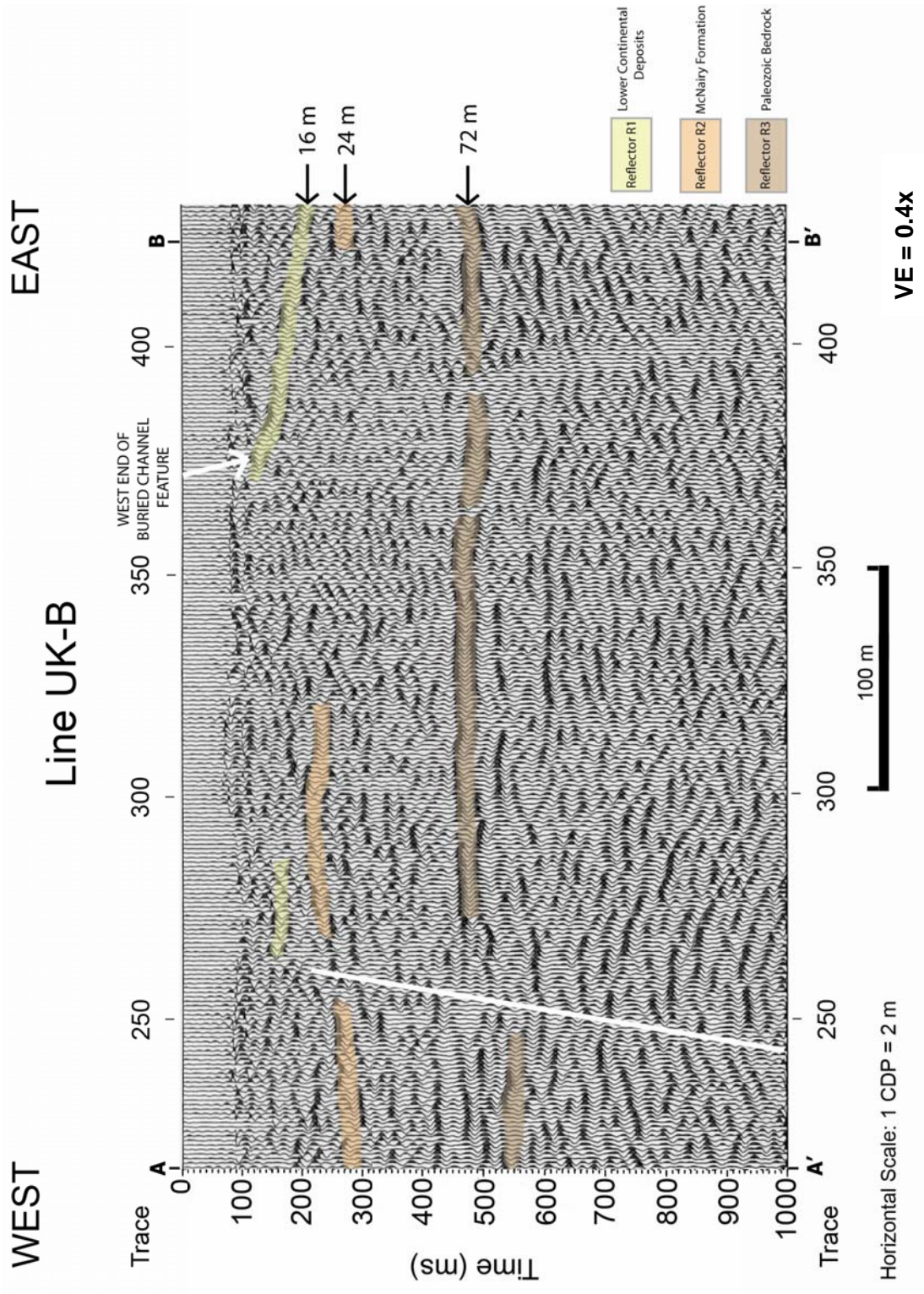


Figure 3.17: Interpreted seismic section UK-B.

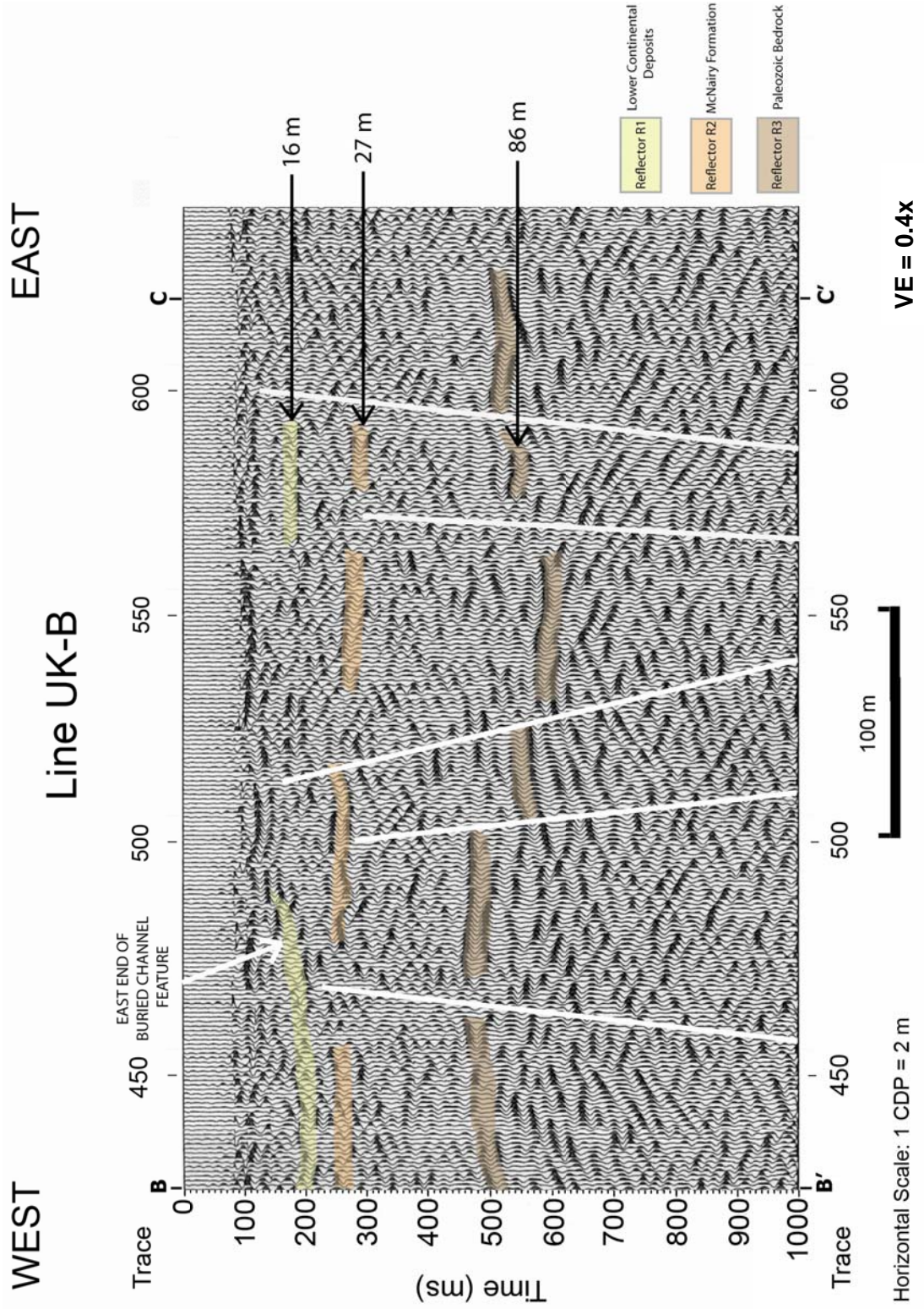


Figure 3.18: Interpreted seismic section UK-B.

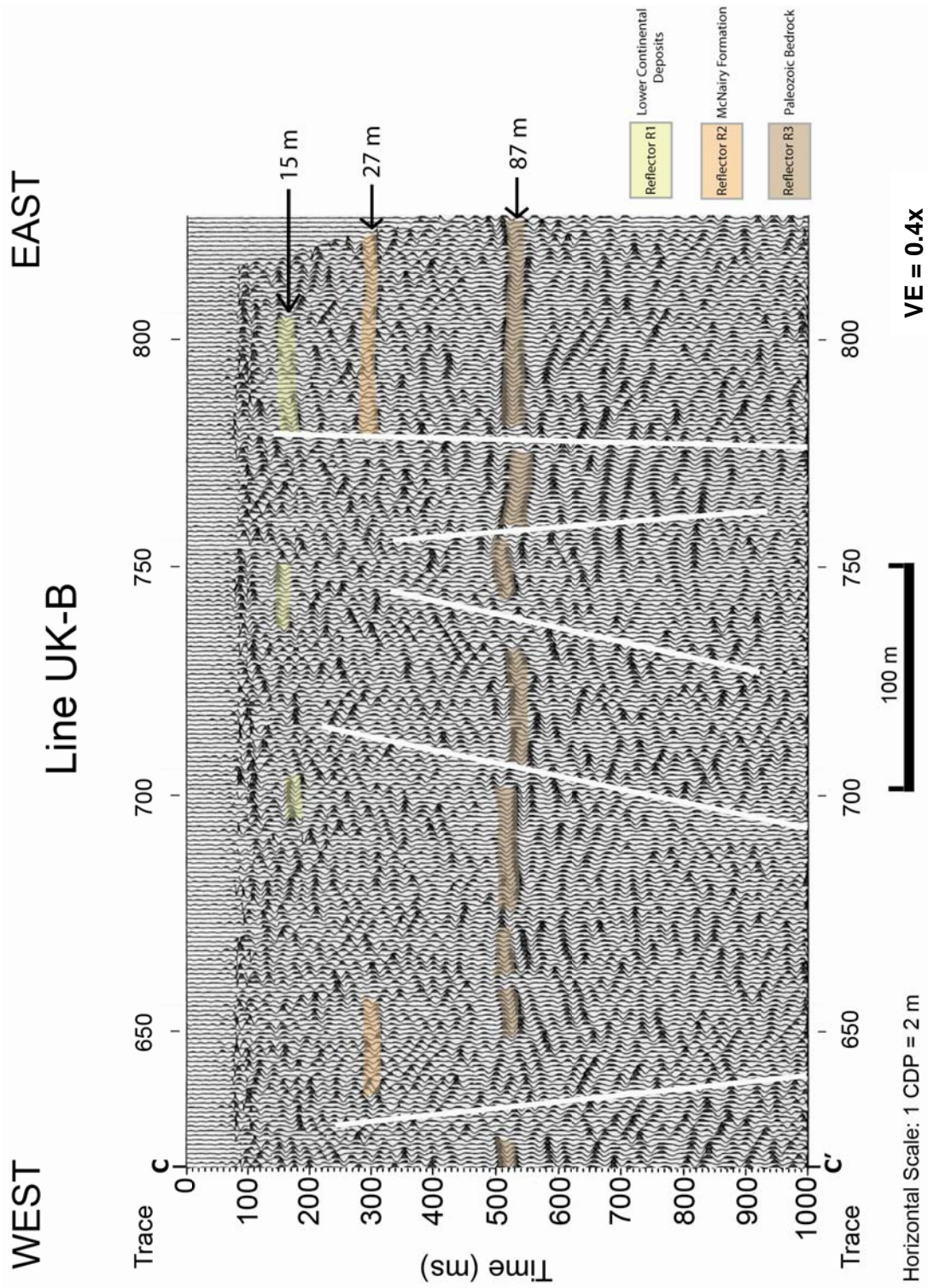


Figure 3.19: Interpreted seismic section UK-B.

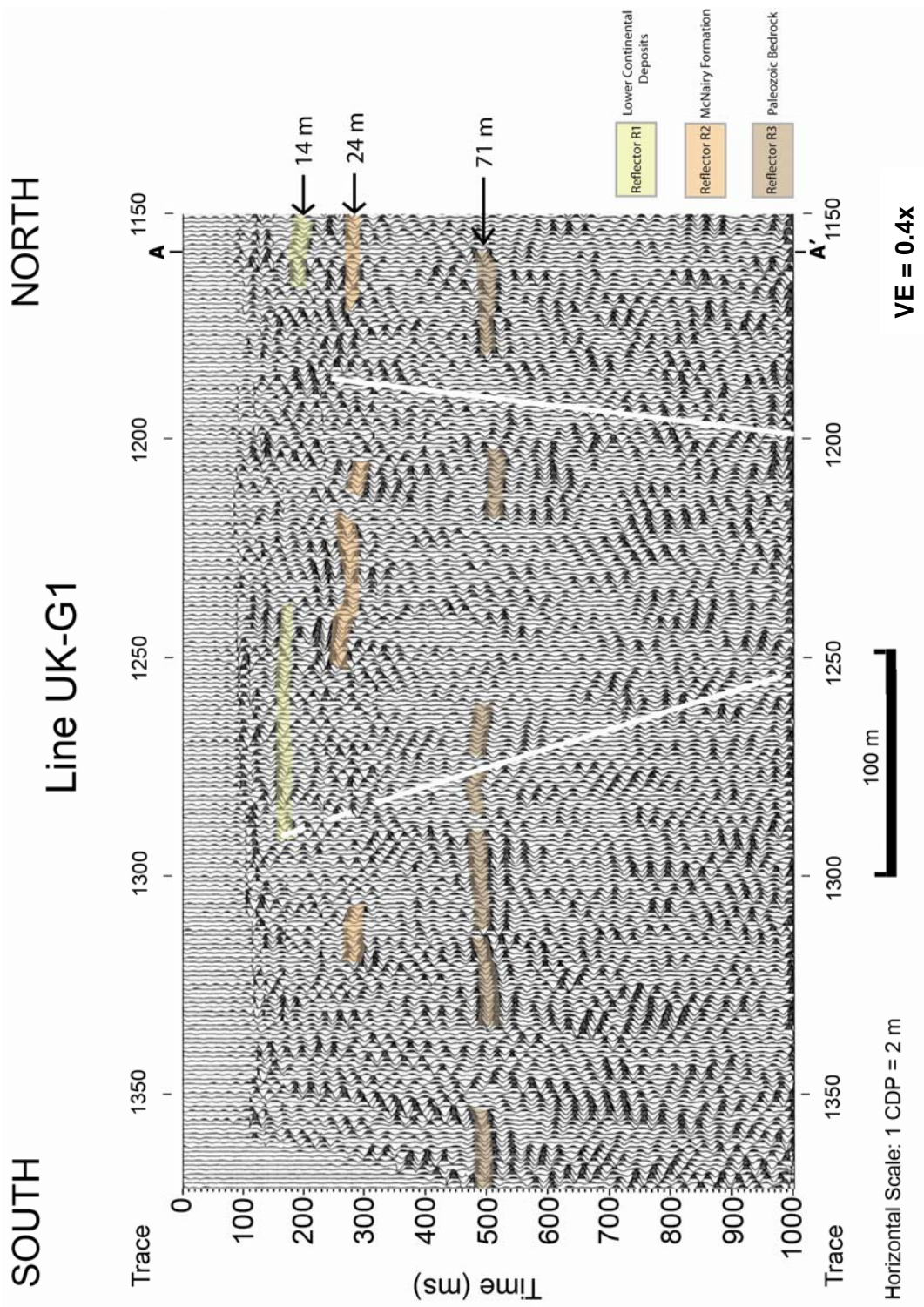


Figure 3.20: Interpreted seismic section UK-G1.

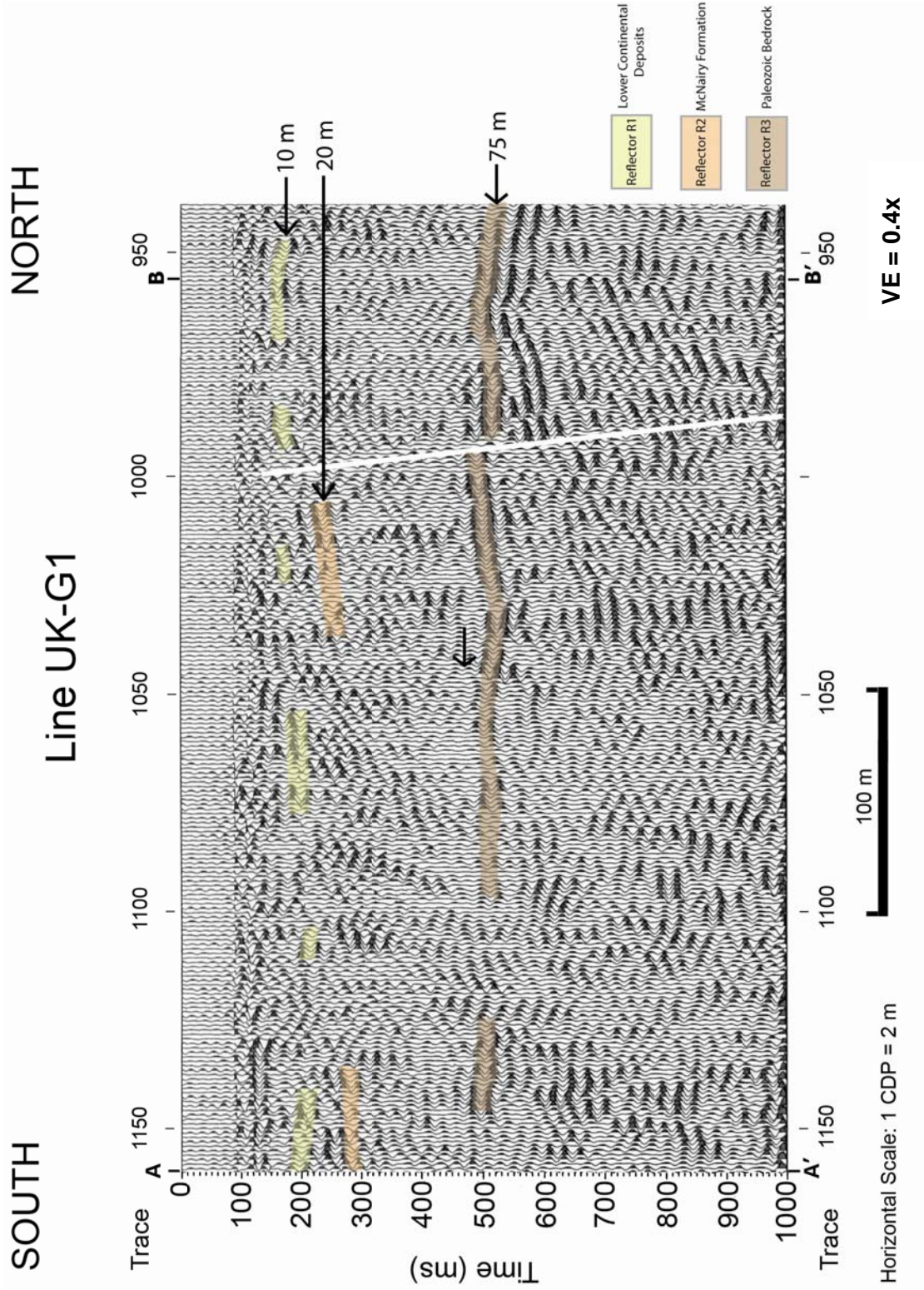


Figure 3.2J: Interpreted seismic section UK-G1.

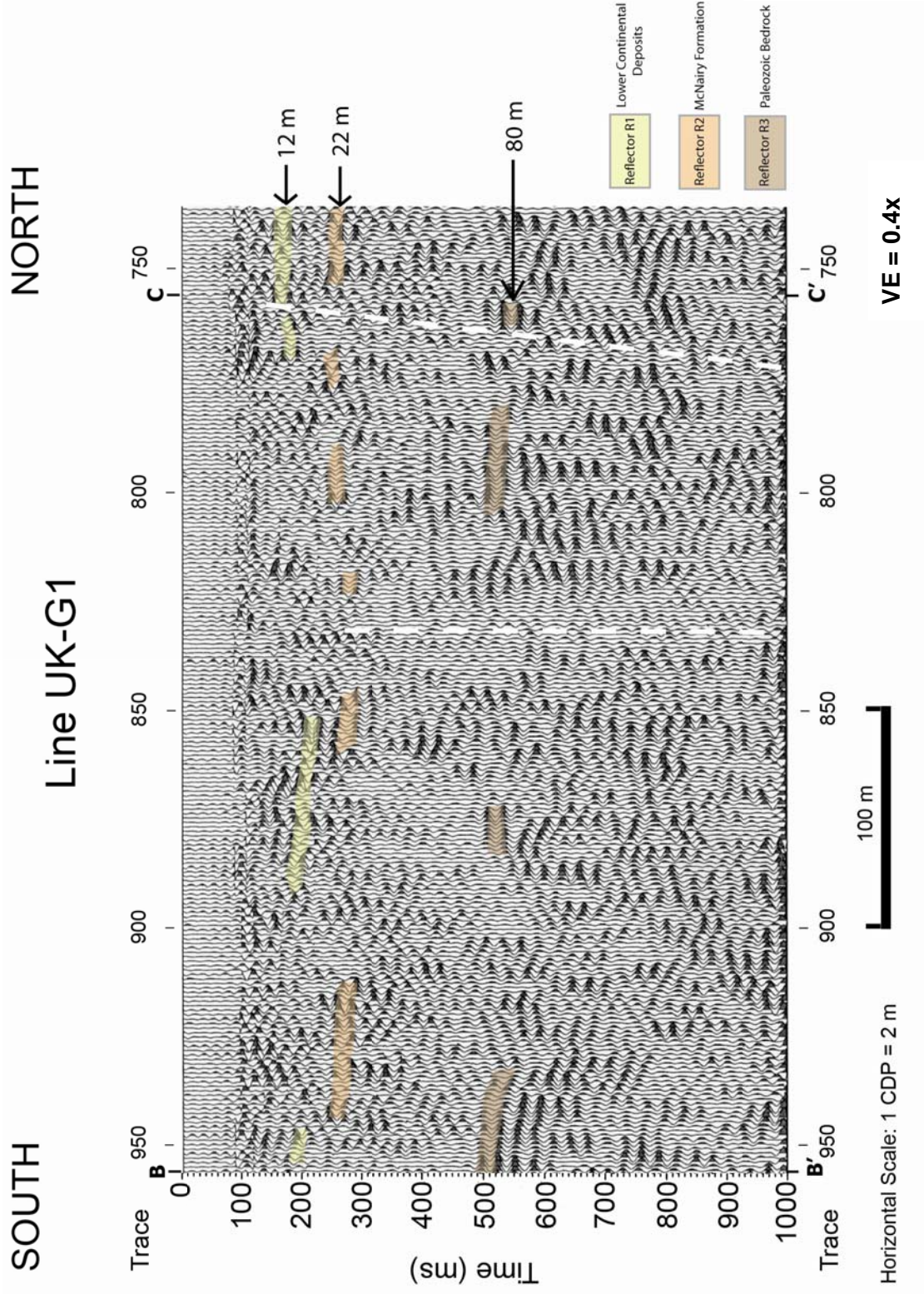


Figure 3.22: Interpreted seismic section UK-G1.

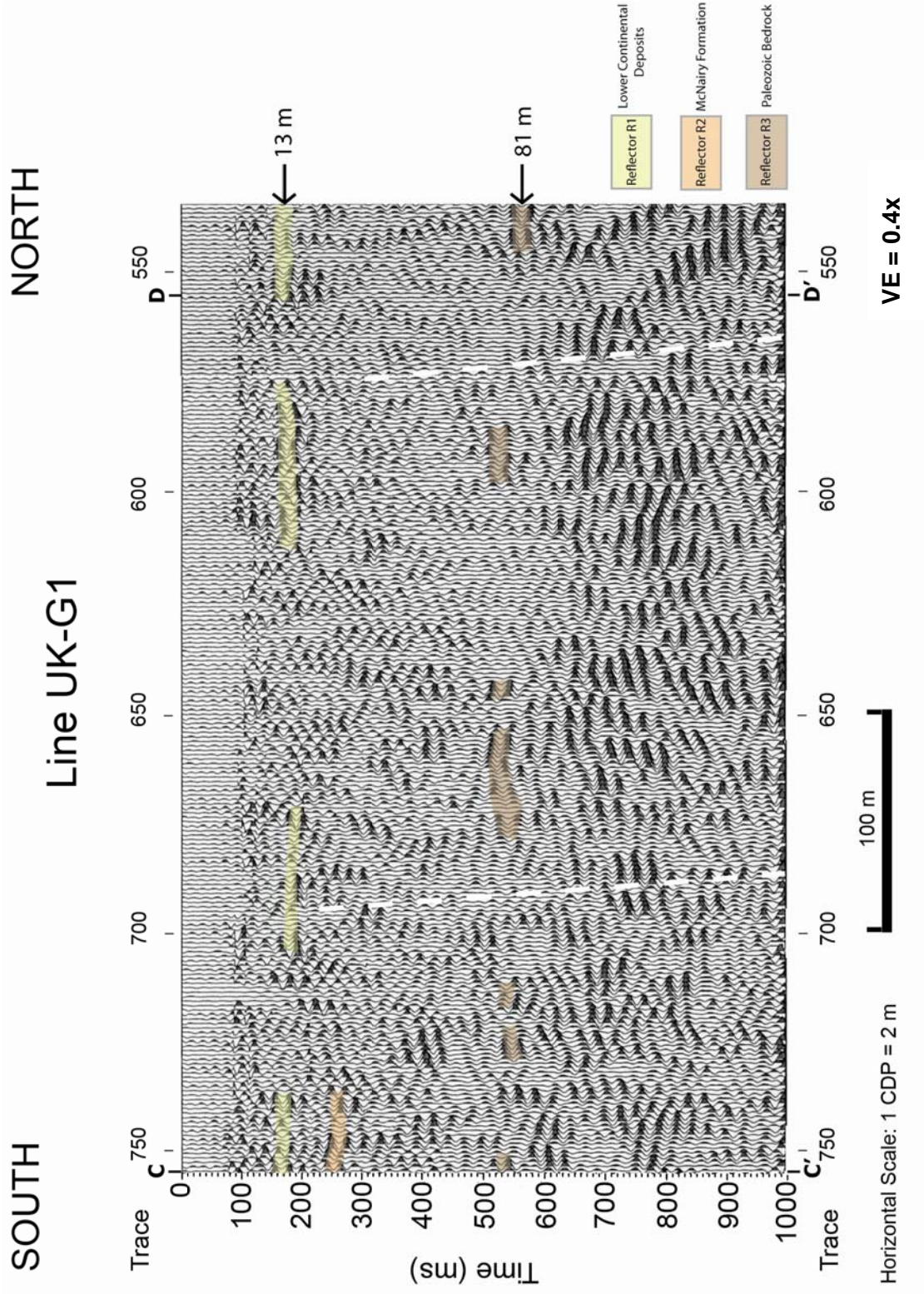


Figure 3.23: Interpreted seismic section UK-G1.

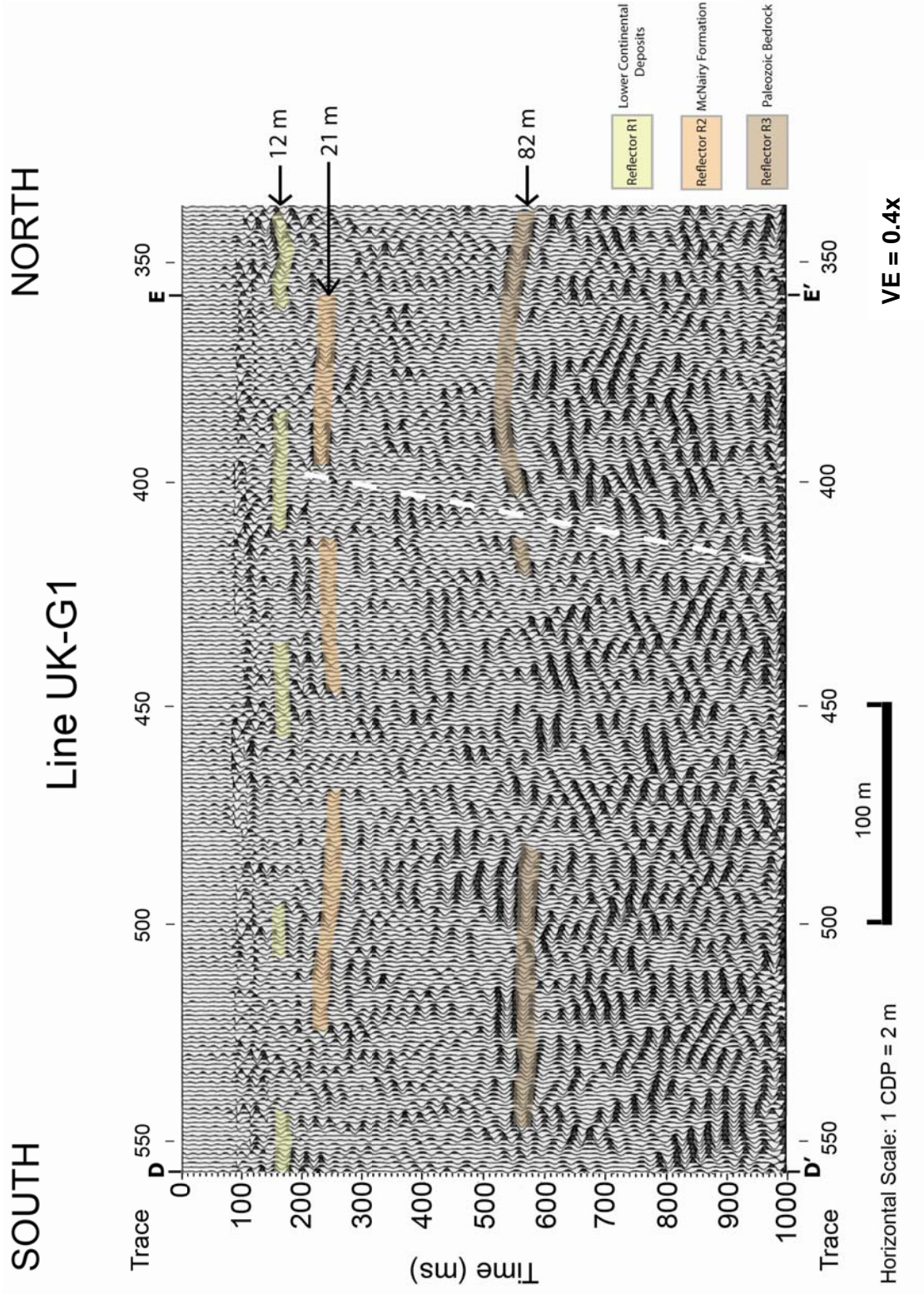


Figure 3.24: Interpreted seismic section UK-G1.

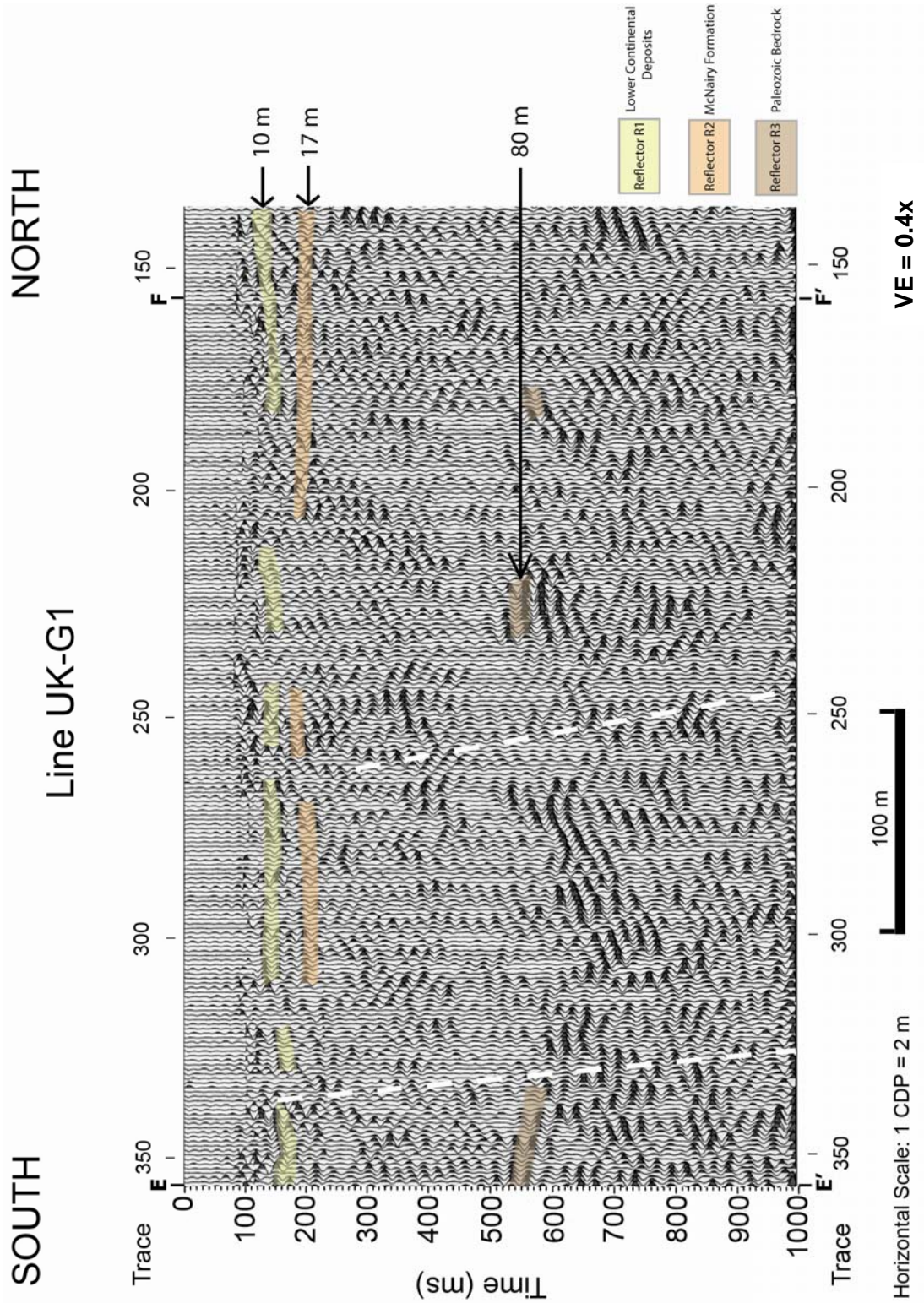


Figure 3.2.5: Interpreted seismic section UK-G1.

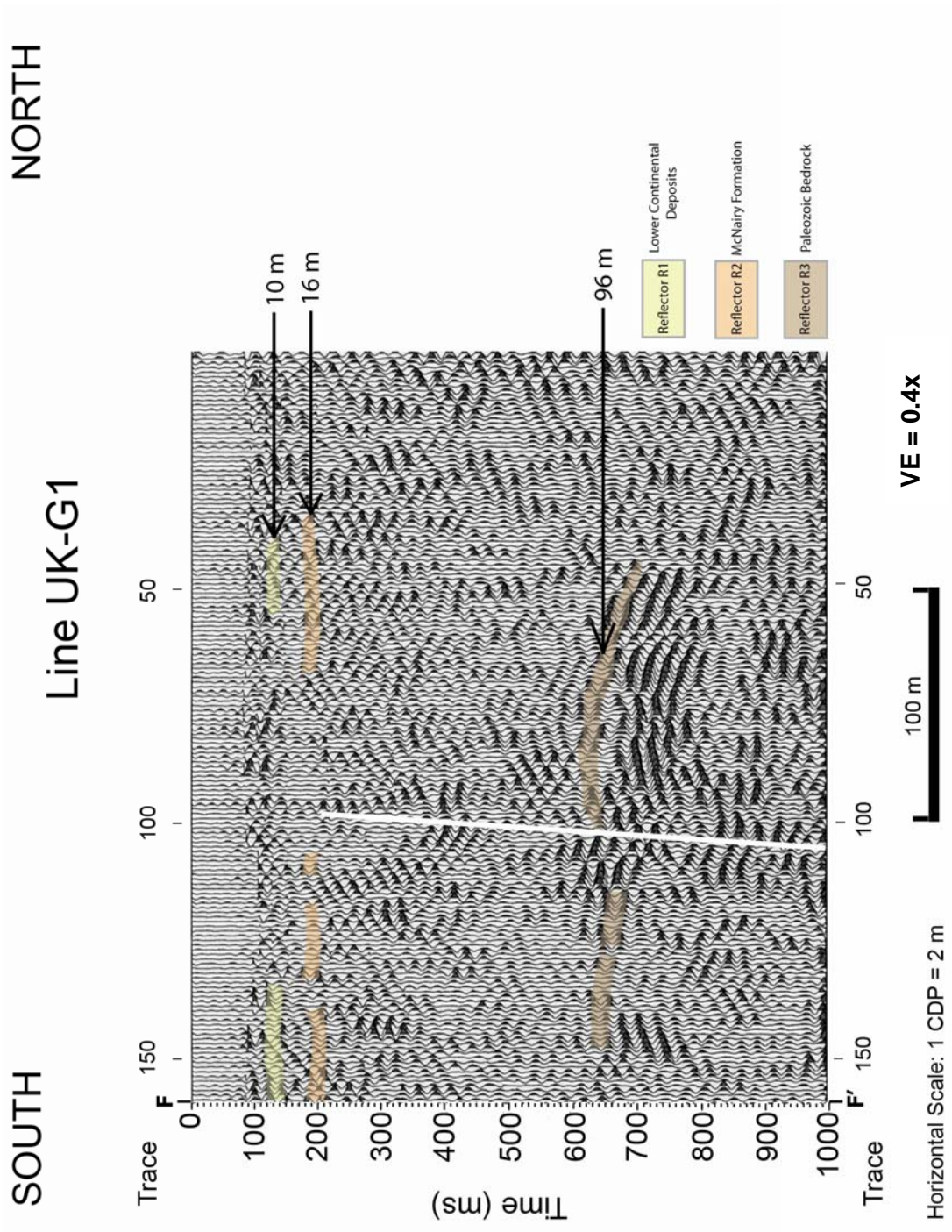


Figure 3.2.6: Interpreted seismic section UK-G1.

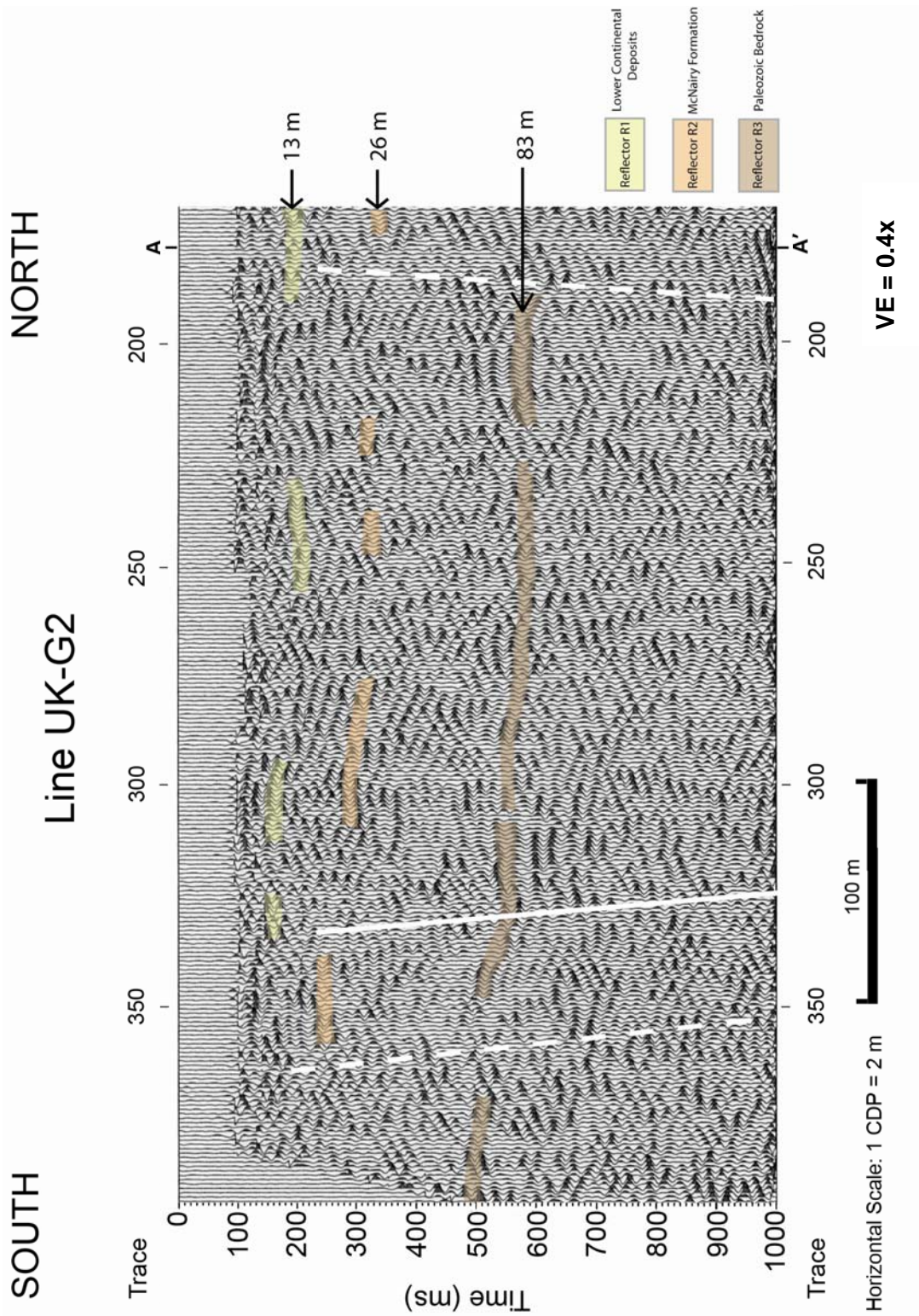


Figure 3.27: Interpreted seismic section UK-G2.

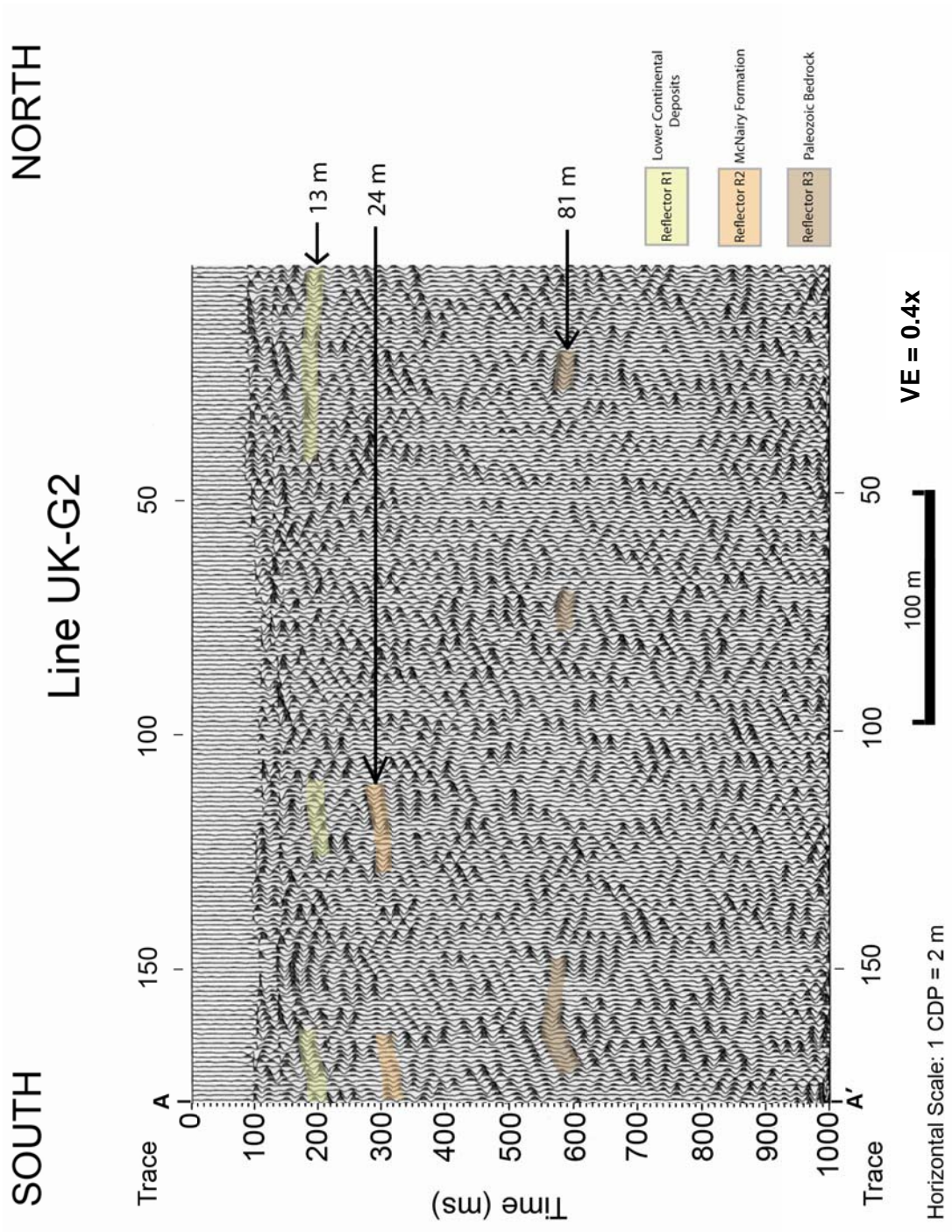


Figure 3.28: Interpreted seismic section UK-G2.

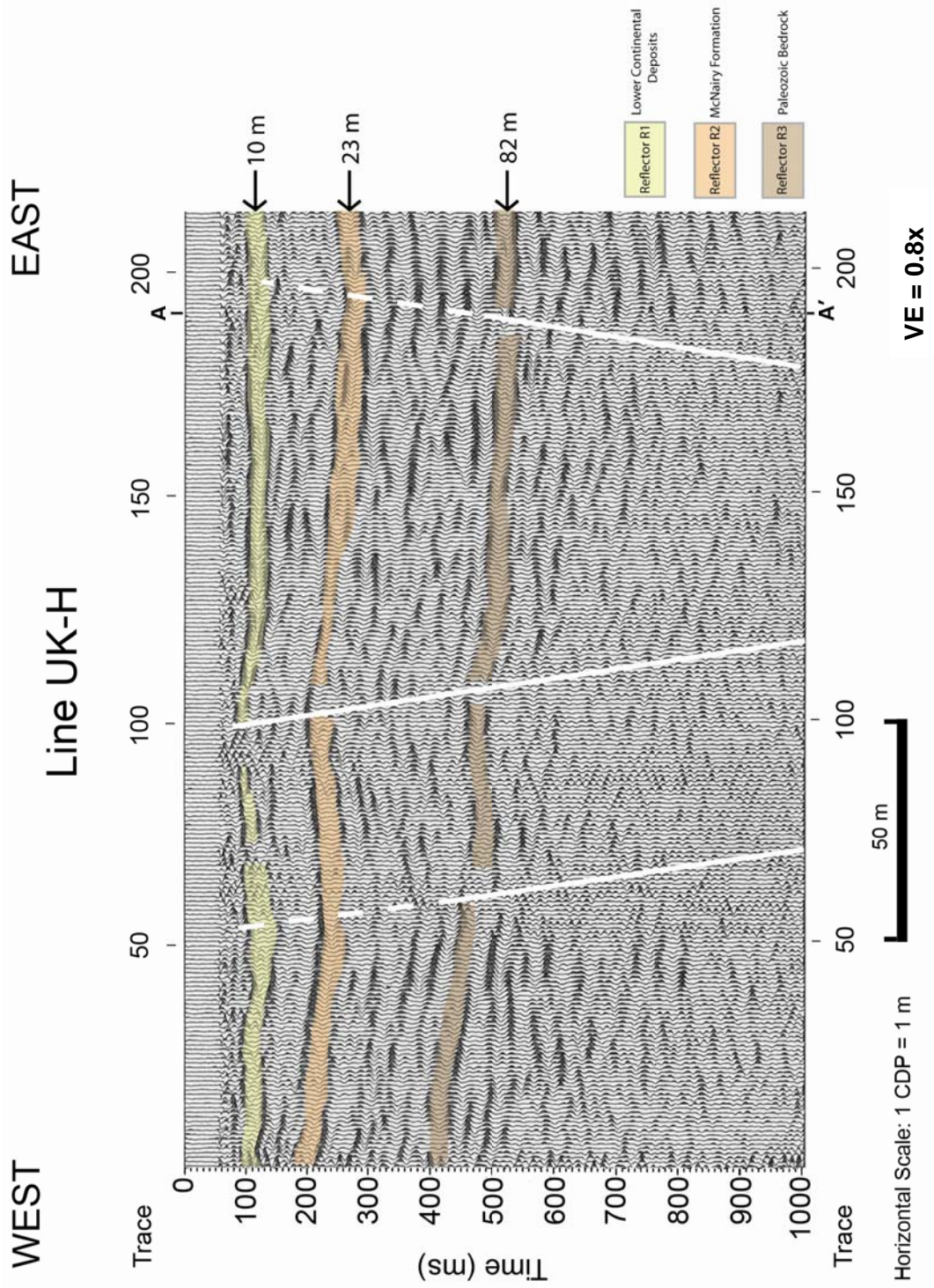


Figure 3.29: Interpreted seismic section UK-H.

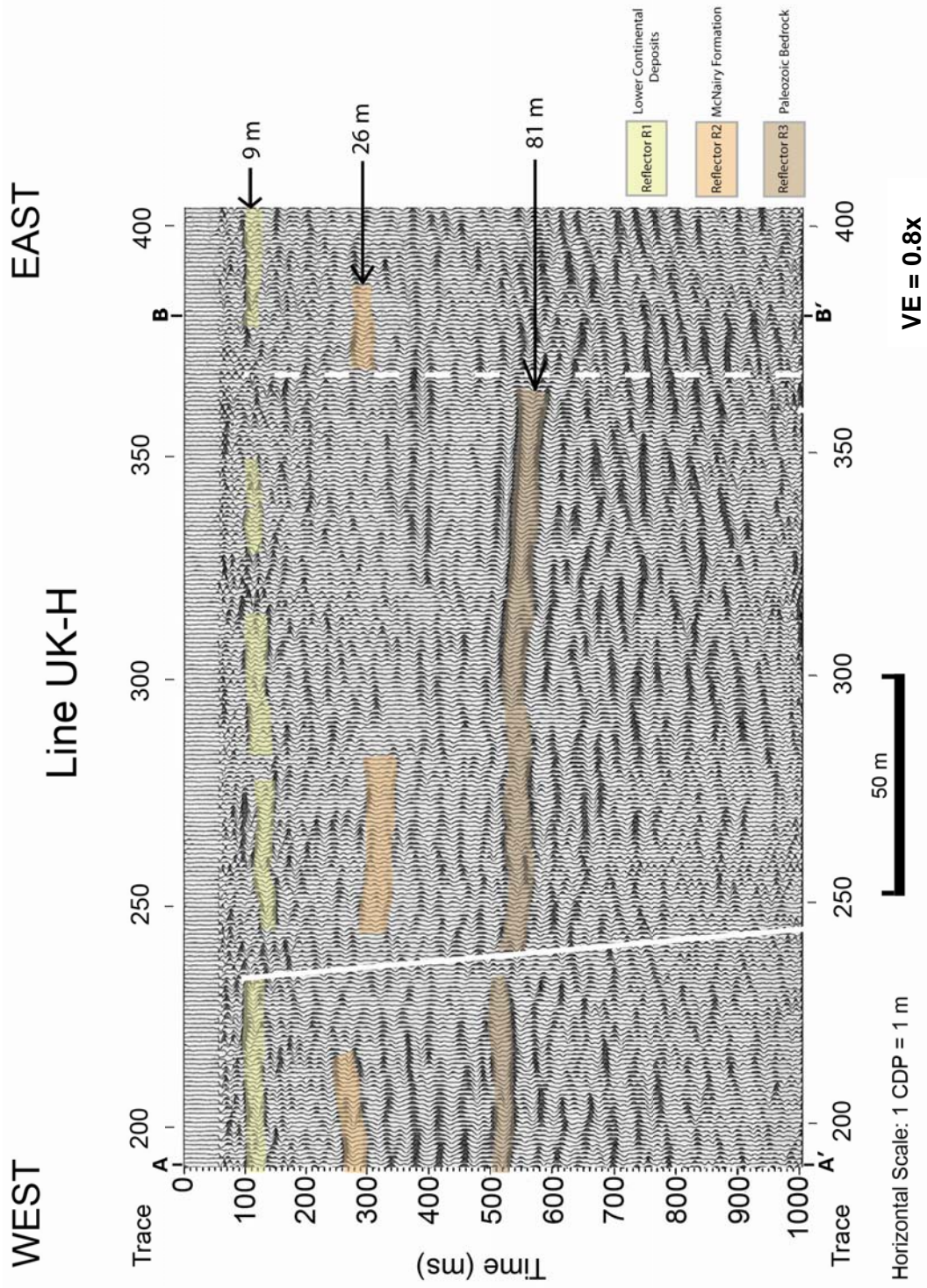


Figure 3.30: Interpreted seismic section UK-H.

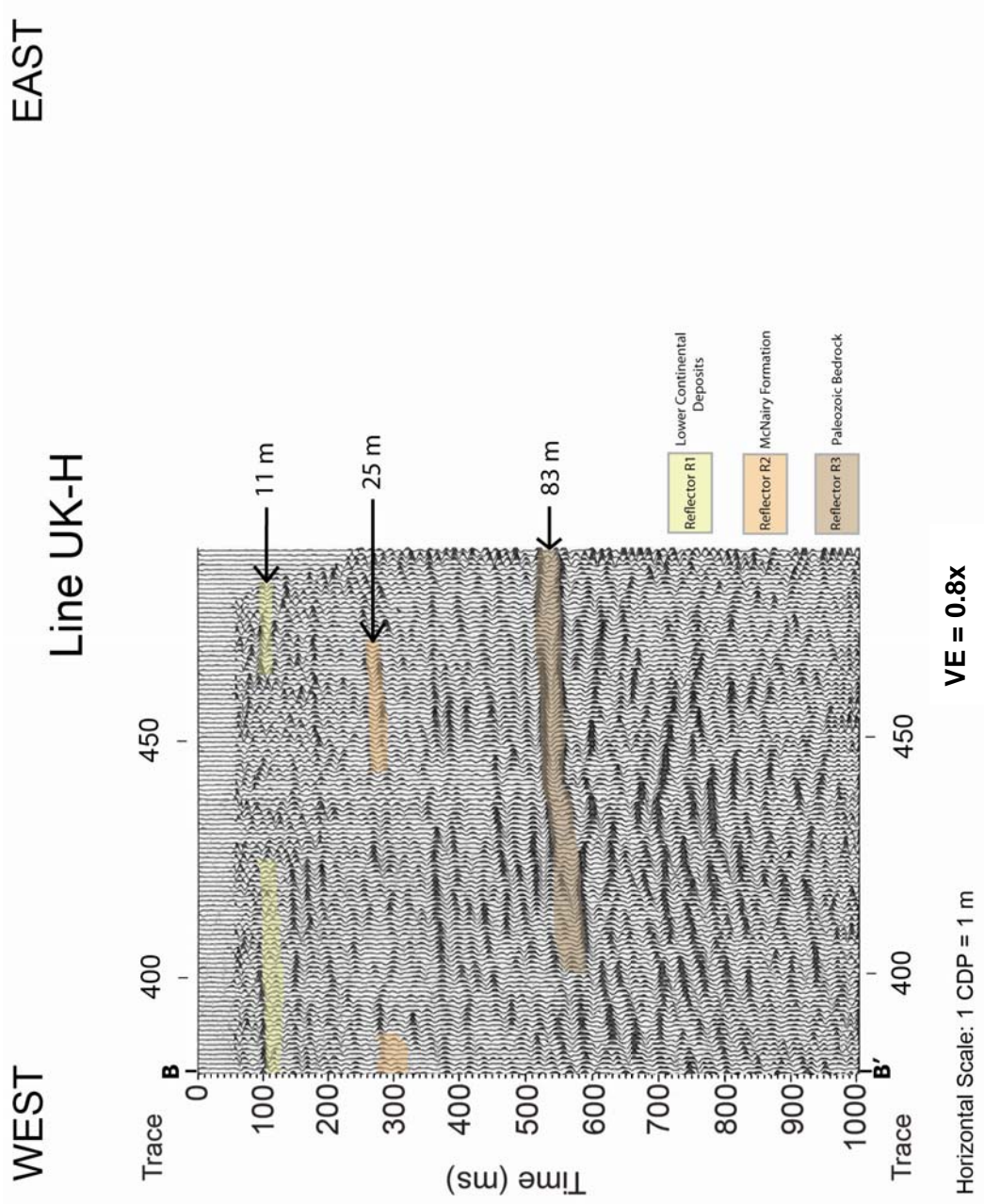


Figure 3.31: Interpreted seismic section UK-H.

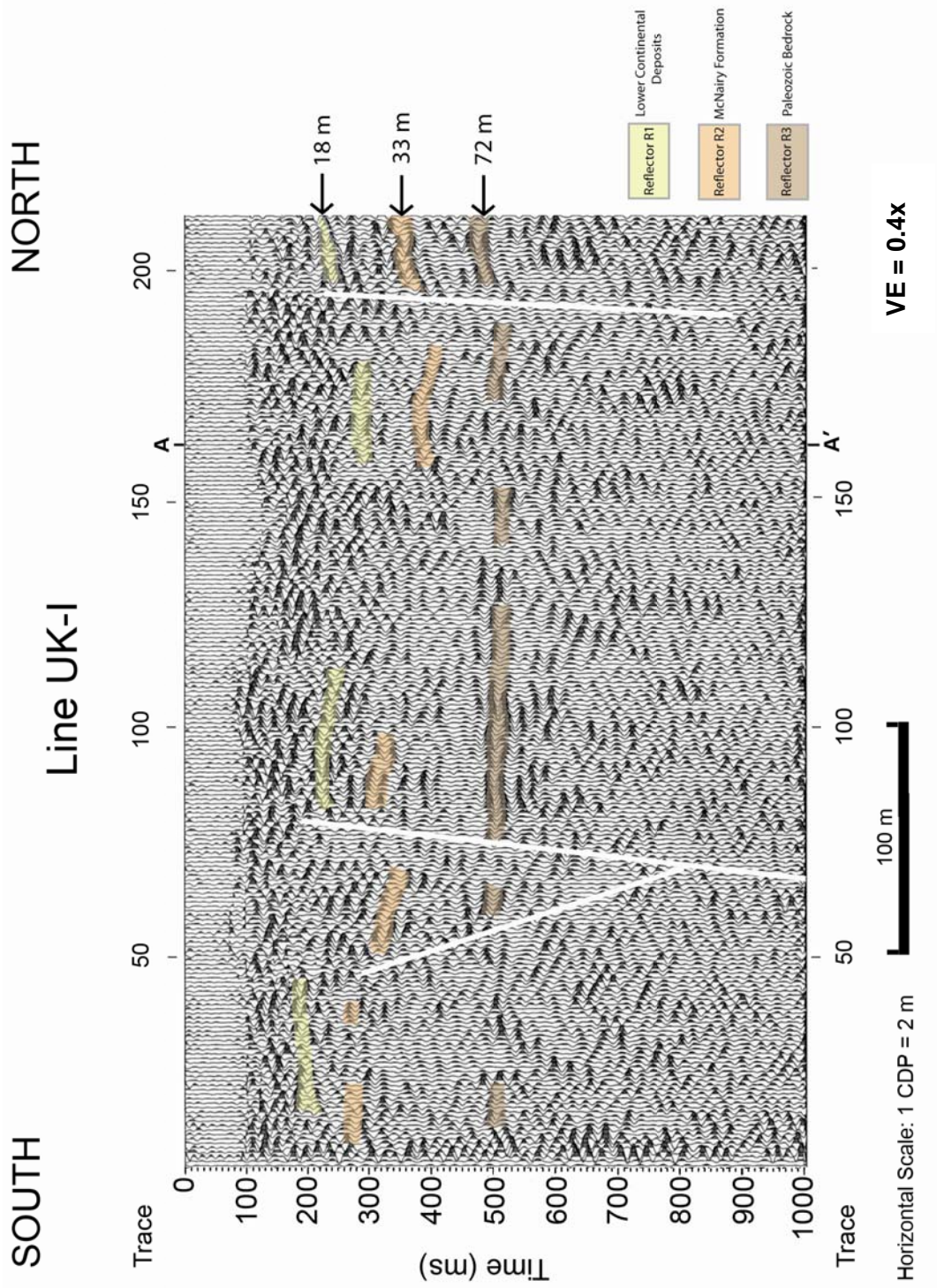


Figure 3.32: Interpreted seismic section UK-I.

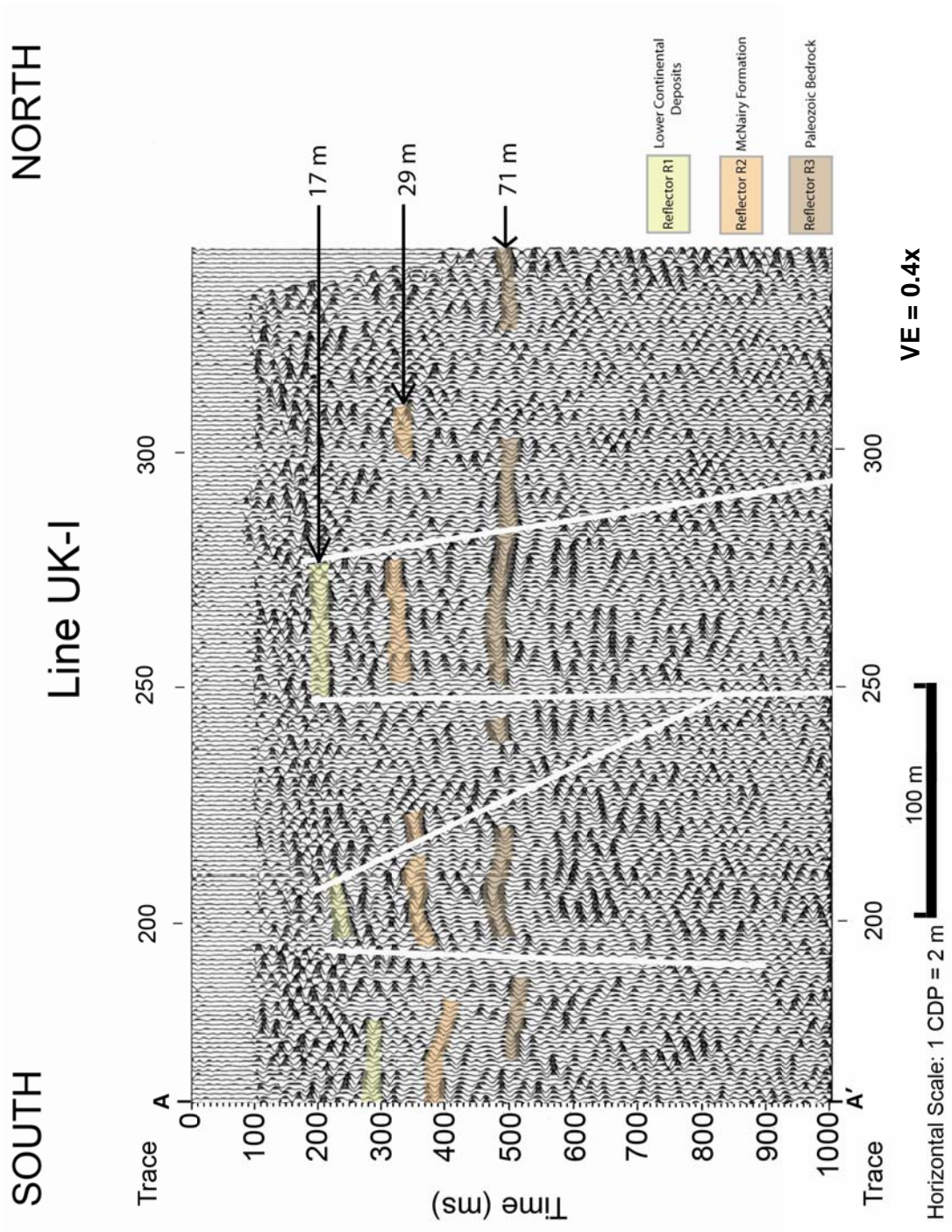


Figure 3.33: Interpreted seismic section UK-I.

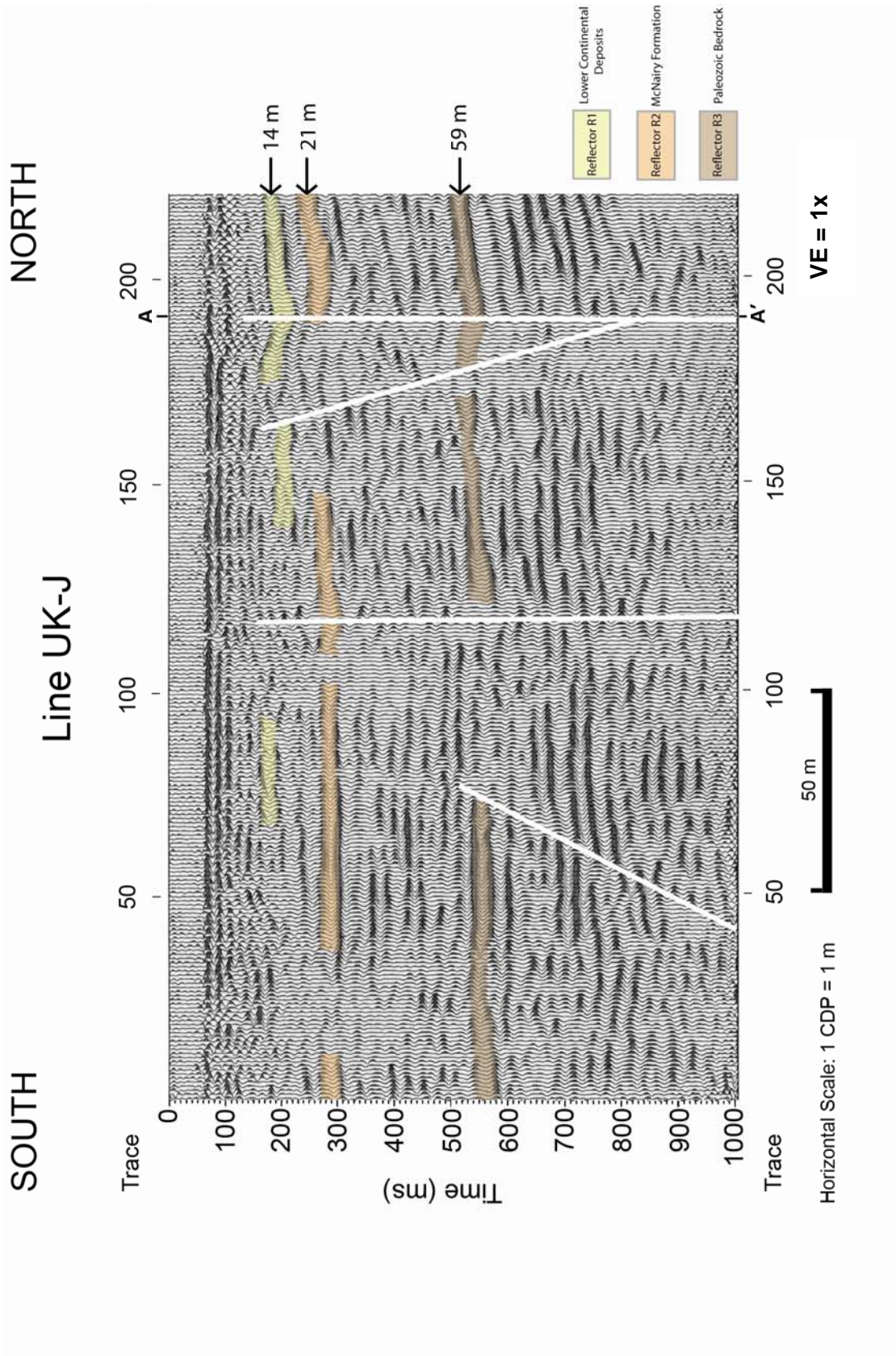


Figure 3.34: Interpreted seismic section UK-J.

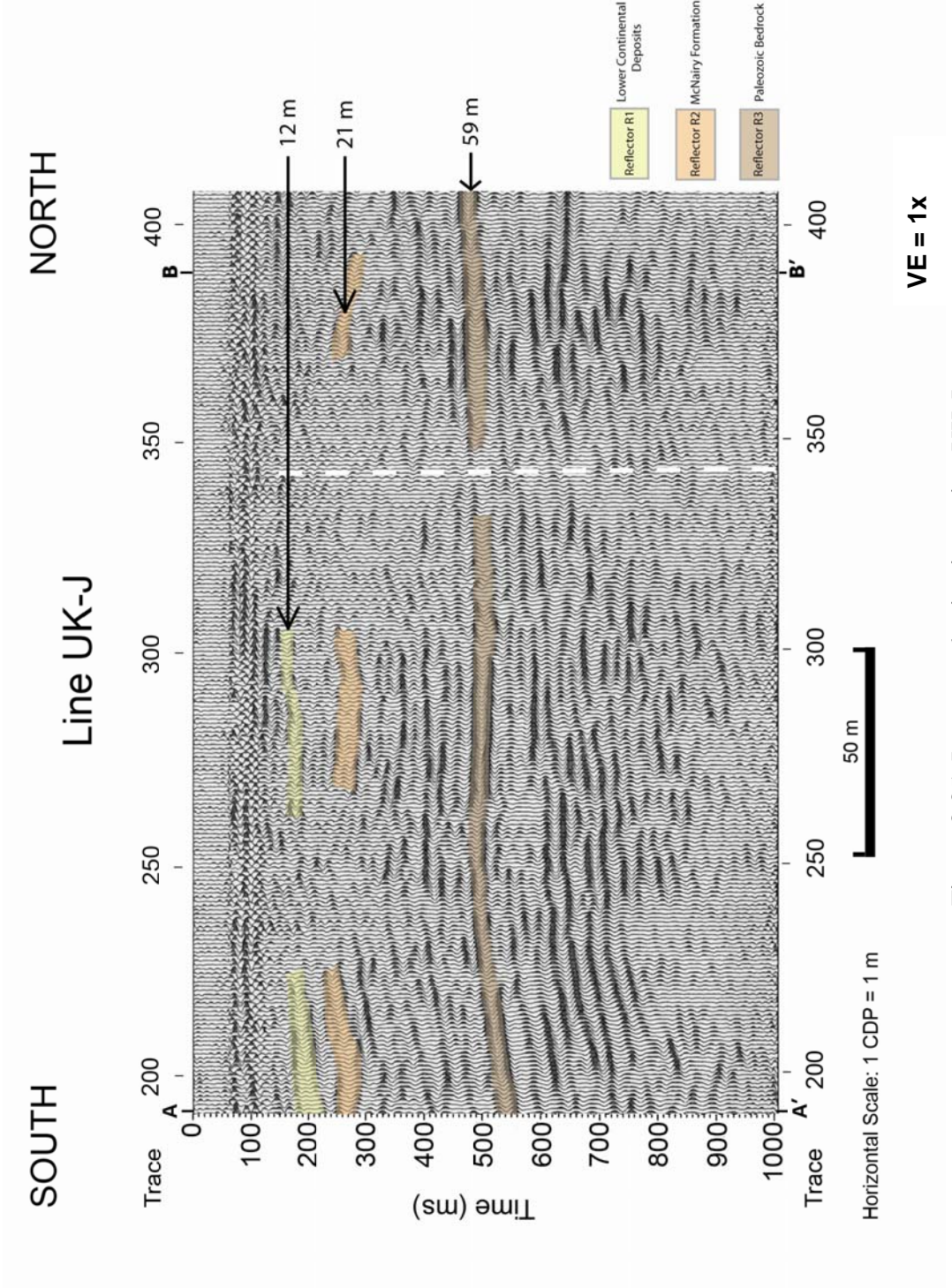


Figure 3.35: Interpreted seismic section UK-J.

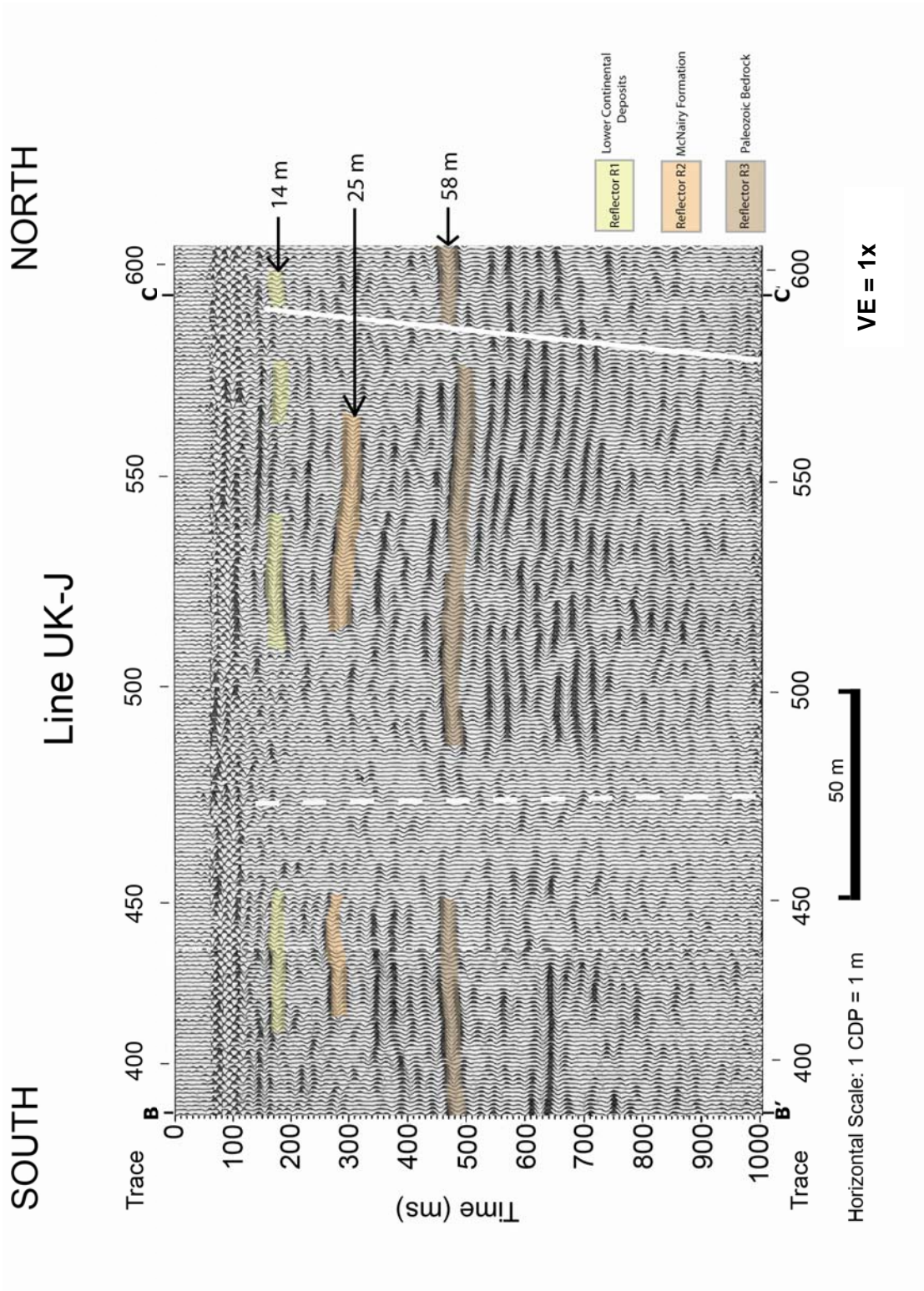


Figure 3.36: Interpreted seismic section UK-J.

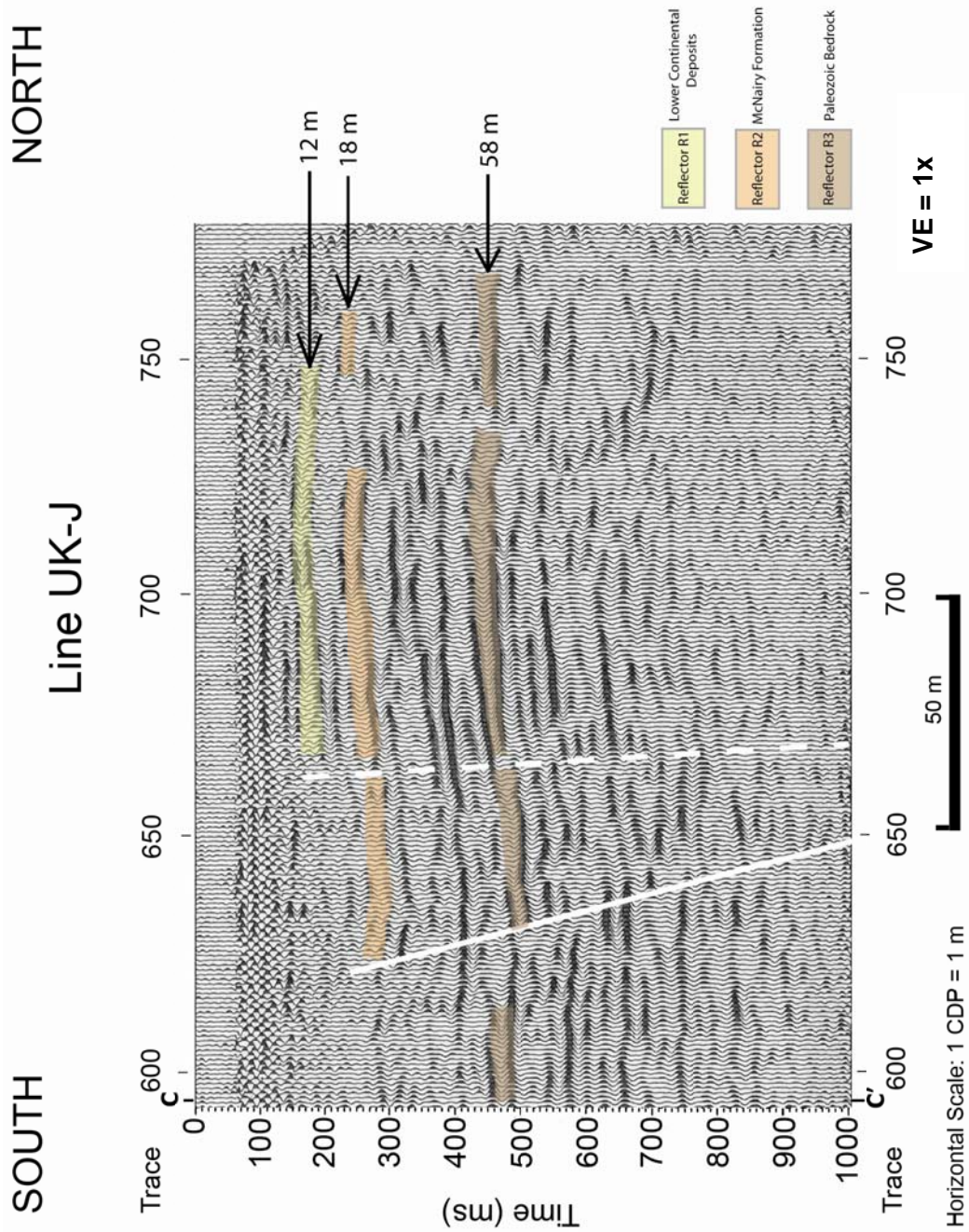


Figure 3.37: Interpreted seismic section UK-J.

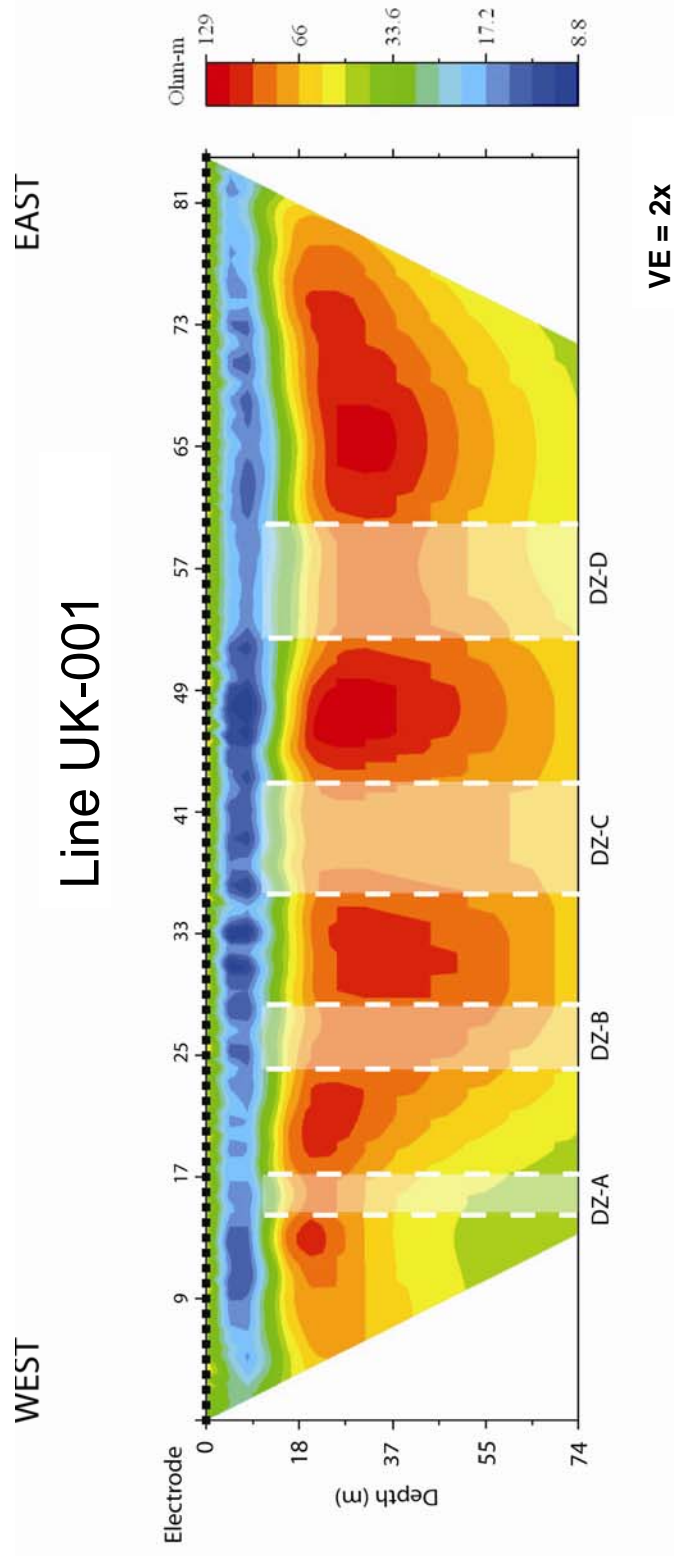


Figure 3.38: Interpreted electrical resistivity section UK-001.

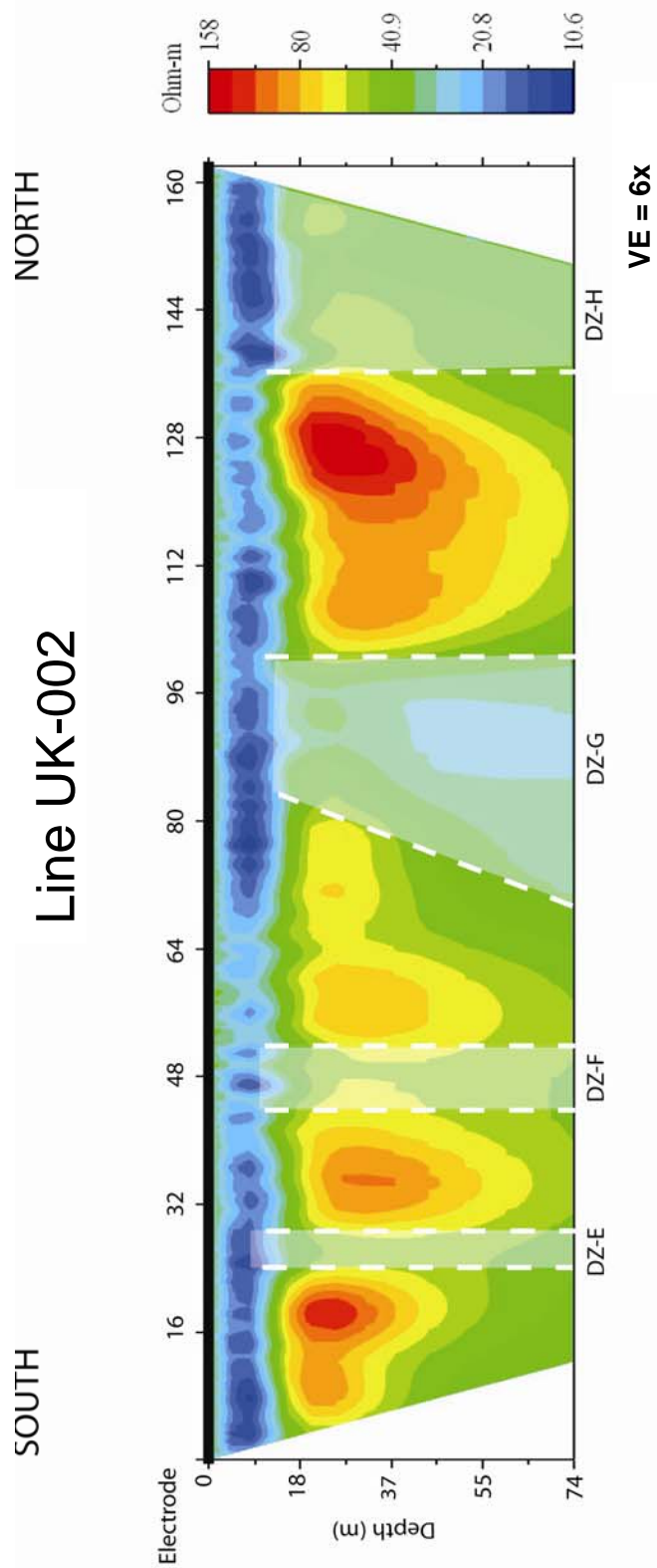


Figure 3.39: Interpreted electrical resistivity section UK-002.

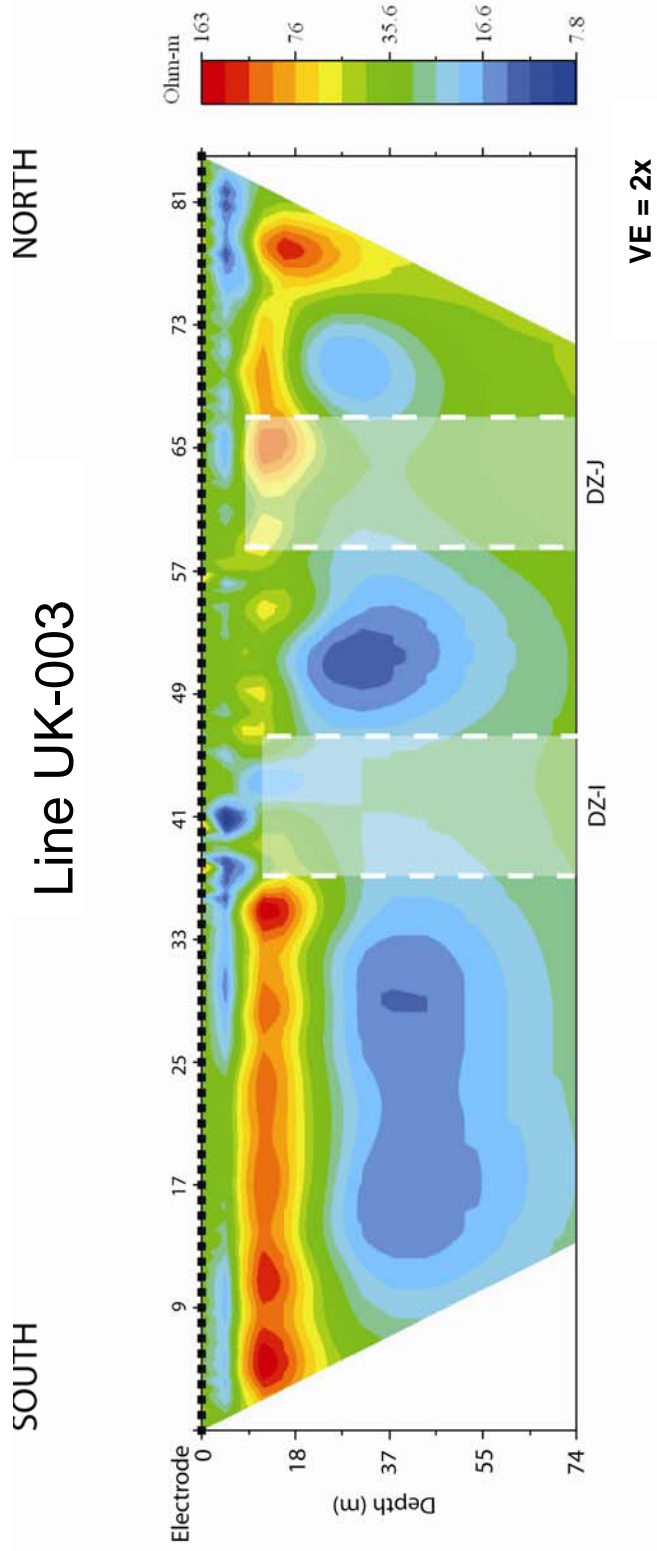


Figure 3.40: Interpreted electrical resistivity section UK-003.

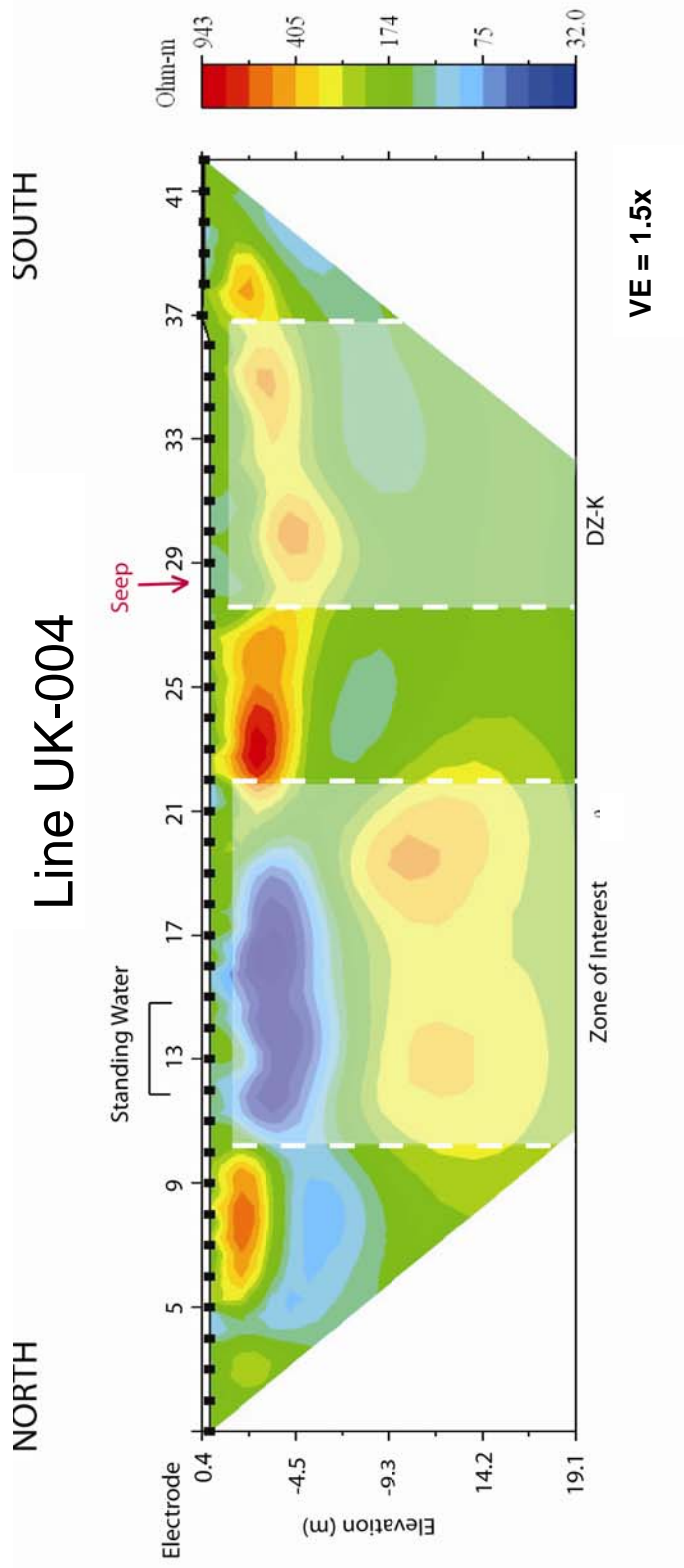


Figure 3.4.1: Interpreted electrical resistivity section UK-004.

CHAPTER FOUR

DISCUSSION

4.1 CORRELATION BETWEEN SEISMIC AND ELECTRICAL METHODS

Seismic reflection profiling and electrical resistivity imaging provide information on very different subsurface properties. As a result, each method has particular strengths and weaknesses. The SH-wave seismic reflection method provides high resolution images of faulting and structural disturbances at depth as well as in the near surface. However, seismic reflection studies, especially those using the close geophone spacing necessary for high-resolution imaging, are extremely laborious and time consuming. Additionally, an appreciable impedance boundary must exist between the horizons of interest. Electrical resistivity imaging is relatively time efficient and can provide information on some lithologic changes not detected by seismic reflection. However, it is essentially a volume averaging technique and as such is not designed to image discrete features such as fault planes. Resistivity values are also highly dependent on subsurface hydrologic conditions, making results difficult to duplicate under changing environmental conditions and often obscuring smaller-scale resistivity contrasts related to lithologic change. Based on these factors, it was determined most efficient to employ electrical resistivity surveying as a reconnaissance method for the siting of high resolution seismic reflection lines.

In general, agreement was good between structural features identified in the seismic reflection profiles and disturbances identified in the electrical resistivity sections. Two identified faults in DZ-11 and one fault inferred from the highly disturbed area of

DZ-12 on line UK-H spatially correlate with three of the deformation zones identified in line UK-001 (Figure 4.1). Furthermore, both sections demonstrate the same net sense of displacement across areas of faulting. Although no deformation zone was identified at the western end of UK-001 due to scarcity of data and rapidly degrading data quality with depth, relatively large horizontal and vertical resistivity changes are present within this area. These changes roughly coincide with the westernmost fault identified in seismic line UK-H.

Seismic section UK-I and electrical resistivity section UK-002 also show good agreement. Based on the interpreted strikes of major faults within the study area, deformation zones DZ-F and DZ-G identified on line UK-002 are thought to correlate to the boundaries of DZ-14 from line UK-I (Figure 4.2). Additionally, deformation zones DZ-E and DZ-13 appear to correlate along a strike of approximately 55° , suggesting the possible presence of an additional small-scale structural feature (Figure 4.3).

Seismic section UK-J and electrical resistivity section UK-003 show correlation between two deformation zones (Figure 4.4). Following a regional strike of approximately 30 to 35° , the northern edge of DZ-15 appears to correlate with DZ-I from electrical resistivity section UK-003. The same sense of offset appears to exist across both of these zones.

4.2 STRUCTURAL STYLE OF DEFORMATION

Structural deformation within the study area generally takes the form of deformation zones composed by clusters of predominantly high-angle normal faults. Faults within the study area generally display dip angles between 79° and 86° , although

angles between 64° and 90° were observed in the study. Offsets of R3, correlated to Paleozoic bedrock, R2 correlated to the Cretaceous McNairy formation, and R1, correlated to the boundary separating the Upper Continental Deposits and Lower Continental Deposits, were observed within the study area.

Offsets generally appeared larger in lines oriented approximately east-west, most likely due to the fact that the fault planes intersected these lines at a less oblique angle than they did with the approximately south-north oriented seismic lines. Offsets along R3 in the individual deformation zones of the WNW–ESE-oriented lines ranged between 70 ms (11 m) and 140 ms (26 m). R3 offsets on SSW–NNE-oriented sections ranged between 15 ms (2 m) and 75 ms (8 m). Offsets of R2 observed in the individual deformation zones were generally between 35-ms (3-m) and 75-ms (8-m). Where R1 was imaged, displacements were relatively small, ranging between 10ms (<1 m) and 35 ms (3 m) across a deformation zone.

In addition to sharp displacements within individual deformation zones, more regional trends are apparent in the study area. Based on observable structural features and changes in depth within seismic sections, both R3 and R2 appear to dip toward the southwest across the area. Seismic lines UK-A3, UK-B and UK-H, oriented approximately WNE-ESE, show R3 at 410 ms (71 m) to 485 ms (79 m) at the western ends of the sections displaced downward to 535 ms (87 m) to 560 ms (84 m) at the eastern ends of the lines. R2 was observed to drop in the time section from 220 ms (19 m) to 255 ms (22 m) in the west and from 275 ms (26 m) to 310 ms (32 m) in the east. Depths to reflectors generally decreased from south to north along lines UK-I and UK-J, with R3 moving from 505 ms (77 m) to 565 ms (73 m) in the south and 480 ms (71 m) to

455 ms (57 m) at the northern ends of the lines. R2 behaved similarly in most cases, moving upward in the time section from 290 ms (24 m) to 225 ms (18 m) along line J. This pattern correlates well with the decreasing depth to bedrock seen between borings Z-16 and Z-12. Alternately, lines UK-G1 and UK-G2 show reflector R3 increasing in depth from 495 ms (71 m) to the south to approximately 550 ms at the northern end of G1. This trend is not seen in the near-surface sediments, with R2 rising in the time section from 290 ms (26 m) to the south to 185 ms (16 m) in the north. Reflector R1 shows similar offsets, rising from 175 ms (14 m) to 135 ms (10 m). The lower quality of the G lines, along with their complex interaction with a major fault believed to exist approximately coincident to the lines, makes this data less reliable in determining depths to lithologic units than higher quality lines such as UK-I and UK-J.

The minimum upward extension of faulting was determined by the location in which clear evidence of deformation was observed. Lines employing 4 m geophone spacings were generally able to place upward extension to within 15 to 20 m of the surface. High-resolution lines with smaller geophone spacing were able to confirm the upward extension of faulting to between 7 and 11 m of the surface.

Offset within the bedrock reflector is commonly two to three times that observed within the reflectors thought to correlate with the McNairy formation and Lower Continental Deposits. This is due to the larger magnitude of offset associated with the original early Paleozoic activity compared with later reactivations. In many lines this reactivation is confirmed to be as recent as Pliocene to late Pleistocene by deformation within R1. A reverse sense of offset does appear to occur in deformation zones in lines UK-B and UK-I, however it is unclear as to whether this actually represents a reverse

sense of fault movement, or whether it is a distortion caused by an oblique angle of intersection between the seismic line and the fault plane. In both cases, these were relatively minor features, with an overall sense of normal reactivation defining the structure.

Eight major faults are identified within the study area, all striking between N40°E and N45°E. Three distinct grabens seem to be outlined within the study area, varying in width from 160 m to approximately 300 m. Apparent offset of bedrock within these grabens generally ranges from 70 ms (11 m) to 140 ms (26 m). Offset is asymmetric, with more displacement occurring to the north-west. The general structure and age of faulting within the study area is in good agreement with the findings associated with grabens in southern Illinois (Nelson et al., 1999).

4.3 IMPLICATIONS FOR GROUNDWATER MOVEMENT

Faults appear to strike approximately parallel to the northwestern contaminant plume, with multiple faults shown intersecting the plume (Figure 4.7). The most striking relationship is between the plume and the easternmost graben, which is coincident with the center of the plume up to the Ohio River. Imaged displacements of reflector R1, thought to correspond to the Lower Continental Deposits, suggest offset of this unit as great as 35 ms (3 m) across a single fault and 45 ms (4 m) across a section. This indicates significant offset of the Regional Gravel Aquifer, composed of the sand and gravel facies of the Lower Continental Deposits (Clausen et al., 1992). Such juxtaposition of units within this groundwater flow system may create a preferential direction for contaminant migration.

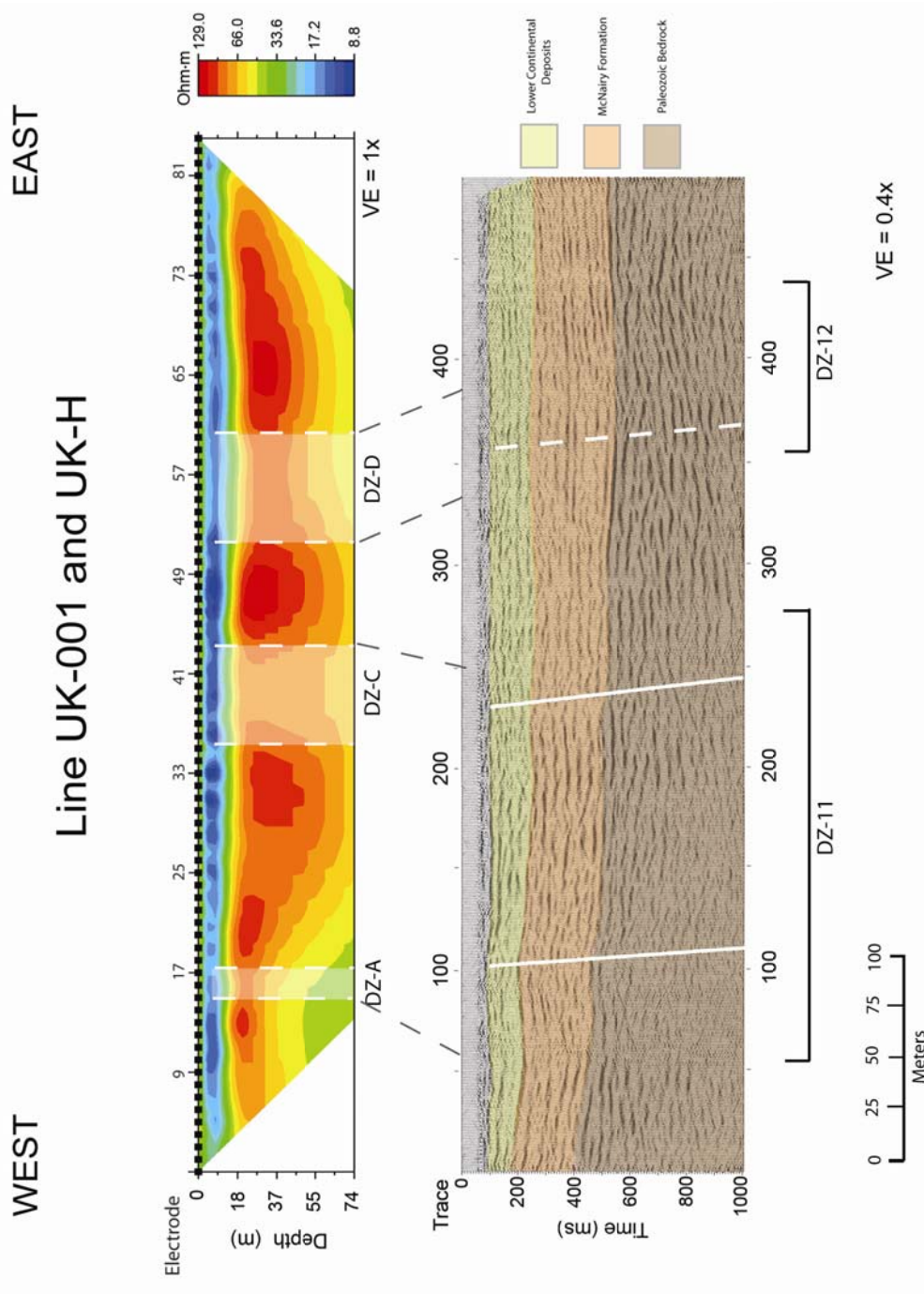


Figure 4.1: Correlation of deformation zones seen in electrical resistivity section UK-001 to structural features observed in seismic reflection profile UK-H.

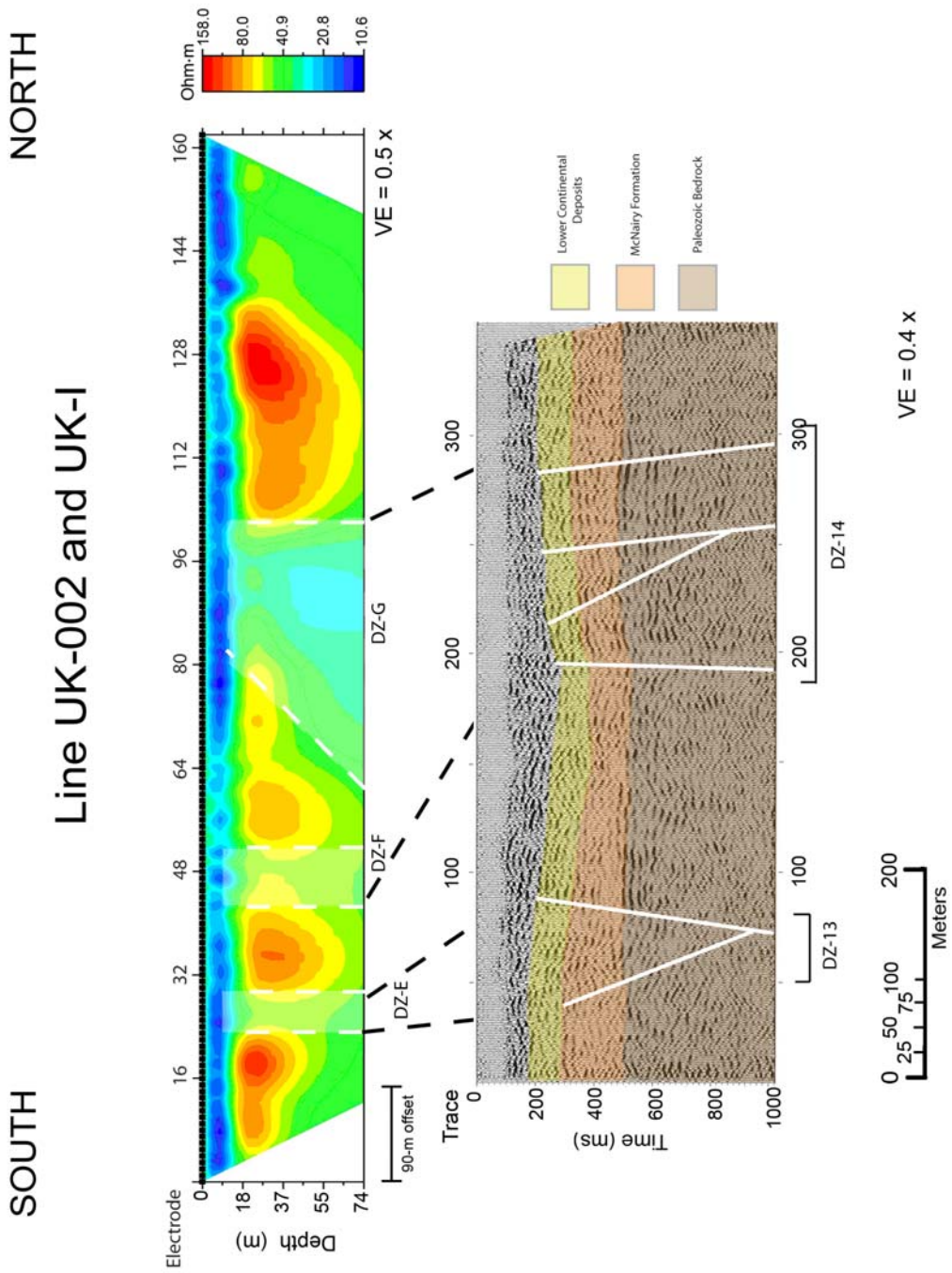


Figure 4.2: Correlation between electrical resistivity section UK-002 and seismic profile UK-I.



Figure 4.3: Close-up map of deformation zones DZ-F through DZ-H on electrical resistivity line UK-002 and zones DZ-12 and DZ-13 on seismic line UK-I. Two large-scale faults are shown intersecting the survey lines with one smaller-scale feature shown striking at approximately 55°.

SOUTH

NORTH

Line UK-003 and UK-J

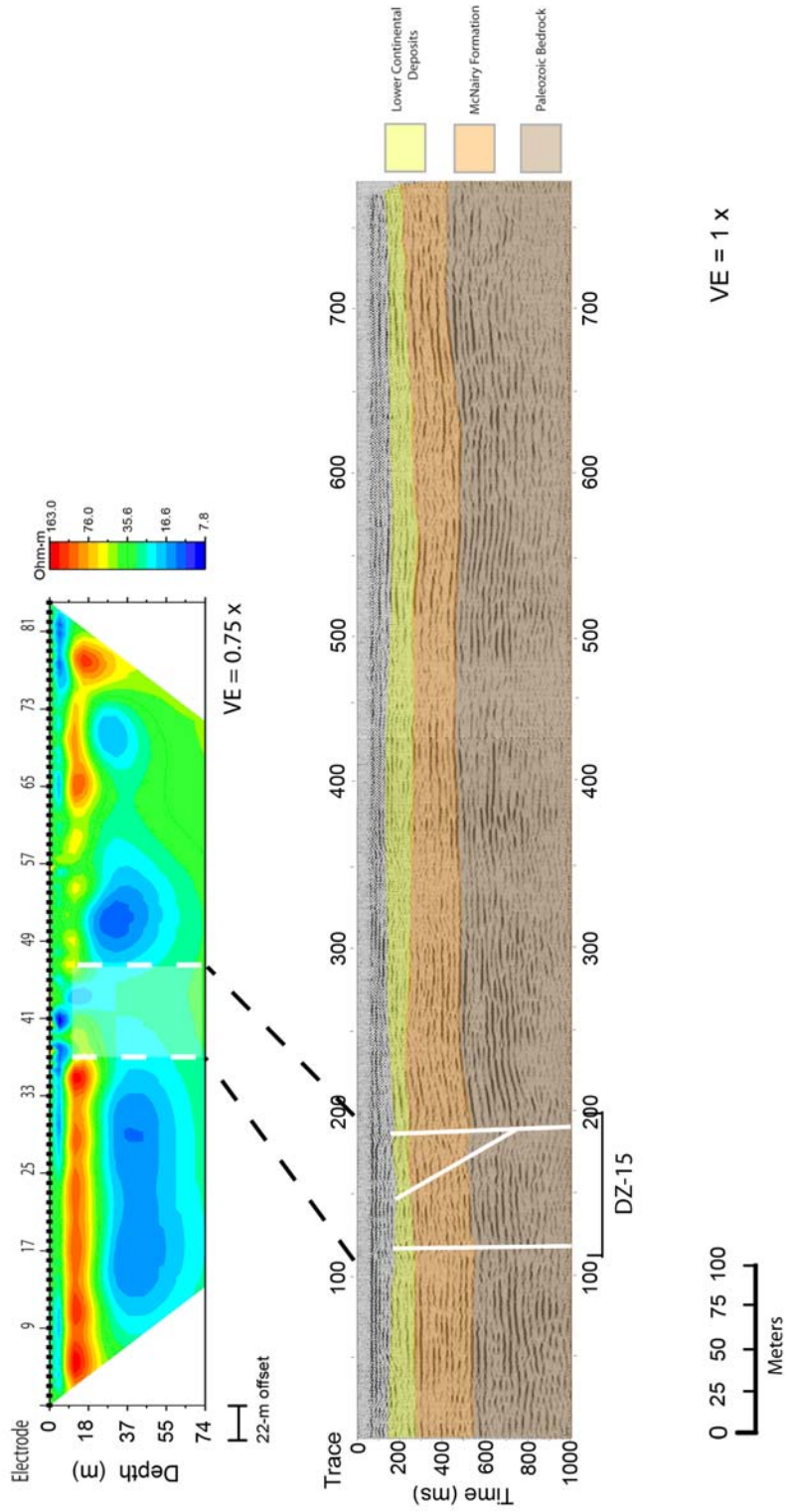


Figure 4.4: Correlation between electrical resistivity section UK-003 and seismic profile UK-J.

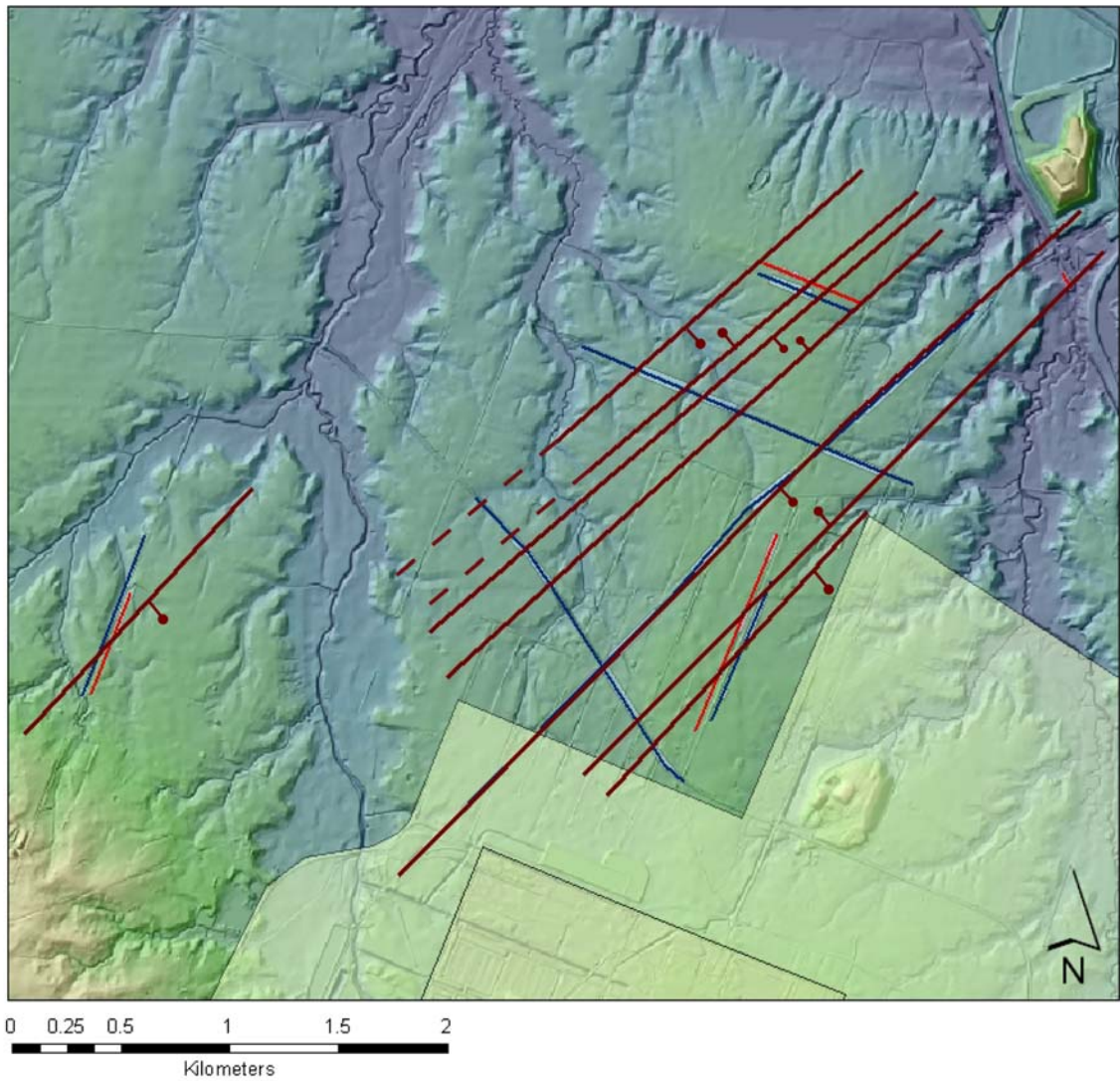


Figure 4.5: Map of major faults within the study area. Three asymmetric graben features are outlined. Local strike ranges from 30° to 45° .

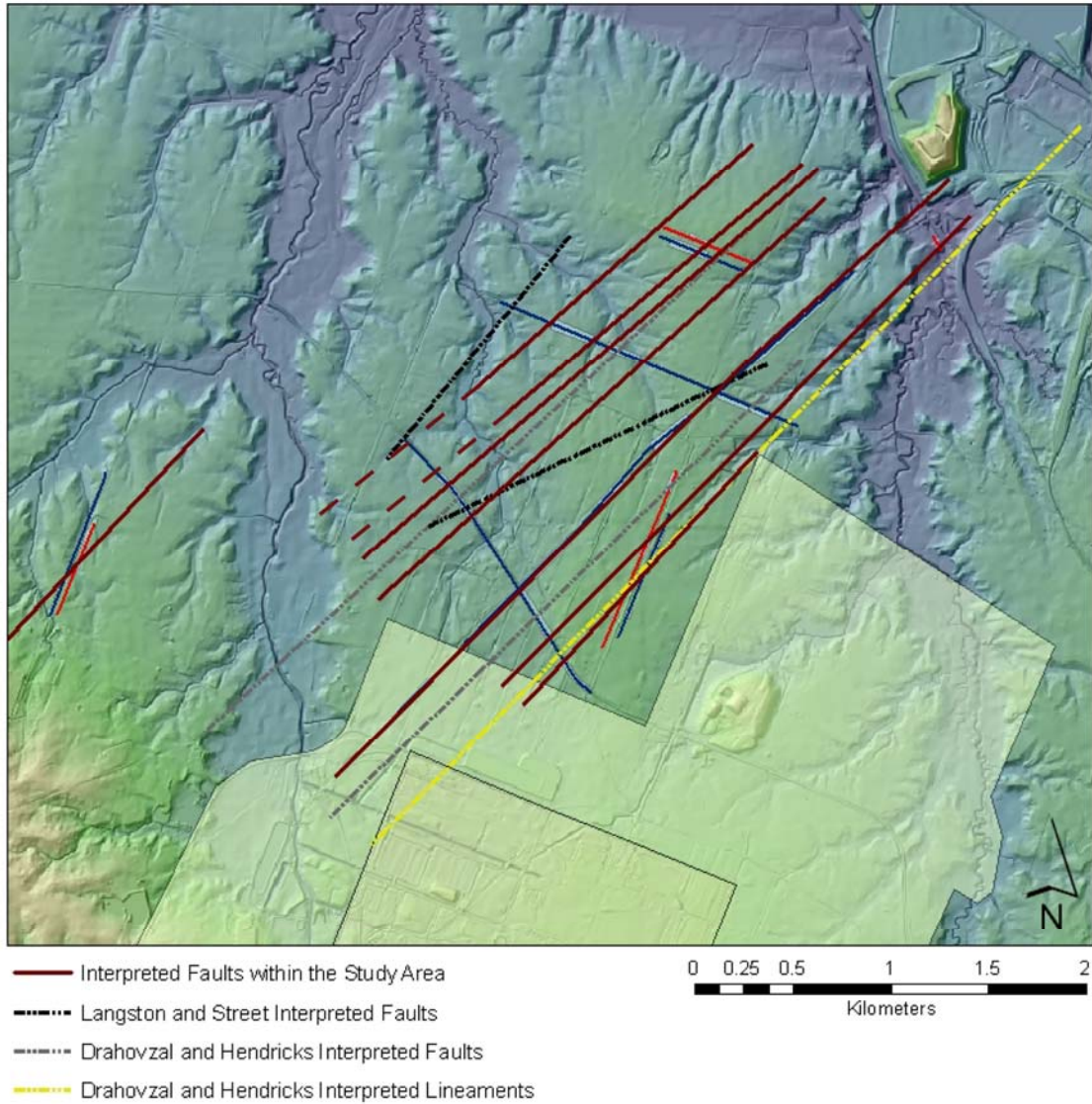


Figure 4.6: Map of major faults identified through this study along with a lineament feature proposed by Drahovzal and Hendricks (1997). The lineament, shown as a dashed yellow line, is approximately coincident with the easternmost fault identified through the interpretation of geophysical survey lines UK-B, UK-I and UK-002.

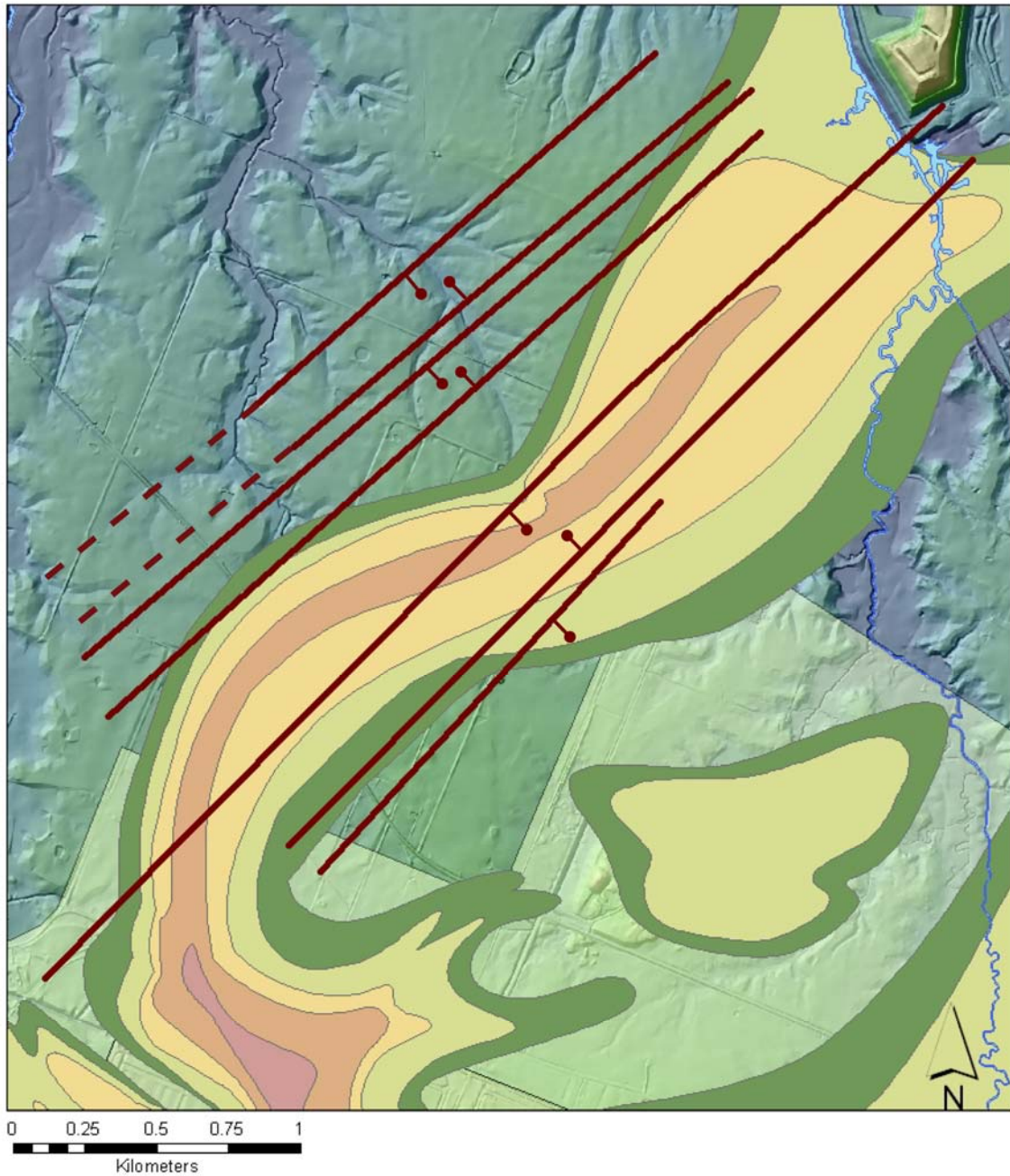


Figure 4.7: Map of the relationship between areas of faulting identified in this study and the northwestern contaminant plume.

CHAPTER FIVE

CONCLUSIONS

Over 7.8 km of seismic reflection data and 2 km of electrical resistivity data were acquired, processed, and interpreted during this multi-method geophysical study. The objective of this study was to better understand subsurface structure in the area of the northwest contaminant plume at PGDP and to determine the potential for a structural control of its migration. The results can contribute to the development and implementation of future high-resolution groundwater contamination assessment and mitigation strategies within the area.

The subsurface structure interpreted from the geophysical surveys correlate with the regional framework described by the outcrop studies of Nelson et al. (1997, 1999) north of the site in southern Illinois.. A series of roughly parallel normal faults striking between N40°E and N45°E were identified and are thought to outline a series of asymmetric grabens with greater downdrop occurring to the southeast. Offset within the grabens is as high as 140 ms (26 m) with the grabens ranging in width from 160 m to almost 300 m.

The propagation of faulting into the non-lithified sedimentary overburden was imaged throughout all of the survey lines. Seismic reflection methods with 4 m geophone spacing were able to image fault extension to within 15 m of the surface, while setups using 2 m spacing were able to image faulting up to 7 m below ground surface. Electrical resistivity methods employing 2 m electrode spacing were able to image deformation thought to be the result of fault displacement to within 3 m of the surface.

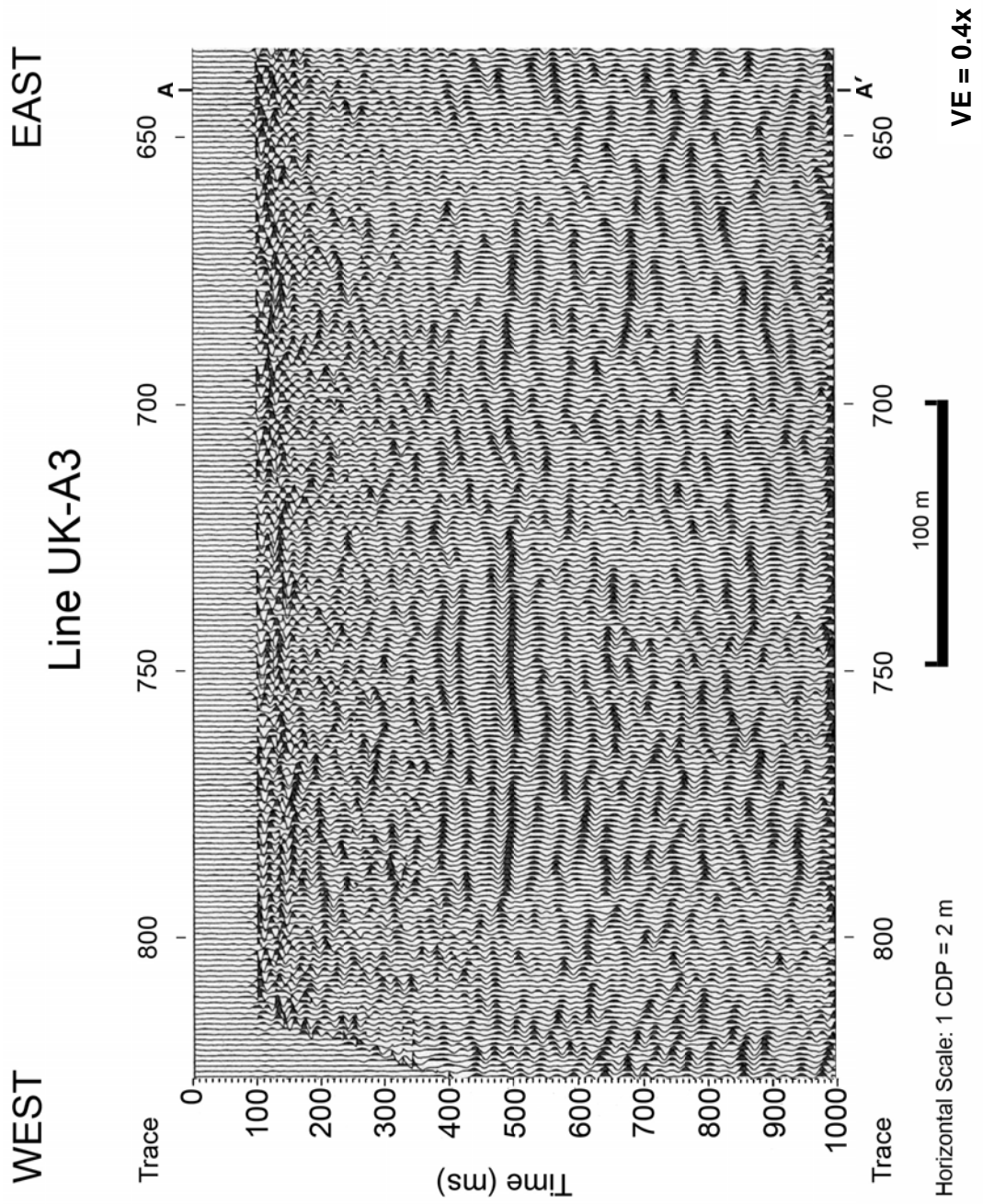
These findings provide a basis for structural control on the movement of groundwater and contaminants in the northwest plume; however, additional high-resolution studies should be conducted for other locations of interest. One area of remaining interest is the area west of Little Bayou Creek approximately coincident with the location of the seep. The acquisition of a seismic reflection profile in this area would not only provide more detailed information on subsurface structure that may be controlling the movement of groundwater in that location, but would serve to further test the appropriateness of the electrical resistivity method in this environment. Additionally, it is suggested that line UK-H be extended to the west, intersecting the structural features imaged in lines UK-B and UK-A3.

APPENDIX A

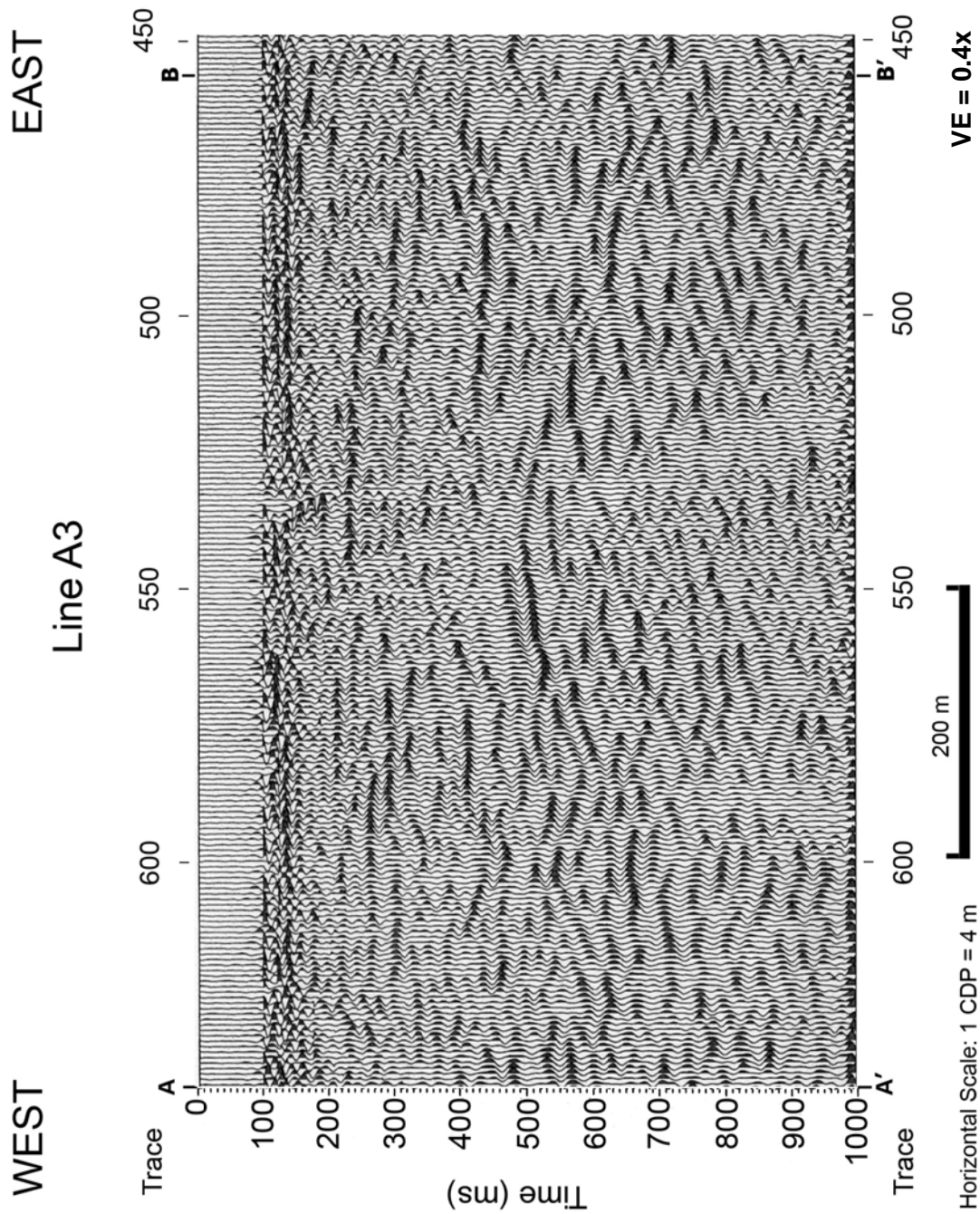
Appendix A

Section 1

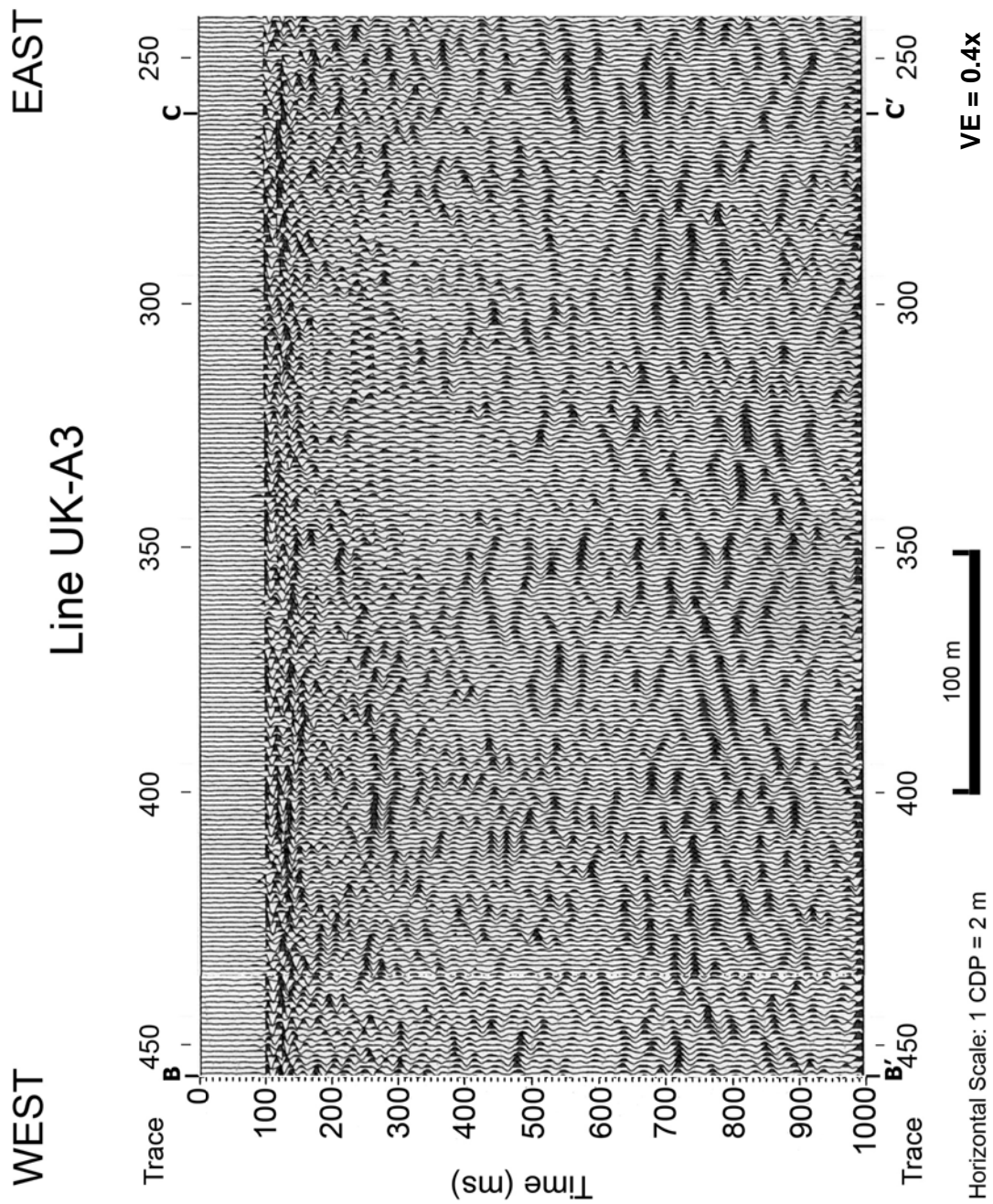
Uninterpreted seismic reflection profiles processed in this study. Processed and unprocessed profiles are shown at the same scale and vertical exaggeration. Where more than one processing method was used to highlight different subsurface features multiple profiles are given.



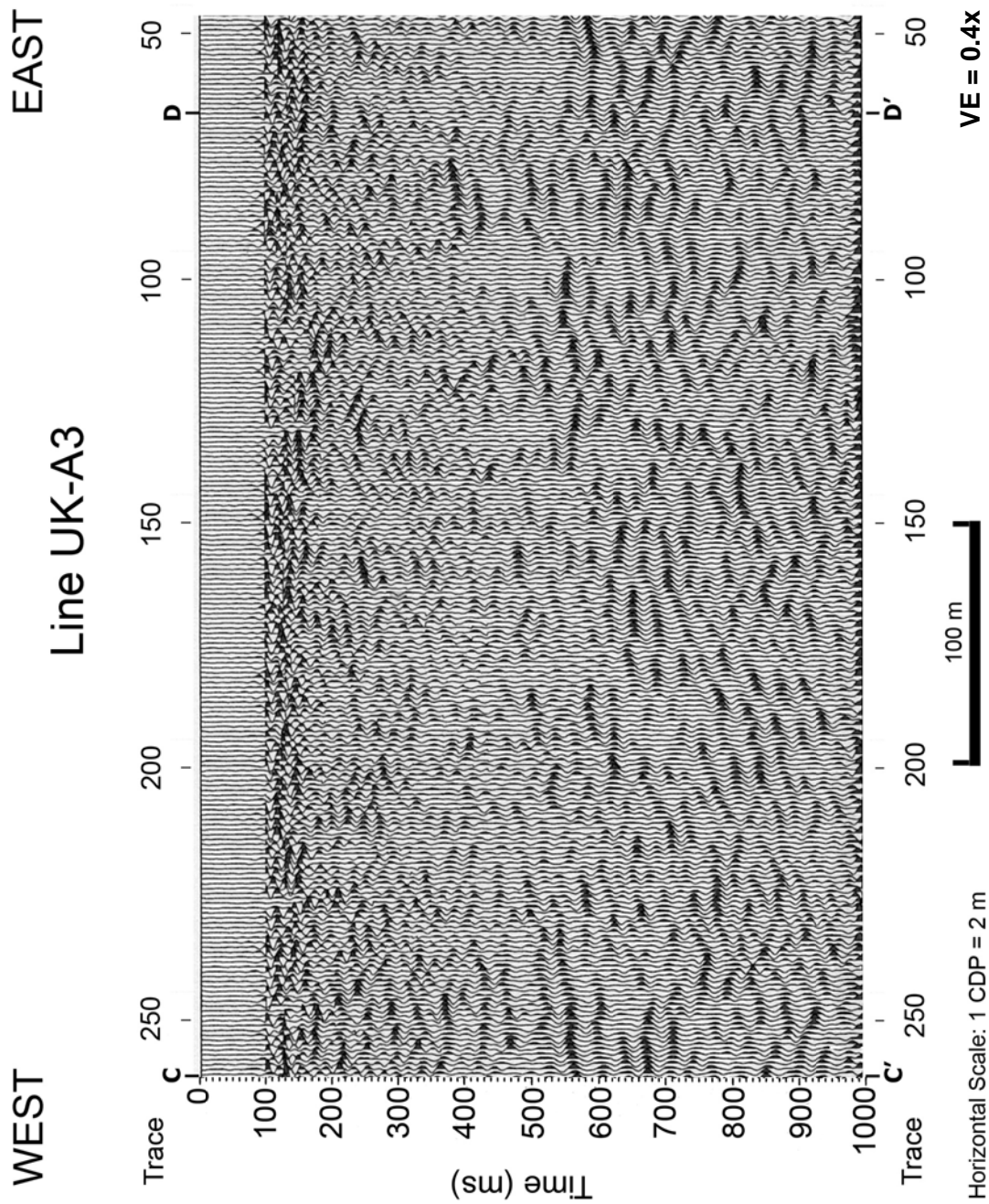
Line UK-A3: F-K filtered profile



Line UK-A3: F-K filtered profile



Line UK-A3: F-K filtered profile

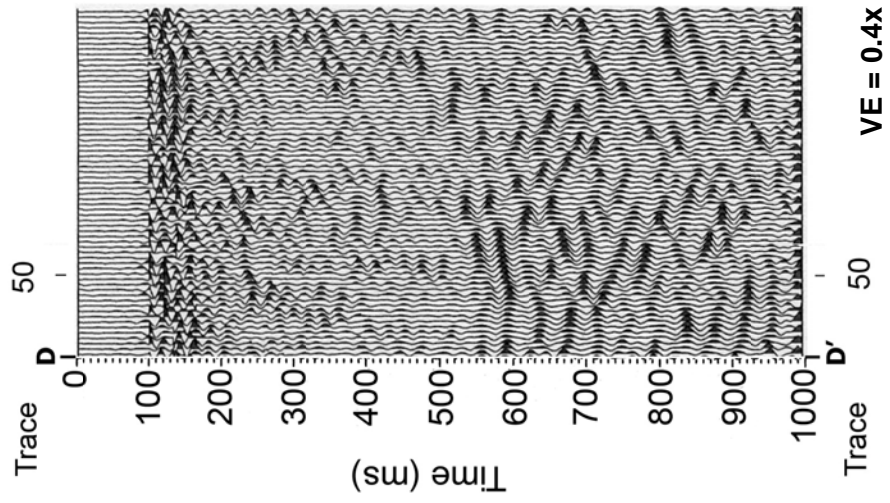


Line UK-A3: F-K filtered profile

WEST

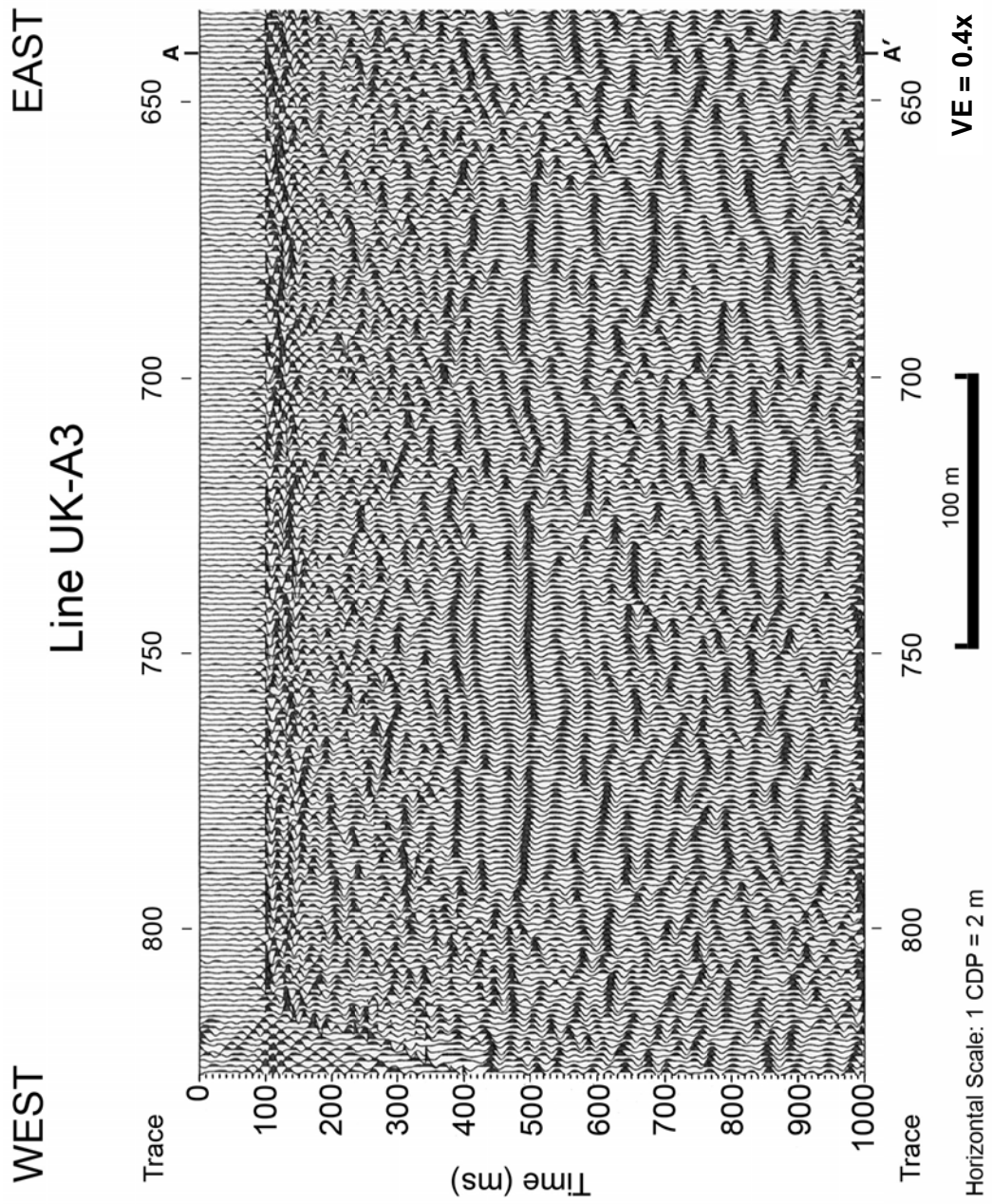
EAST

Line UK-A3

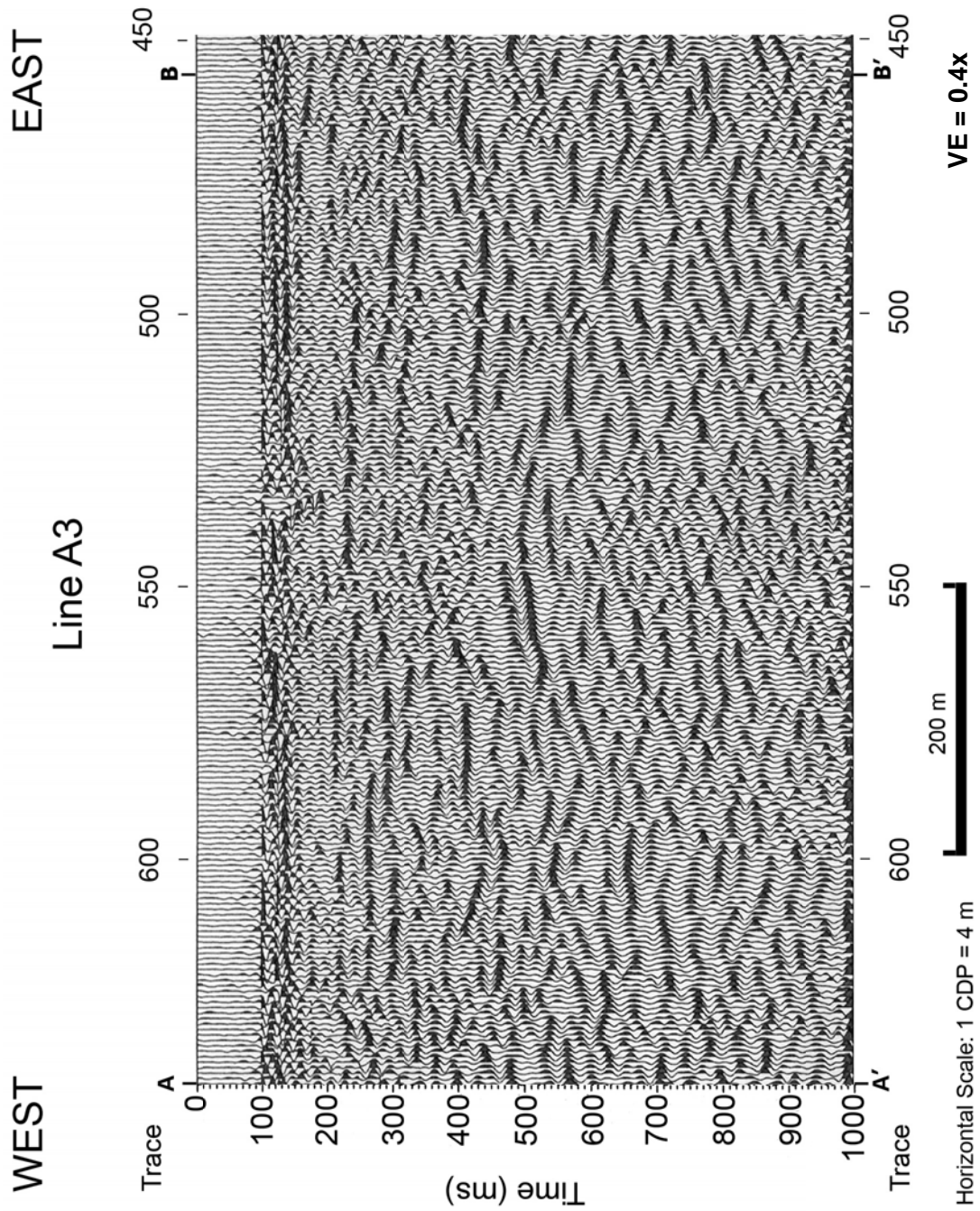


Horizontal Scale: 1 CDP = 2 m

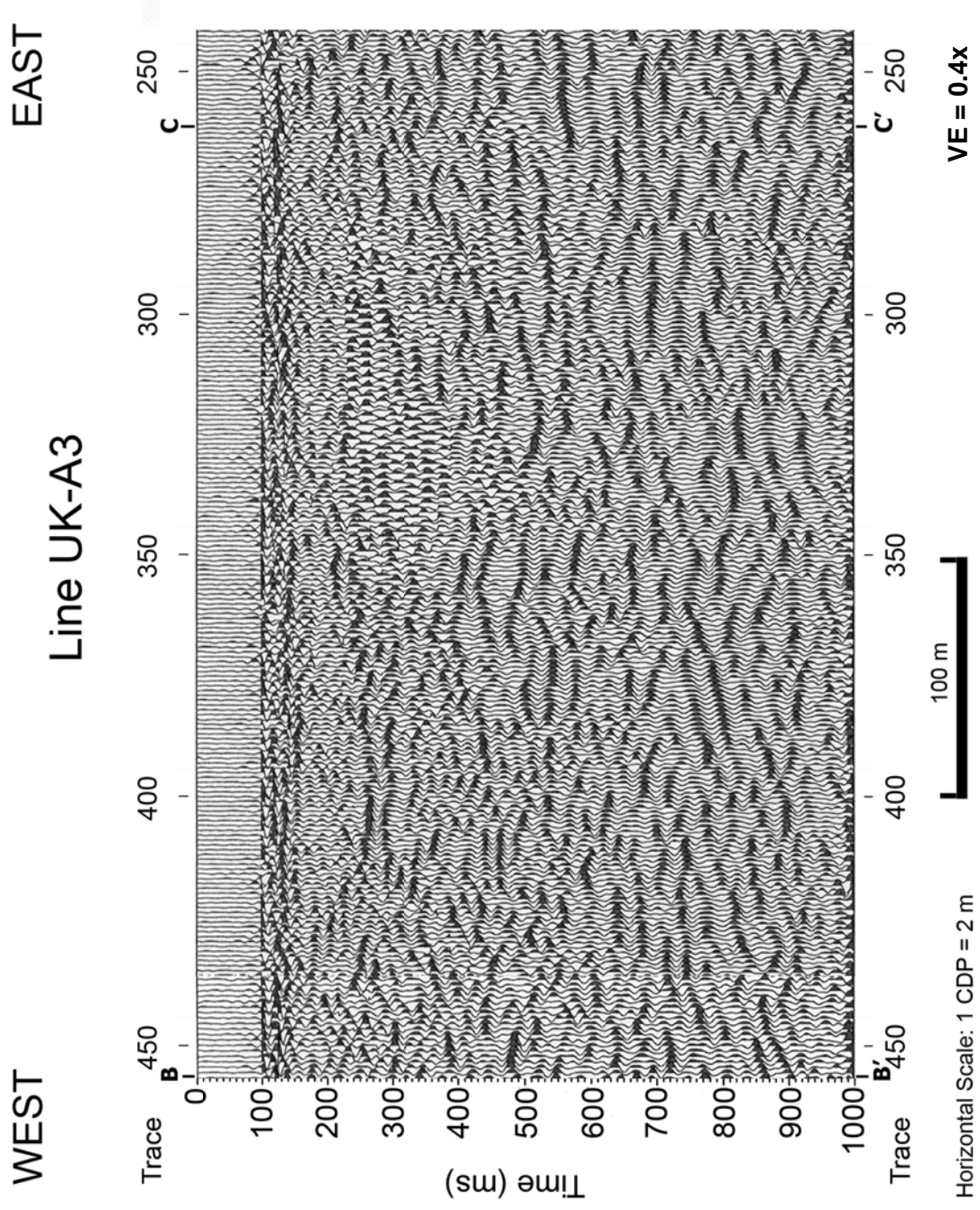
Line UK-A3: F-K filtered profile



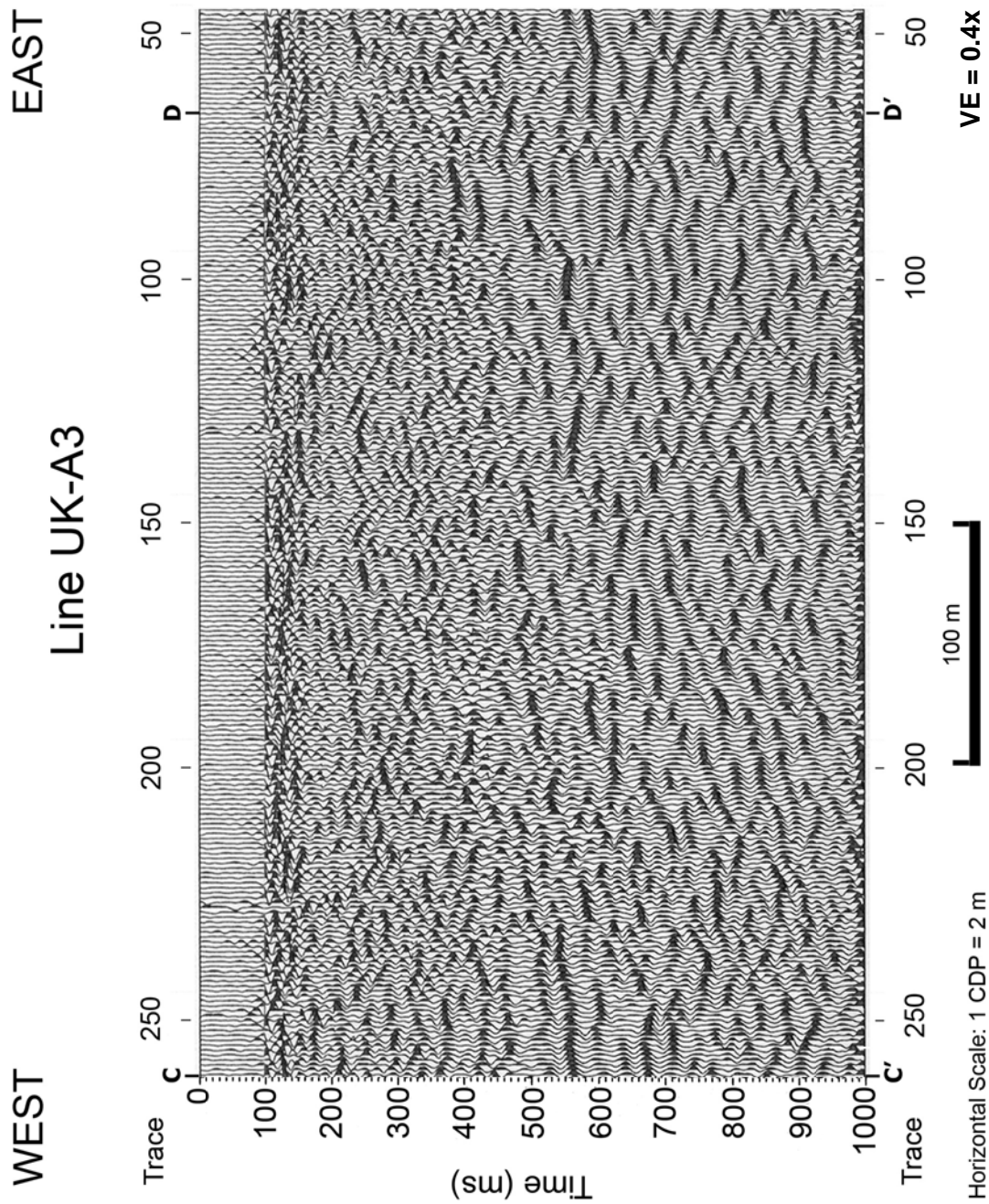
Line UK-A3: F-K filtered profile with 150 ms AGC applied



Line UK-A3: F-K filtered profile with 150 ms AGC applied



Line UK-A3: F-K filtered profile with 150 ms AGC applied

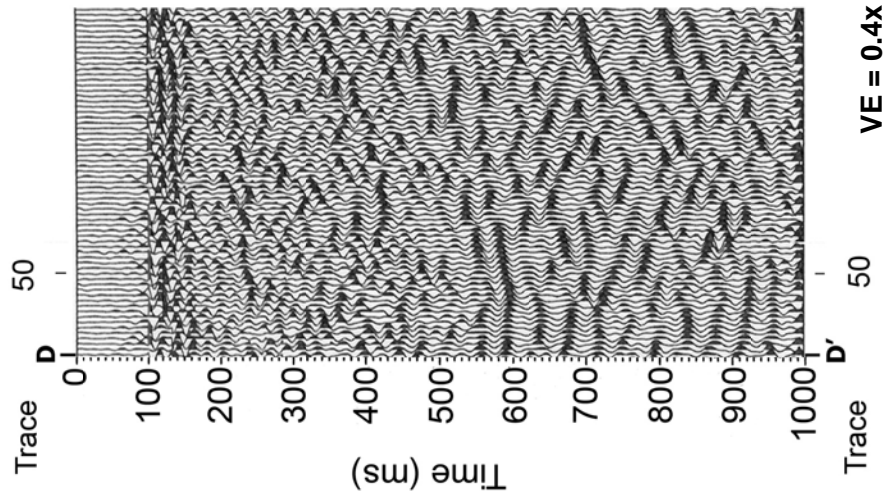


Line UK-A3: F-K filtered profile with 150 ms AGC applied

WEST

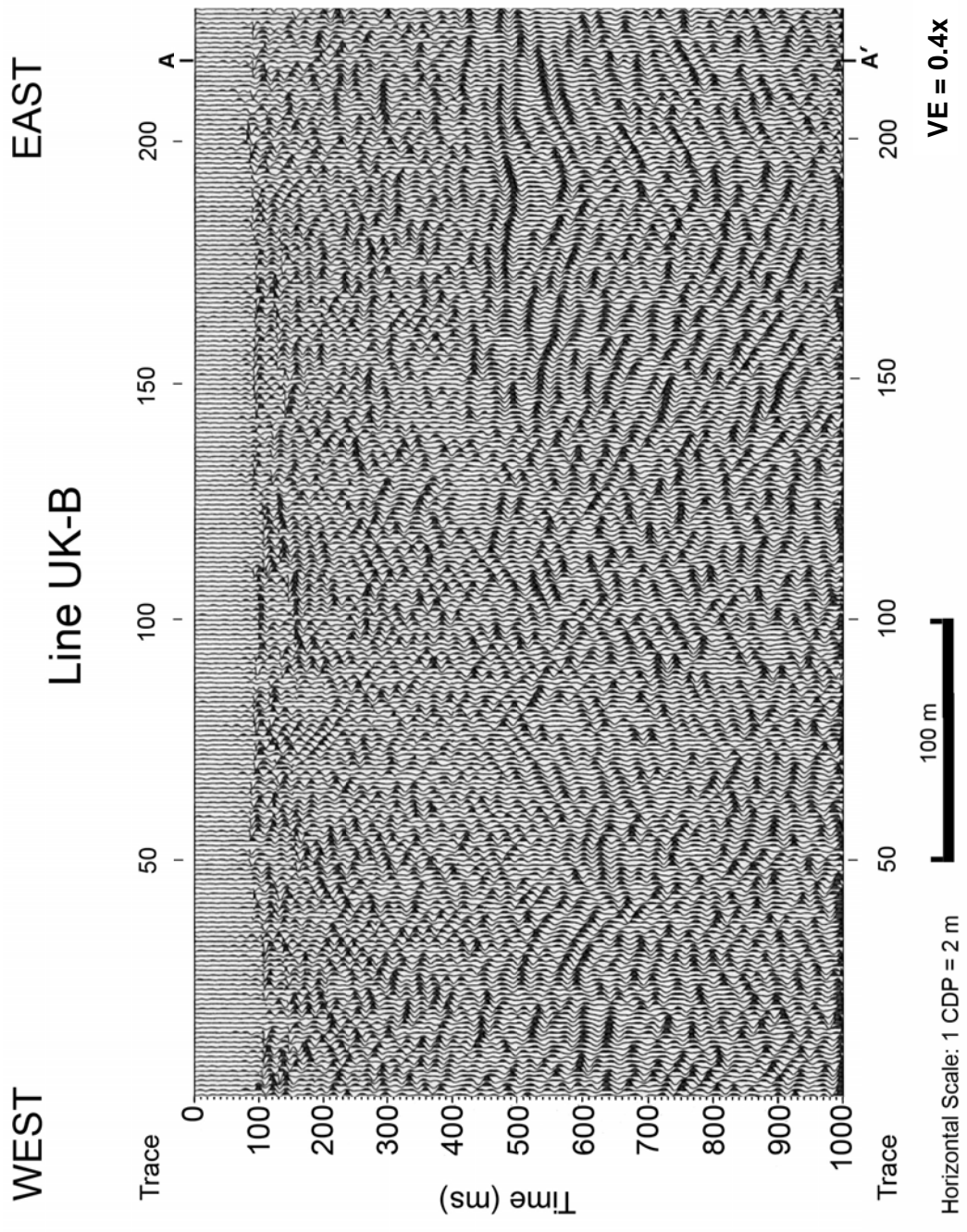
EAST

Line UK-A3

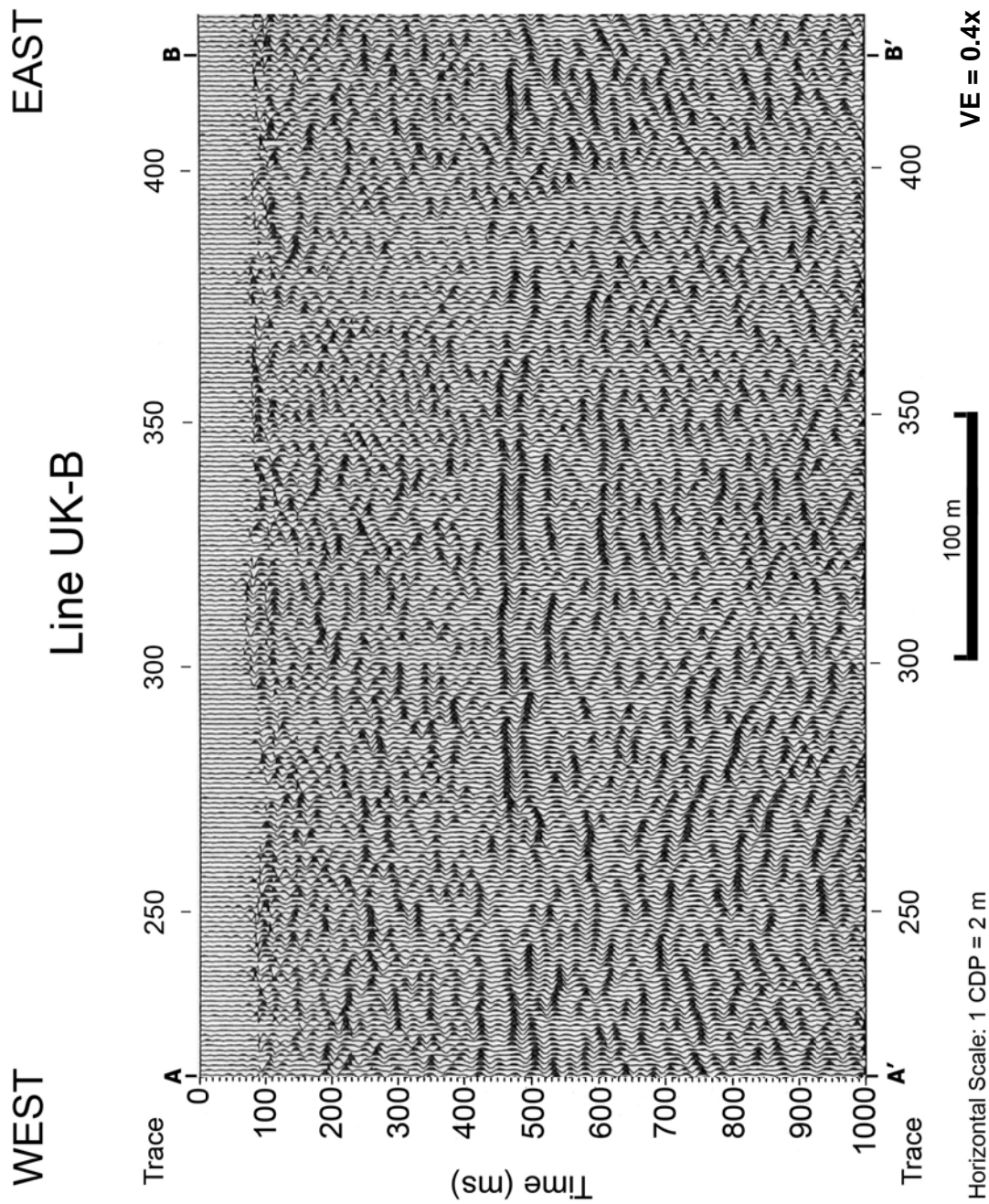


Horizontal Scale: 1 CDP = 2 m

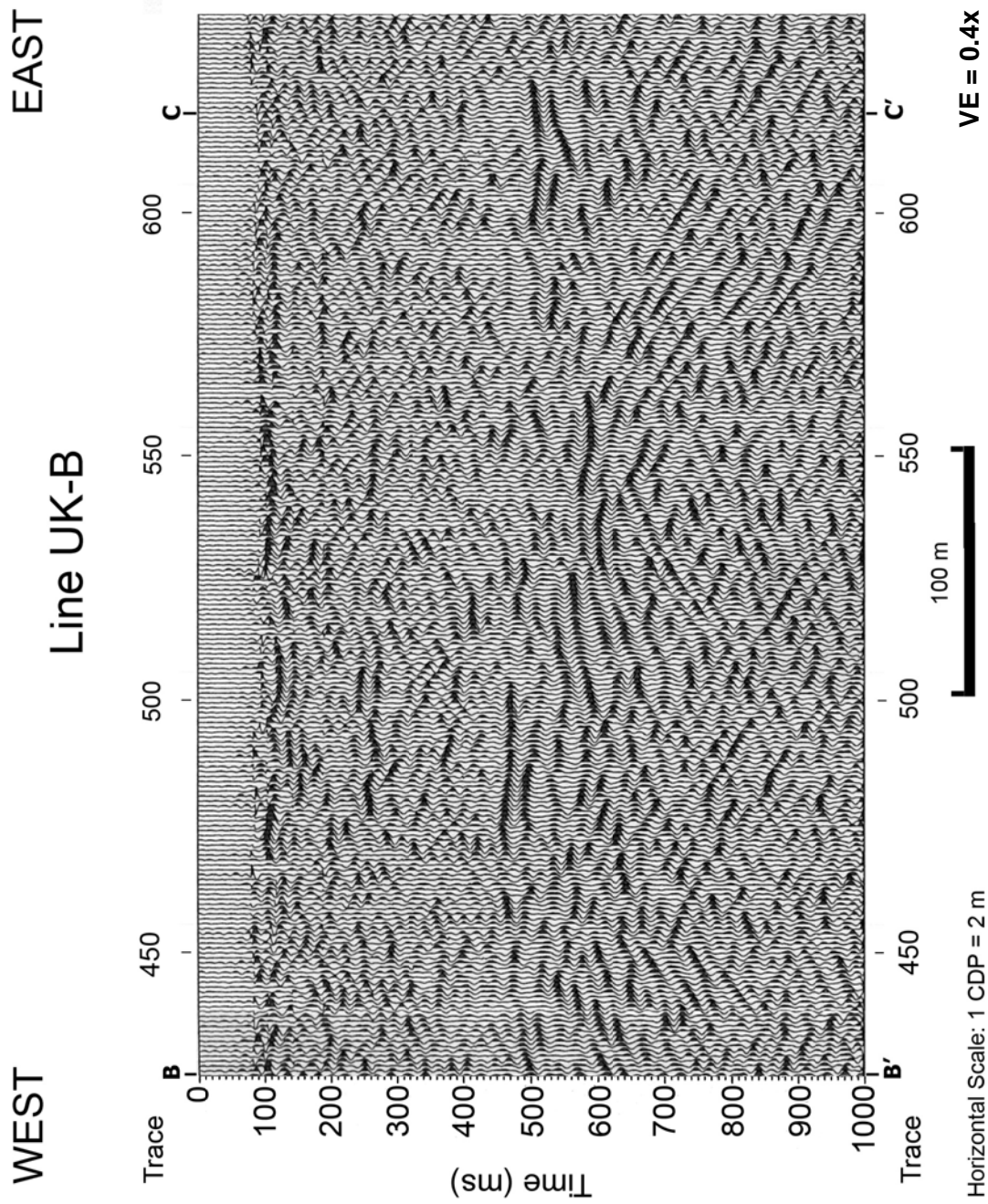
Line UK-A3: F-K filtered profile with 150 ms AGC applied



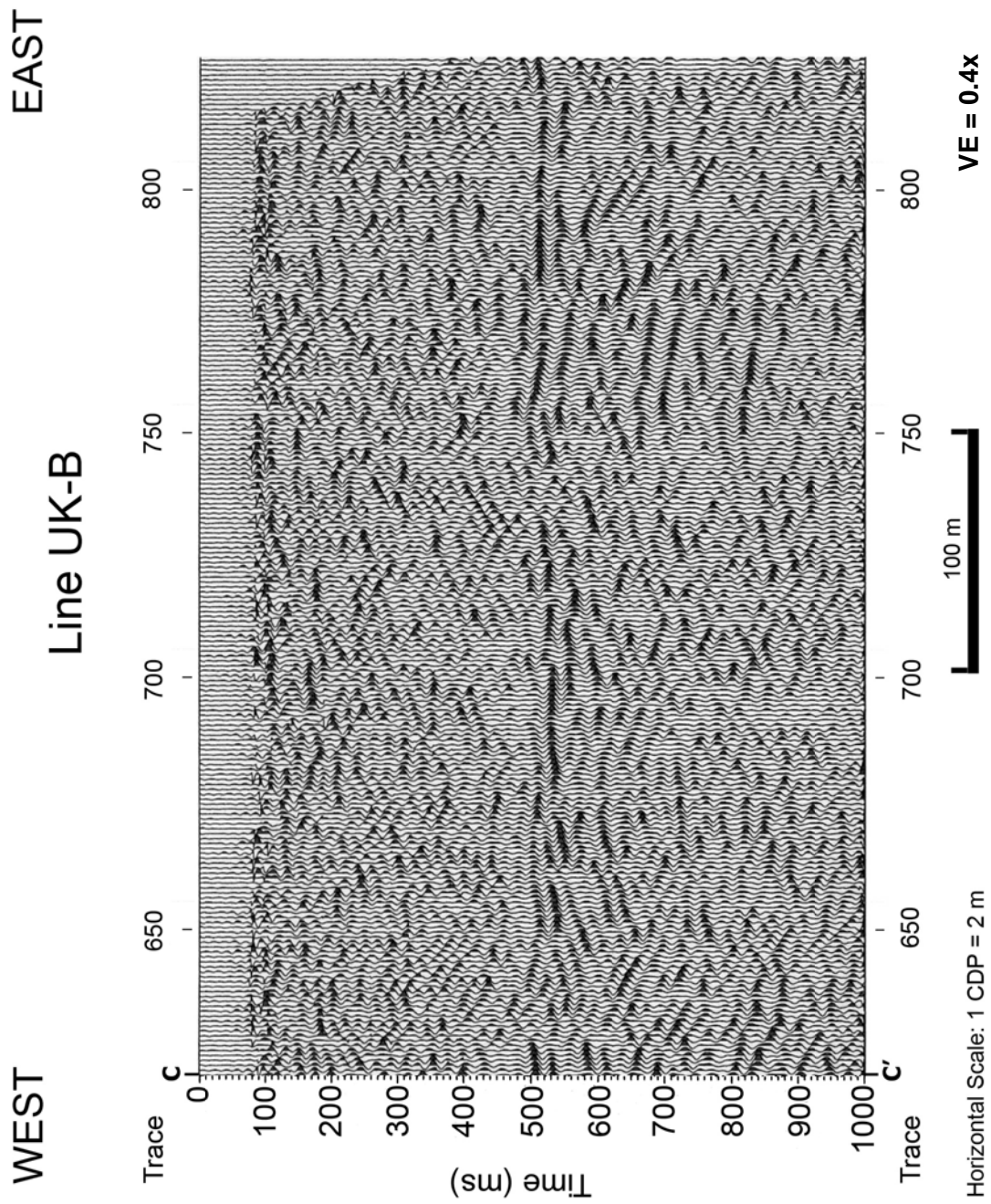
Line UK-B: F-K filtered profile



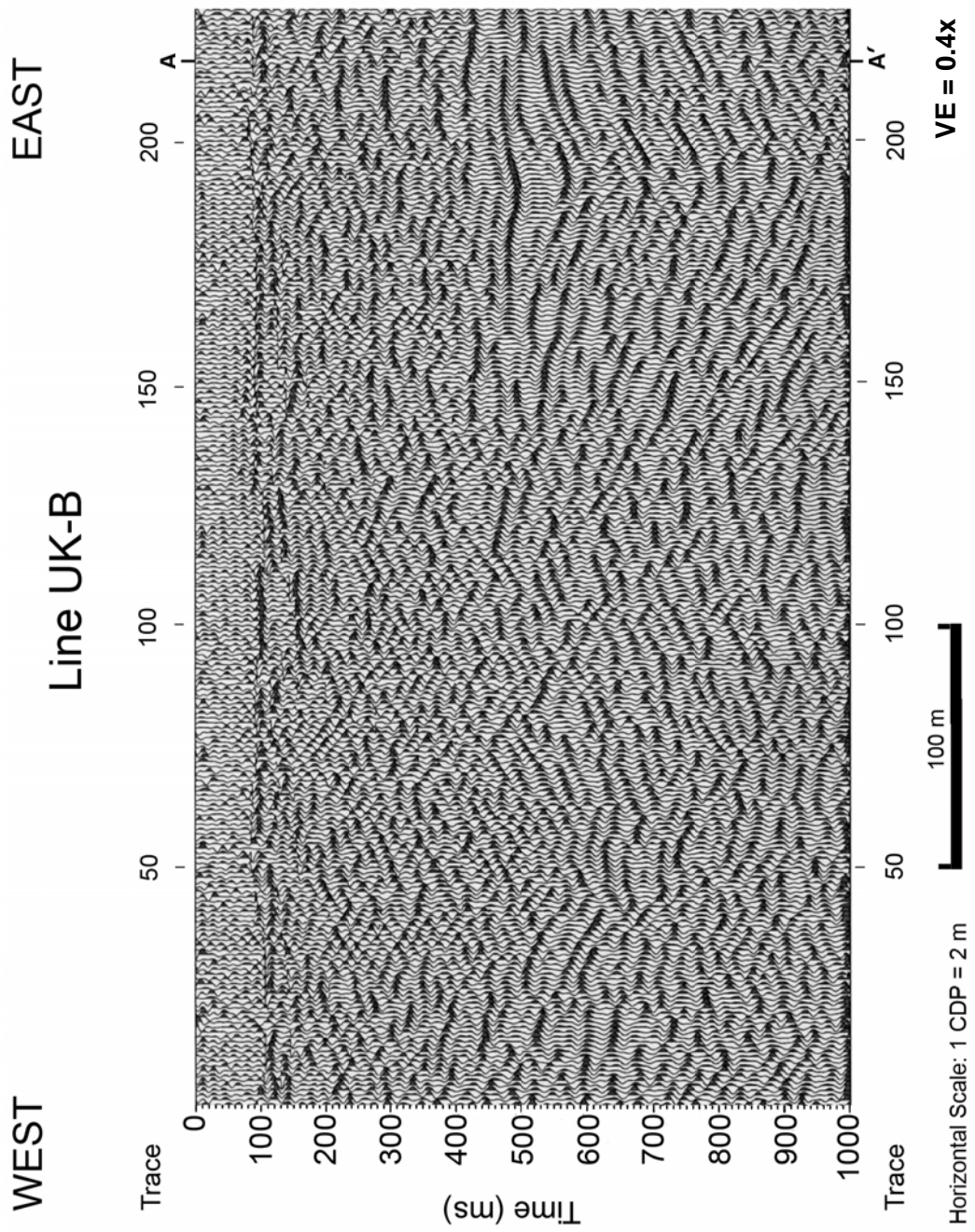
Line UK-B: F-K filtered profile



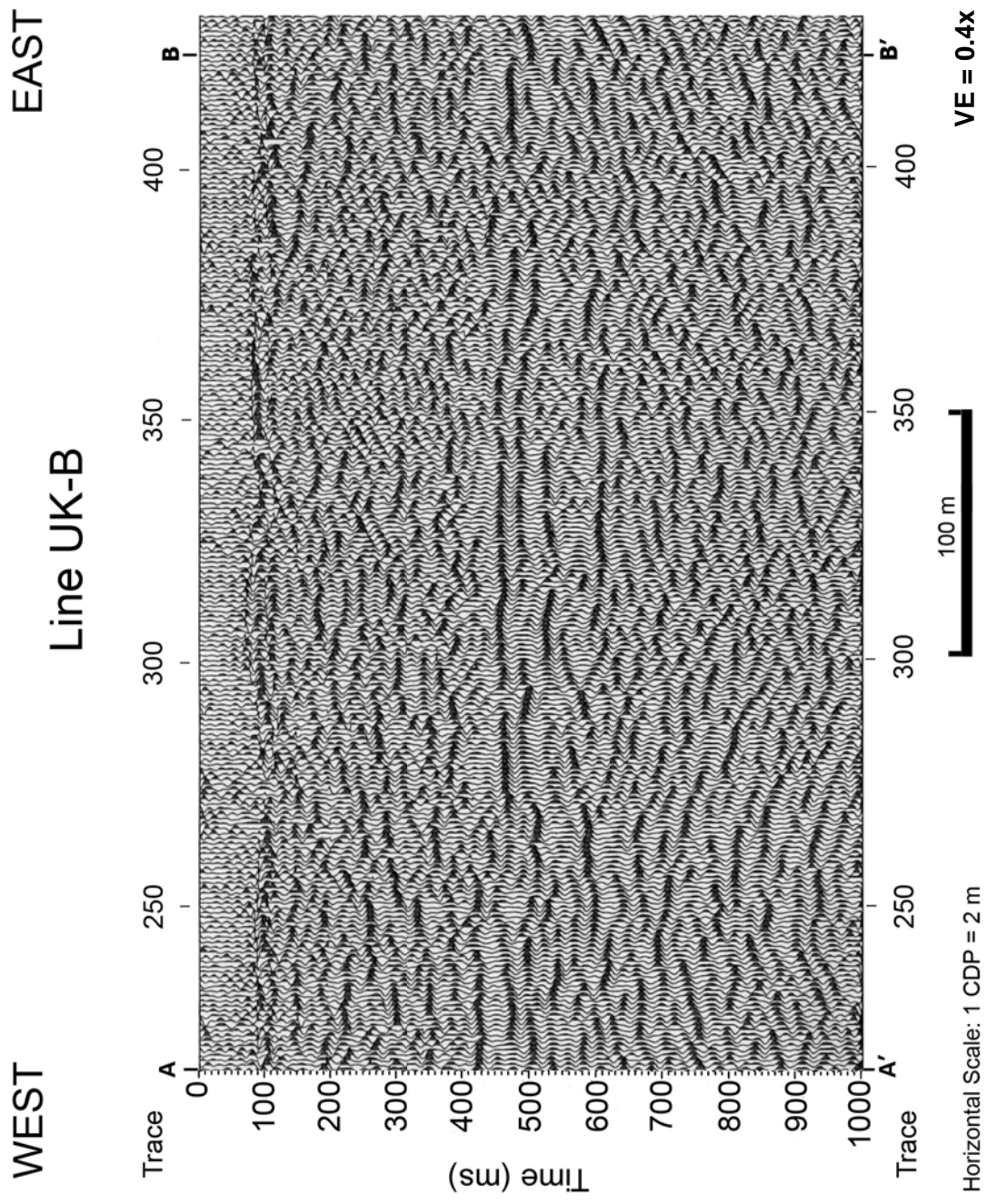
Line UK-B: F-K filtered profile



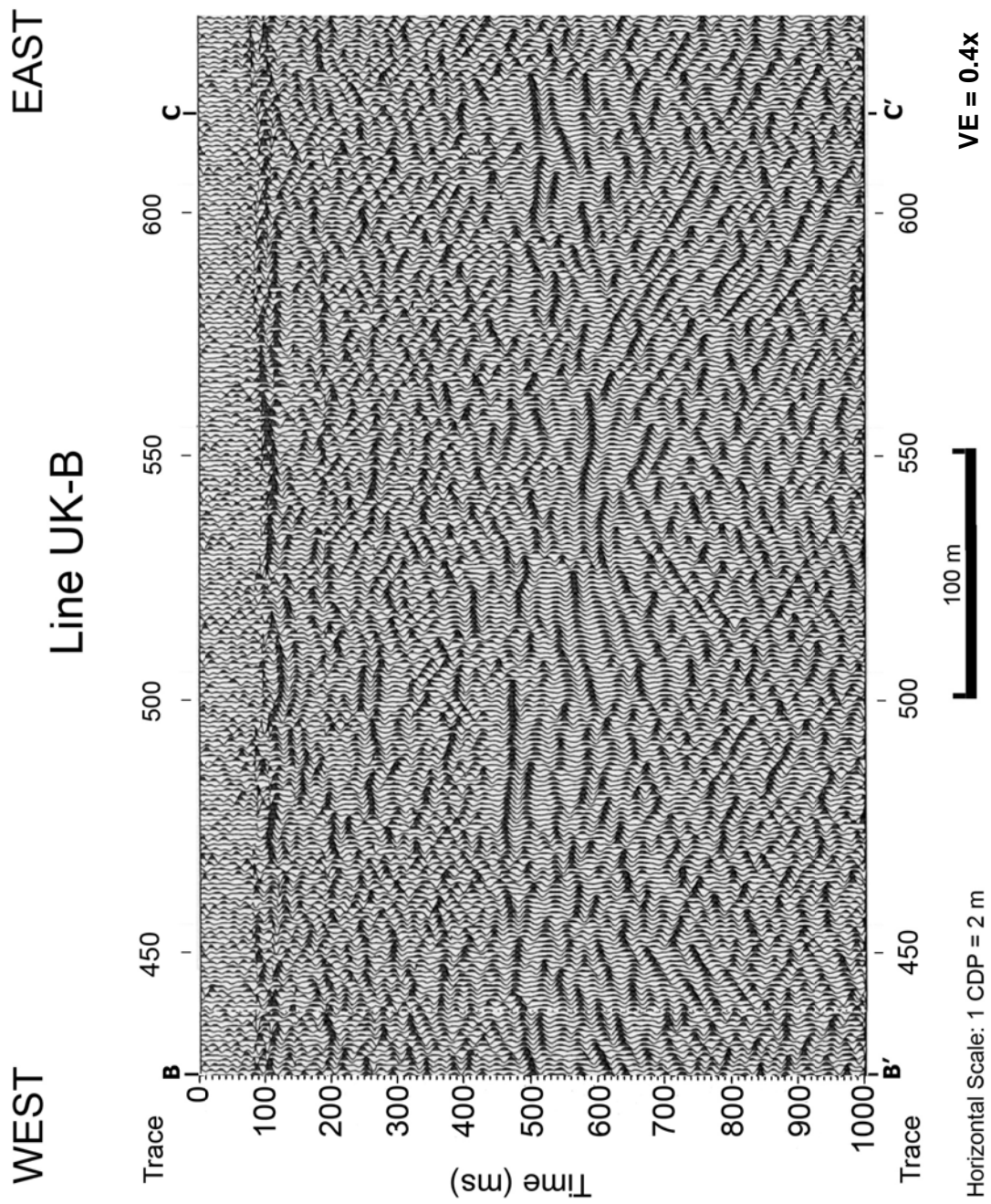
Line UK-B: F-K filtered profile



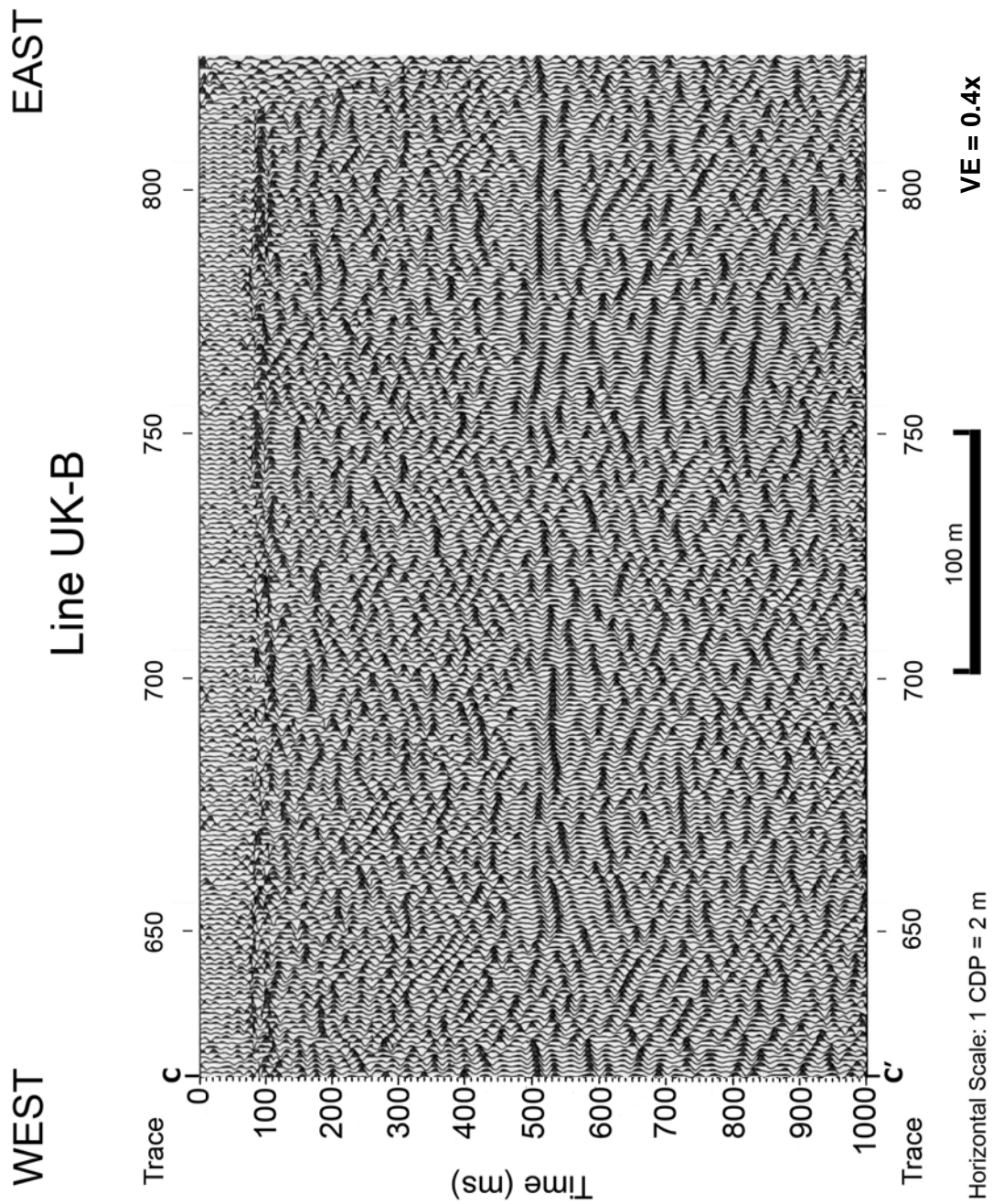
Line UK-B: F-K filtered profile with 100 ms AGC applied



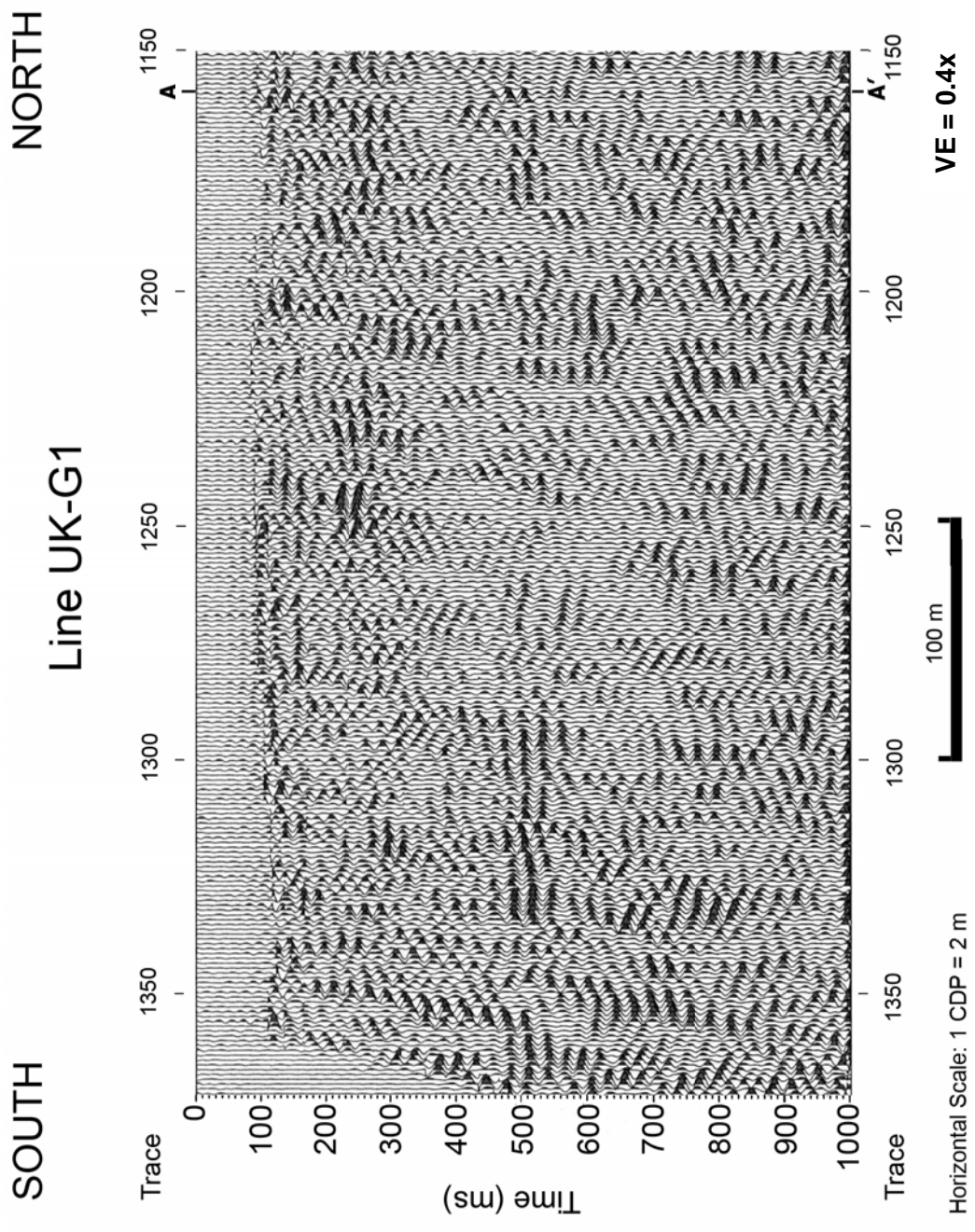
Line UK-B: F-K filtered profile with 100 ms AGC applied



Line UK-B: F-K filtered profile with 100 ms AGC applied

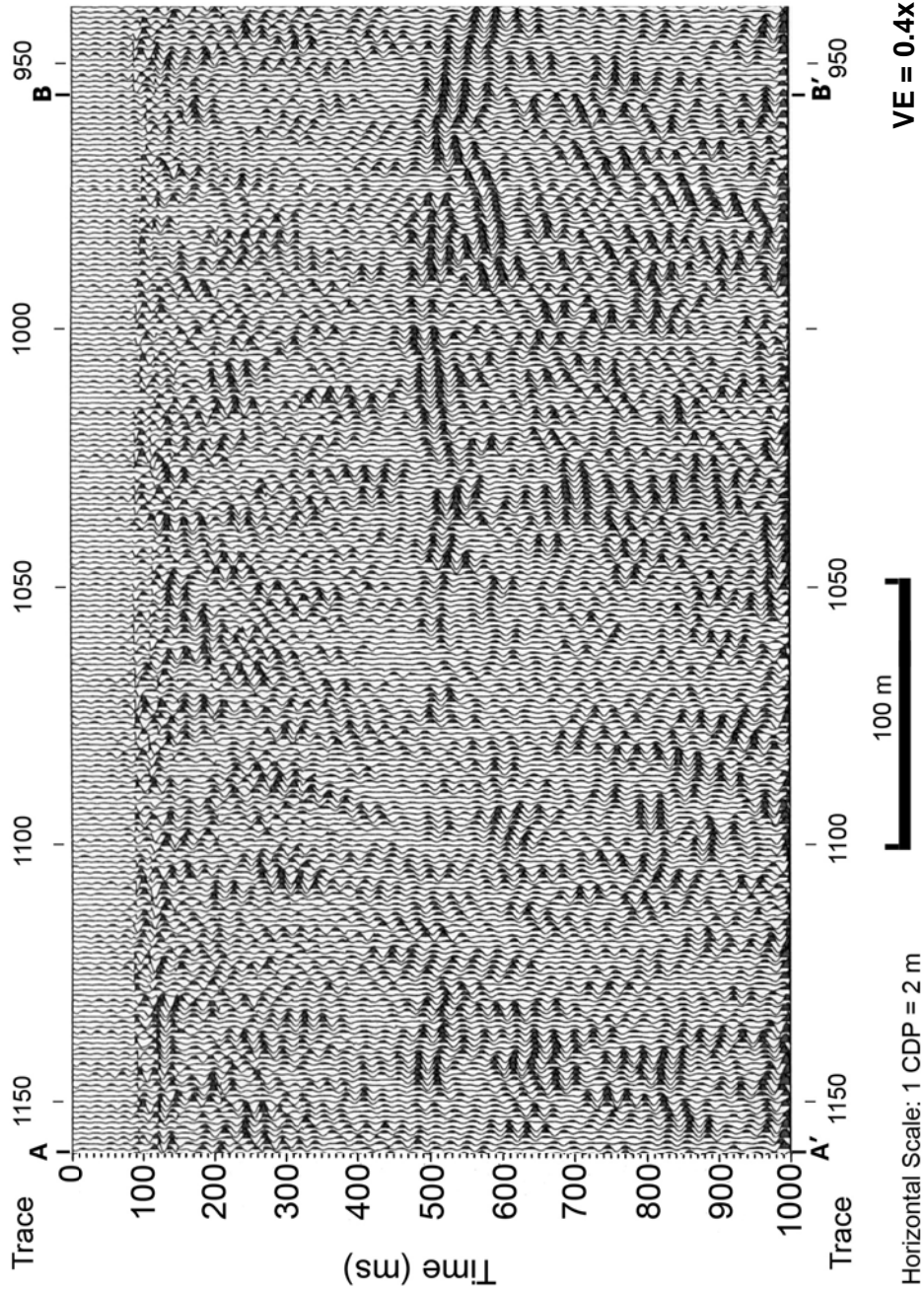


Line UK-B: F-K filtered profile with 100 ms AGC applied



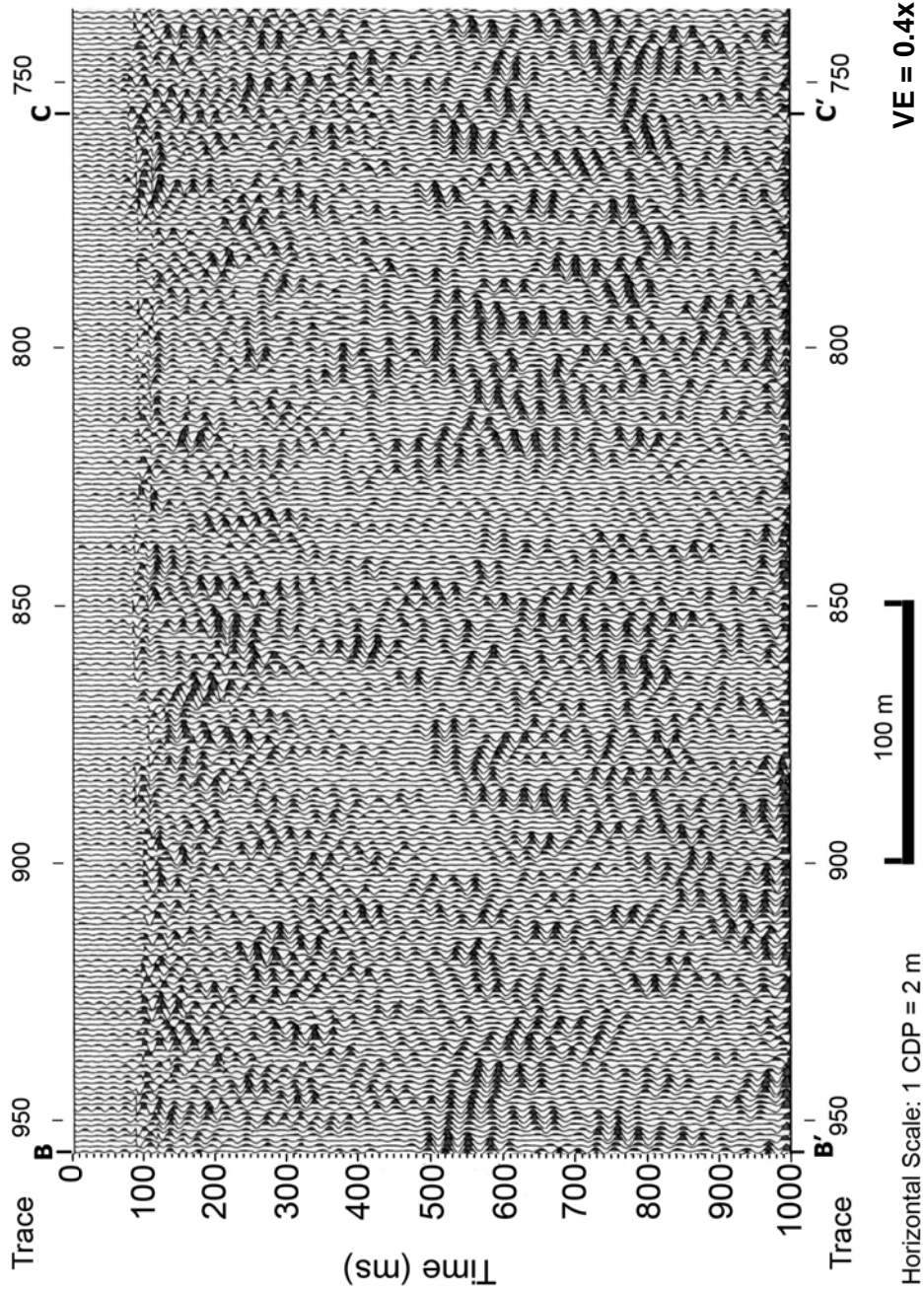
Line UK-G1: F-K filtered profile

SOUTH NORTH
Line UK-G1



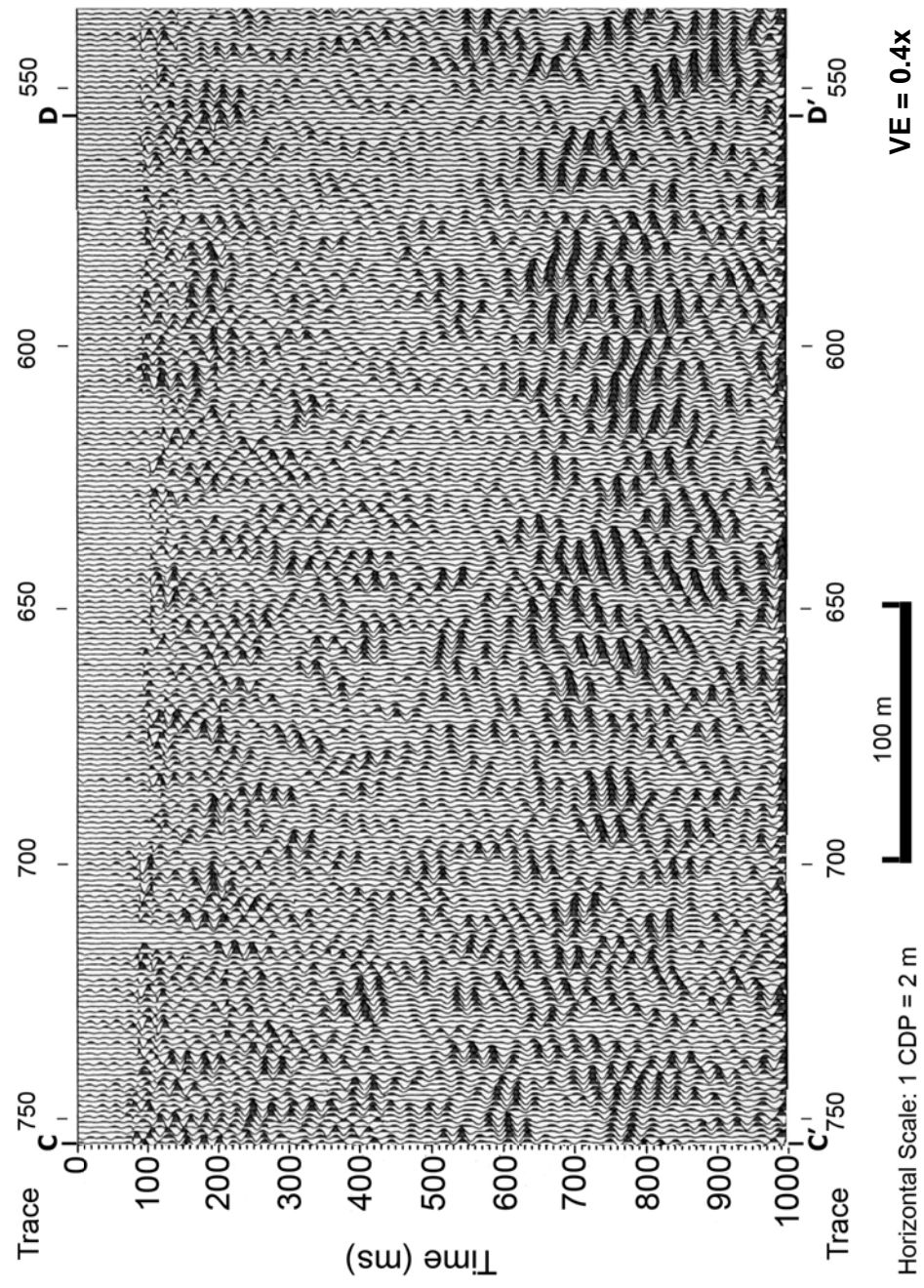
Line UK-G1: F-K filtered profile

SOUTH NORTH
Line UK-G1



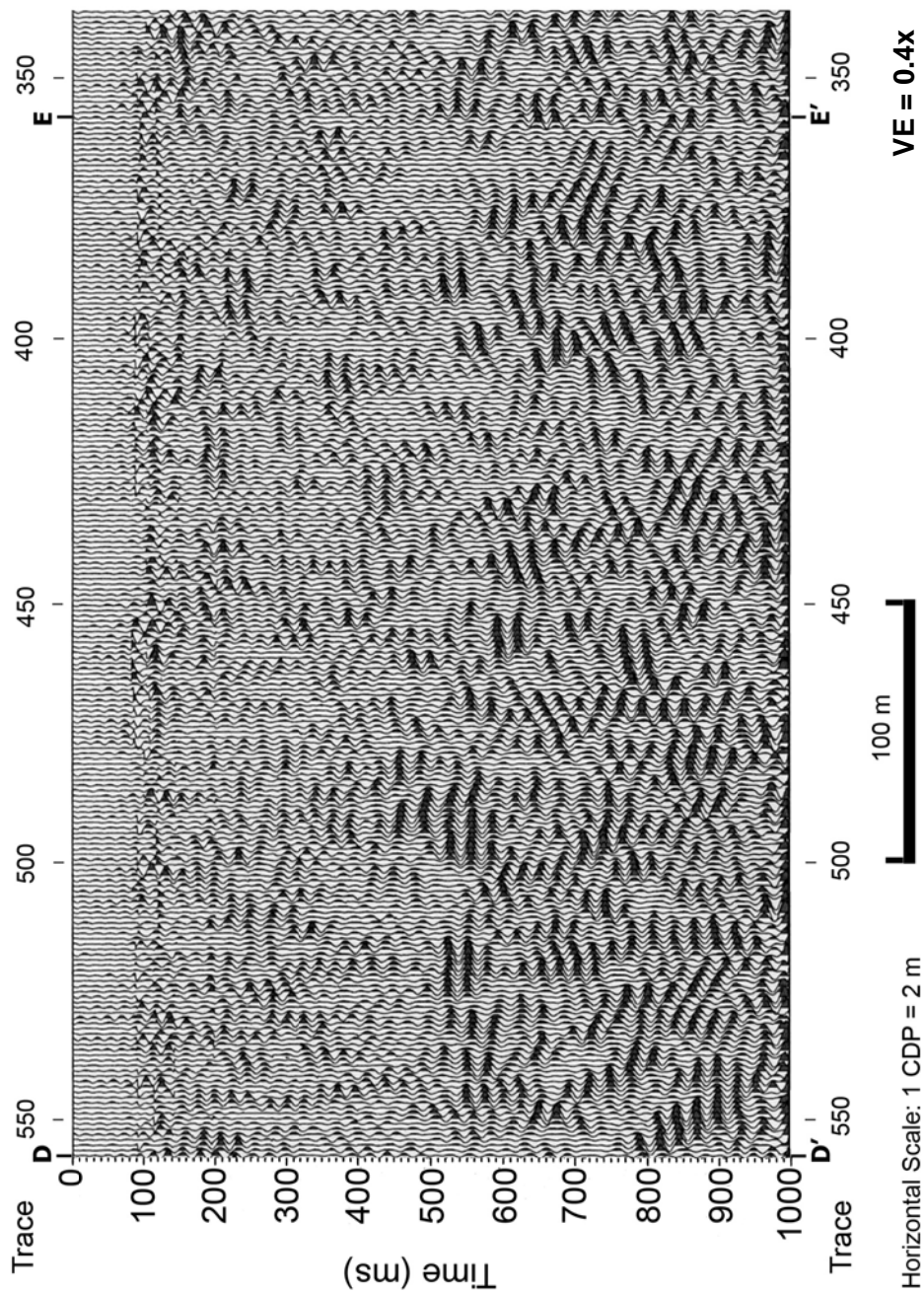
Line UK-G1: F-K filtered profile

SOUTH NORTH
Line UK-G1



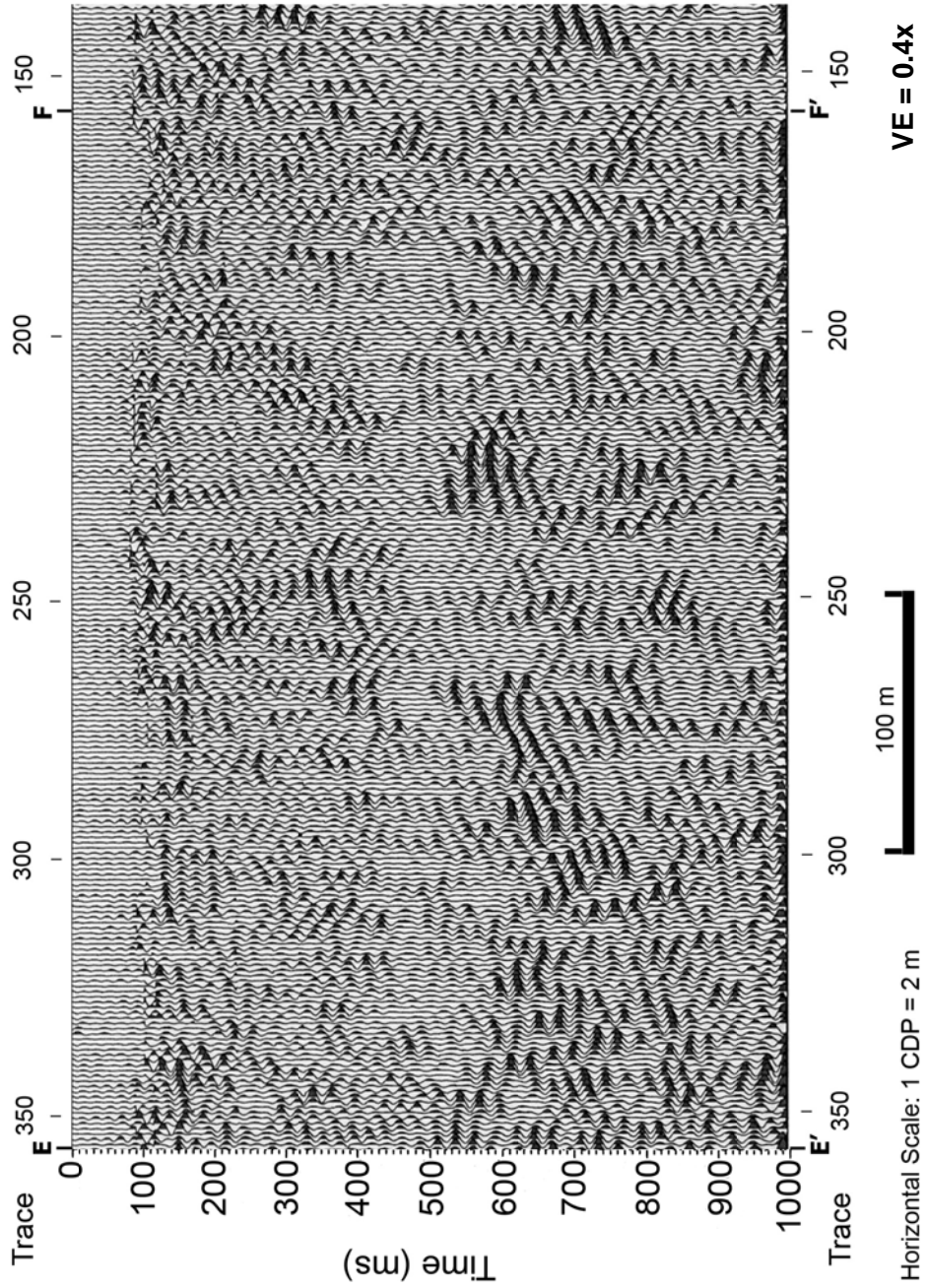
Line UK-G1: F-K filtered profile

SOUTH NORTH
Line UK-G1



Line UK-G1: F-K filtered profile

SOUTH NORTH
Line UK-G1

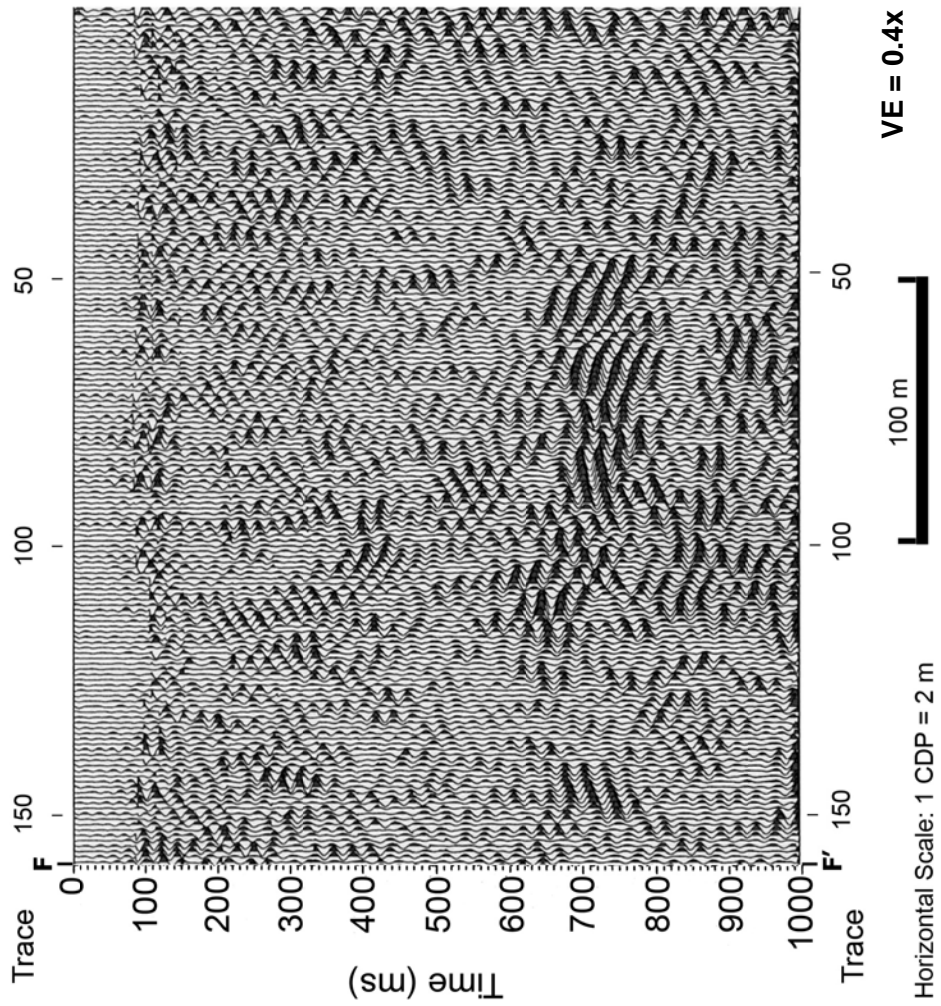


Line UK-G1: F-K filtered profile

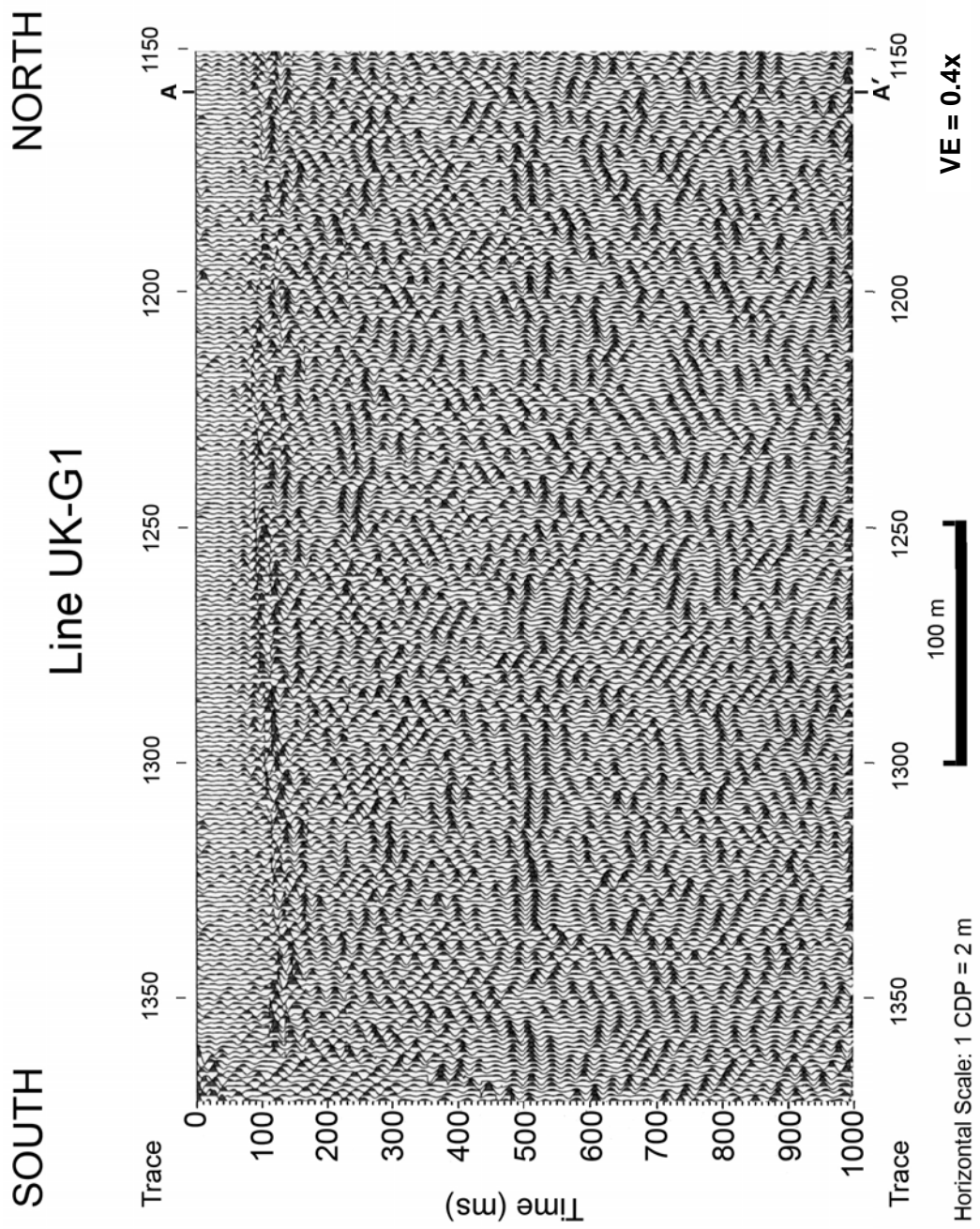
NORTH

SOUTH

Line UK-G1

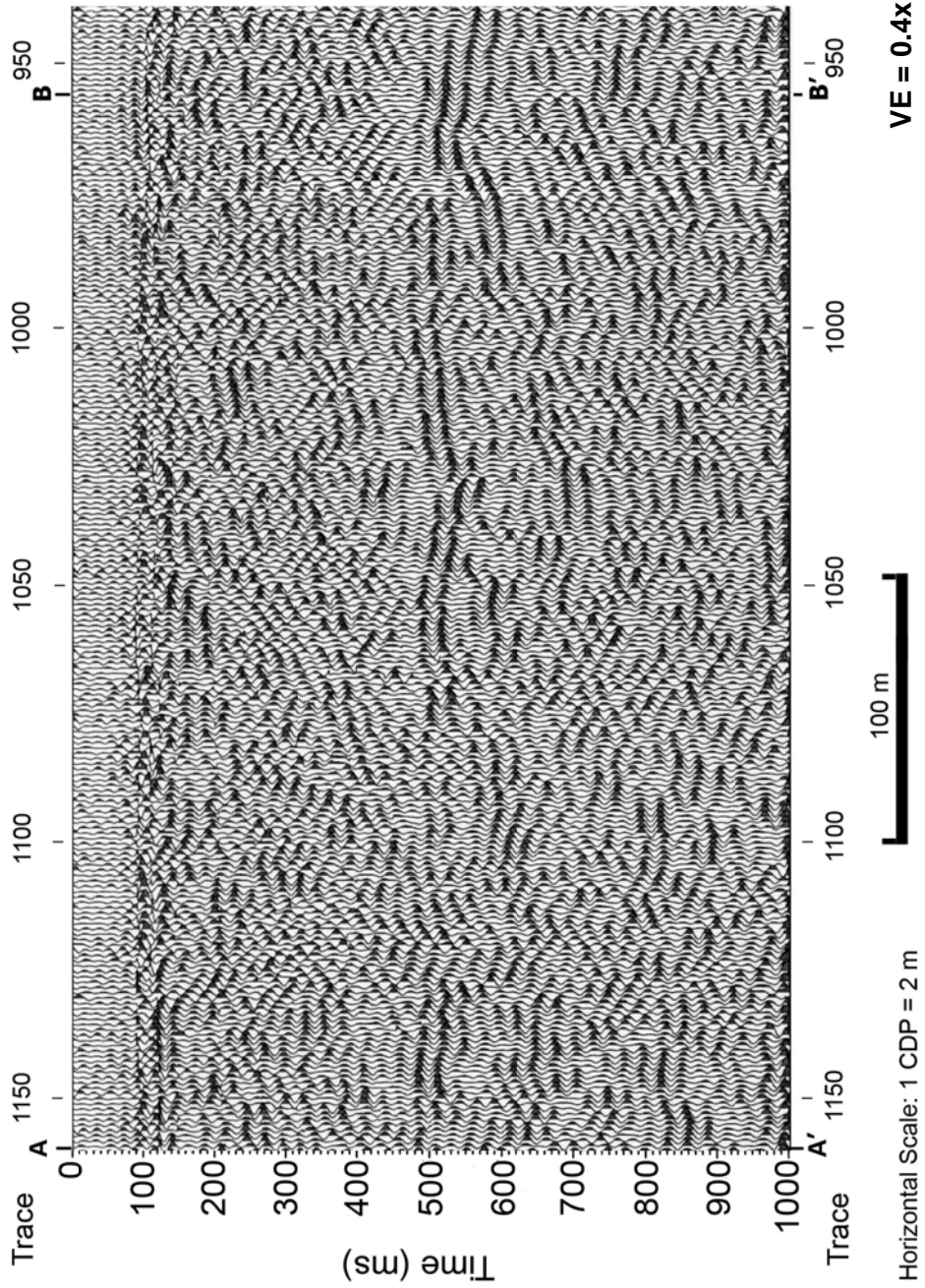


Line UK-G1: F-K filtered profile



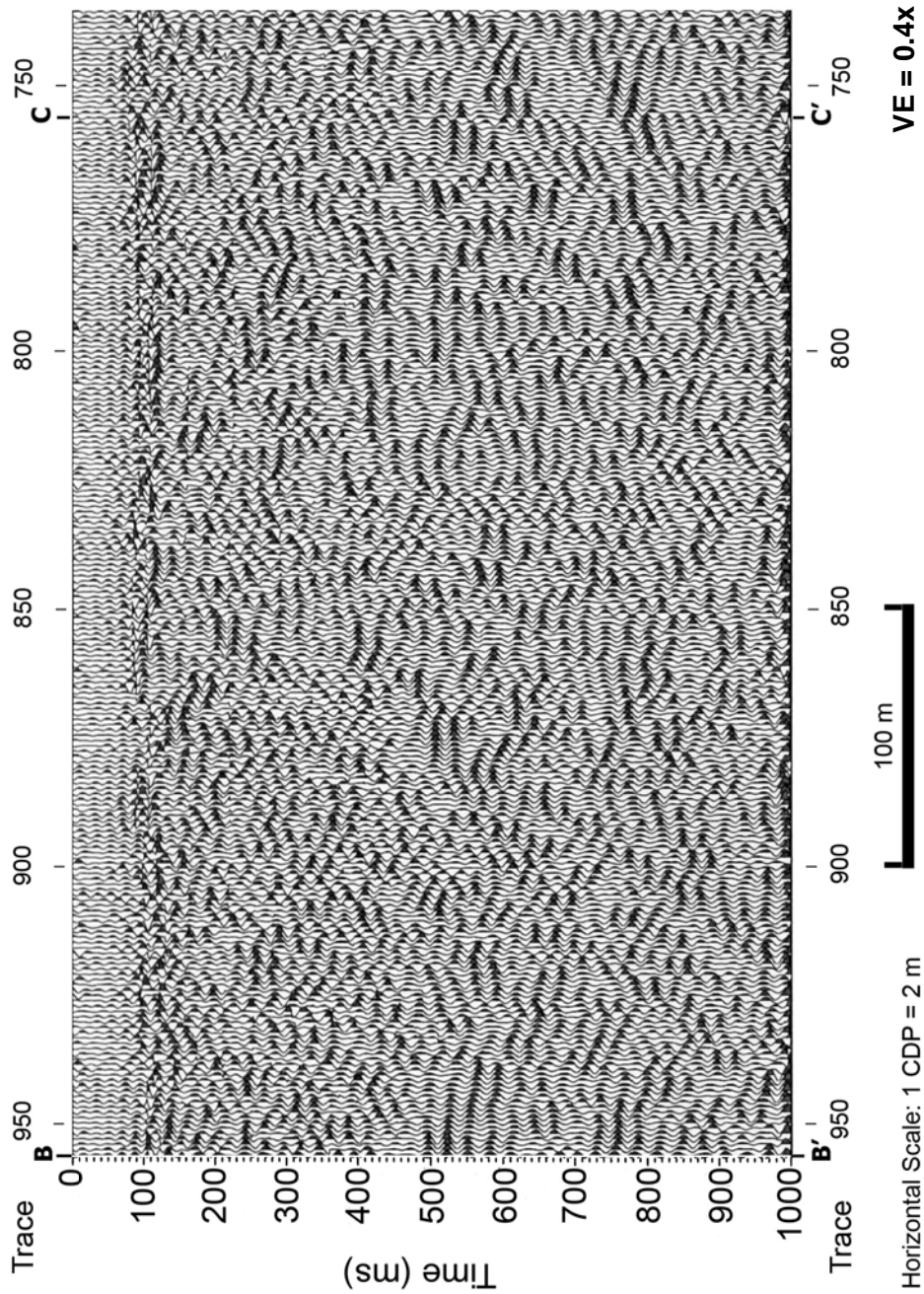
Line UK-G1: F-K filtered profile with 150 ms AGC applied

SOUTH NORTH
Line UK-G1



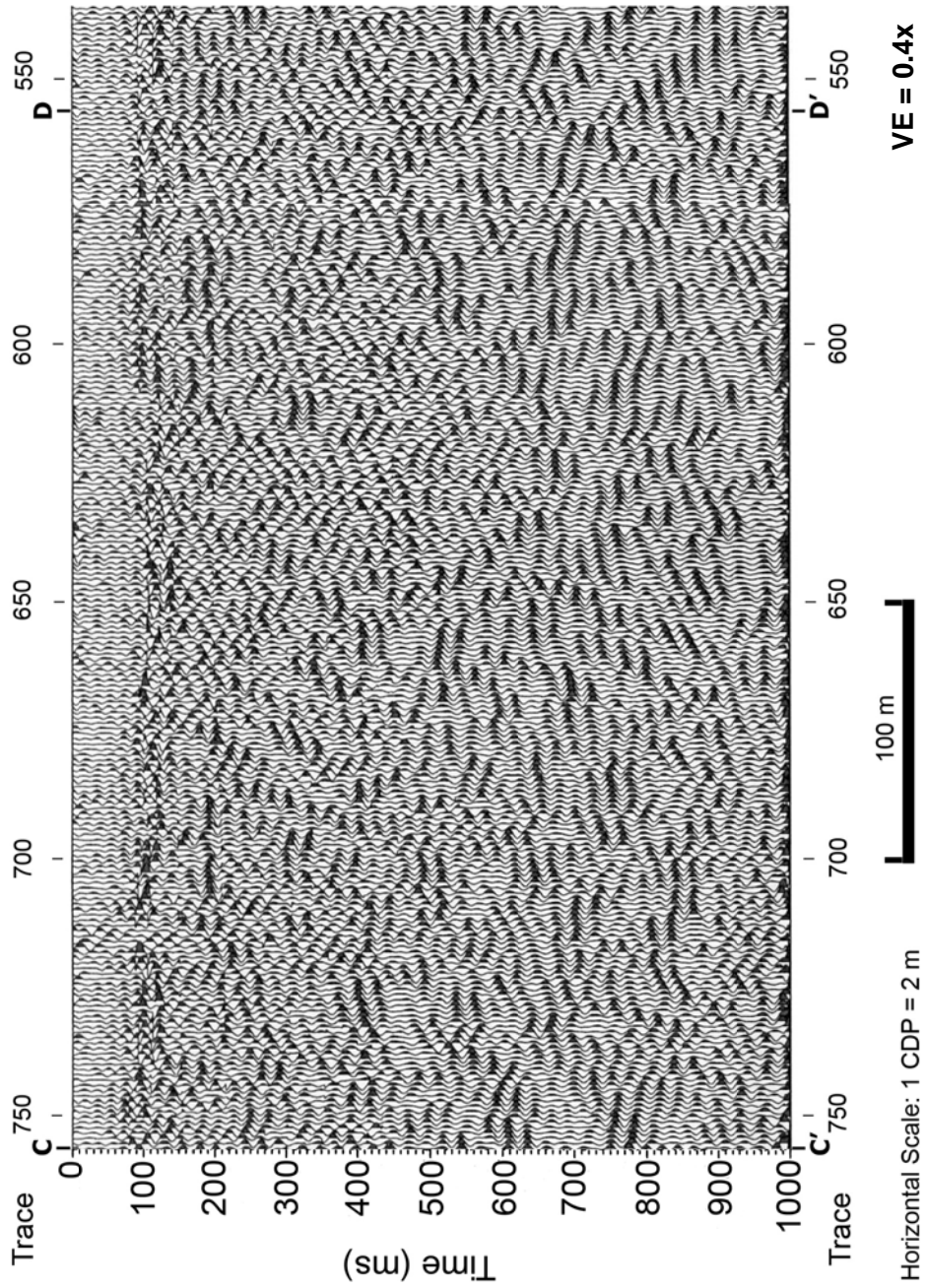
Line UK-G1: F-K filtered profile with 150 ms AGC applied

SOUTH NORTH
Line UK-G1



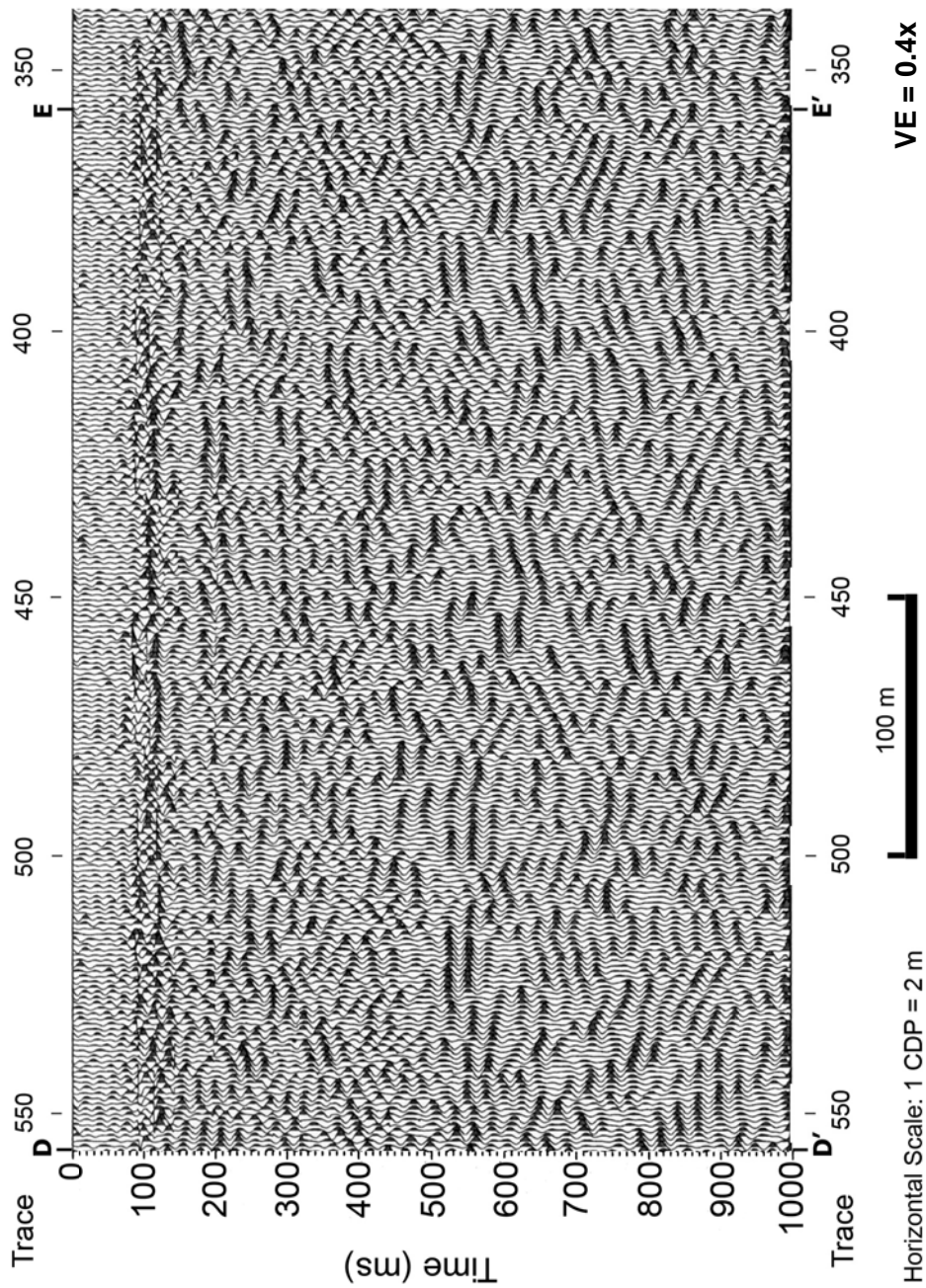
Line UK-G1: F-K filtered profile with 150 ms AGC applied

SOUTH NORTH
Line UK-G1



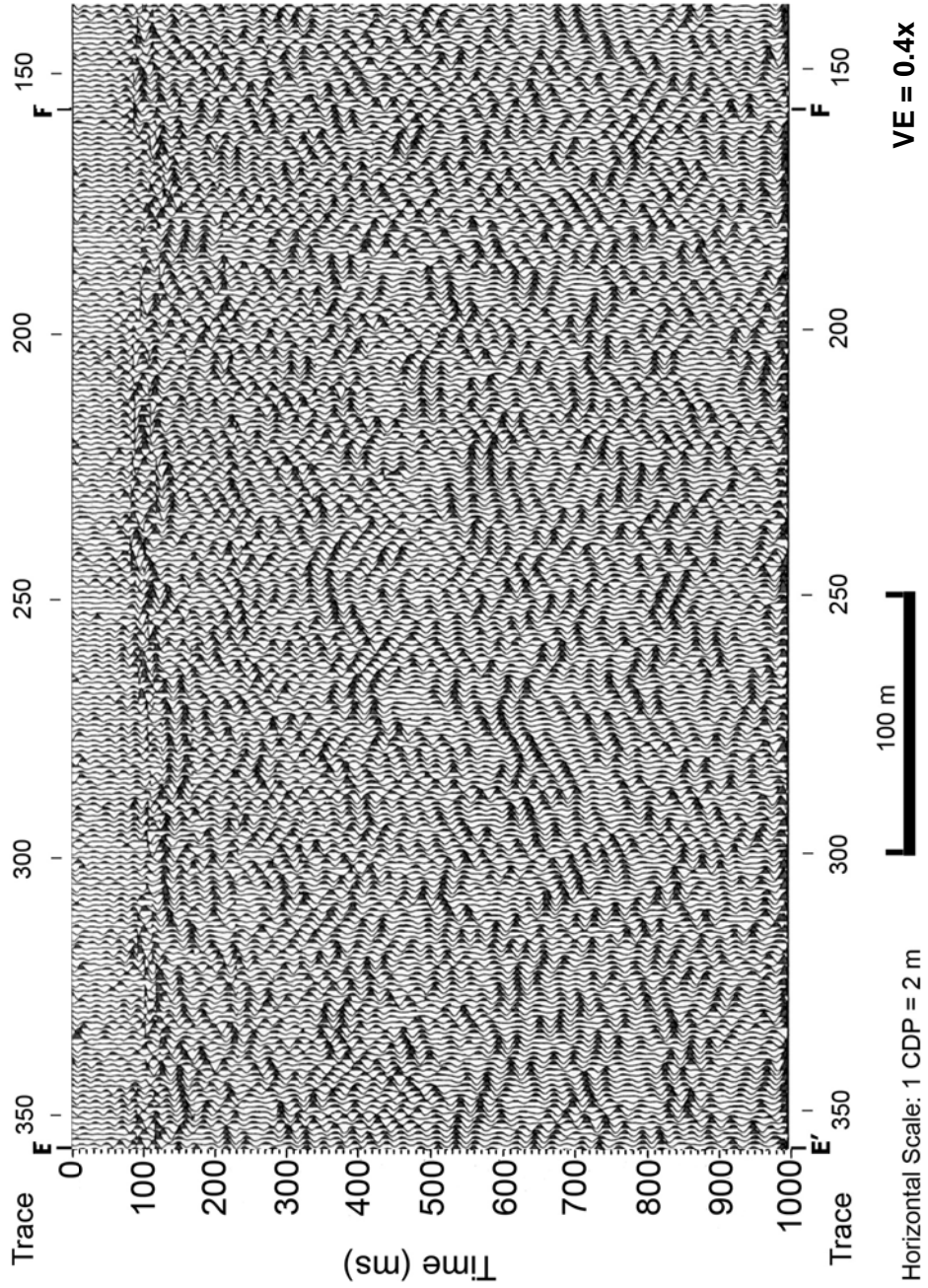
Line UK-G1: F-K filtered profile with 150 ms AGC applied

SOUTH NORTH
Line UK-G1



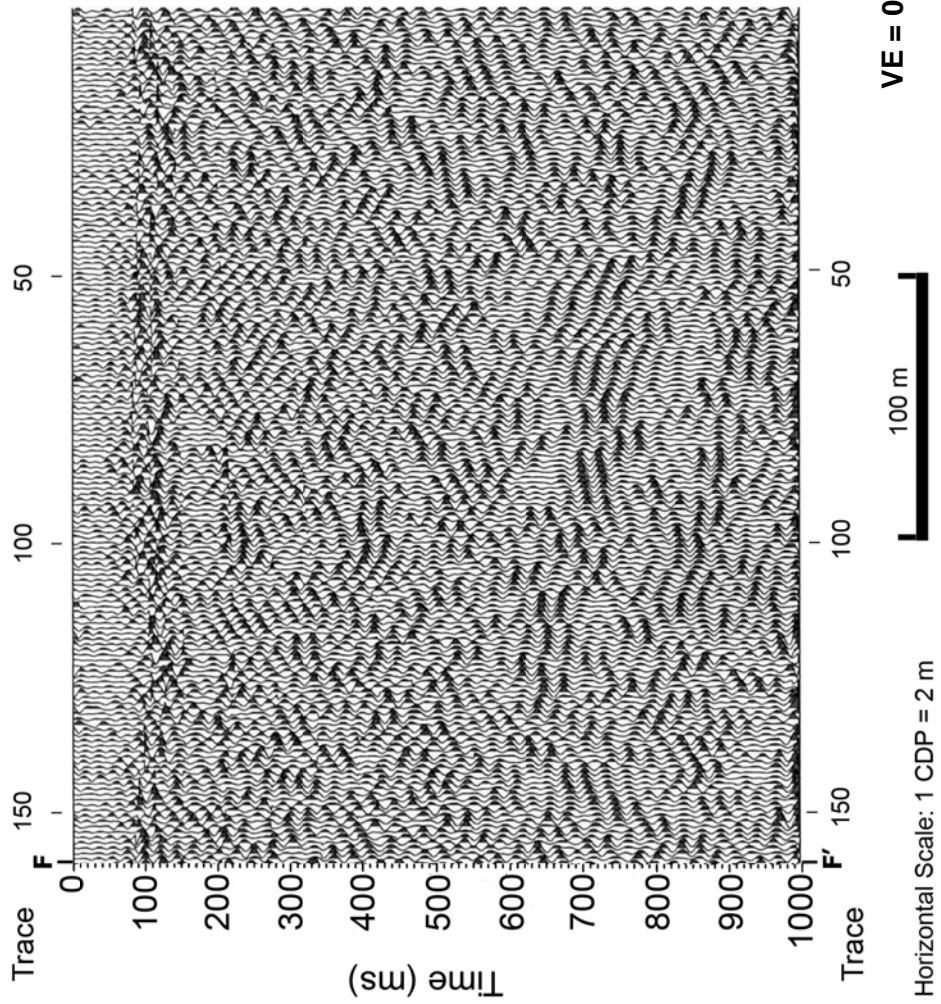
Line UK-G1: F-K filtered profile with 150 ms AGC applied

SOUTH NORTH
Line UK-G1

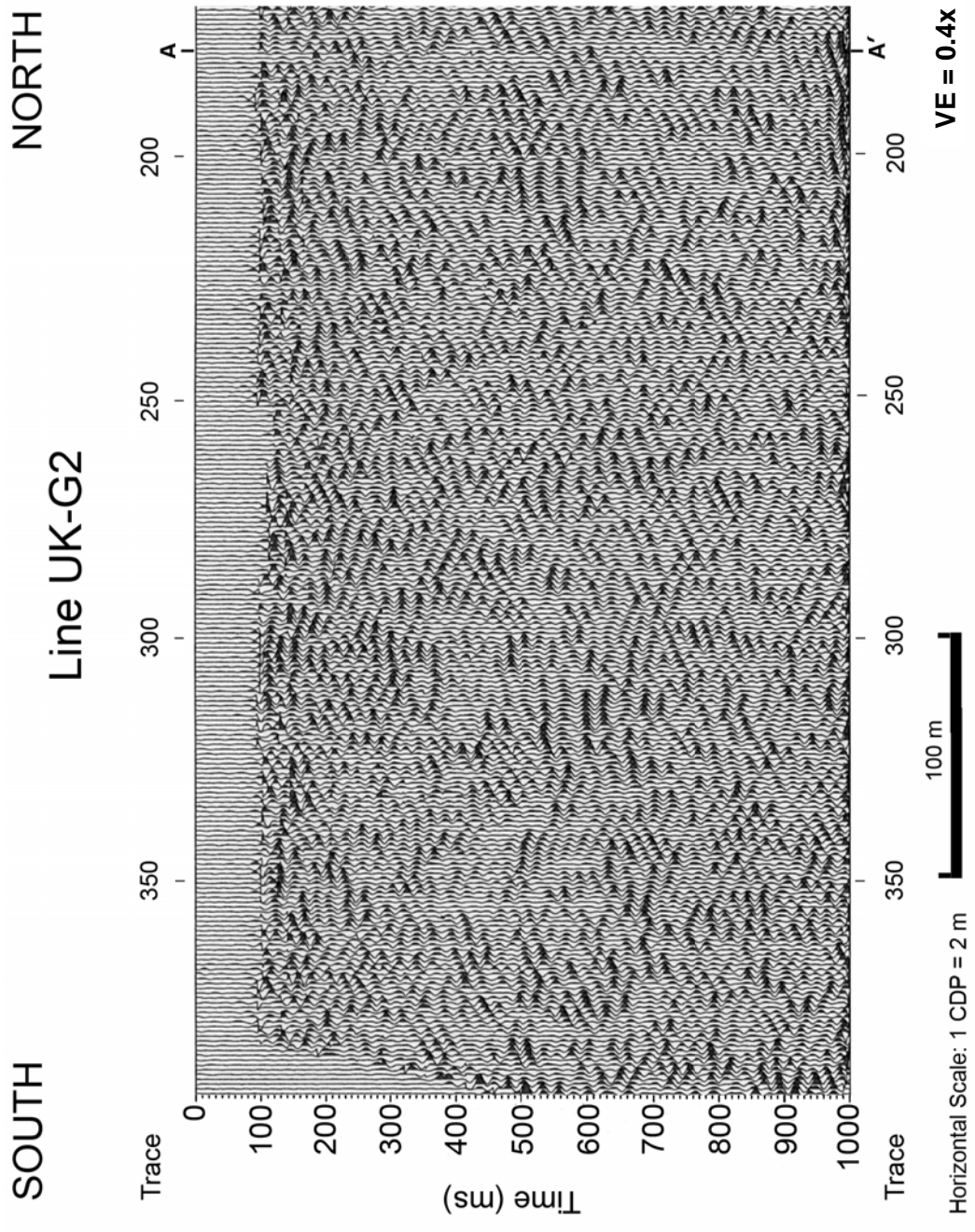


Line UK-G1: F-K filtered profile with 150 ms AGC applied

SOUTH NORTH
Line UK-G1



Line UK-G1: F-K filtered profile with 150 ms AGC applied

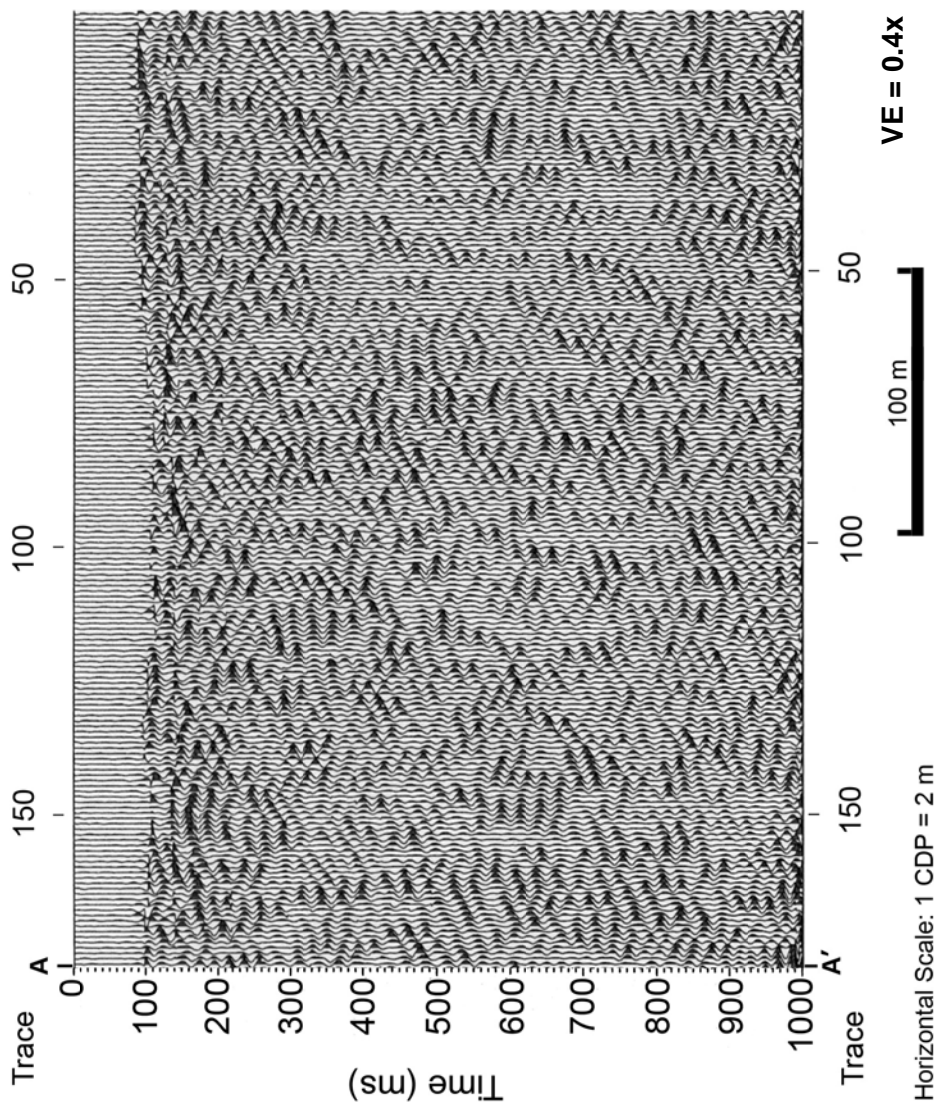


Line UK-G2: F-K filtered profile

NORTH

Line UK-G2

SOUTH

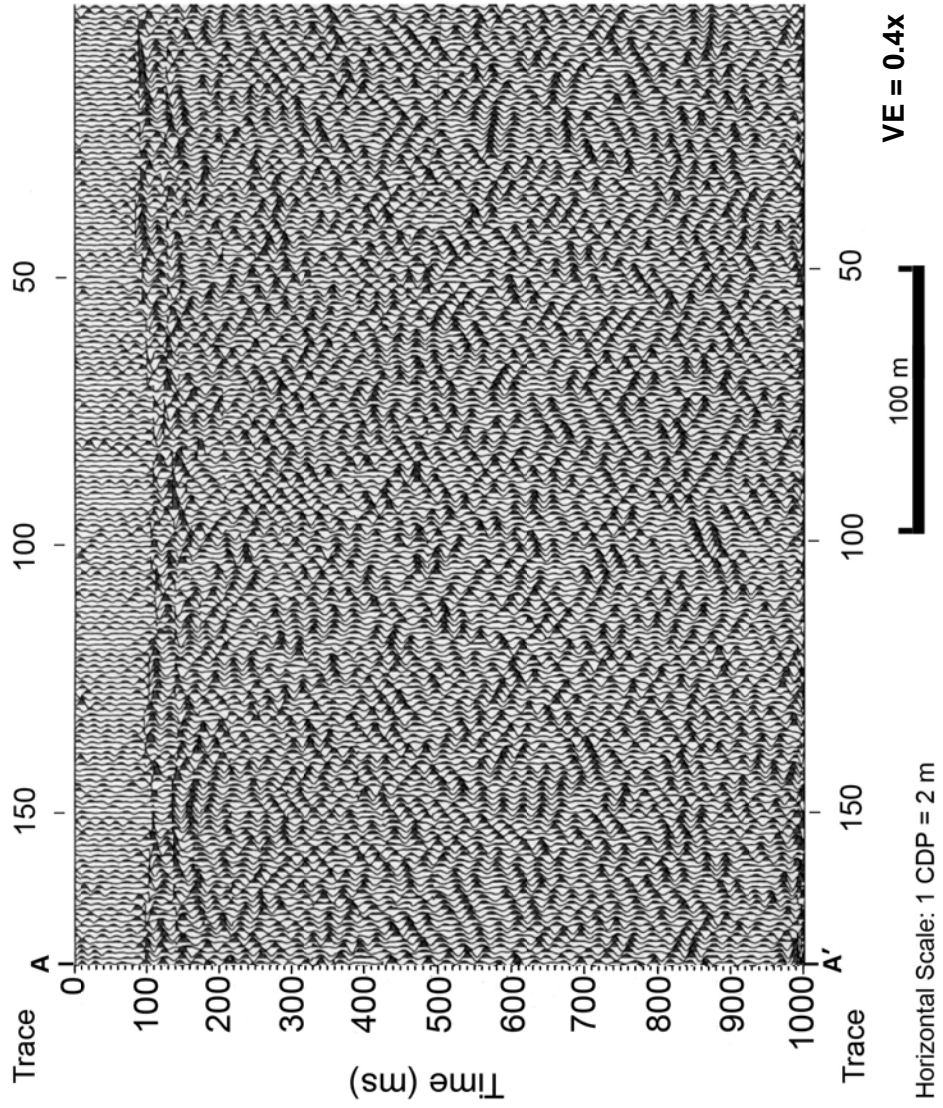


Line UK-G2: F-K filtered profile

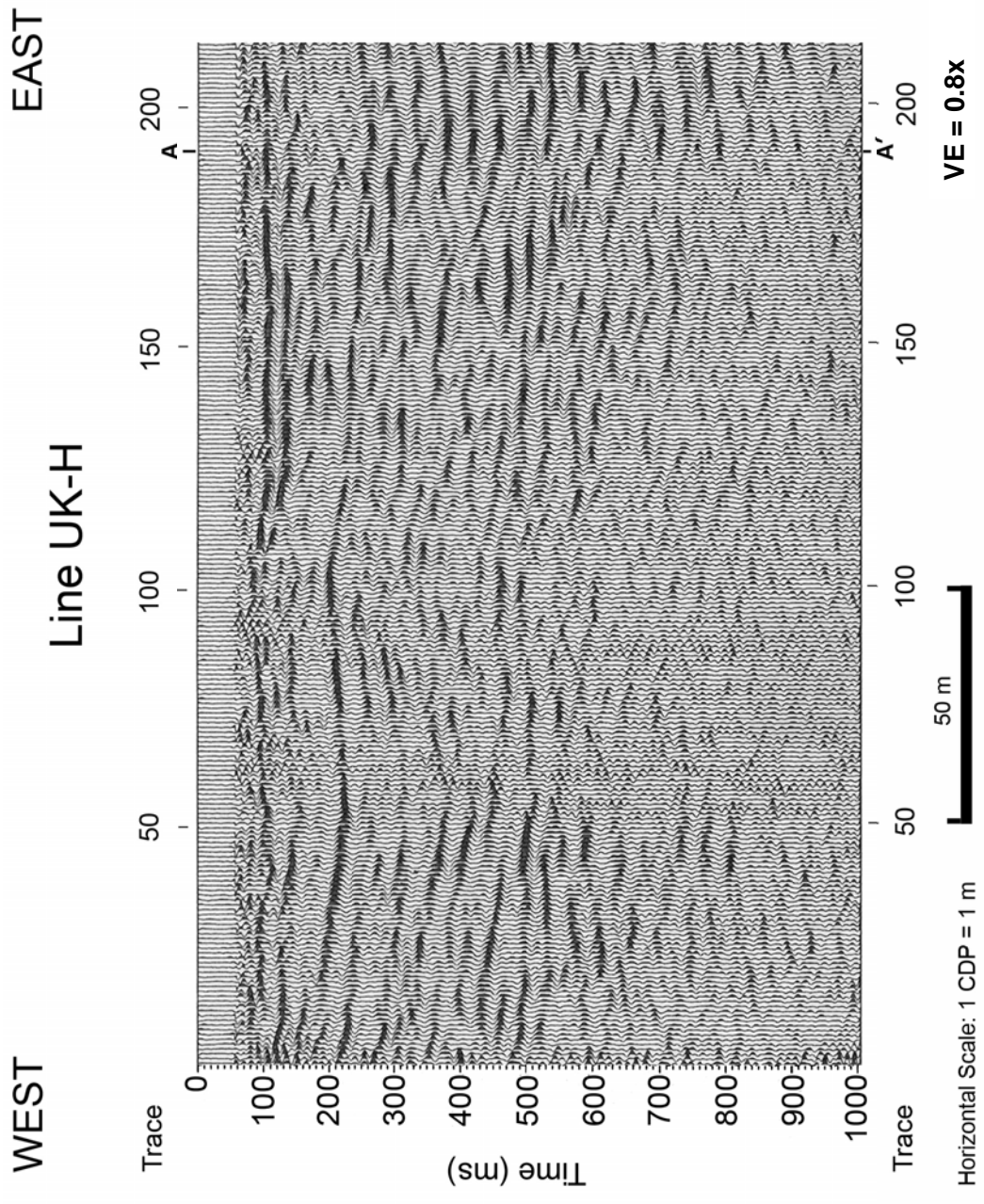
NORTH

Line UK-G2

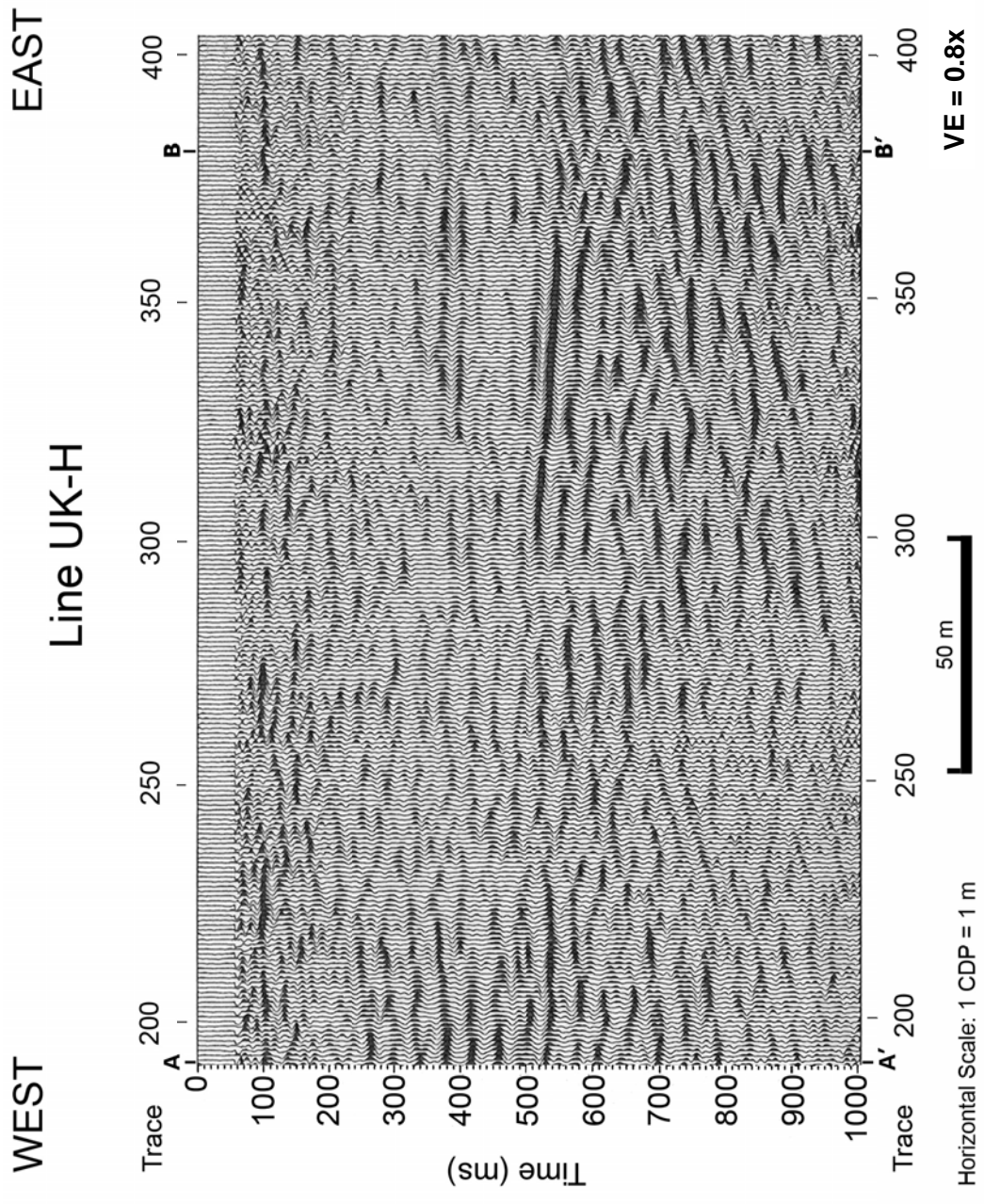
SOUTH



Line UK-G2: F-K filtered profile with 150 ms AGC applied



Line UK-H: F-K filtered profile

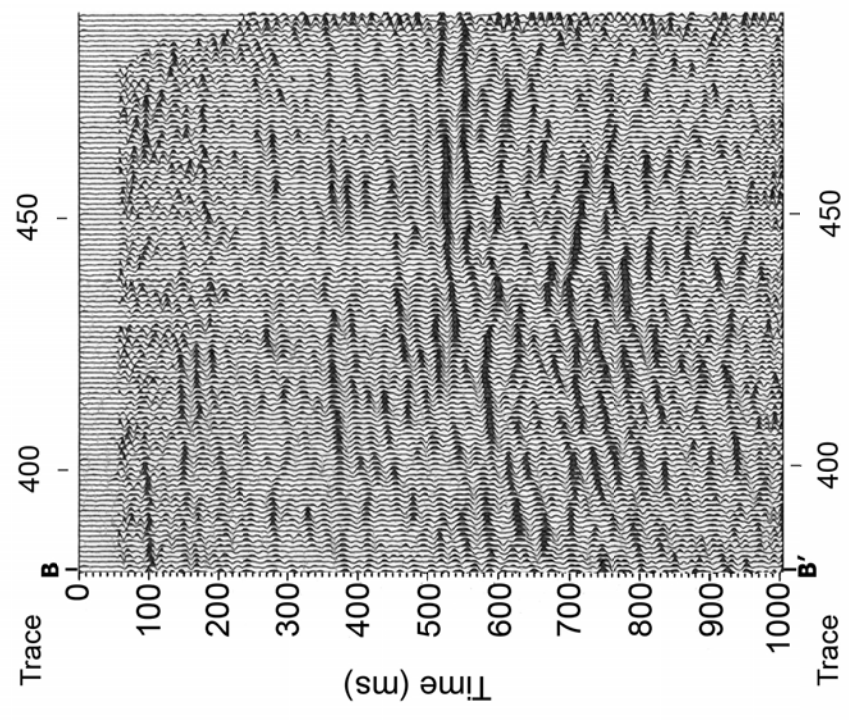


Line UK-H: F-K filtered profile

EAST

Line UK-H

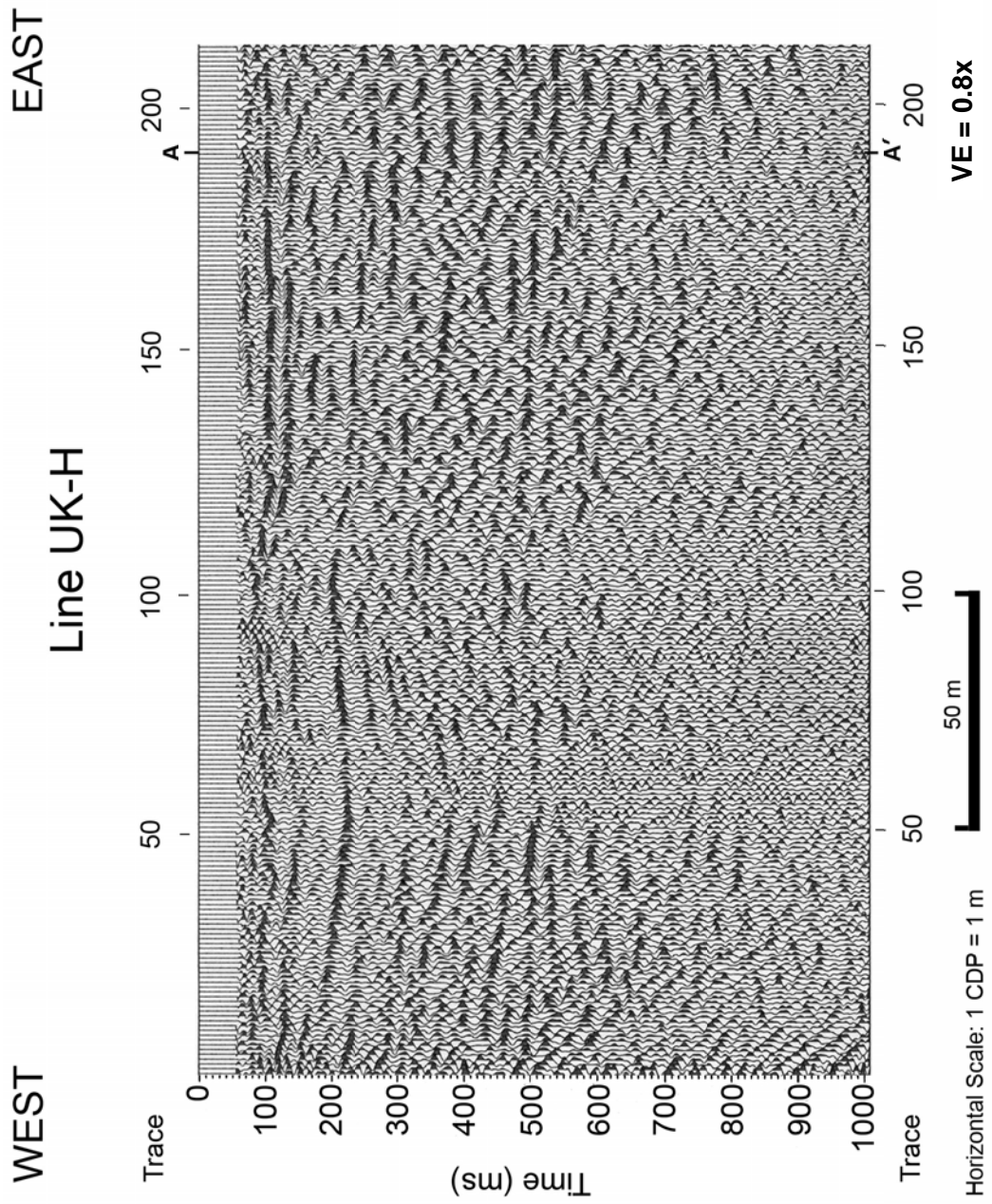
WEST



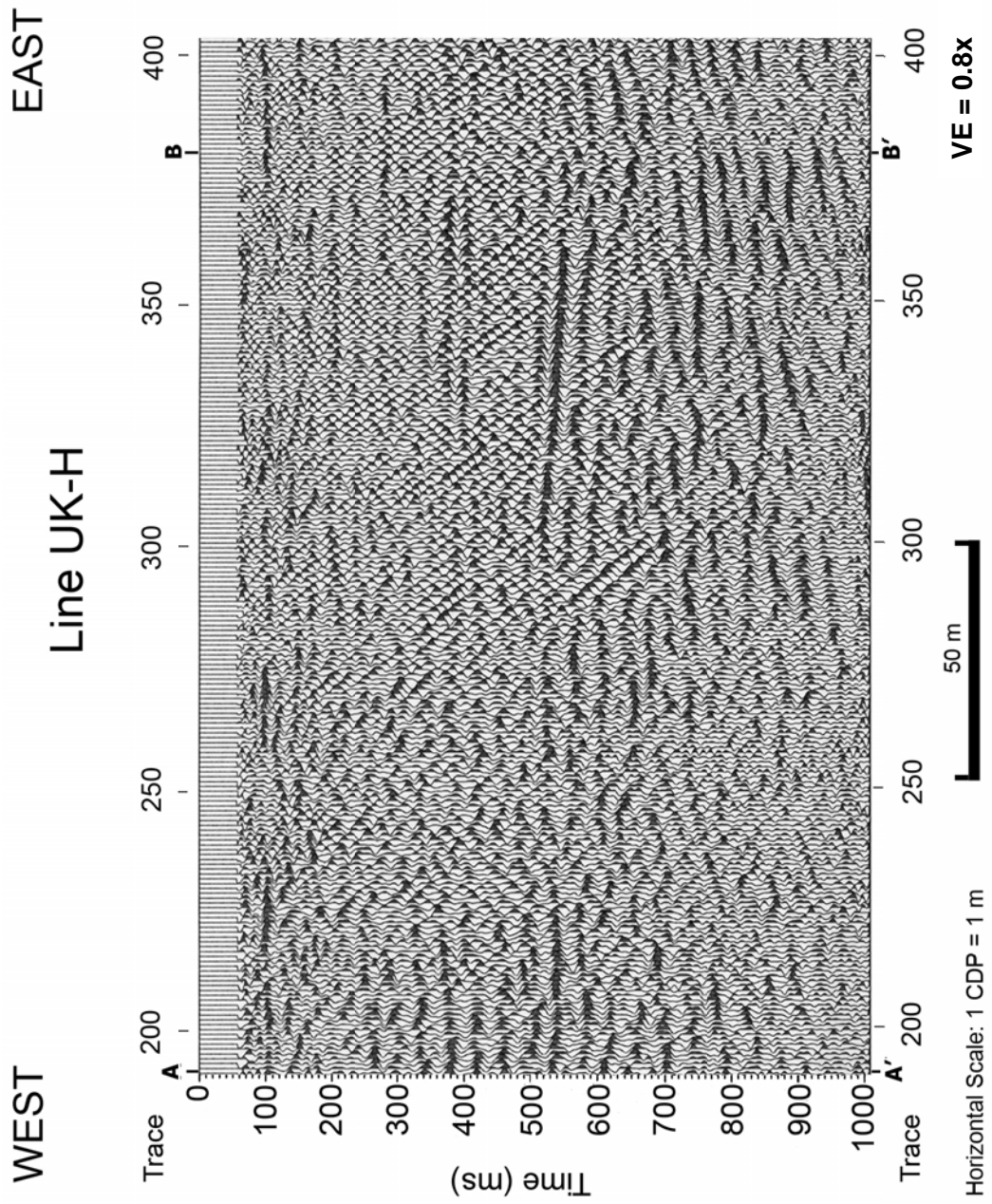
VE = 0.8x

Horizontal Scale: 1 CDP = 1 m

Line UK-H: F-K filtered profile



Line UK-H: F-K filtered profile with surface consistent statics applied

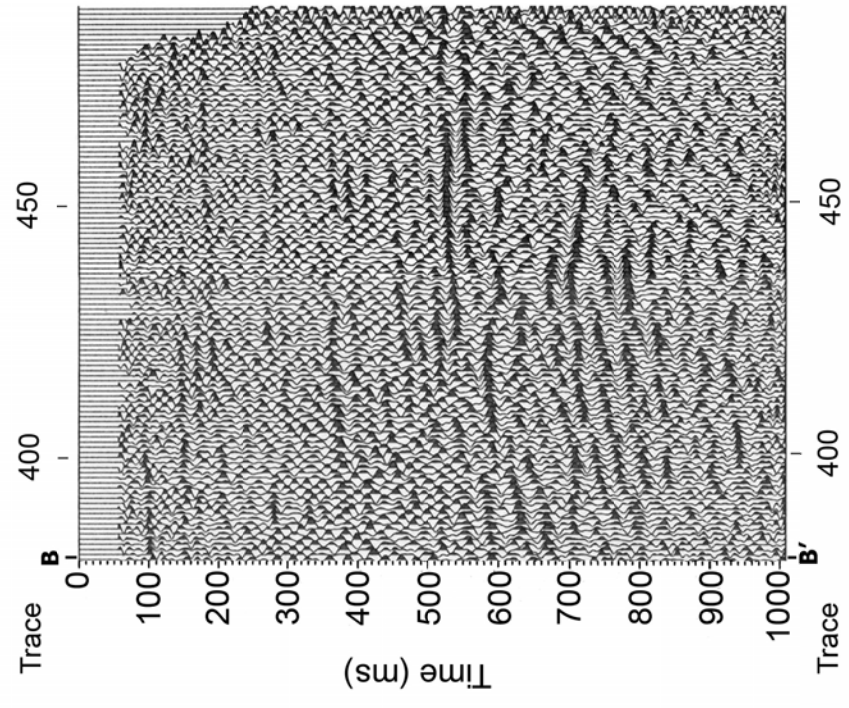


Line UK-H: F-K filtered profile with surface consistent statics applied

EAST

Line UK-H

WEST



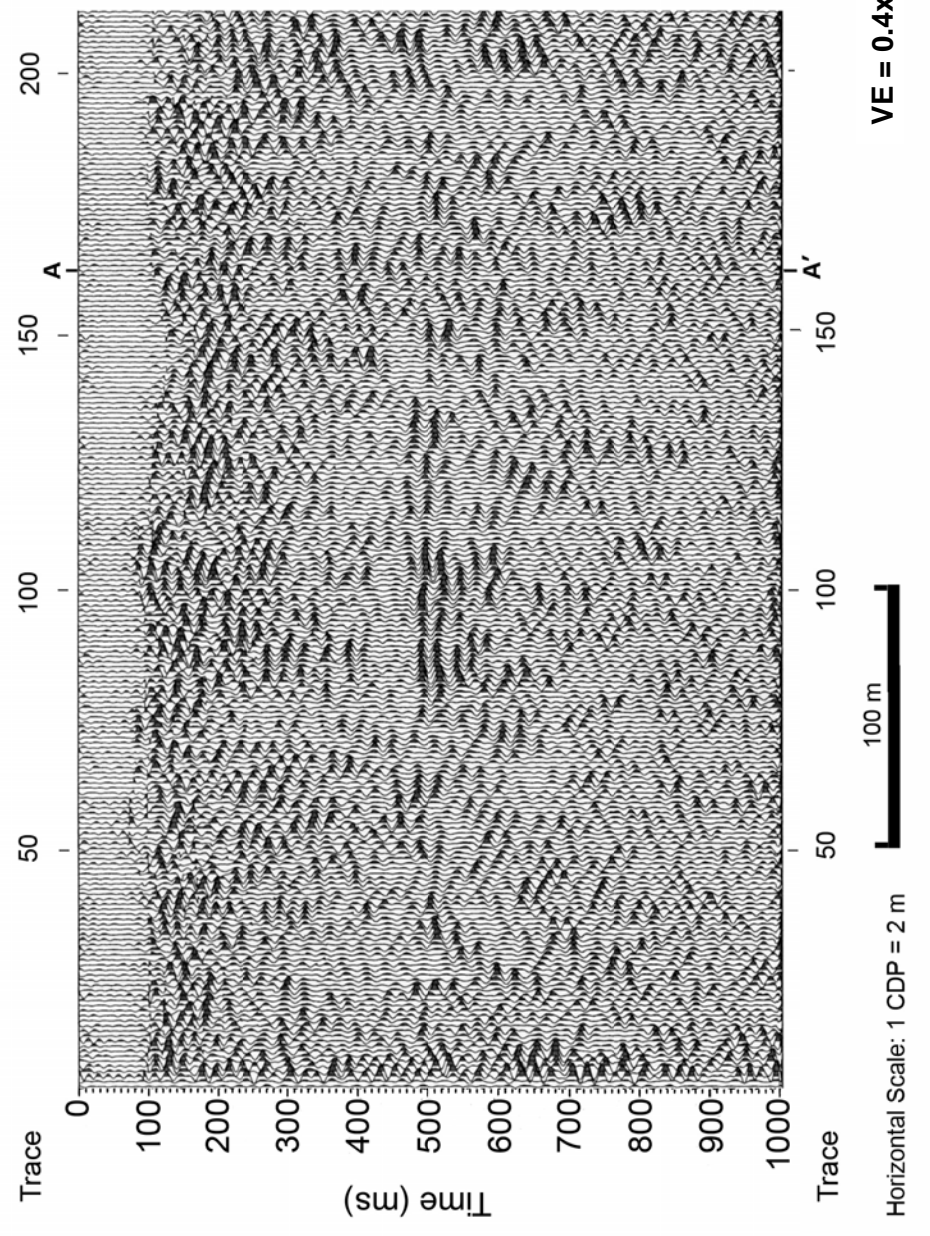
Horizontal Scale: 1 CDP = 1 m
VE = 0.8x

Line UK-H: F-K filtered profile with surface consistent statics applied

SOUTH

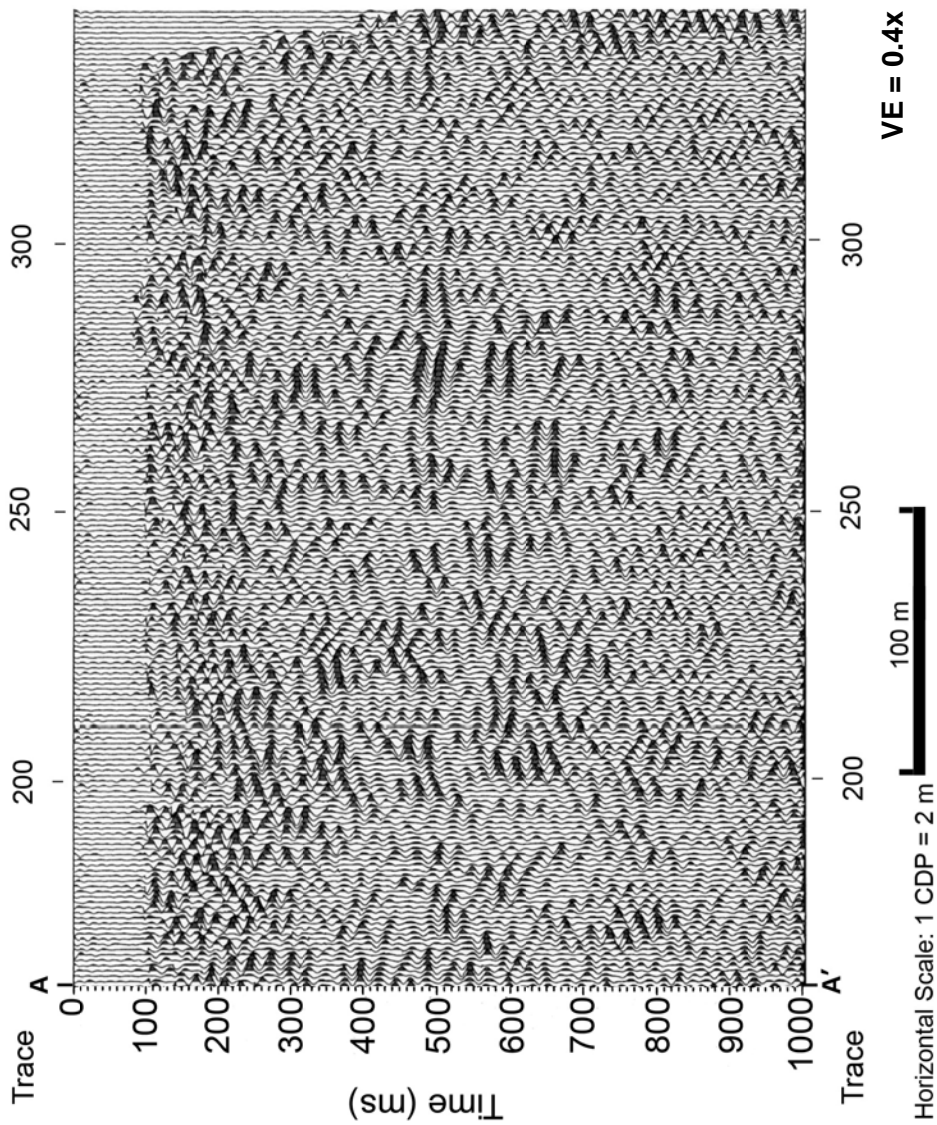
NORTH

Line UK-I

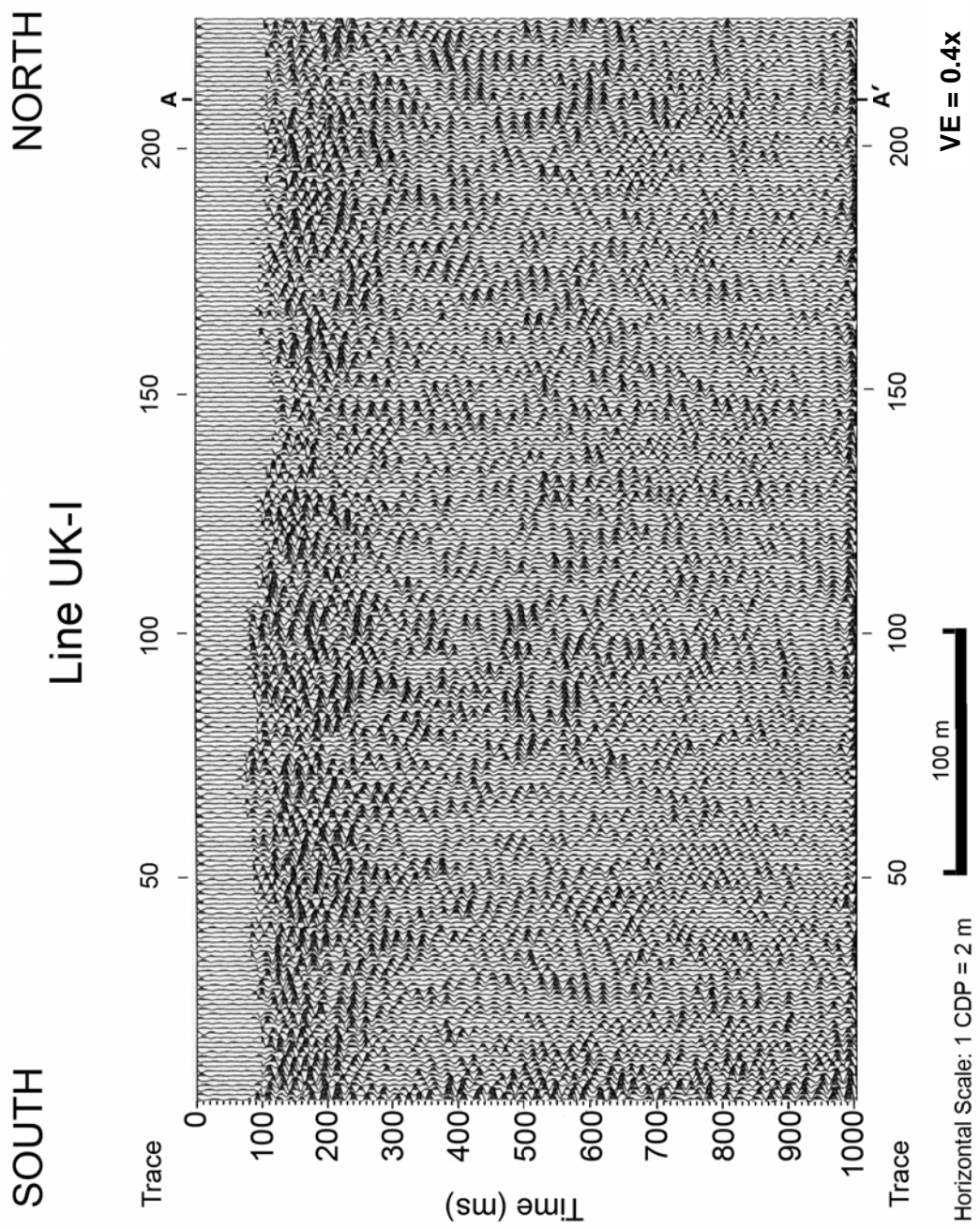


Line UK-I: F-K filtered profile

SOUTH NORTH
Line UK-I



Line UK-I: F-K filtered profile

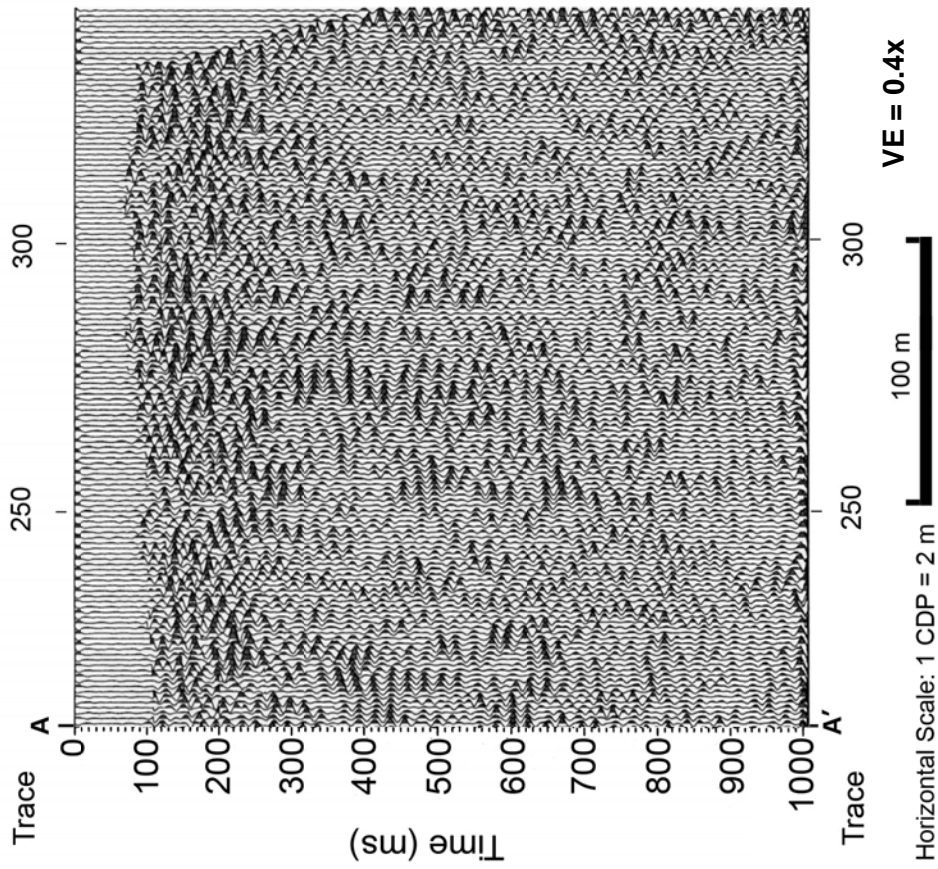


Line UK-I: F-K filtered profile with pre-stack F-K filtering applied

NORTH

SOUTH

Line UK-I

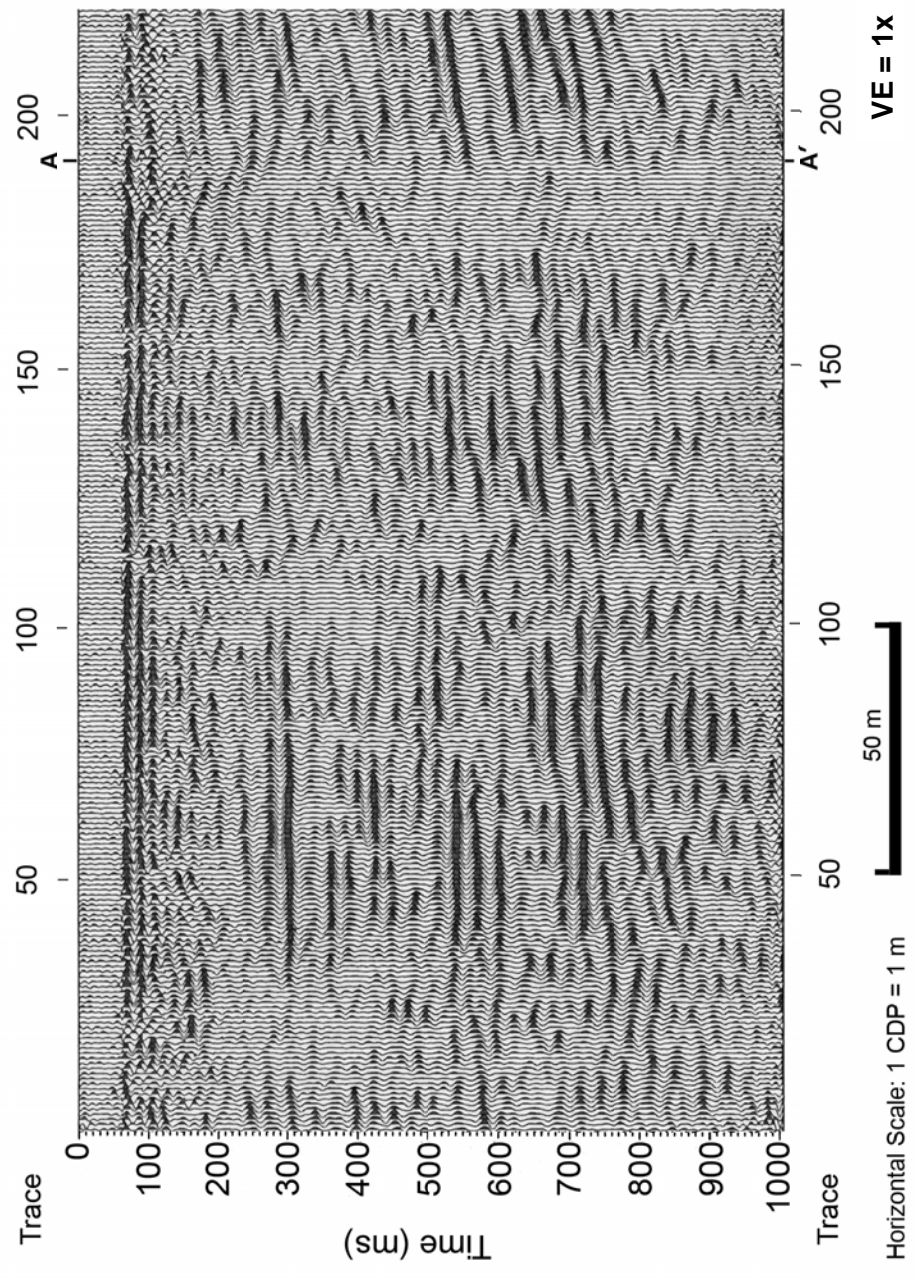


Line UK-I: F-K filtered profile with pre-stack F-K filtering applied

SOUTH

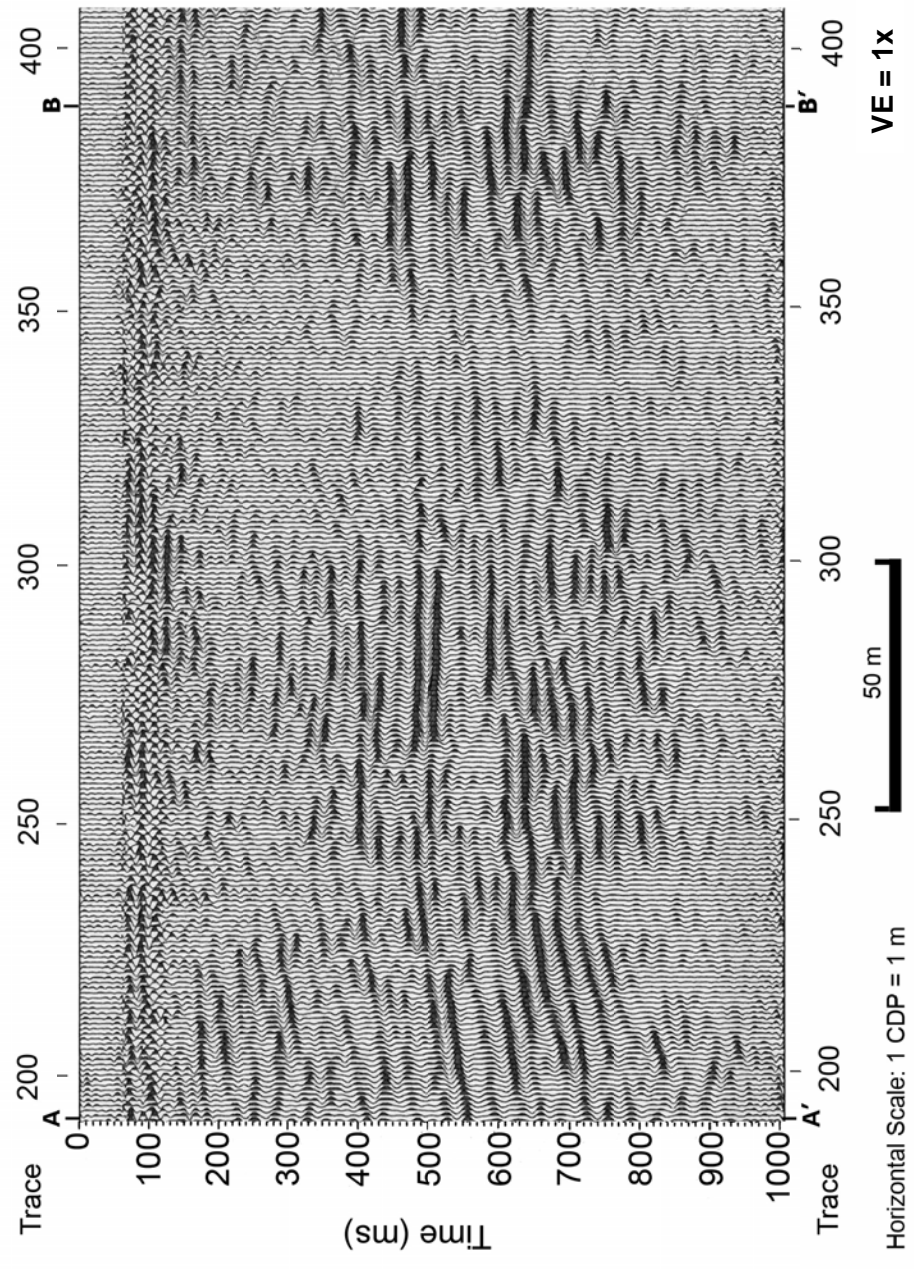
NORTH

Line UK-J



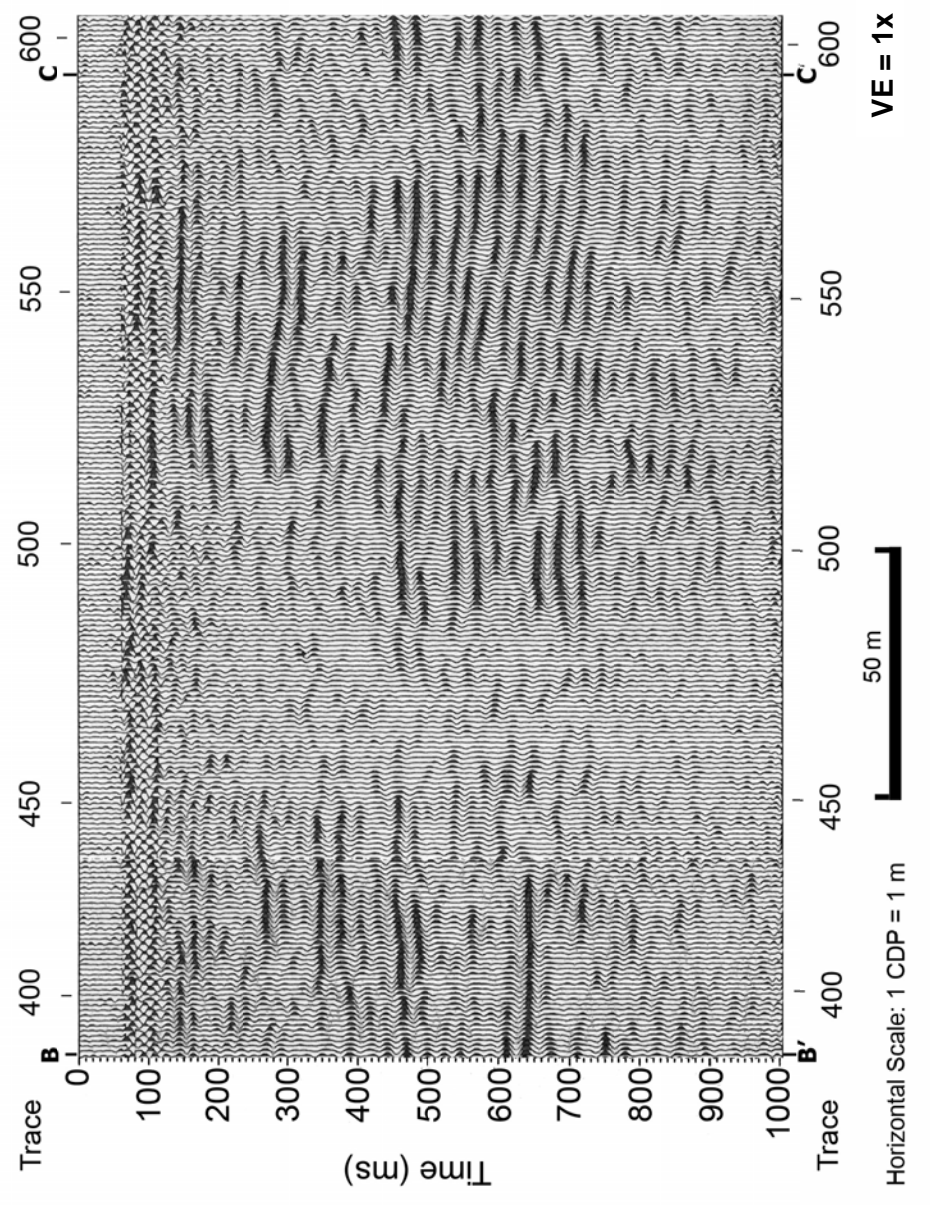
Line UK-J: F-K filtered profile

SOUTH NORTH
Line UK-J



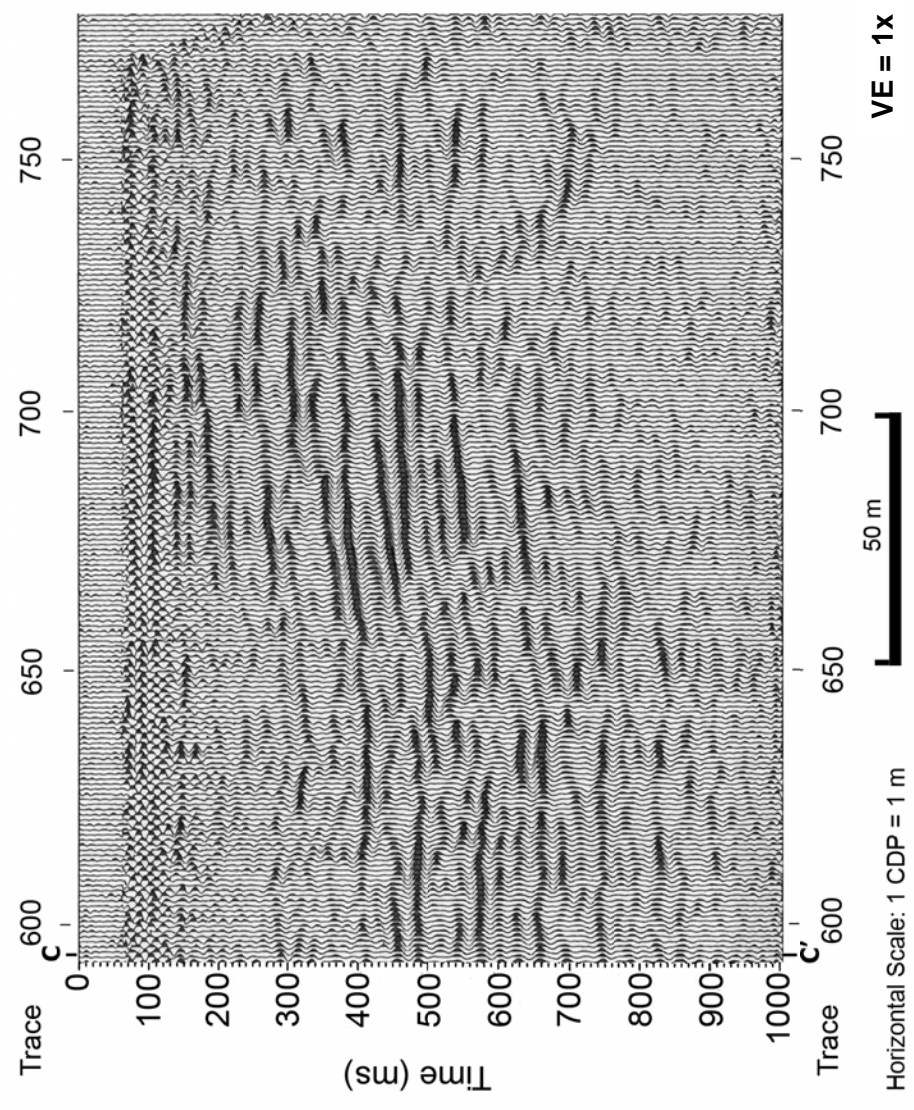
Line UK-J: F-K filtered profile

SOUTH NORTH
Line UK-J

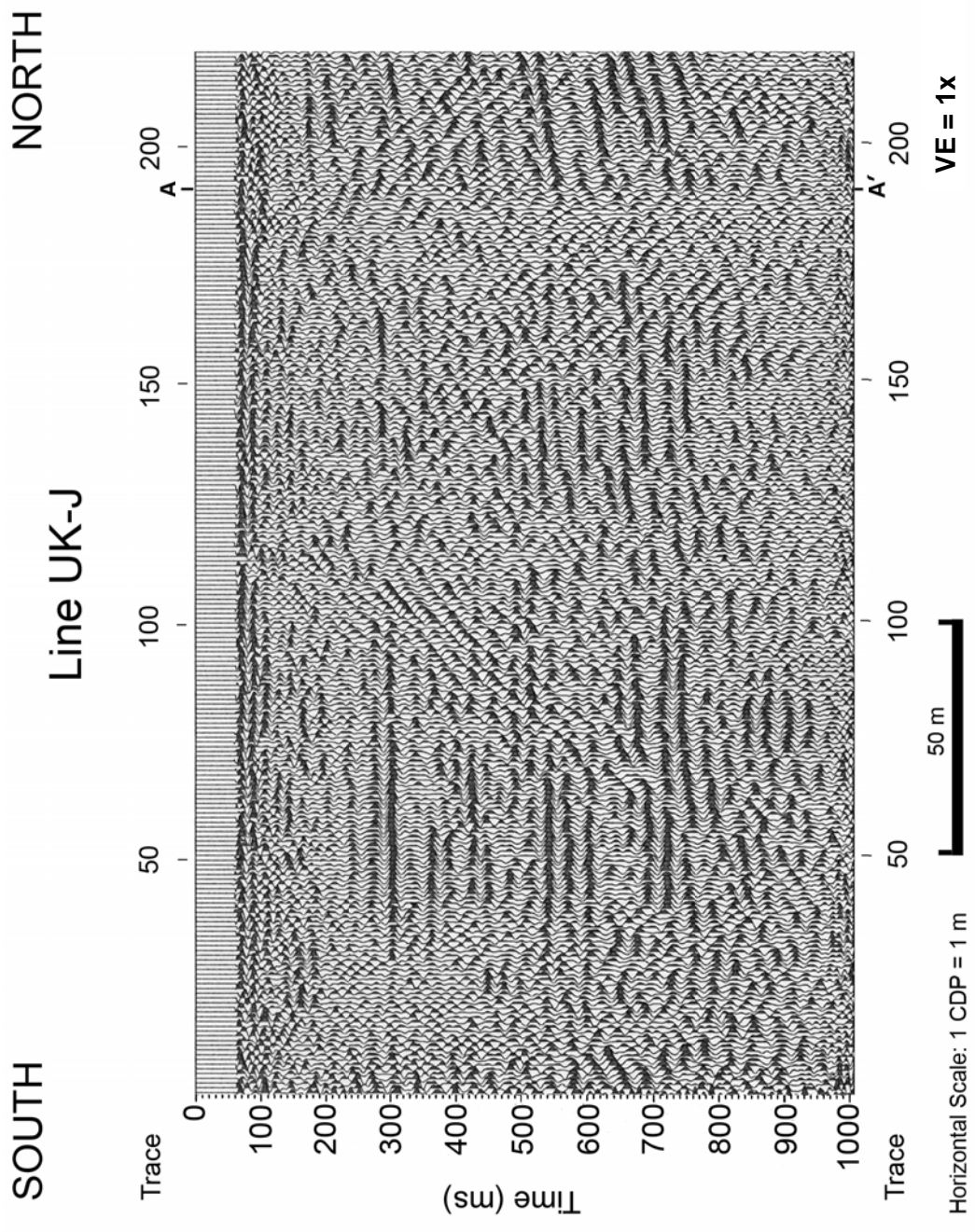


Line UK-J: F-K filtered profile

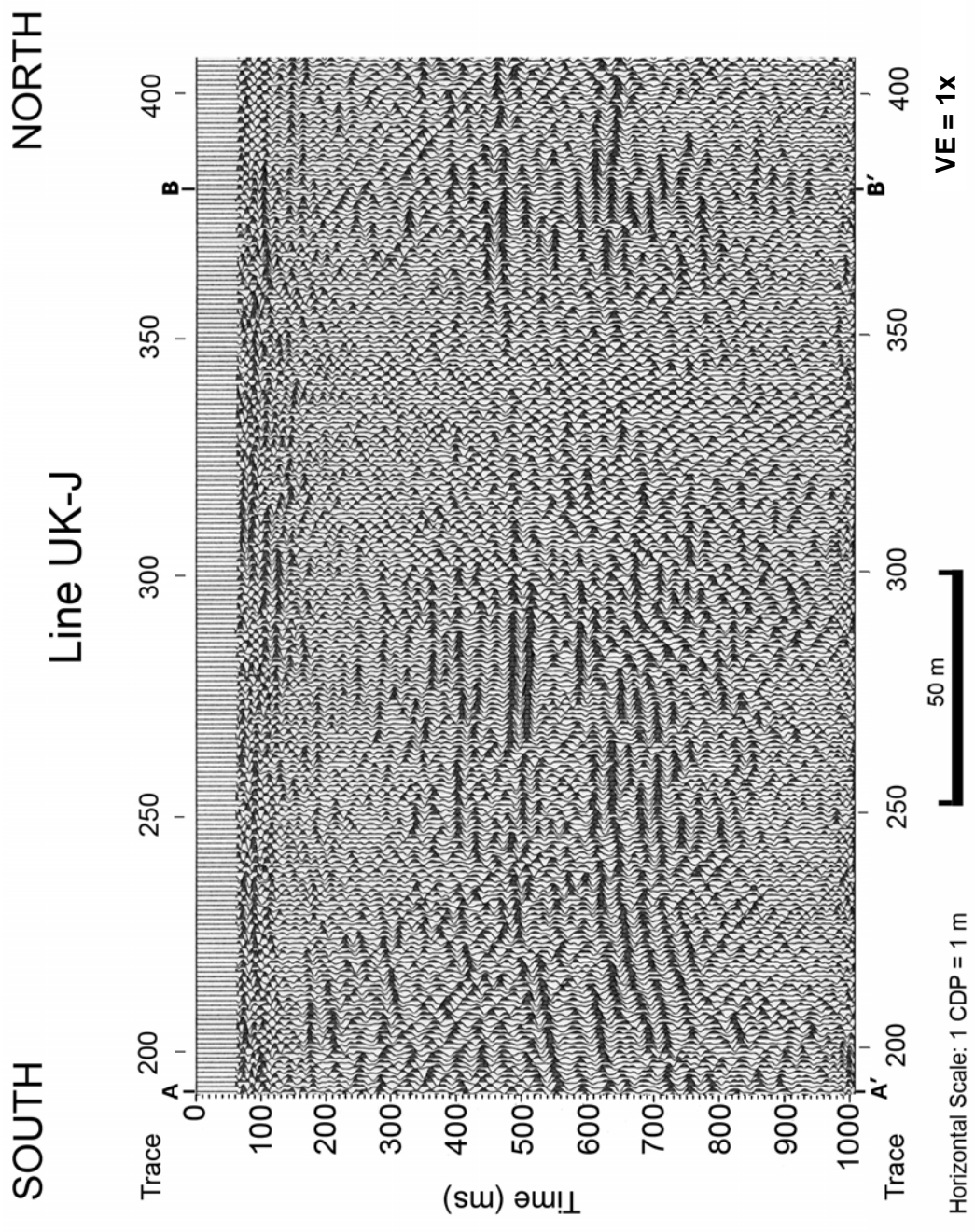
SOUTH NORTH
Line UK-J



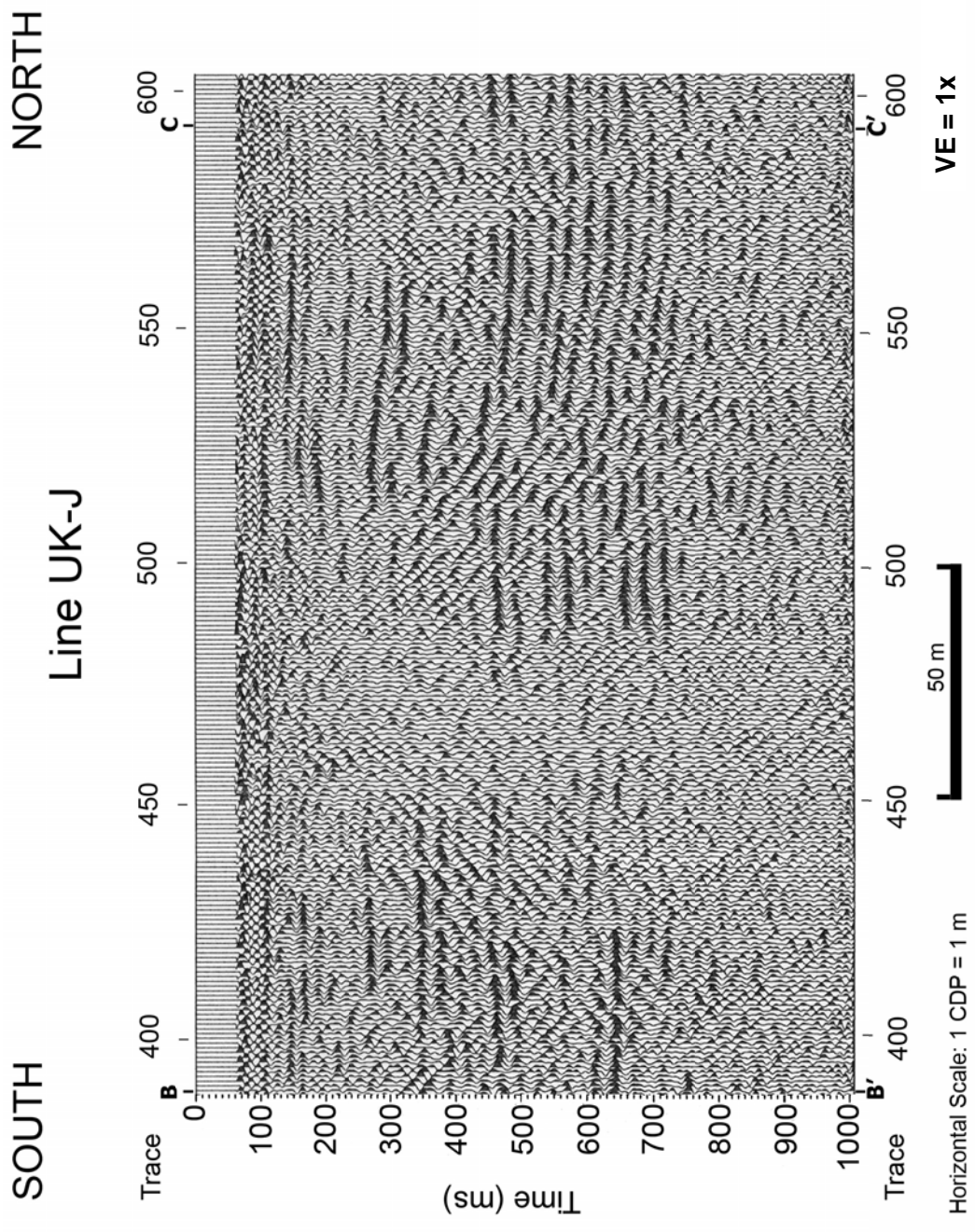
Line UK-J: F-K filtered profile



Line UK-J: F-K filtered profile with surface consistent statics applied

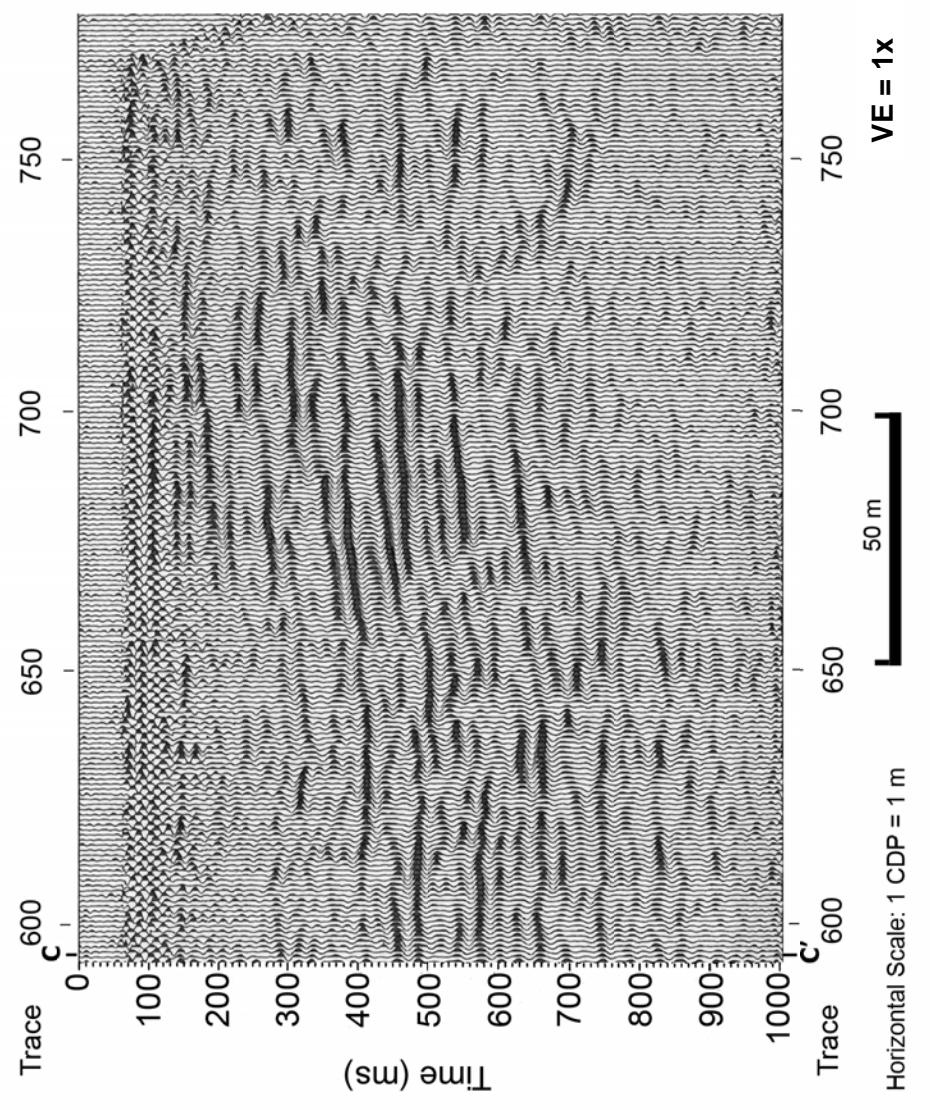


Line UK-J: F-K filtered profile with surface consistent statics applied



Line UK-J: F-K filtered profile with surface consistent statics applied

SOUTH NORTH
Line UK-J



Line UK-J: F-K filtered profile with surface consistent statics applied

Appendix A

Section 2

Detailed processing procedure of seismic reflection data. The following commands are for 12-channel data sets only. Raw and partially processed 12 and 24-channel data are shown in section 3 of appendix A.

Line UK-A3: Processing Commands for Vista 7.0

- 1) MACRO A3spec.mac
- 2) MACRO A348_24.mac
- 3) MACRO A324_12.mac
- 4) COMB put a A312.cmb
- 5) GAIN a put b 8
- 6) MEAN b put c 1.00
- 7) FILT c put d 15 25 60 70
- 8) AGC d put e 300 1.0
- 9) DEL a to d
- 10) MOVE e put a 0 1000 0
- 11) DEL e
- 12) GEOM A3geo.sgy A3geo
- 13) HEAD A3geo.sgy put a
- 14) SET MOUSE ON
- 15) IKIL a 12
- 16) SAVE a put A3kil.sgy f
- 17) IMUT a 12
- 18) SAVE a put A3mut.sgy f
- 19) SORT a[1-288] put b offsetput b[4609-4896] offset
- 20) STACK b put j offset....
- 21) SEMB j put r 100 1500 25....
- 22) VPICK j and r put A3vel.dat....
- 23) DEL b to y

- 24) NMO a put b A3vel.dat m 5
- 25) SAVE b put A3nmo.sgy f
- 26) SORT b put c cdp
- 27) STACK c put d cdp
- 28) SAVE d put A3stk.sgy f
- 29) AGC d put e 125 1.0
- 30) FKFIL e put f 15 70 -24 1.0
- 31) SAVE f put A3fkfil.sgy f
- 32) AGC f put g 150 1.0
- 33) SAVE g put A3fkagc.sgy f
- 34) MCORR c with g put h and i 100 700 10 15 25 60 70 A3.st1
- 35) ITERATE A3.st1 A3.st2 3
- 36) ASTAT c put j A3.st2
- 37) SORT j put k cdp
- 38) STACK k put l cdp
- 39) SAVE l put A3ast.sgy f

Line UK-B: Processing Commands for Vista 7.0

- 1) MACRO Bspec.mac
- 2) CREATE a[1-48] 0.5 0 1000 t
- 3) SAVE a put 48009.sgy f
- 4) SAVE a put 48221.sgy f
- 5) SAVE a put 48346.sgy f
- 6) DEL a
- 7) MACRO B48_24.mac
- 8) MACRO B24_12.mac
- 9) COMB put a B12.cmb
- 10) GAIN a put b 8
- 11) MEAN b put c 1.00
- 12) FILT c put d 20 30 60 70
- 13) AGC d put e 175 1.0
- 14) DEL a to d
- 15) MOVE e put a 0 1000 0
- 16) DEL e
- 17) GEOM Bgeo.sgy Bgeo
- 18) HEAD Bgeo.sgy put a
- 19) SET MOUSE ON
- 20) IKIL a 12
- 21) SAVE a put Bkil.sgy f
- 22) IMUT a 12
- 23) SAVE a put Bmut.sgy f

- 24) SORT a[1-288] put b offsetput a[4609-4896] offset
- 25) STACK b put j offset....
- 26) SEMB j put r 100 1500 25....
- 27) VPICK j and r put Bvel.dat....
- 28) DEL b to y
- 29) NMO a put b Bvel.dat m 5
- 30) SAVE b put Bnmo.sgy f
- 31) SORT b put c cdp
- 32) STACK c put d cdp
- 33) SAVE d put Bstk.sgy f
- 34) AGC d put e 100 1.0
- 35) FKFIL e put f 20 70 -24 1.0
- 36) SAVE f put Bkfil.sgy f
- 37) AGC f put g 100 1.0
- 38) SAVE g put Bfkagc.sgy f

Line UK-G1: Processing Commands for Vista 7.0

- 1) MACRO G1spec.mac
- 2) CREATE a[1-48] 0.5 0 1000 t
- 3) SAVE a put 48356.sgy f
- 4) SAVE a put 48357.sgy f
- 5) DEL a
- 6) MACRO G48_241.mac
- 7) MACRO G24_121.mac
- 8) COMB put a G121.cmb
- 9) GAIN a put b 8
- 10) MEAN b put c 1.00
- 11) FILT c put d 25 35 50 60
- 12) AGC d put e 225 1.0
- 13) DEL a to d
- 14) MOVE e put a 0 1000 0
- 15) DEL e
- 16) GEOM Ggeo.sgy Ggeo
- 17) HEAD Ggeo.sgy put a
- 18) SET MOUSE ON
- 19) IKIL a 12
- 20) SAVE a put Gkil.sgy f
- 21) IMUT a 12
- 22) SAVE a put Gmut2.sgy f
- 23) SORT a[1-288] put b offsetput e[7777-8064] offset

- 24) STACK b put j offset....
- 25) SEMB j put r 100 1500 25....
- 26) VPICK j and r put Gvel.dat....
- 27) DEL b to y
- 28) NMO a put b Gvel.dat m 5
- 29) SAVE b put Gnmo.sgy f
- 30) SORT b put c cdp
- 31) STACK c put d cdp
- 32) SAVE d put Gstk.sgy f
- 33) FKFIL d put e 25 60 -24 1.0
- 34) SAVE e put Gfkfil.sgy f
- 35) AGC e put f 150 1.0
- 36) SAVE f put Gfkagc.sgy f

Line UK-G2: Processing Commands for Vista 7.0

- 1) MACRO Gspec2.mac
- 2) CREATE a[1-48] 0.5 0 1000 t
- 3) SAVE a put 48913b.sgy f
- 4) DEL a
- 5) MACRO G48_242.mac
- 6) MACRO G24_122.mac
- 7) COMB put a G122.cmb
- 8) GAIN a put b 8
- 9) MEAN b put c 1.00
- 10) FILT c put d 25 35 50 60
- 11) AGC d put e 225 1.0
- 12) DEL a to d
- 13) MOVE e put a 0 1000 0
- 14) DEL e
- 15) GEOM G2geo.sgy G2geo
- 16) HEAD G2geo.sgy put a
- 17) SET MOUSE ON
- 18) IKIL a 12
- 19) SAVE a put G2kil.sgy f
- 20) IMUT a 12
- 21) SAVE a put G2mut.sgy f
- 22) SORT a[1-288] put b offsetput i[2017-2304] offset
- 23) STACK b put j offset....

- 24) SEMB j put r 100 1500 25....
- 25) VPICK j and r put Bvel.dat....
- 26) DEL b to y
- 27) NMO a put b G2vel.dat m 5
- 28) SAVE b put G2nmo.sgy f
- 29) SORT b put c cdp
- 30) STACK c put d cdp
- 31) SAVE d put G2stk.sgy f
- 32) AGC d put e 100 1.0
- 33) SAVE e put G2stkagc.sgy f
- 34) FKFIL e put f 25 60 -24 1.0
- 35) SAVE f put G2fkfil.sgy f
- 36) AGC f put g 150 1.0
- 37) SAVE g put G2fkagc.sgy f

Line UK-H: Processing Commands for Vista 7.0

- 1) MACRO Hspec.mac
- 2) MACRO H48_24.mac
- 3) MACRO H24_12.mac
- 4) COMB put a H12.cmb
- 5) GAIN a put b 8
- 6) MEAN b put c 1.00
- 7) FILT c put d 15 25 85 95
- 8) AGC d put e 100 1.0
- 9) DEL a to d
- 10) MOVE e put a 0 1024 0
- 11) DEL e
- 12) GEOM Hgeo.sgy Hgeo
- 13) HEAD Hgeo.sgy put a
- 14) SET MOUSE ON
- 15) IKIL a 12
- 16) SAVE a put Hkil.sgy f
- 17) IMUT a 12
- 18) SAVE a put Hmut.sgy f
- 19) SORT a[1-288] put b offsetput e[2737-2880] offset
- 20) STACK b put j offset....
- 21) SEMB j put r 100 1500 25....
- 22) VPICK j and r put Hvel.dat....
- 23) DEL b to y

- 24) NMO a put b Hvel.dat m 15
- 25) SAVE b put Hnmo.sgy f
- 26) SORT b put c cdp
- 27) STACK c put d cdp
- 28) SAVE d put Hstk.sgy f
- 29) FKFIL d put e 15 100 -24 1.0
- 30) SAVE e put Hkfil.sgy f
- 31) MCORR c with e put f and g 80 700 10 15 25 85 95 H.st1
- 32) ITERATE H.st1 H.st2 3
- 33) ASTAT c put h H.st2
- 34) SORT h put i cdp
- 35) STACK i put j cdp
- 36) SAVE j put Hast.sgy f

Line UK-I: Processing Commands for Vista 7.0

- 1) MACRO BRspec.mac
- 2) CREATE a[1-48] 0.25 0 1024 t
- 3) SAVE a put 48001.sgy f
- 4) DEL a
- 5) MACRO BR48_24.mac
- 6) MACRO BR24_12.mac
- 7) COMB put a BR12.cmb
- 8) GAIN a put b 8
- 9) MEAN b put c 1.00
- 10) FILT c put d 25 35 65 75
- 11) AGC d put e 150 1.0
- 12) DEL a to d
- 13) MOVE e put a 0 1024 0
- 14) DEL e
- 15) GEOM BRgeo.sgy BRgeo
- 16) HEAD BRgeo.sgy put a
- 17) SET MOUSE ON
- 18) IKIL a 12
- 19) SAVE a put BRkil.sgy f
- 20) IMUT a 12
- 21) SAVE a put BRmut2.sgy f
- 22) SORT a[1-288] put b offsetput h[1729-2016] offset
- 23) STACK b put j offset....

- 24) SEMB j put r 100 1500 25....
- 25) VPICK j and r put BRvel2.dat....
- 26) DEL b to x
- 27) NMO a put b BRvel2.dat m 5
- 28) SAVE b put BRnmo2.sgy f
- 29) SORT b put c cdp
- 30) STACK c put d cdp
- 31) SAVE d put BRstk2.sgy f
- 32) FKFIL d put e 25 100 -24 1.0
- 33) SAVE e put BRfkfil2.sgy f
- 34) AGC e put f 150 1.0
- 35) SAVE f put BRfkagc2.sgy f
- 36) MCORR c with e put g and h 100 700 35 45 70 80 BR2.st1
- 37) ITERATE BR2.st1 BR2.st2 3
- 38) ASTAT c put i BR2.st2
- 39) SORT i put j cdp
- 40) STACK j put k cdp
- 41) SAVE k put BRast2.sgy f

Line UK-J: Processing Commands for Vista 7.0

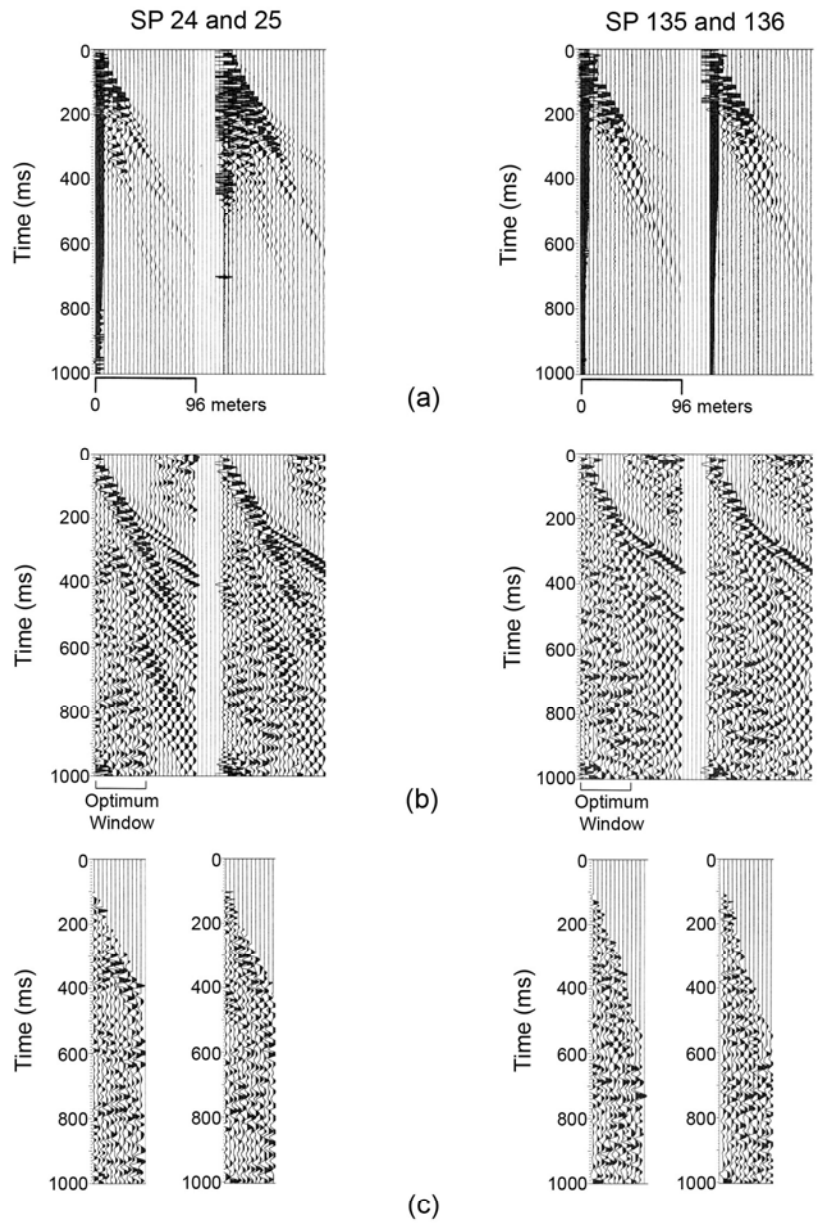
- 1) MACRO BCRspec.mac
- 2) MACRO BCR48_24.mac
- 3) MACRO BCR24_12.mac
- 4) COMB put a BCR12.cmb
- 5) GAIN a put b 8
- 6) MEAN b put c 1.00
- 7) FILT c put d 20 30 80 90
- 8) AGC d put e 120 1.0
- 9) DEL a to d
- 10) MOVE e put a 0 1024 0
- 11) DEL e
- 12) GEOM BCRgeo.sgy BCRgeo
- 13) HEAD BCRgeo.sgy put a
- 14) SET MOUSE ON
- 15) IKIL a 12
- 16) SAVE a put BCRkil.sgy f
- 17) IMUT a 12
- 18) SAVE a put BCRmut.sgy f
- 19) SORT a[1-288] put b offsetput i[4321-4608] offset
- 20) STACK b put j offset....
- 21) SEMB j put r 100 1500 25....
- 22) VPICK j and r put BCRvel.dat....
- 23) DEL b to y

- 24) NMO a put b BCRvel.dat m 10
- 25) SAVE b put BCRnmo.sgy f
- 26) SORT b put c cdp
- 27) STACK c put d cdp
- 28) SAVE d put BCRstk.sgy f
- 29) FKFIL d put e 20 90 -24 1.0
- 30) SAVE e put BCRfkfil.sgy f
- 31) MCORR c with e put f and g 100 700 10 20 30 80 90 BCR.st1
- 32) ITERATE BCR.st1 BCR.st2 3
- 33) ASTAT c put h BCR.st2
- 34) SORT h put i cdp
- 35) STACK i put j cdp
- 36) SAVE j put BCRast.sgy f

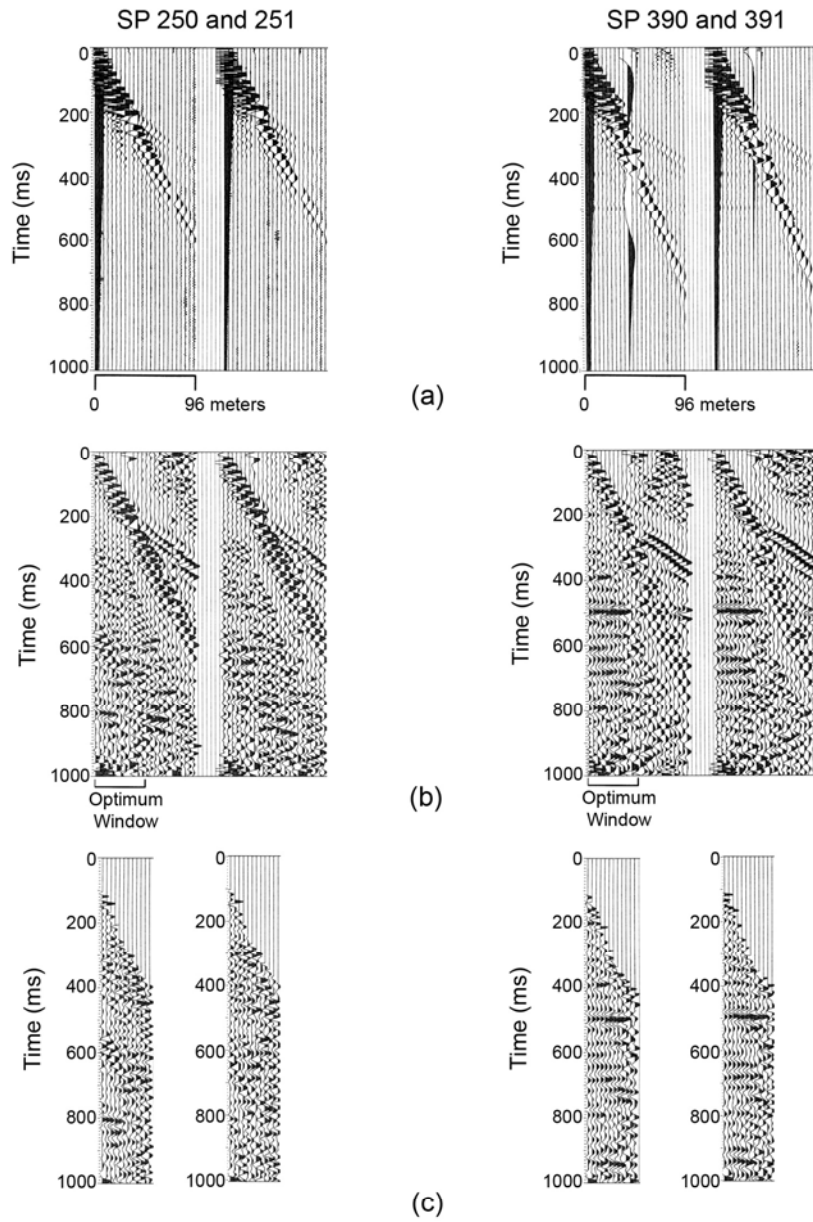
Appendix A

Section 3

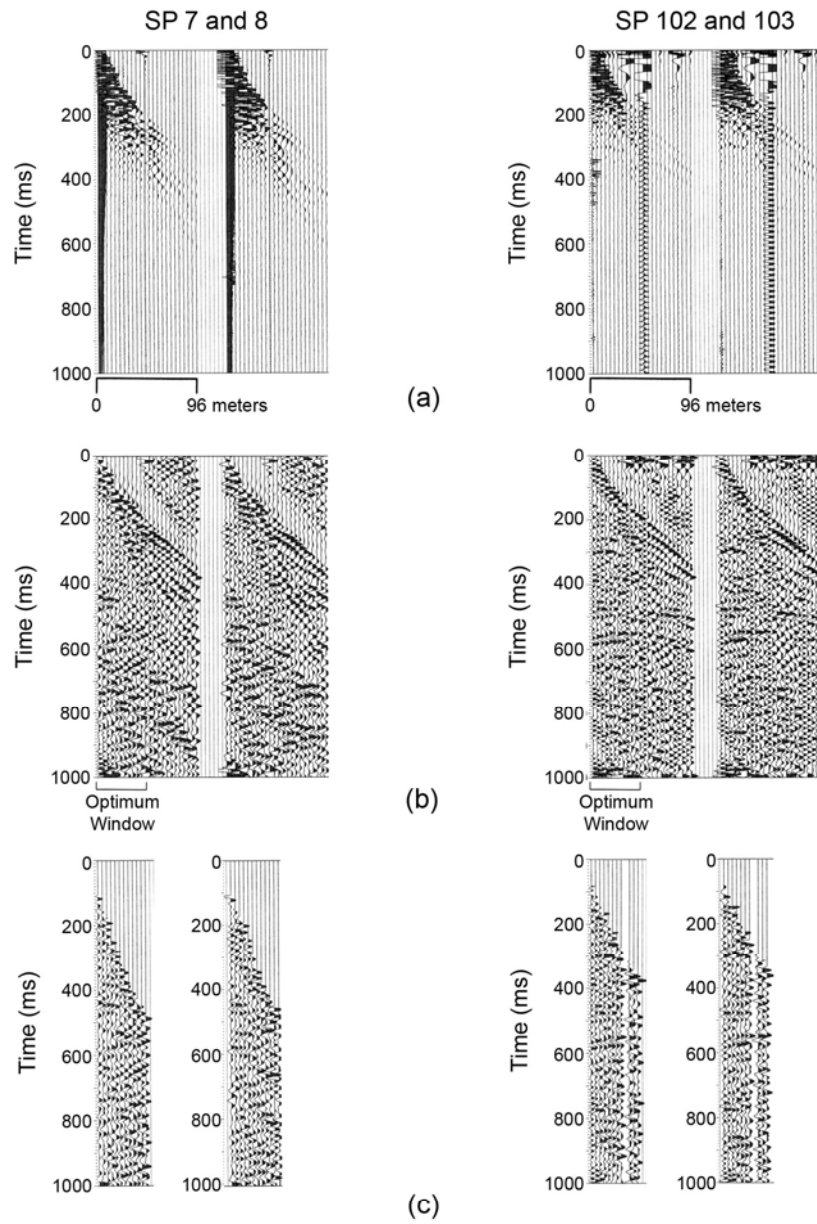
Representative raw 24-channel and partially processed 24- and 12-channel field files from each line processed in this study.



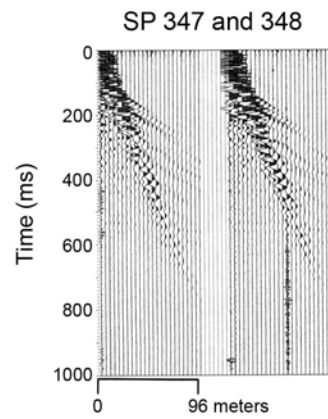
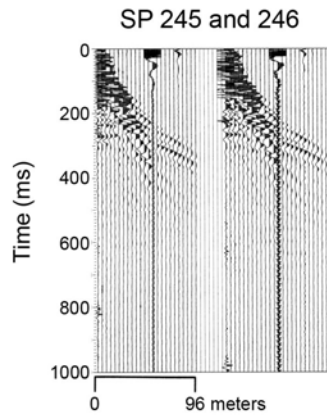
Line UK-A3: (a) raw 24-channel field files, (b) bandpass filtered (25/60) with AGC (250 and 200 ms), and muted files with AGC (300 and 350 ms) from the optimum shear wave time window



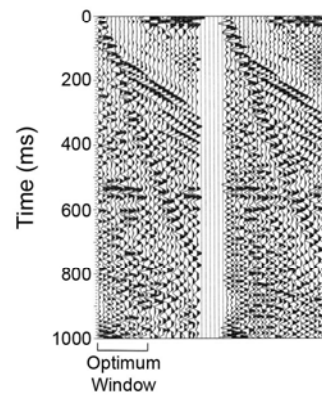
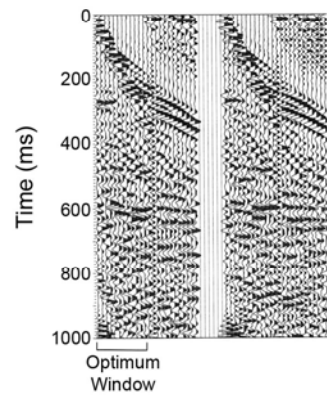
Line UK-A3: (a) raw 24-channel field files, (b) bandpass filtered (25/60) with AGC (250 ms), and muted files with AGC (300 and 250 ms) from the optimum shear wave time window



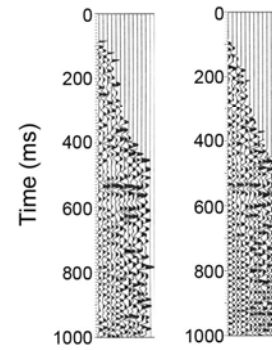
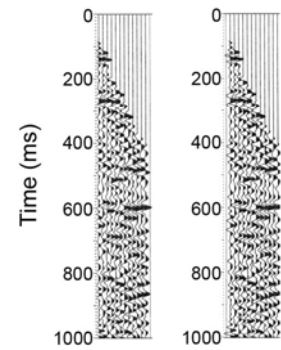
Line UK- B: (a) raw 24-channel field files, (b) bandpass filtered (30/60) with AGC (200 and 150 ms), and muted files with AGC (250 and 200 ms) from the optimum shear wave time window



(a)

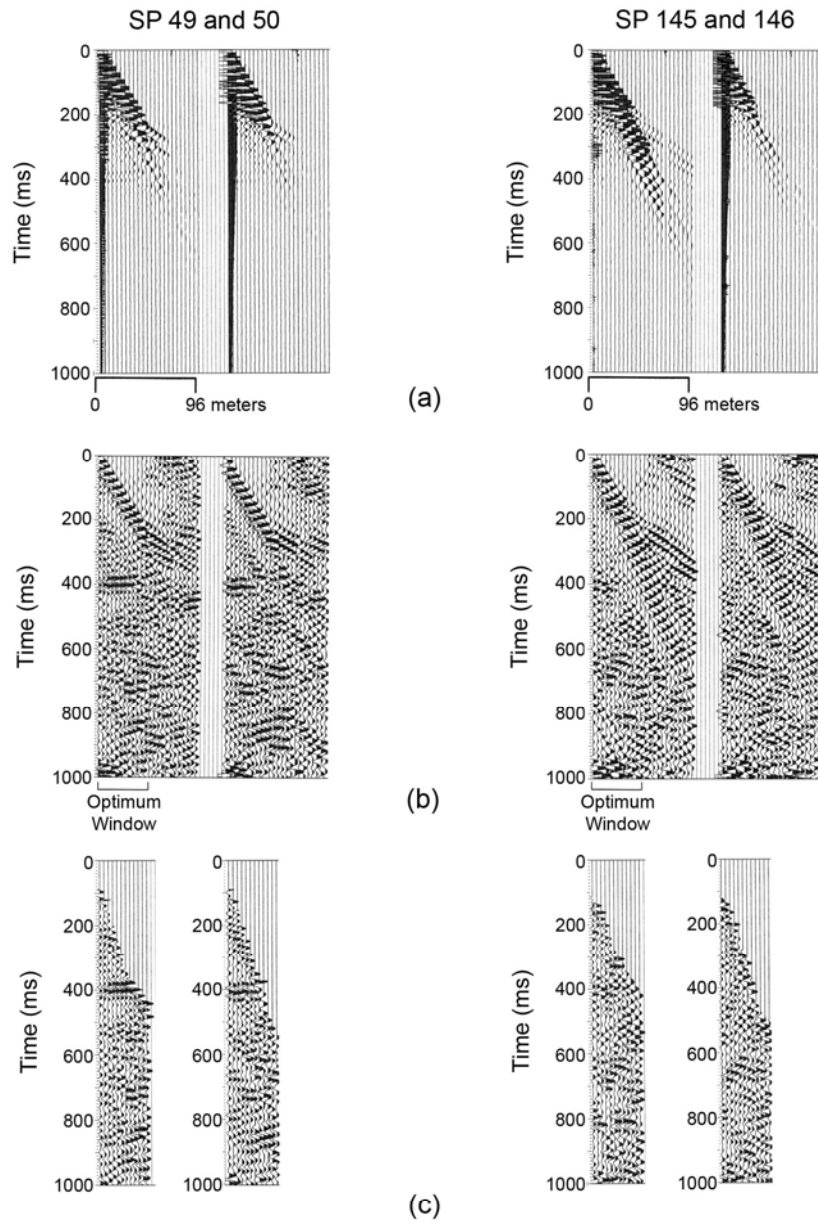


(b)

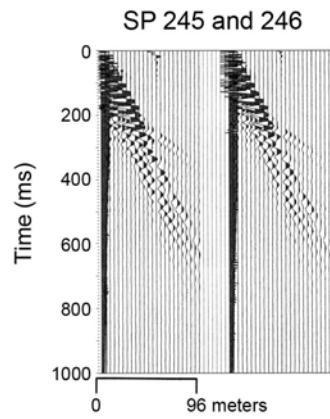


(c)

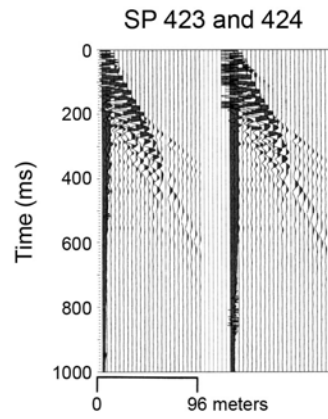
Line UK-B: (a) raw 24-channel field files, (b) bandpass filtered (30/60) with AGC (200 and 175 ms), and muted files with AGC (250 and 150 ms) from the optimum shear wave time window



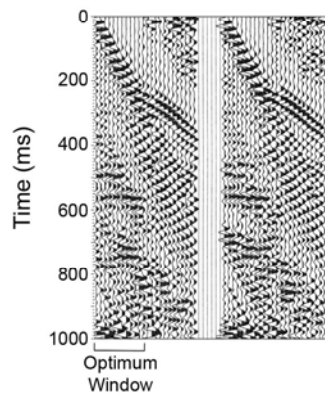
Line UK-G1: (a) raw 24-channel field files, (b) bandpass filtered (35/50) with AGC (175 and 200 ms), and muted files with AGC (250 and 300 ms) from the optimum shear wave time window



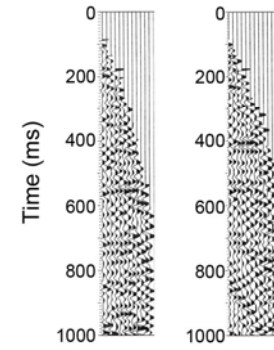
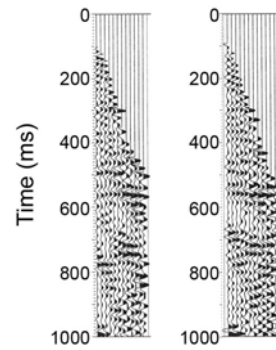
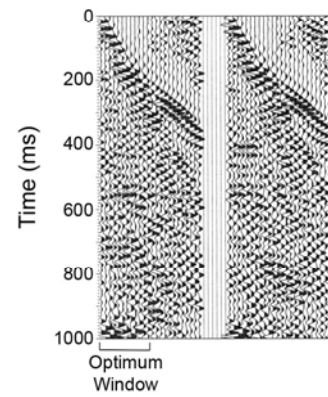
(a)



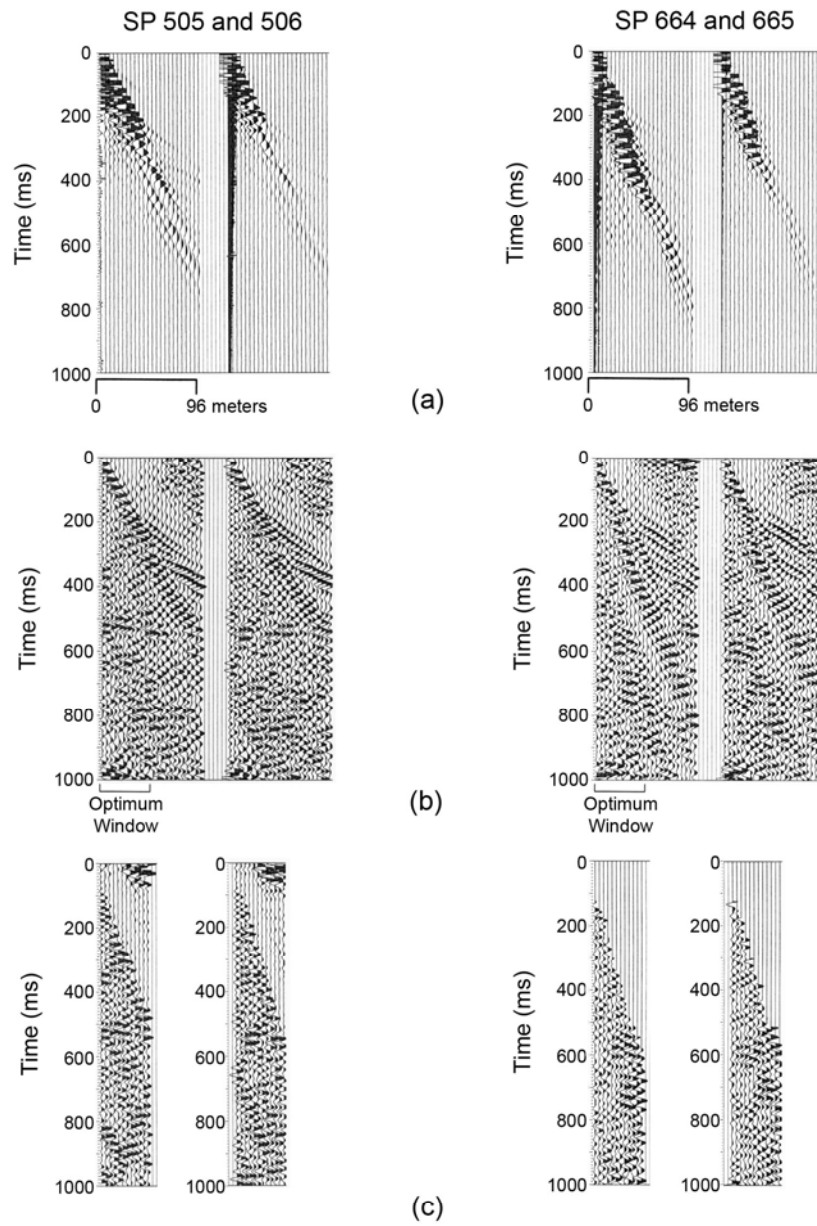
(b)



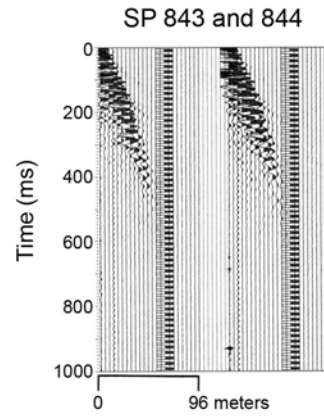
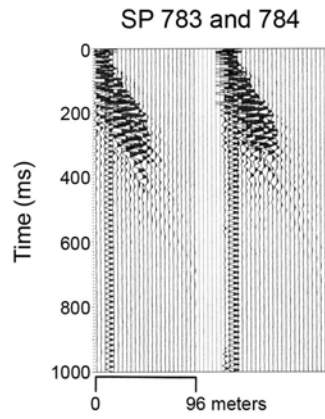
(c)



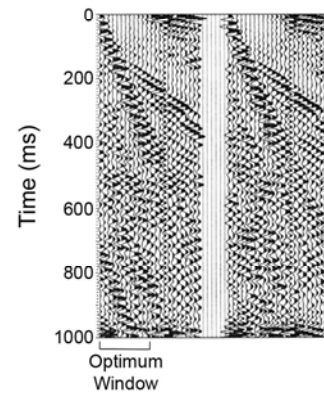
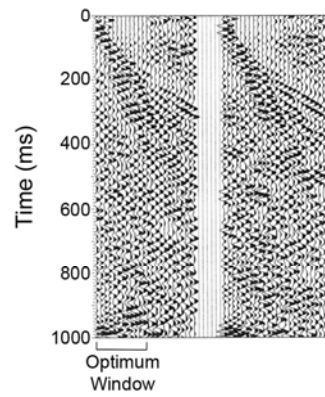
Line UK-G1: (a) raw 24-channel field files, (b) bandpass filtered (35/50) with AGC (200 ms), and muted files with AGC (250 and 150 ms) from the optimum shear wave time window



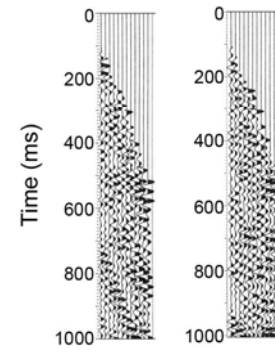
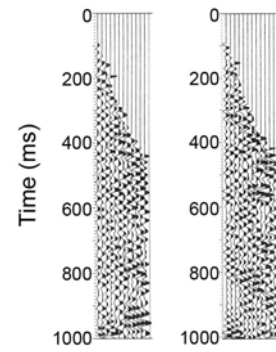
Line UK-G1: (a) raw 24-channel field files, (b) bandpass filtered (35/50) with AGC (175 ms), and muted files with AGC (300 ms) from the optimum shear wave time window



(a)

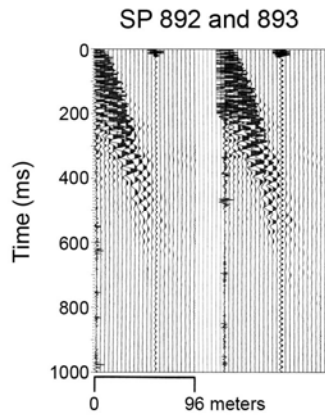


(b)

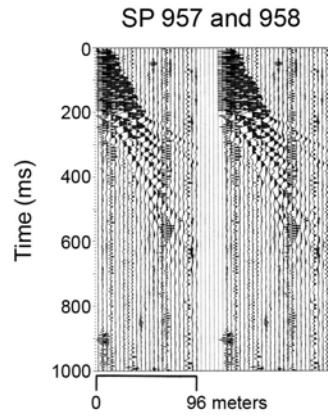


(c)

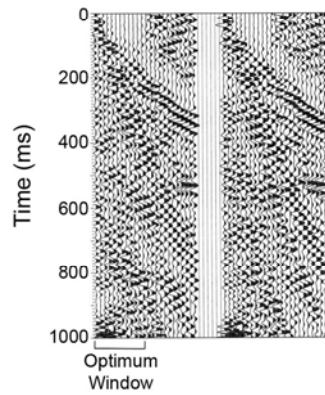
Line UK-G2: (a) raw 24-channel field files, (b) bandpass filtered (35/50) with AGC (175 and 200 ms), and muted files with AGC (300 and 250 ms) from the optimum shear wave time window



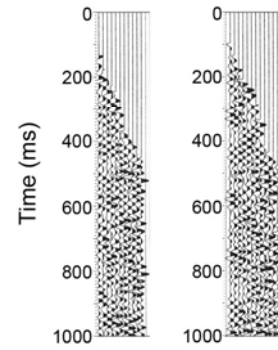
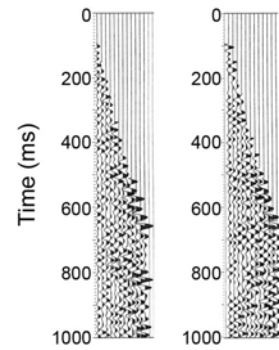
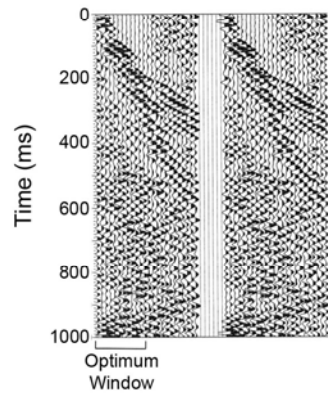
(a)



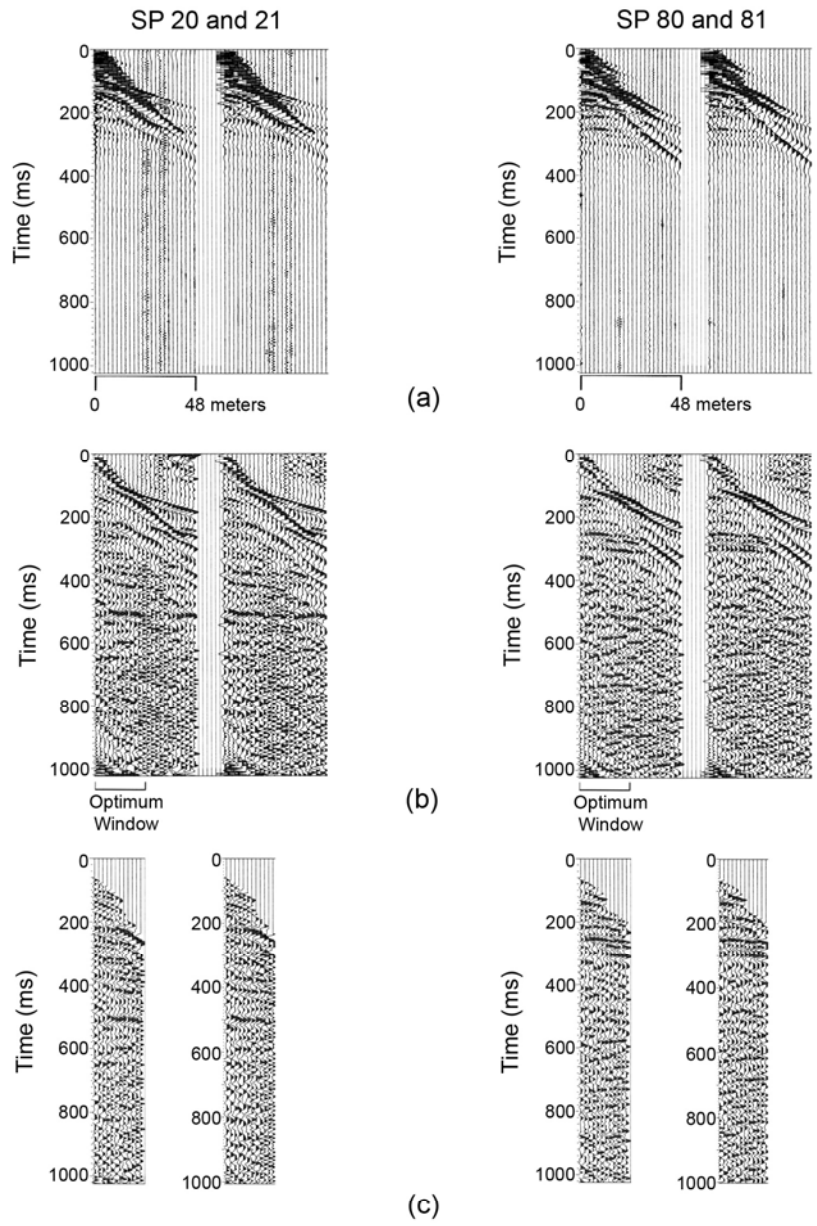
(b)



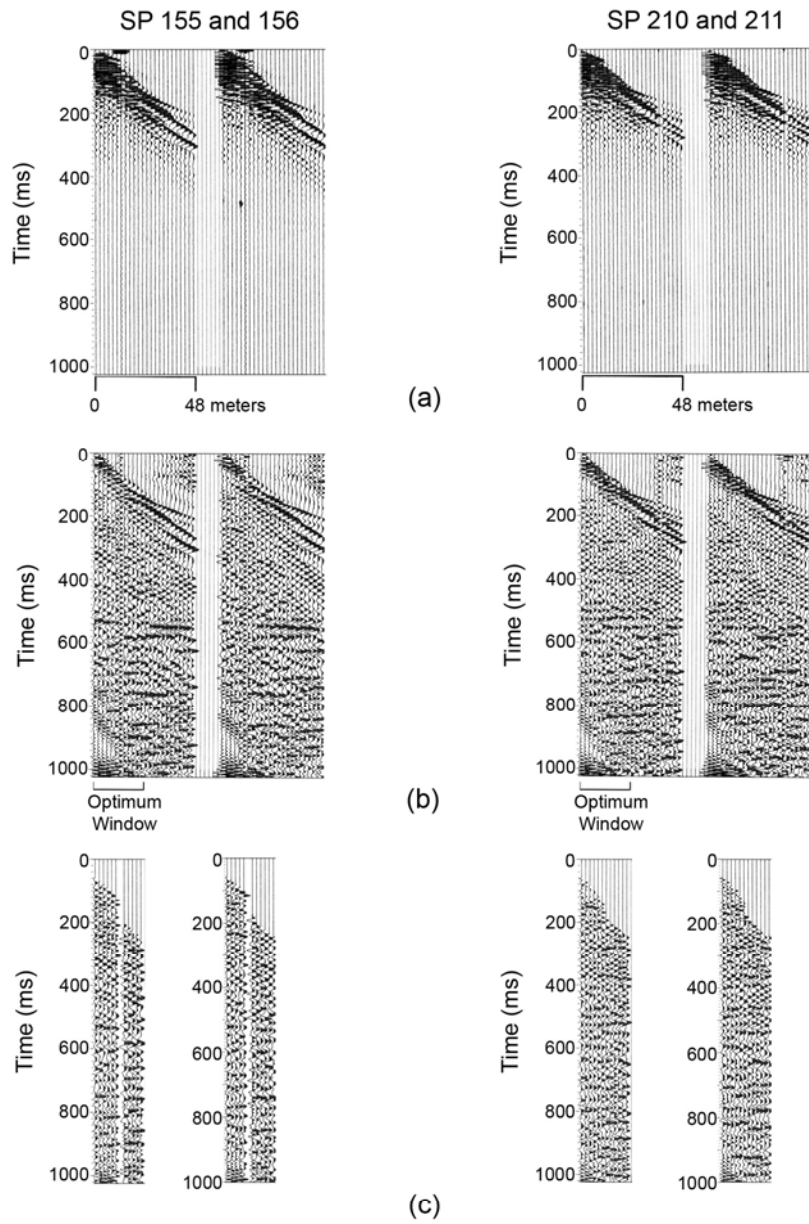
(c)



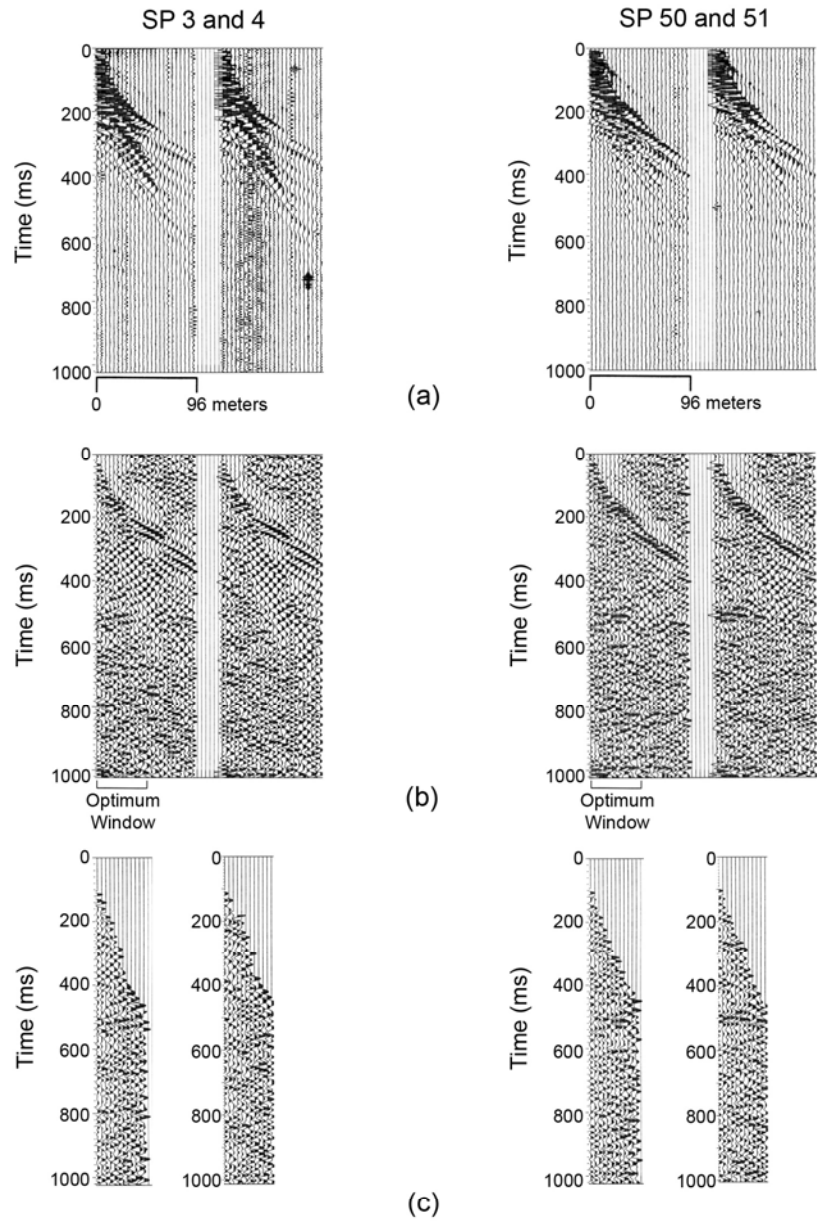
Line UK-G2: (a) raw 24-channel field files, (b) bandpass filtered (35/50) with AGC (200 and 225 ms), and muted files with AGC (200 and 250 ms) from the optimum shear wave time window



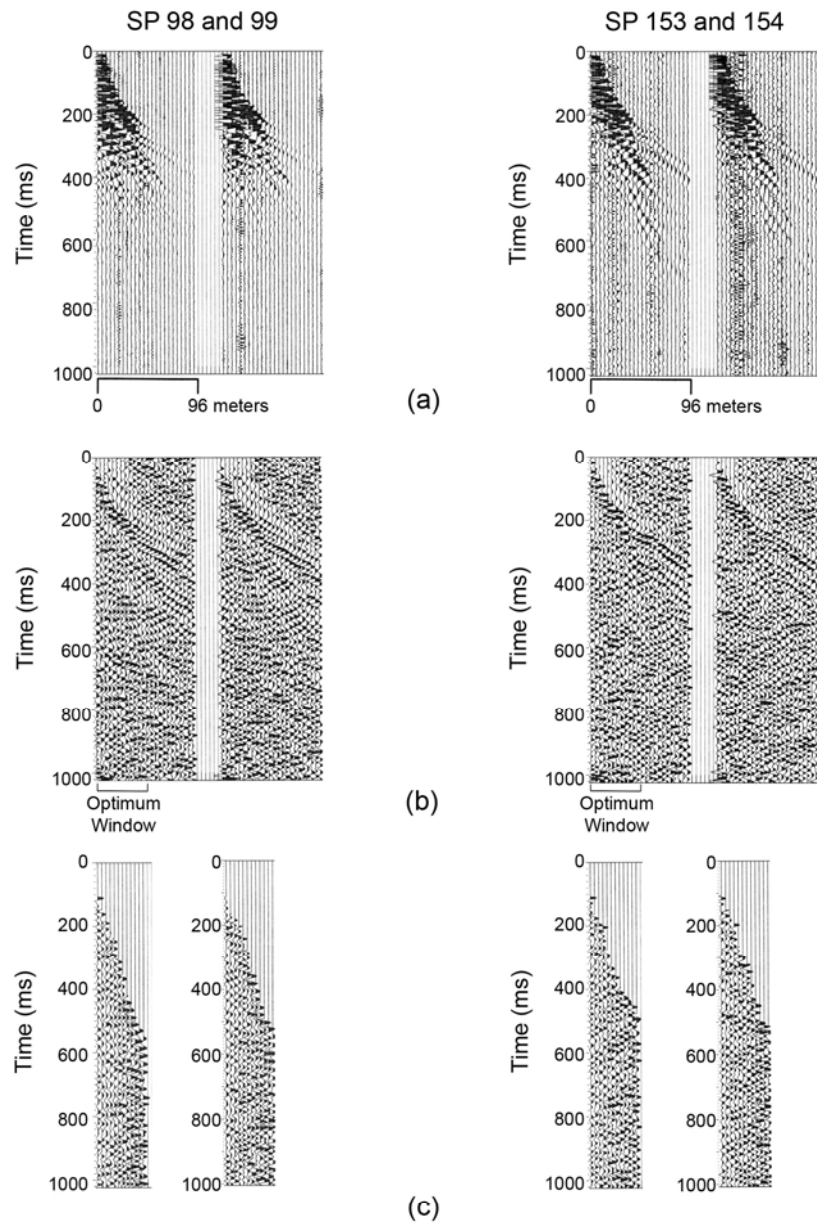
Line UK-H: (a) raw 24-channel field files, (b) bandpass filtered (25/85) with AGC (150 ms), and muted files with AGC (500 and 450 ms) from the optimum shear wave time window



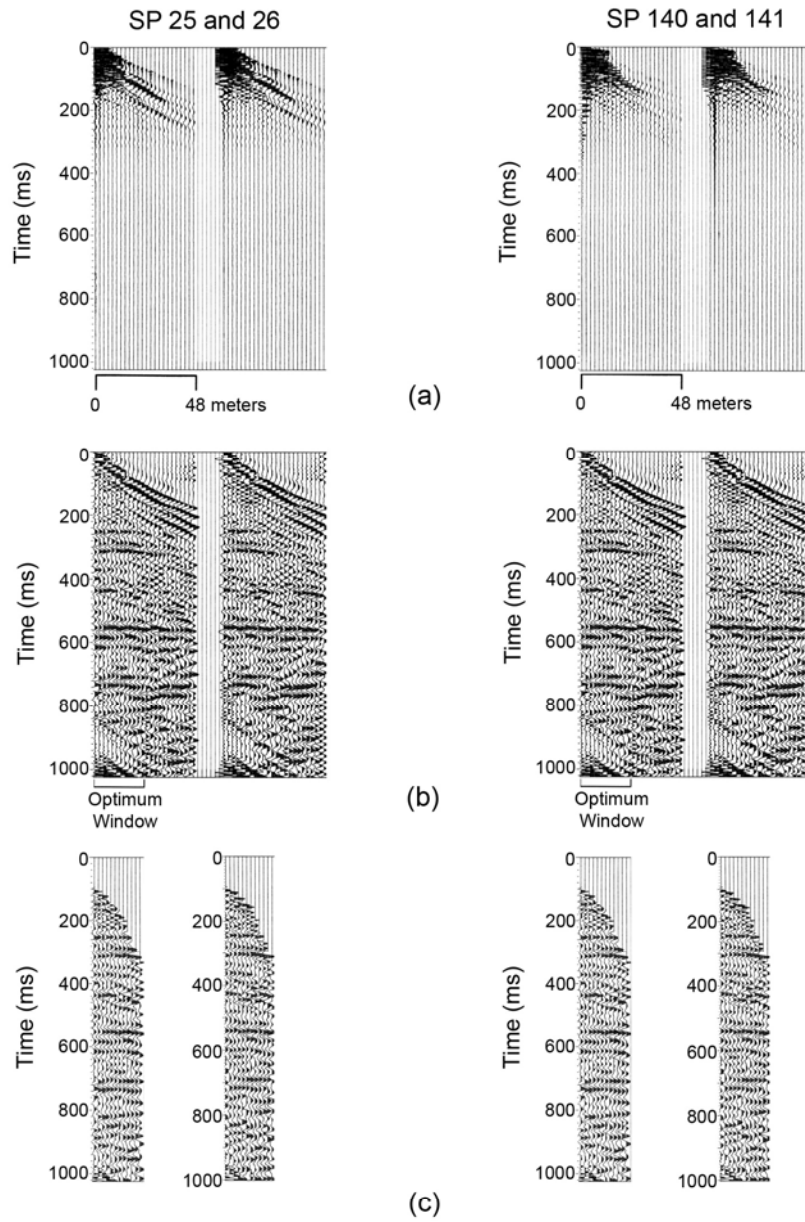
Line UK-H: (a) raw 24-channel field files, (b) bandpass filtered (25/85) with AGC (150 and 175 ms), and muted files with AGC (500 ms) from the optimum shear wave time window



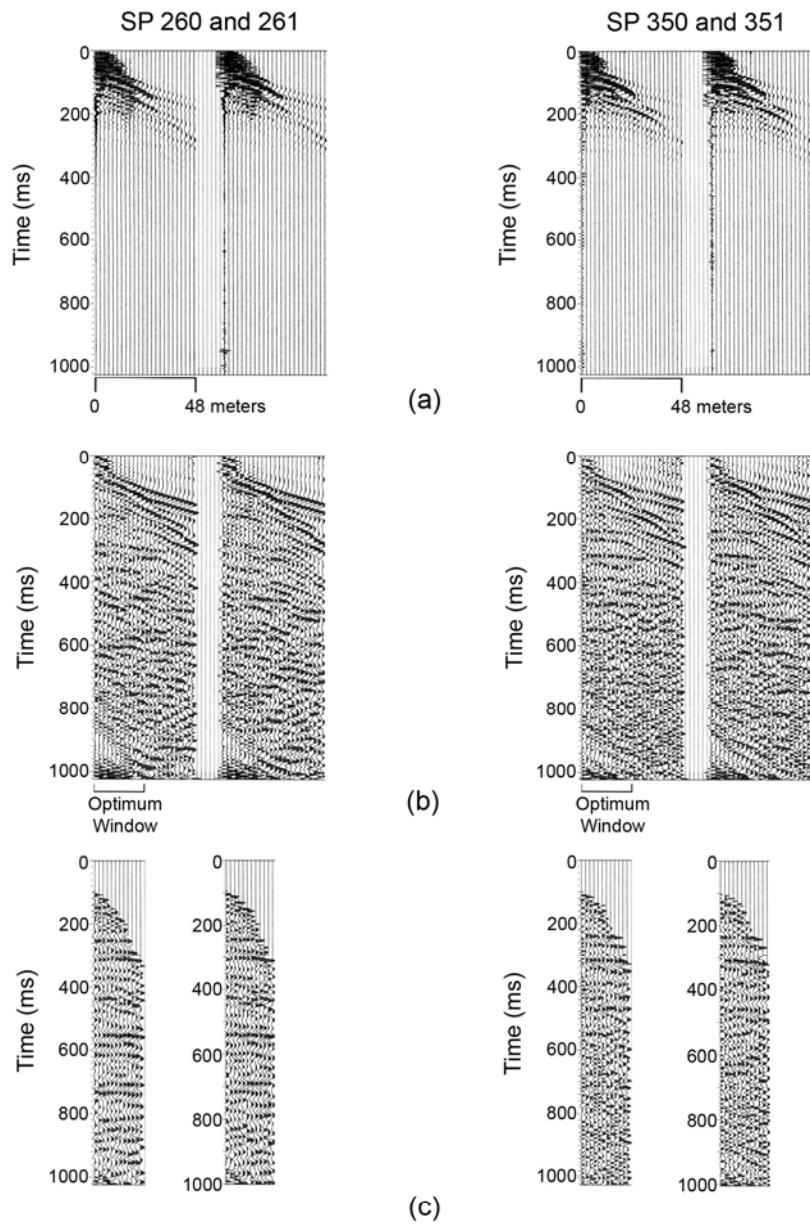
Line UK-I: (a) raw 24-channel field files, (b) bandpass filtered (35/65) with AGC (150 ms), and muted files with AGC (200 ms) from the optimum shear wave time window



Line UK-I: (a) raw 24-channel field files, (b) bandpass filtered (35/65) with AGC (125 and 150 ms), and muted files with AGC (150 ms) from the optimum shear wave time window



Line UK-J: (a) raw 24-channel field files, (b) bandpass filtered (30/80) with AGC (175 and 125 ms), and muted files with AGC (150 and 200 ms) from the optimum shear wave time window



Line UK- J: (a) raw 24-channel field files, (b) bandpass filtered (30/80) with AGC (150 and 125 ms), and muted files with AGC (200 ms) from the optimum shear wave time window

APPENDIX B

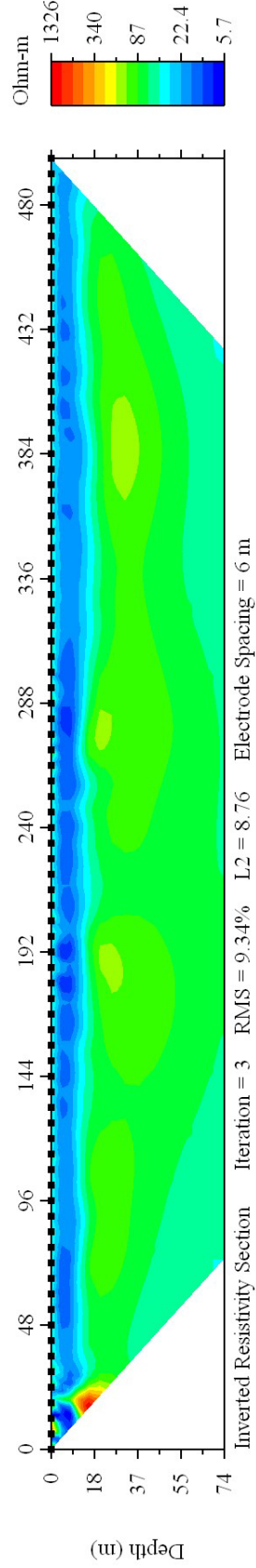
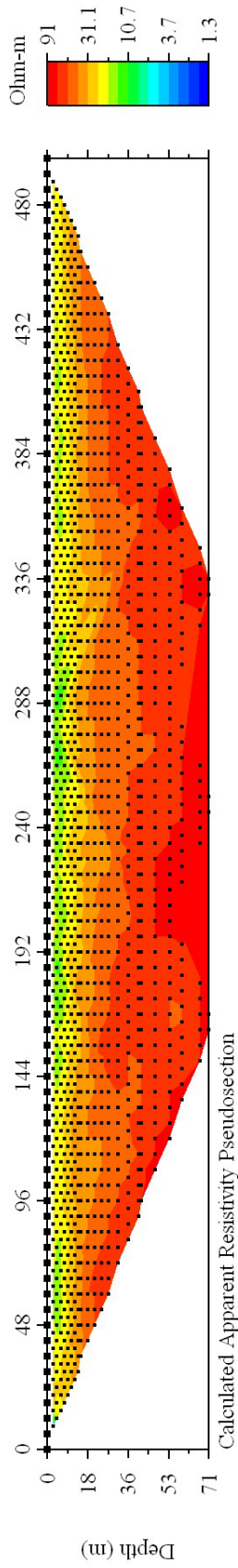
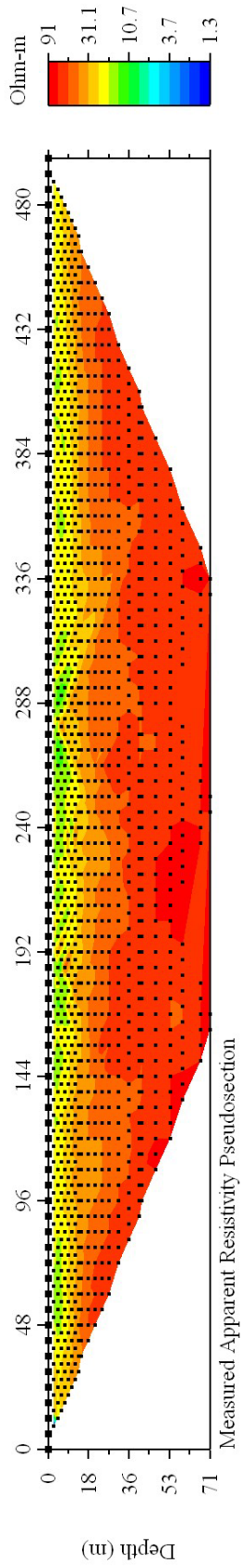
Appendix B

Section 1

Uninterpreted electrical resistivity imaging profiles. The top profile depicts the apparent resistivity pseudosection measured in the field, the middle profile depicts the apparent resistivity pseudosection calculated from the model, and the bottom profile represents true earth resistivities associated with the calculated pseudosection. Profiles are shown with no misfit data removed and data with relative misfit from 10% to 21% removed. Profiles are shown with the resistivity scales which best demonstrates vertical and horizontal changes in subsurface resistivity while representing all measured values.

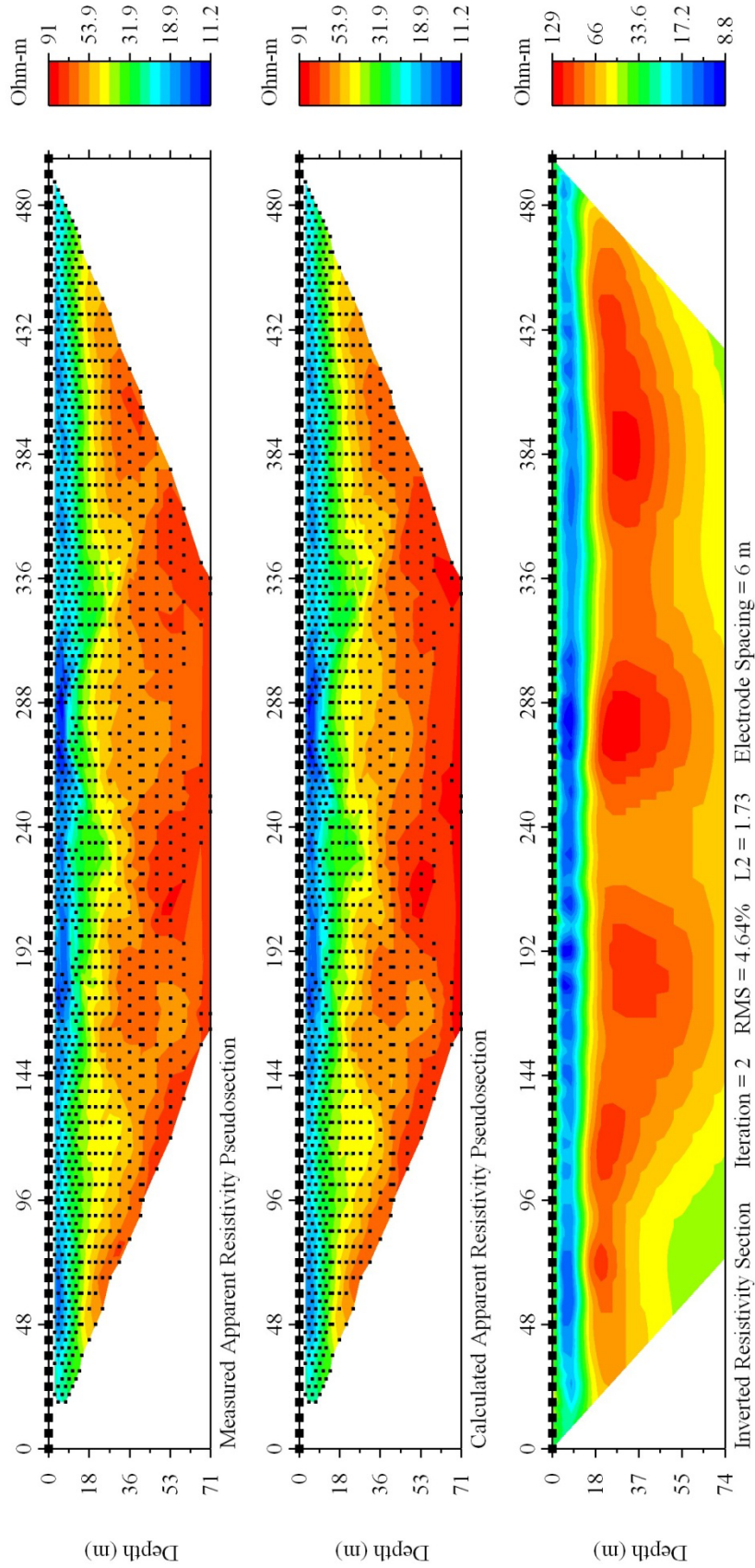
LINE UK-001

No Misfit Data Removed



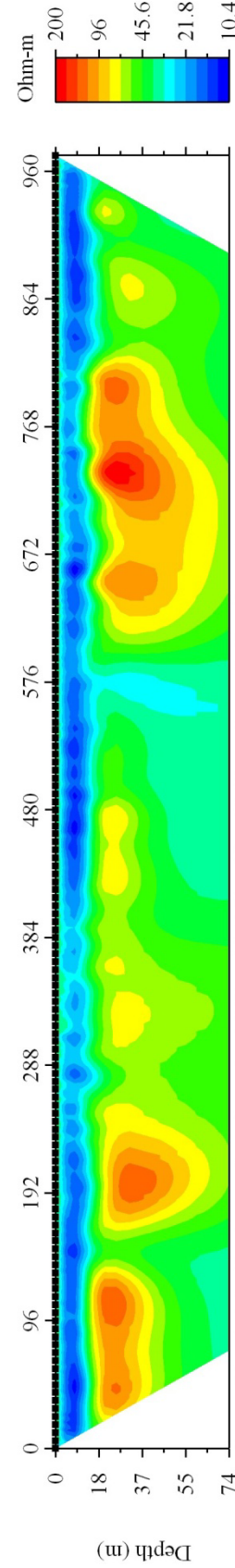
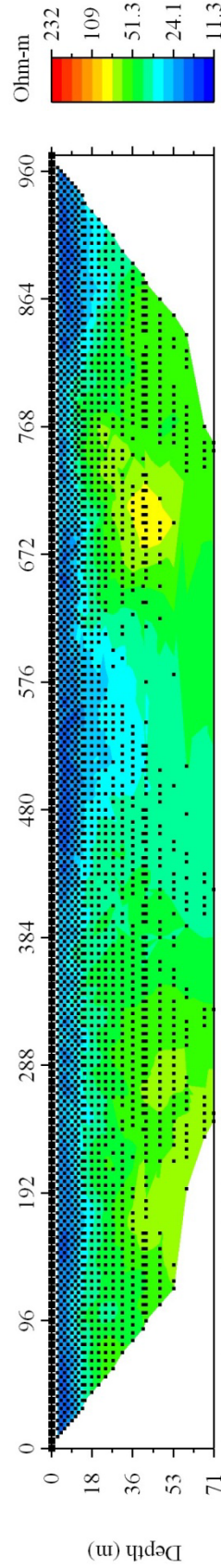
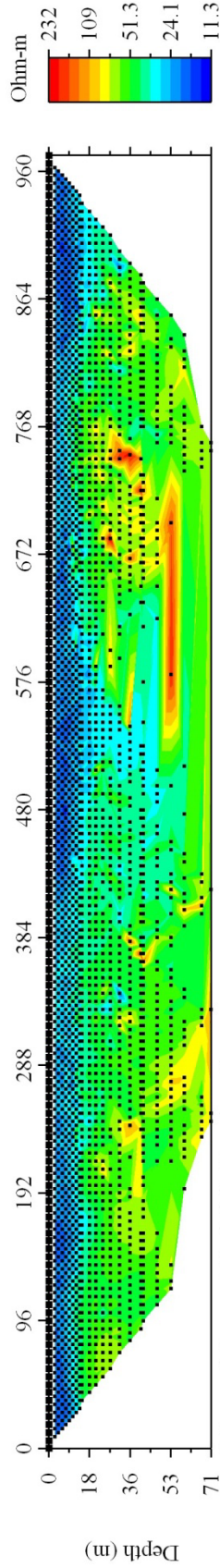
LINE UK-001

Data with Relative Misfit Above 10% Removed



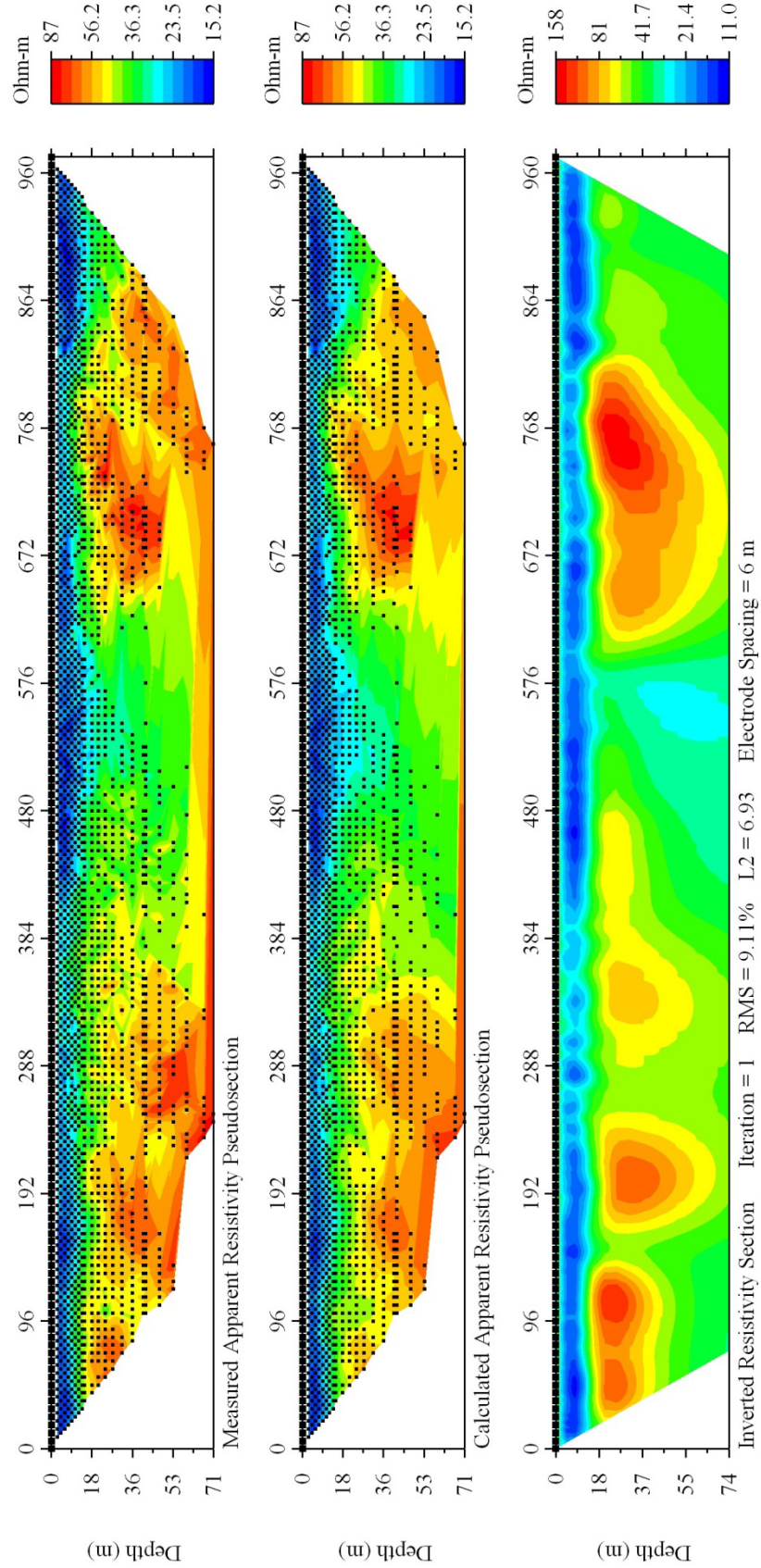
LINE UK-002

No Misfit Data Removed



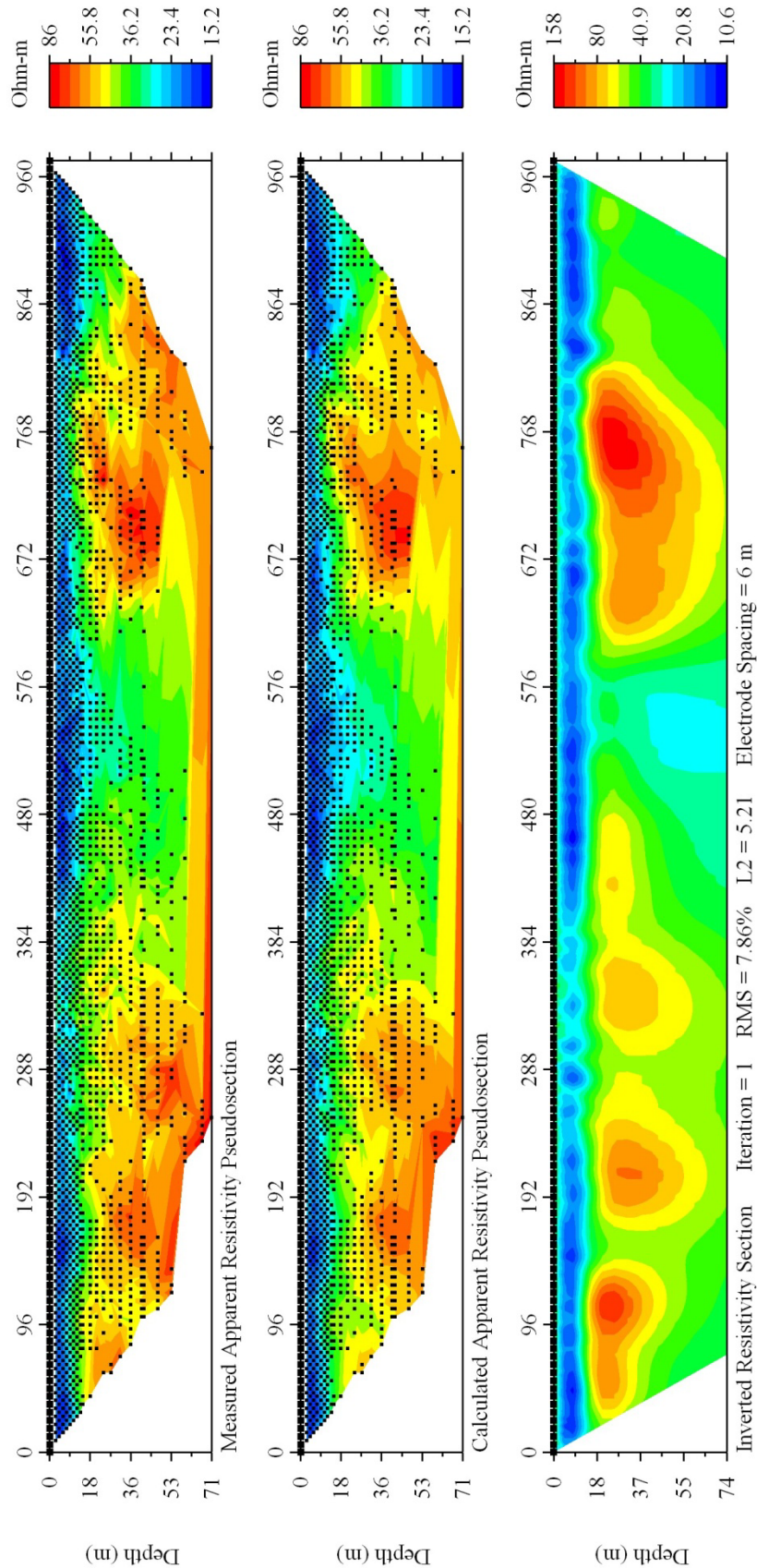
LINE UK-002

Data with Relative Misfit Above 21% Removed



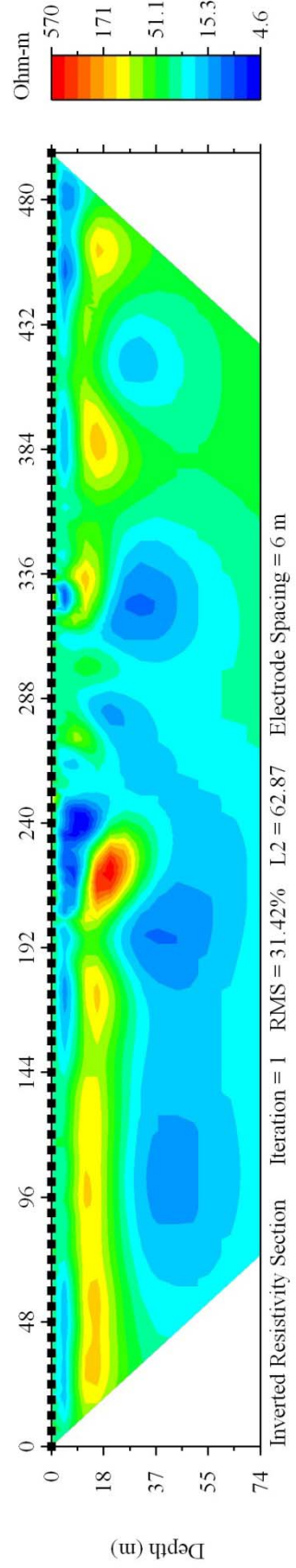
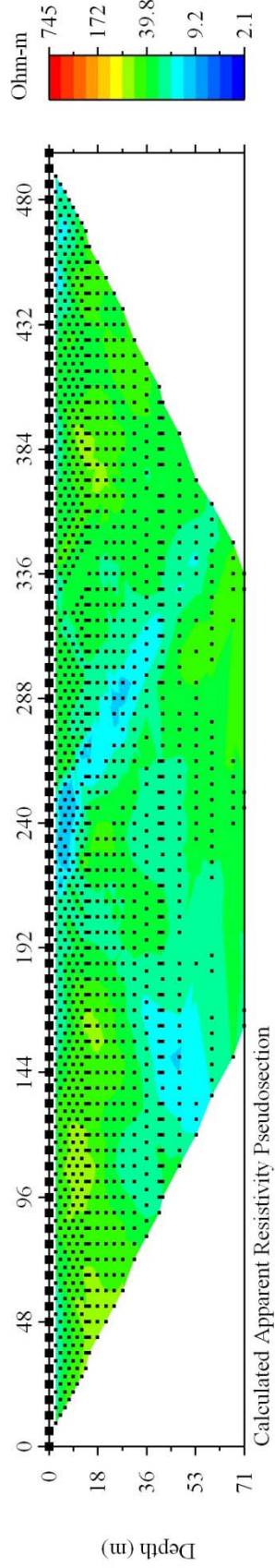
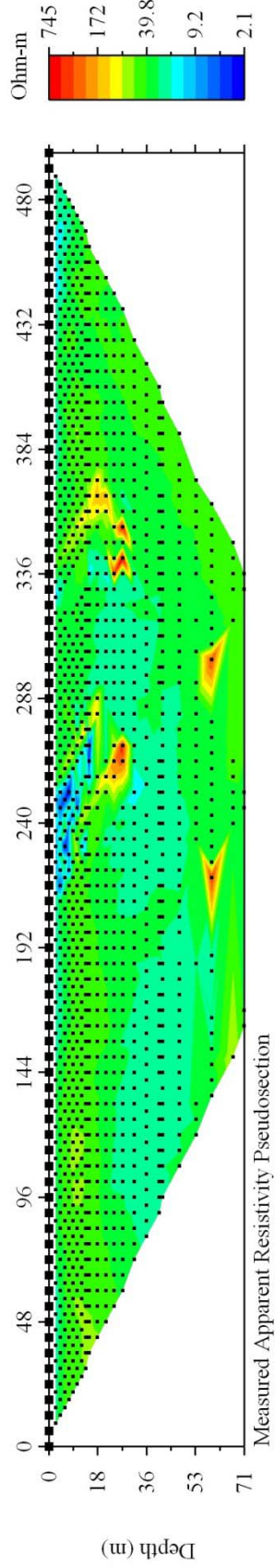
LINE UK-002

Data with Relative Misfit Above 16.5% Removed



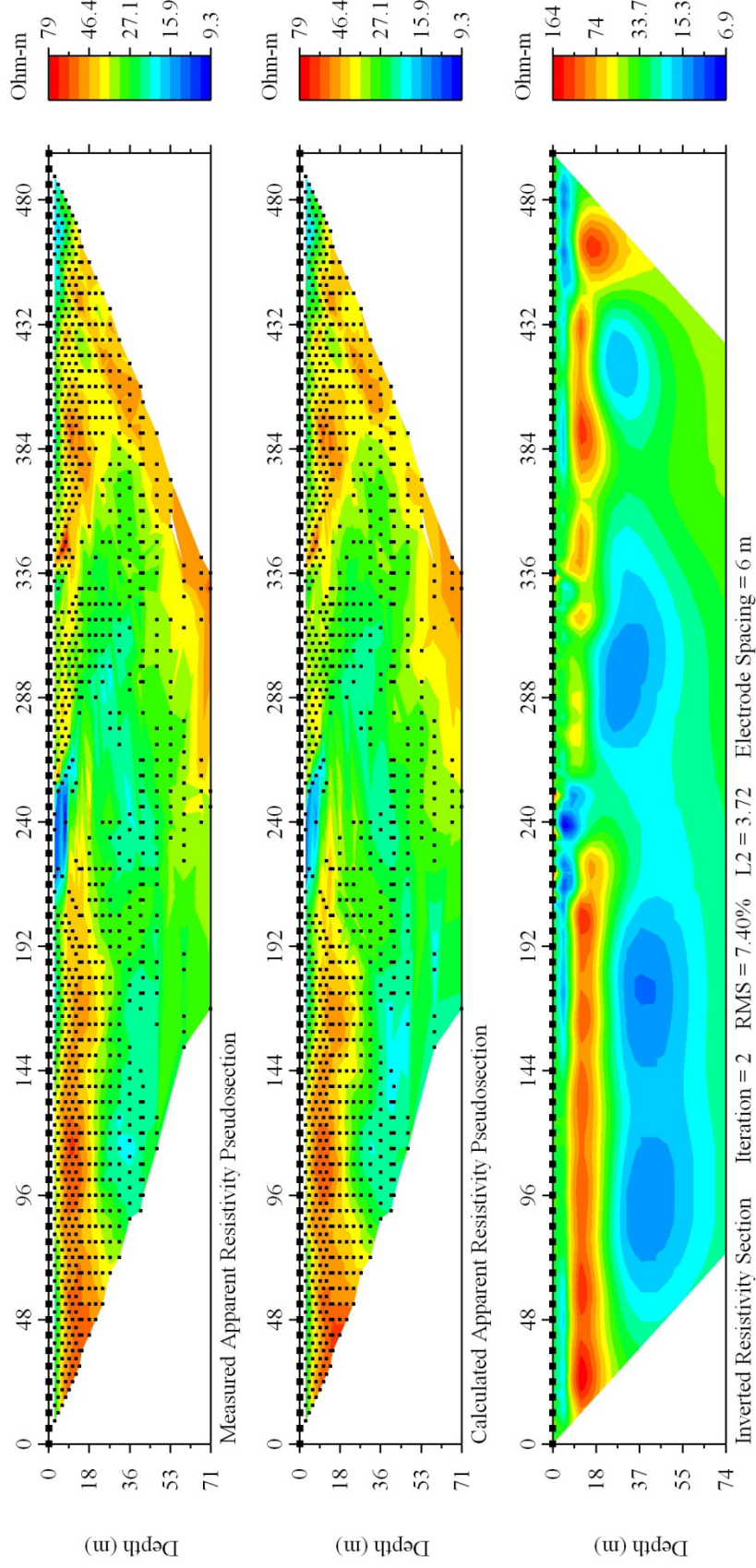
LINE UK-003

No Misfit Data Removed



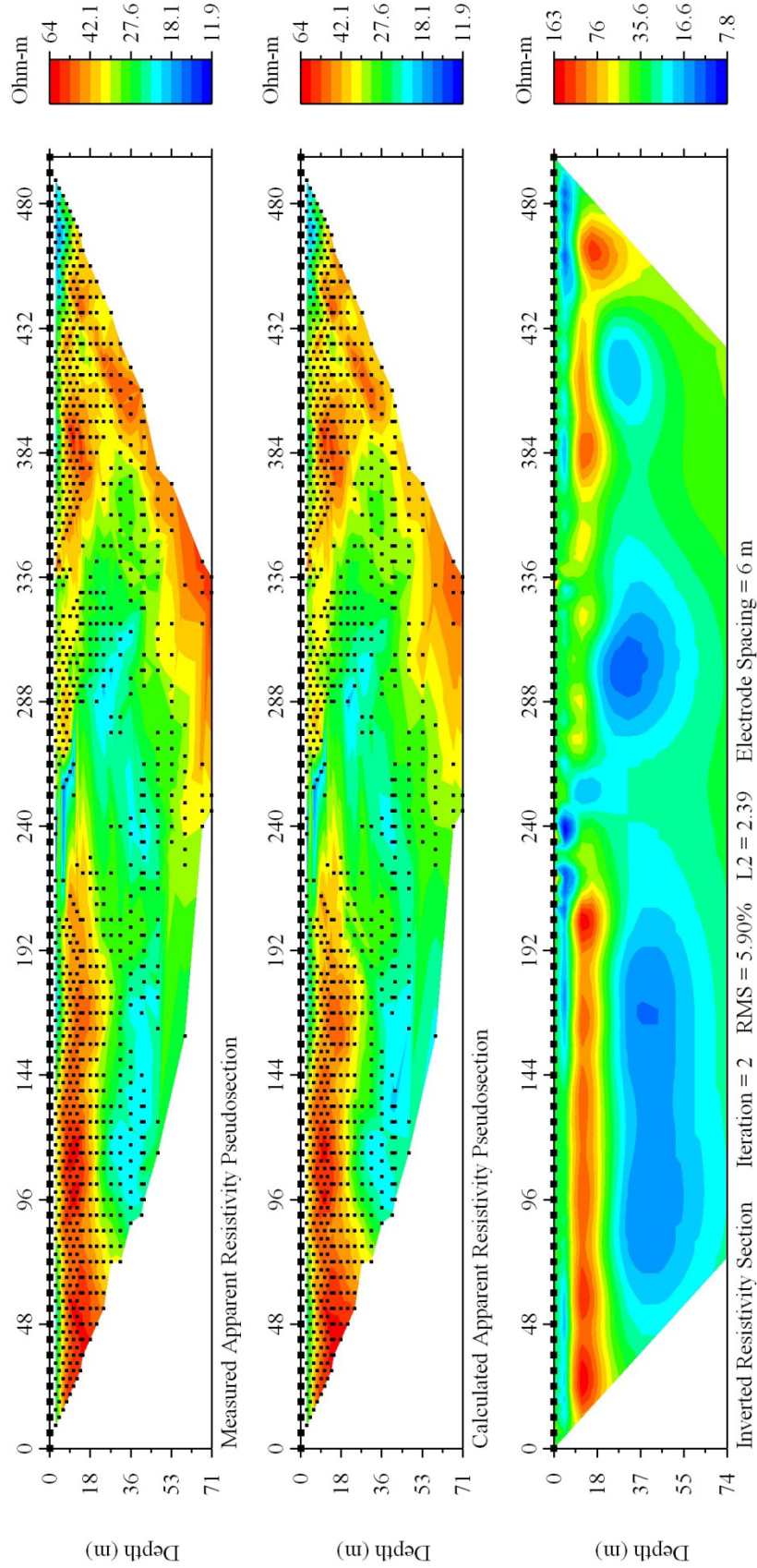
LINE UK-003

Data with Relative Misfit Above 20% Removed



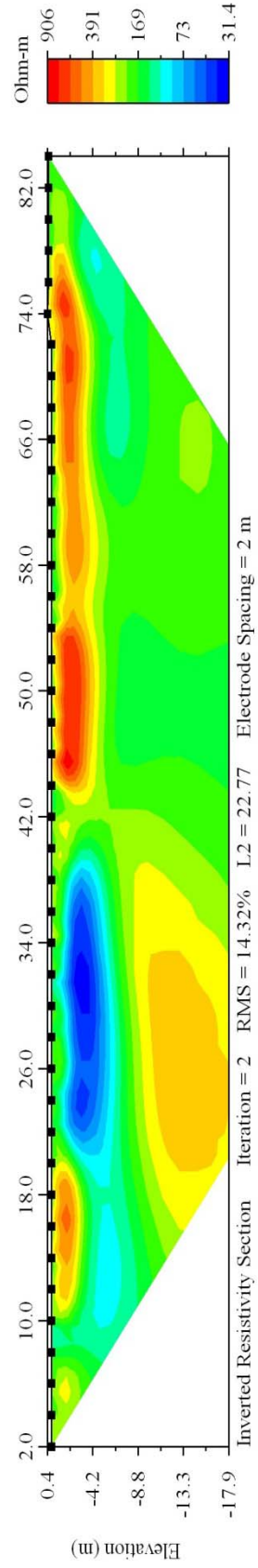
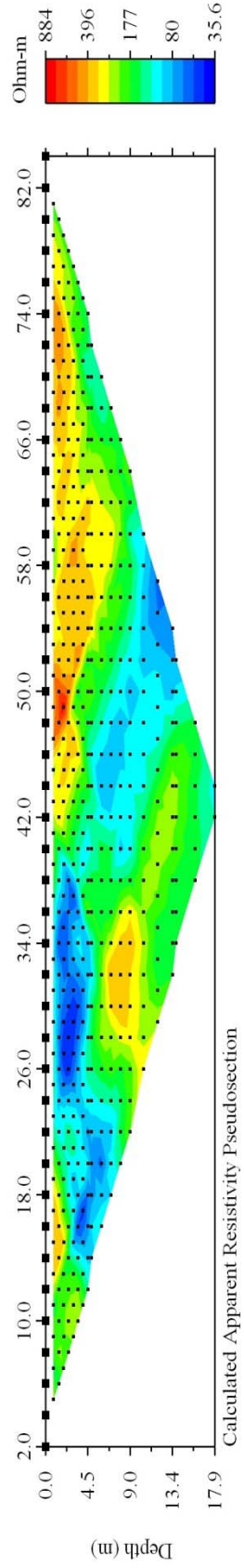
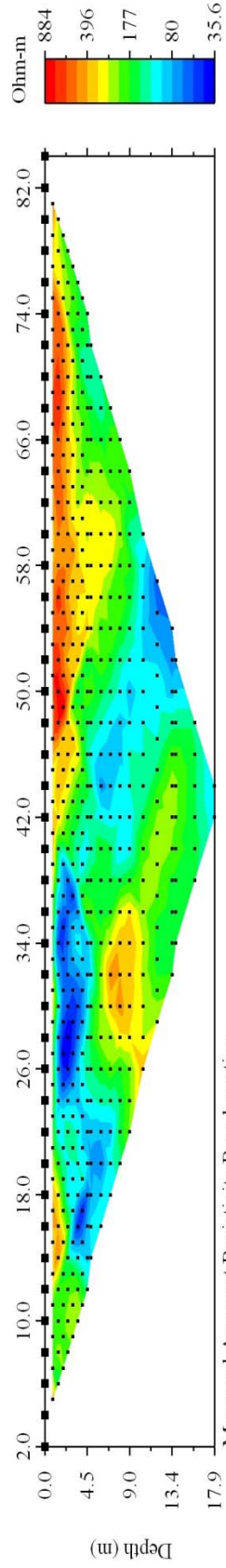
LINE UK-003

Data with Relative Misfit Above 14% Removed



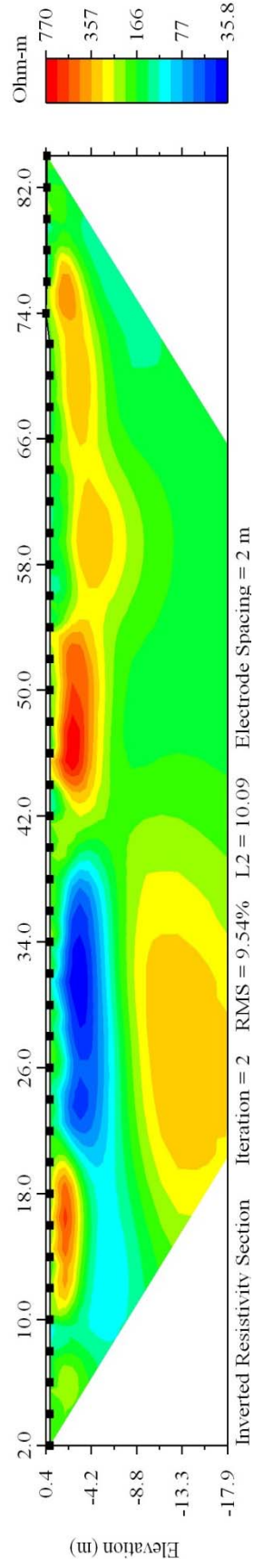
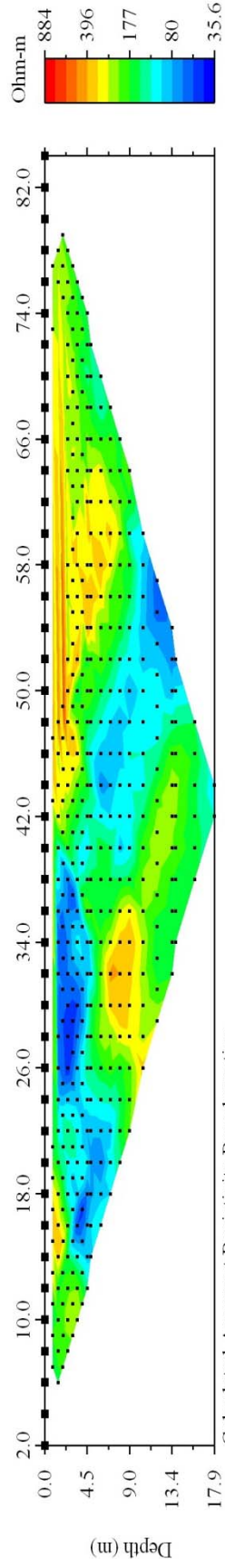
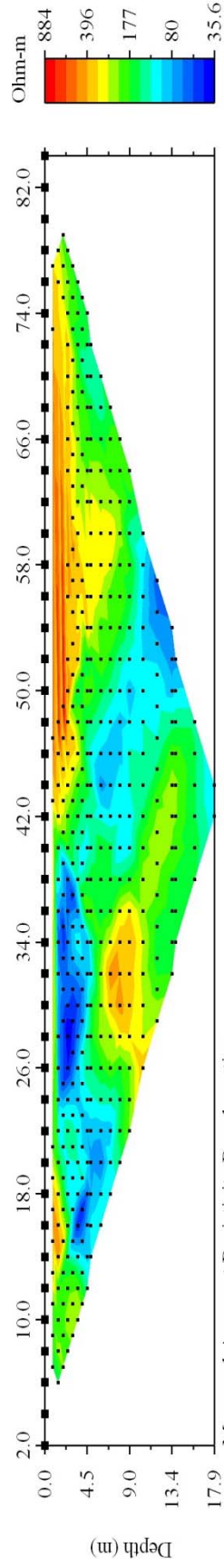
LINE UK-004

No Misfit Data Removed



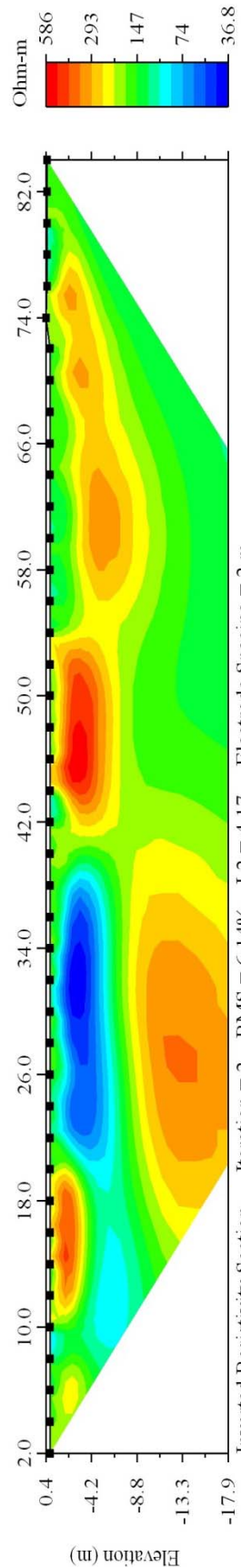
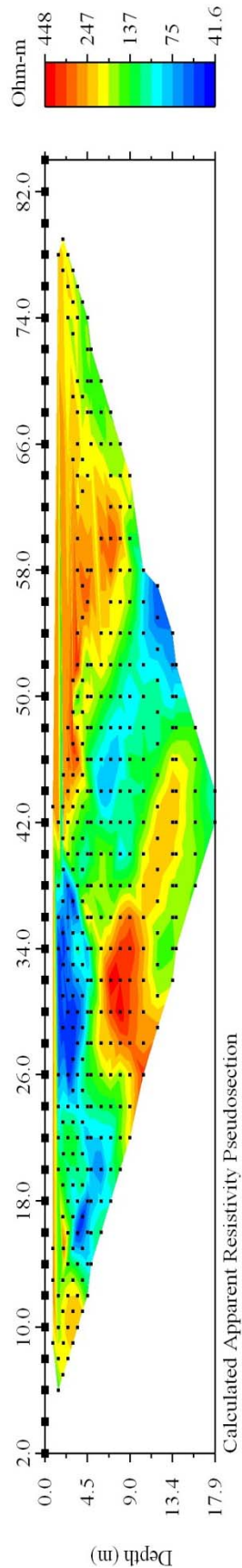
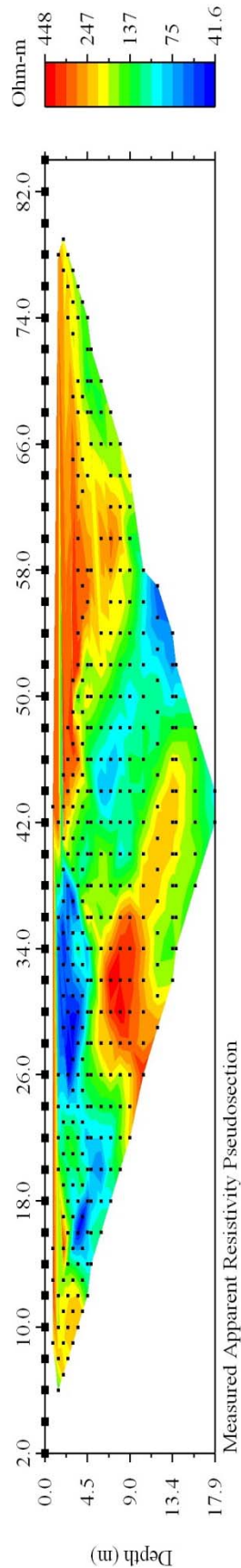
LINE UK-004

Data with Relative Misfit Above 17.5% Removed



LINE UK-004

Data with Relative Misfit Above 12.5% Removed



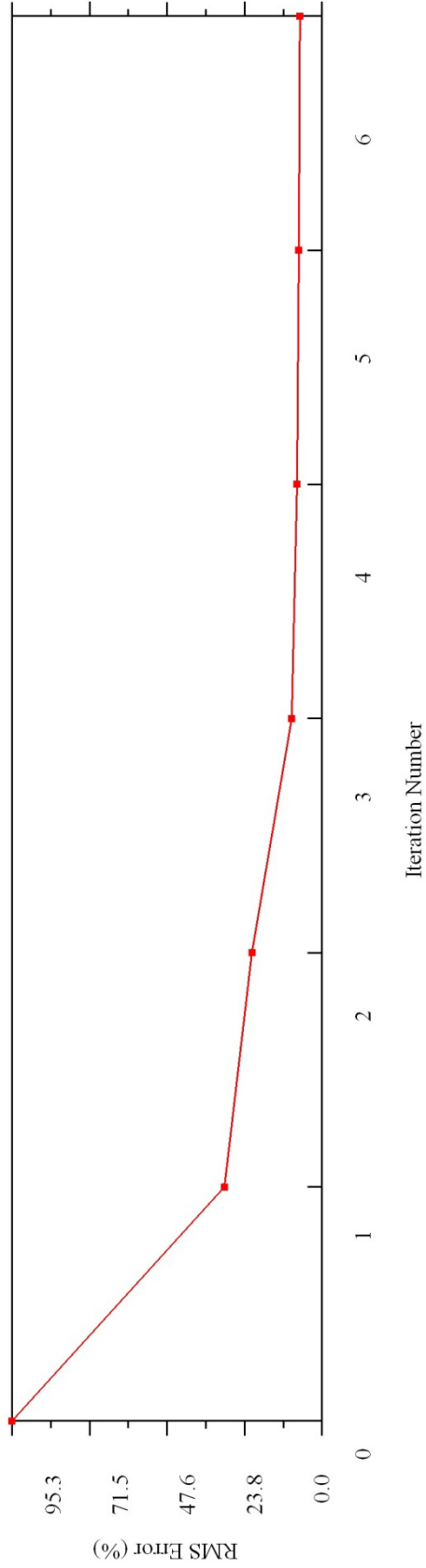
Appendix B

Section 2

Convergence curves of resistivity inversions. These curves represent the convergence of reduction in RMS error with successive iterations.

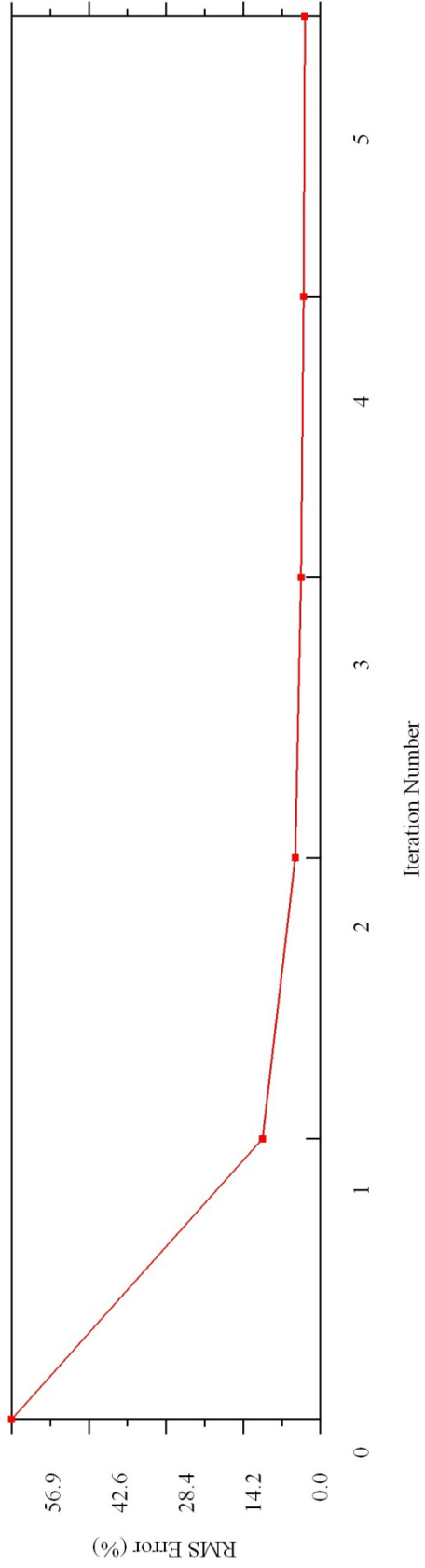
LINE UK-001

No Misfit Data Removed



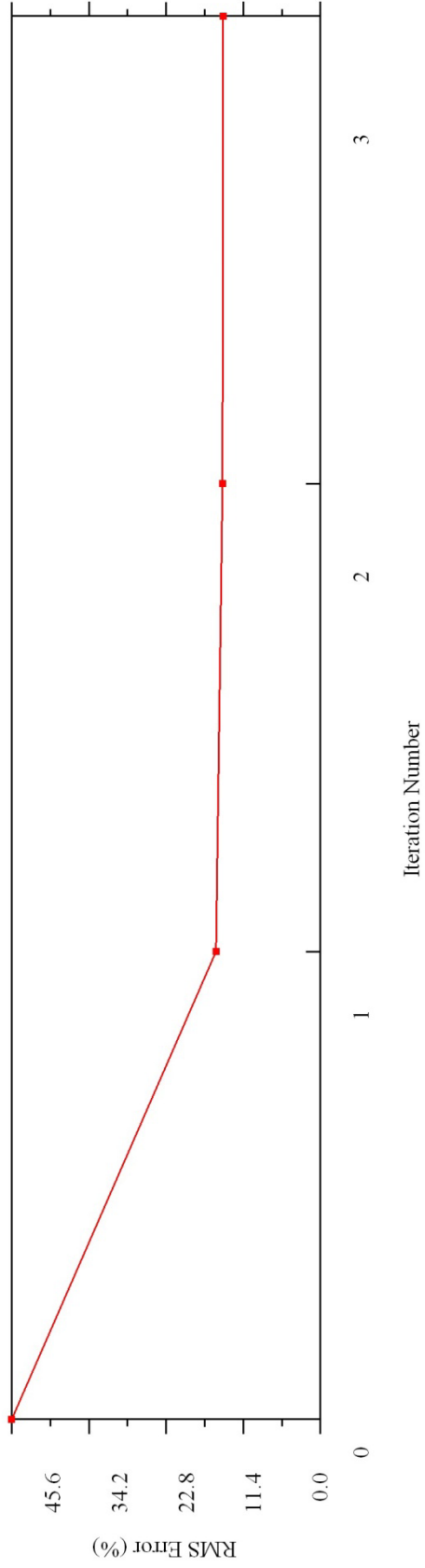
LINE UK-001

Data with Relative Misfit Above 10% Removed

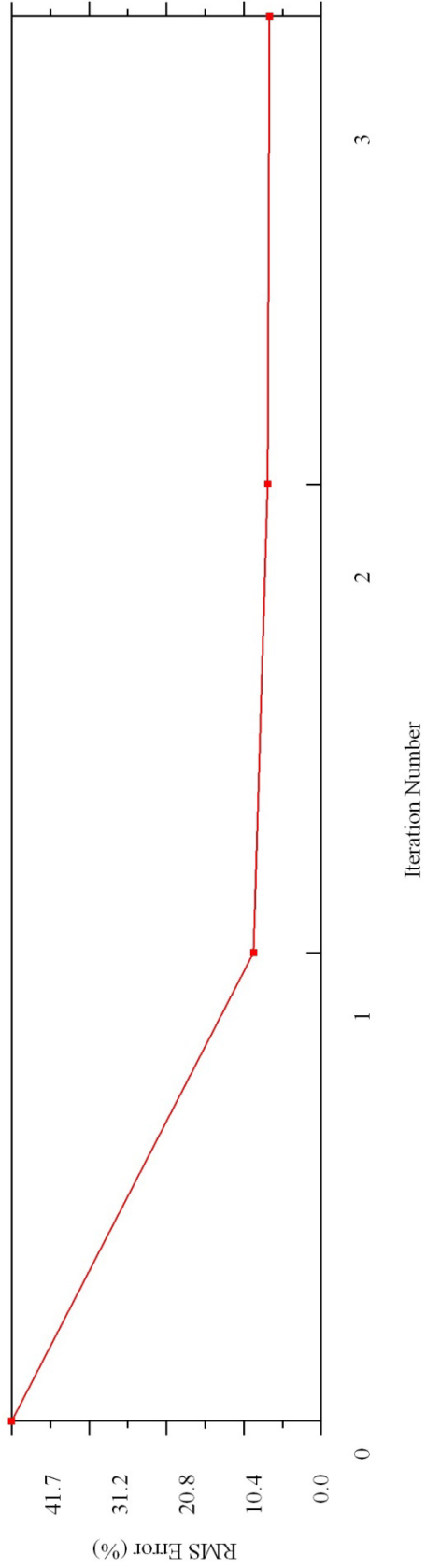


LINE UK-002

No Misfit Data Removed

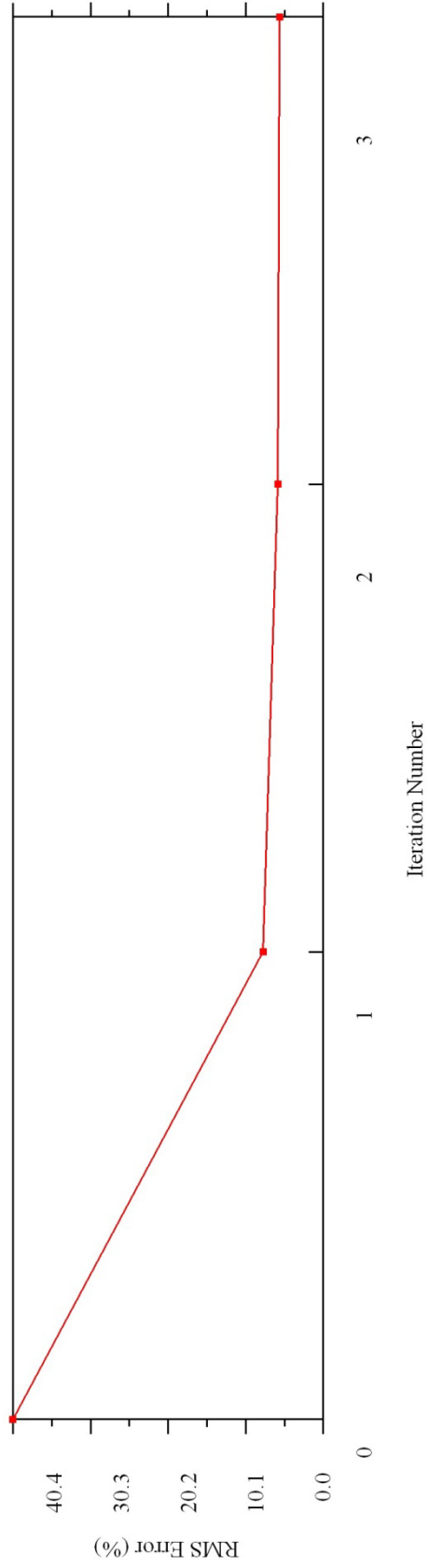


LINE UK-002
Data with Relative Misfit Above 21% Removed



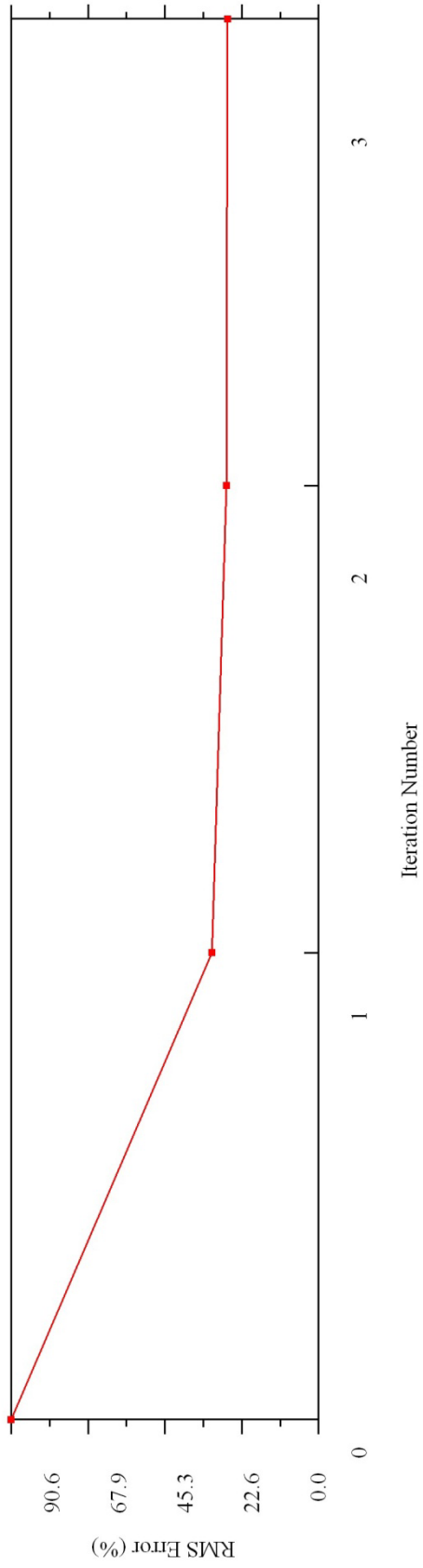
LINE UK-002

Data with Relative Misfit Above 16.5% Removed



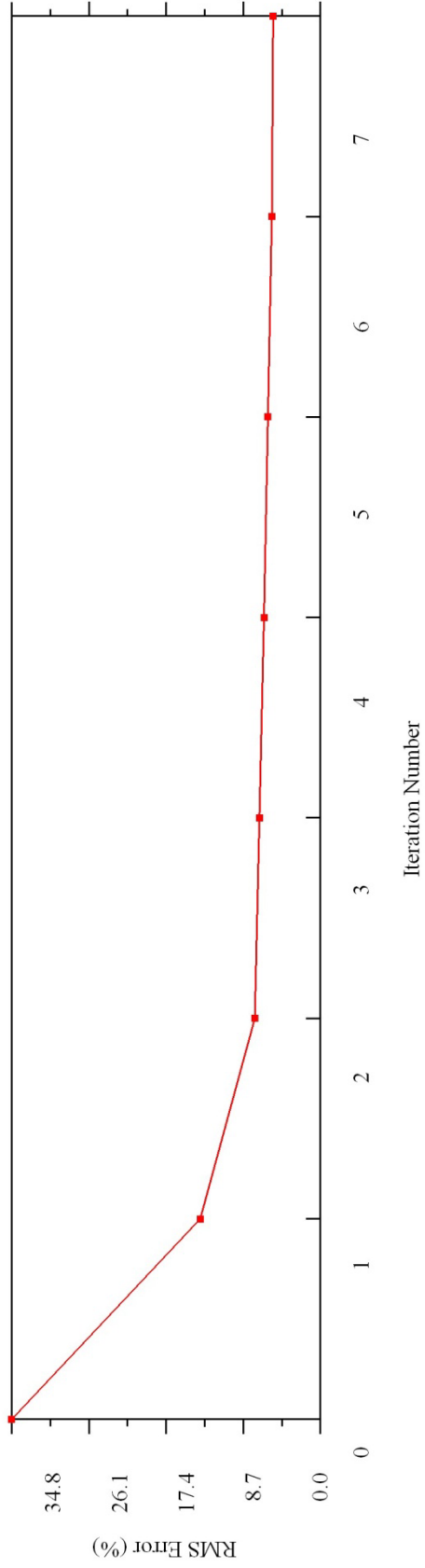
LINE UK-003

No Misfit Data Removed



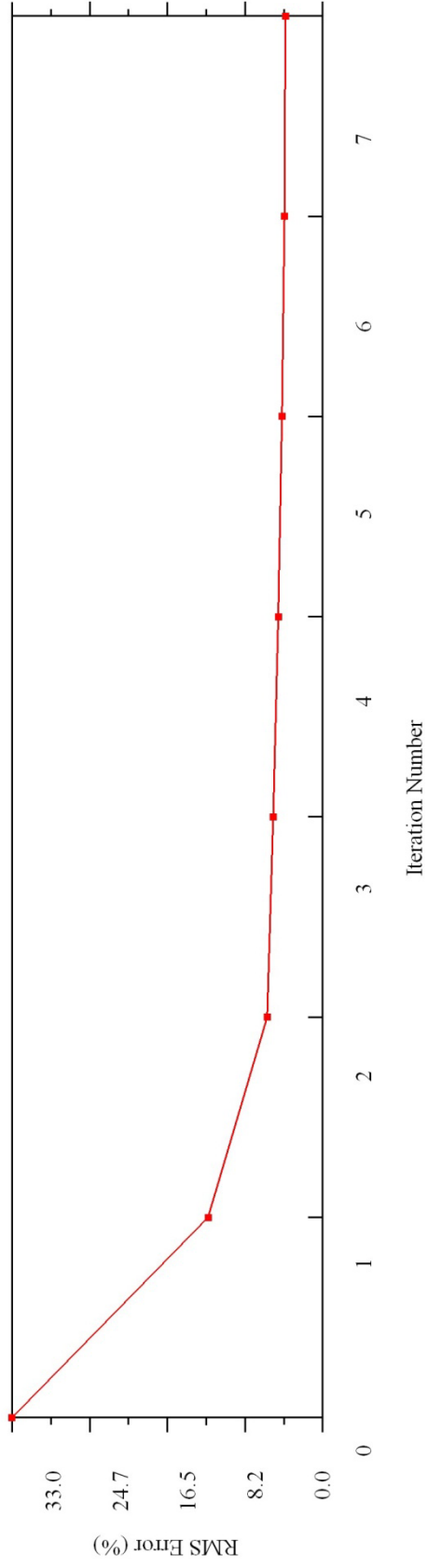
LINE UK-003

Data with Relative Misfit Above 20% Removed



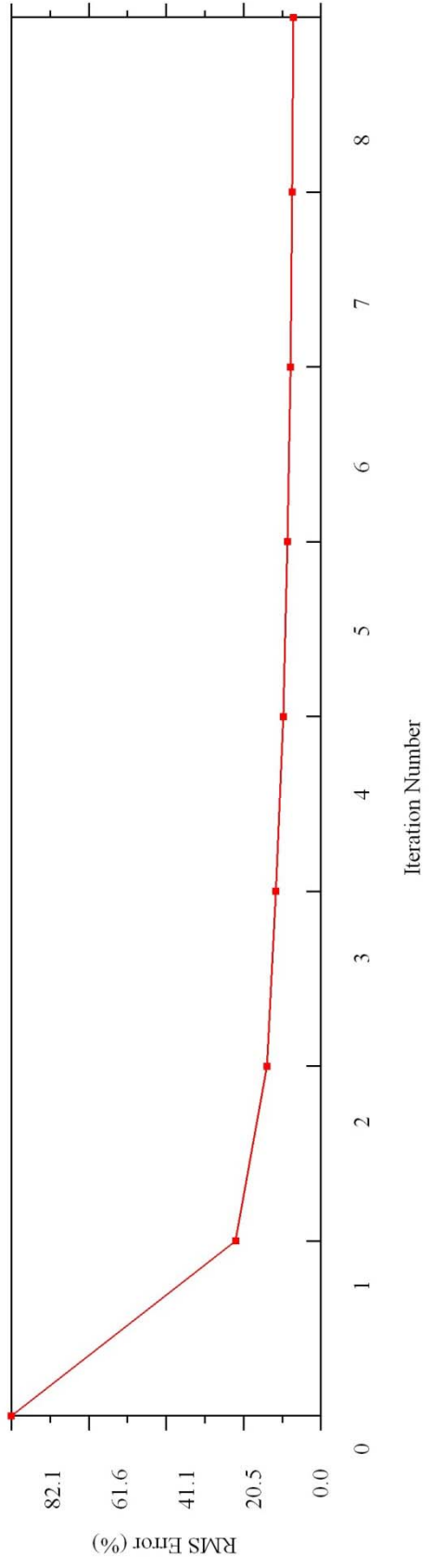
LINE UK-003

Data with Relative Misfit Above 14% Removed



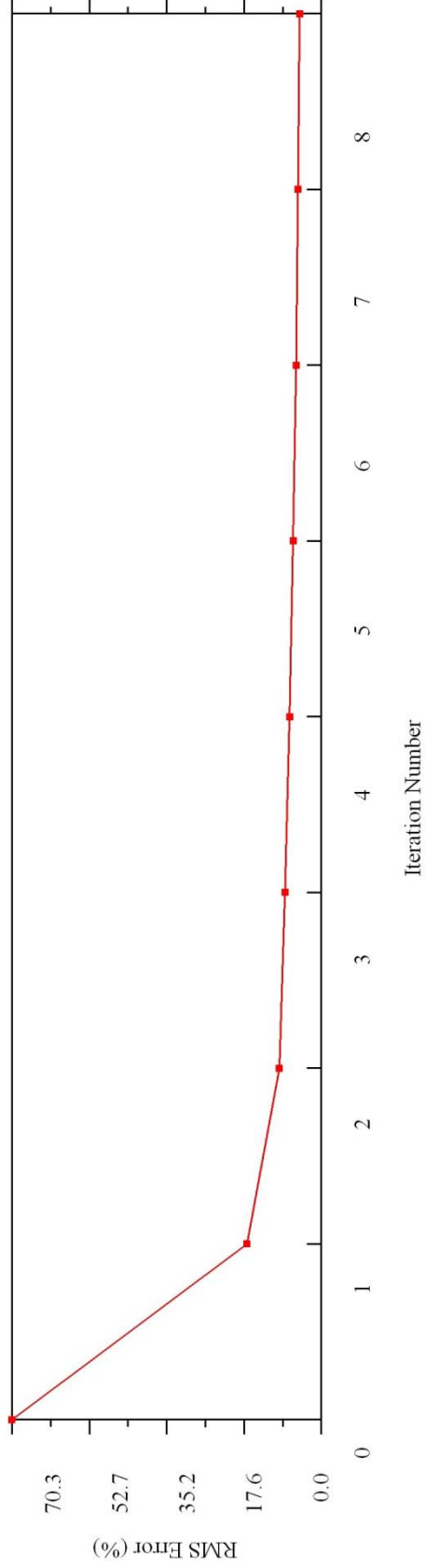
LINE UK-004

No Misfit Data Removed



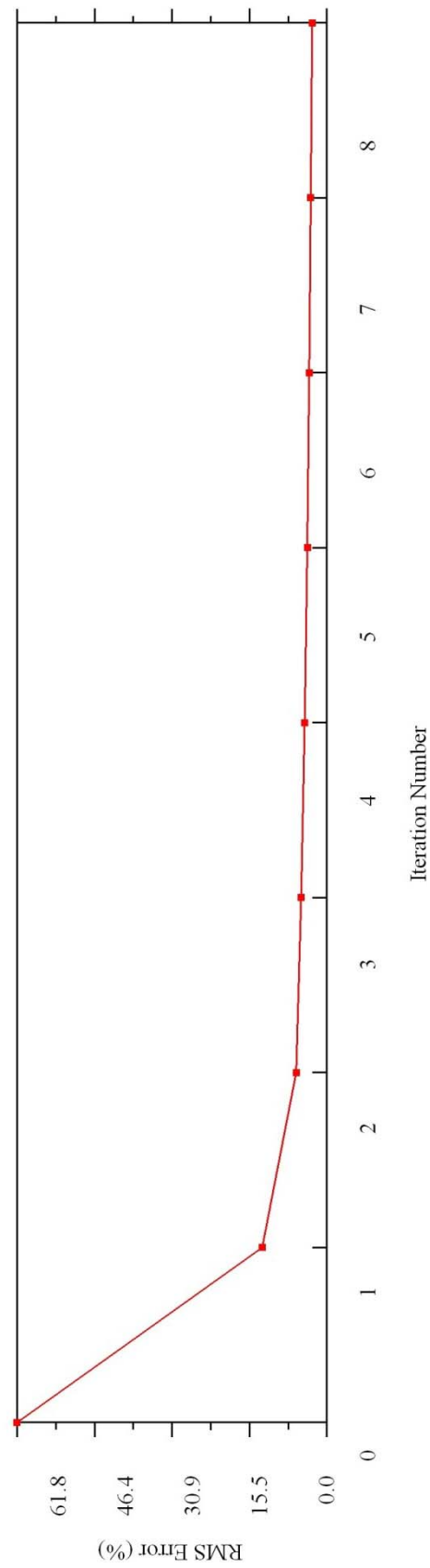
LINE UK-004

Data with Relative Misfit Above 17.5% Removed



LINE UK-004

Data with Relative Misfit Above 12.5% Removed



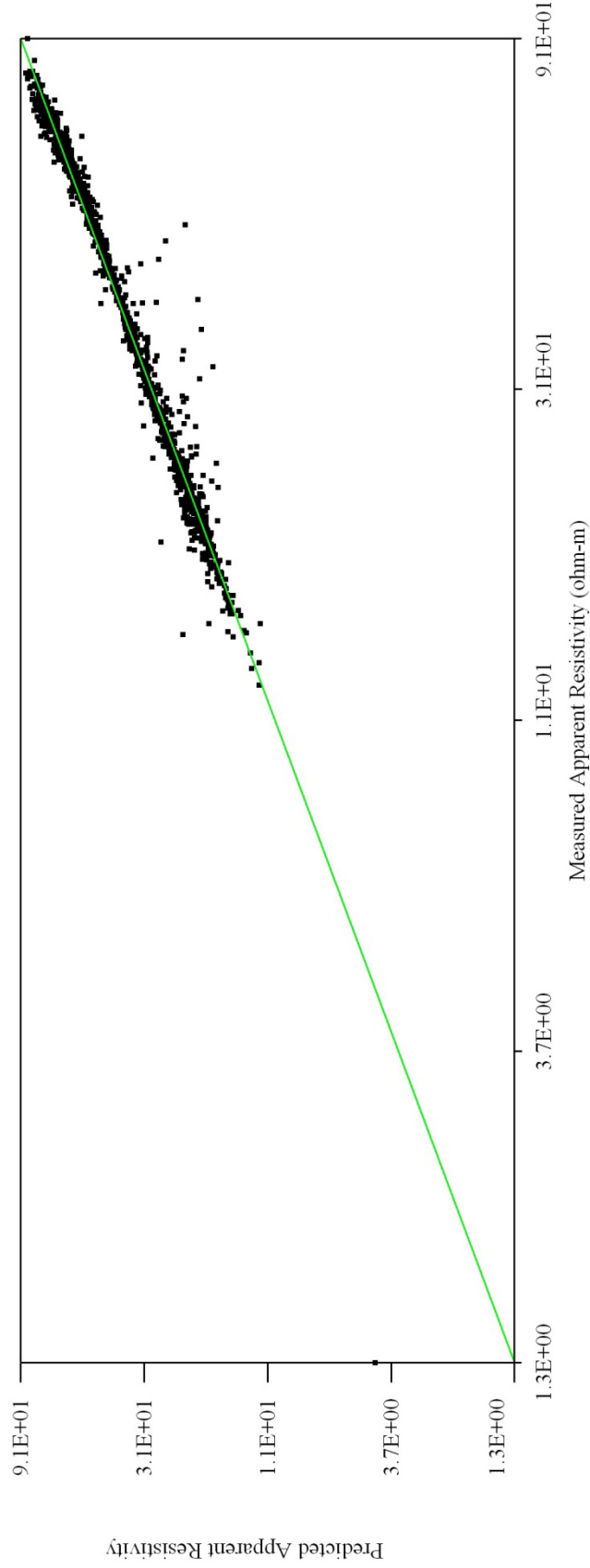
Appendix B

Section 3

Cross-plots of measured vs. predicted resistivity data. The scatter plots show the closeness of fit between the two data points in relation to a 1:1 line representing complete agreement between the measured and predicted values.

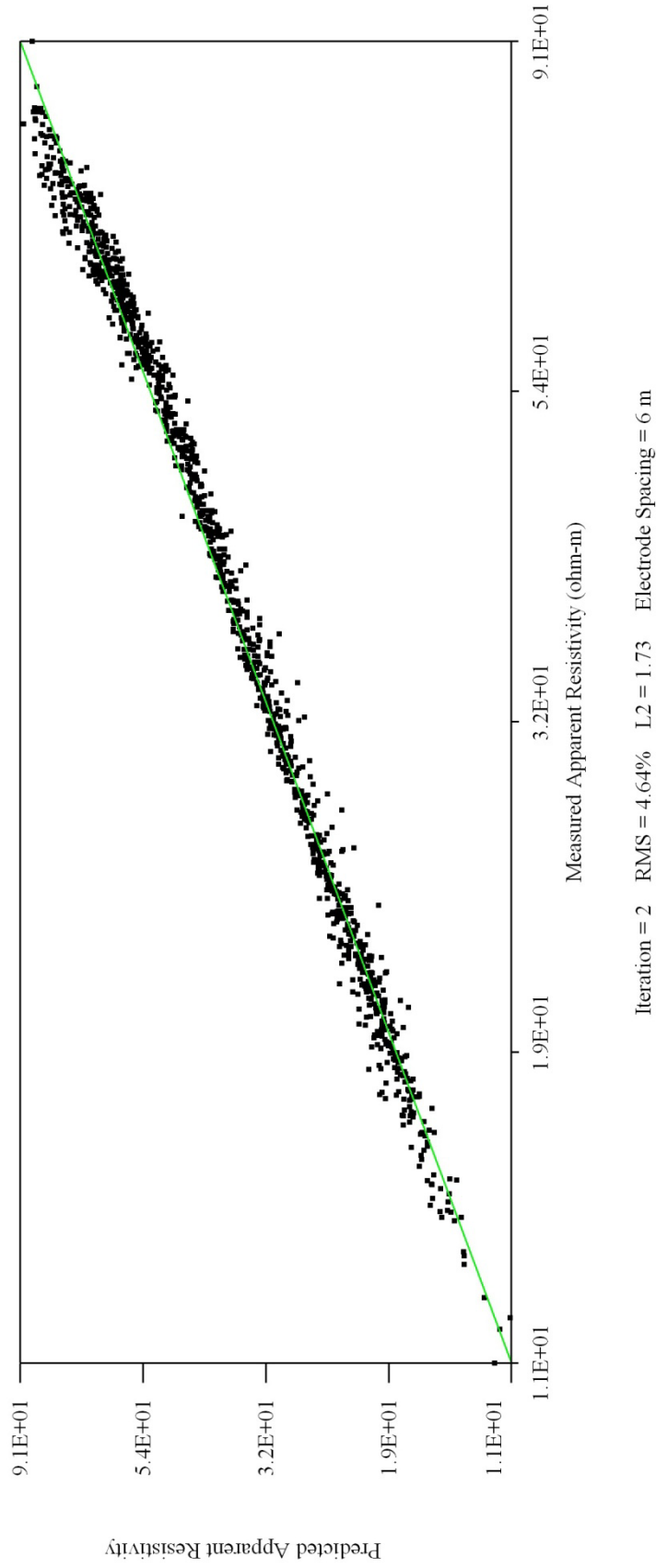
LINE UK-001

No Misfit Data Removed



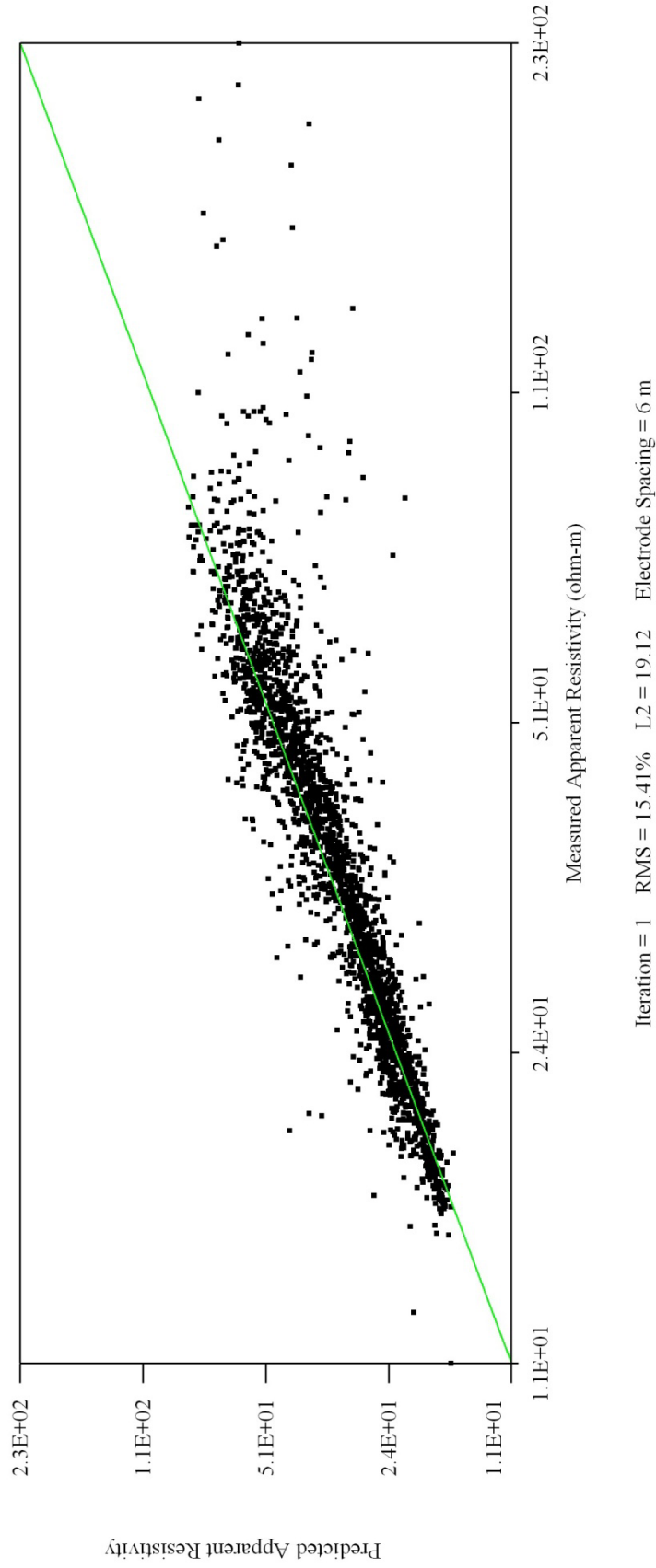
LINE UK-001

Data with Relative Misfit Above 10% Removed



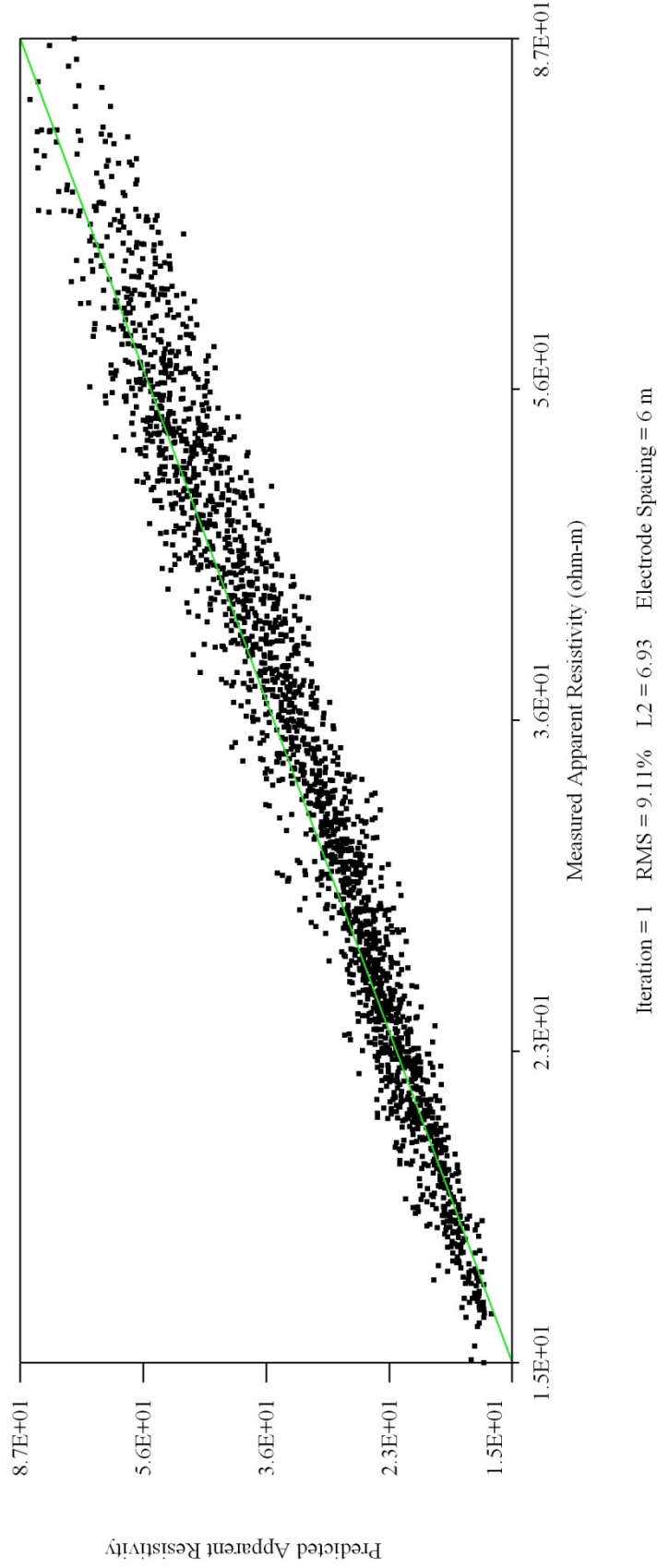
LINE UK-002

No Misfit Data Removed



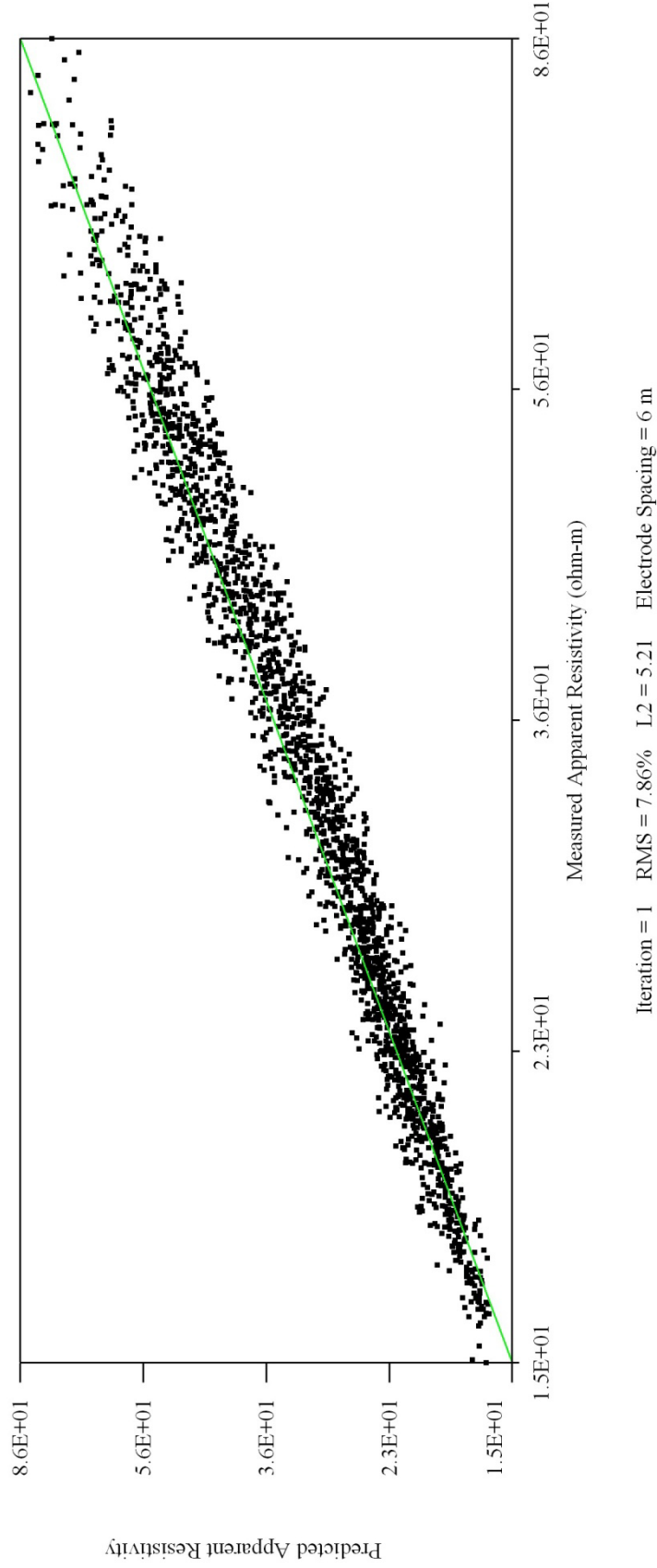
LINE UK-002

Data with Relative Misfit Above 21% Removed



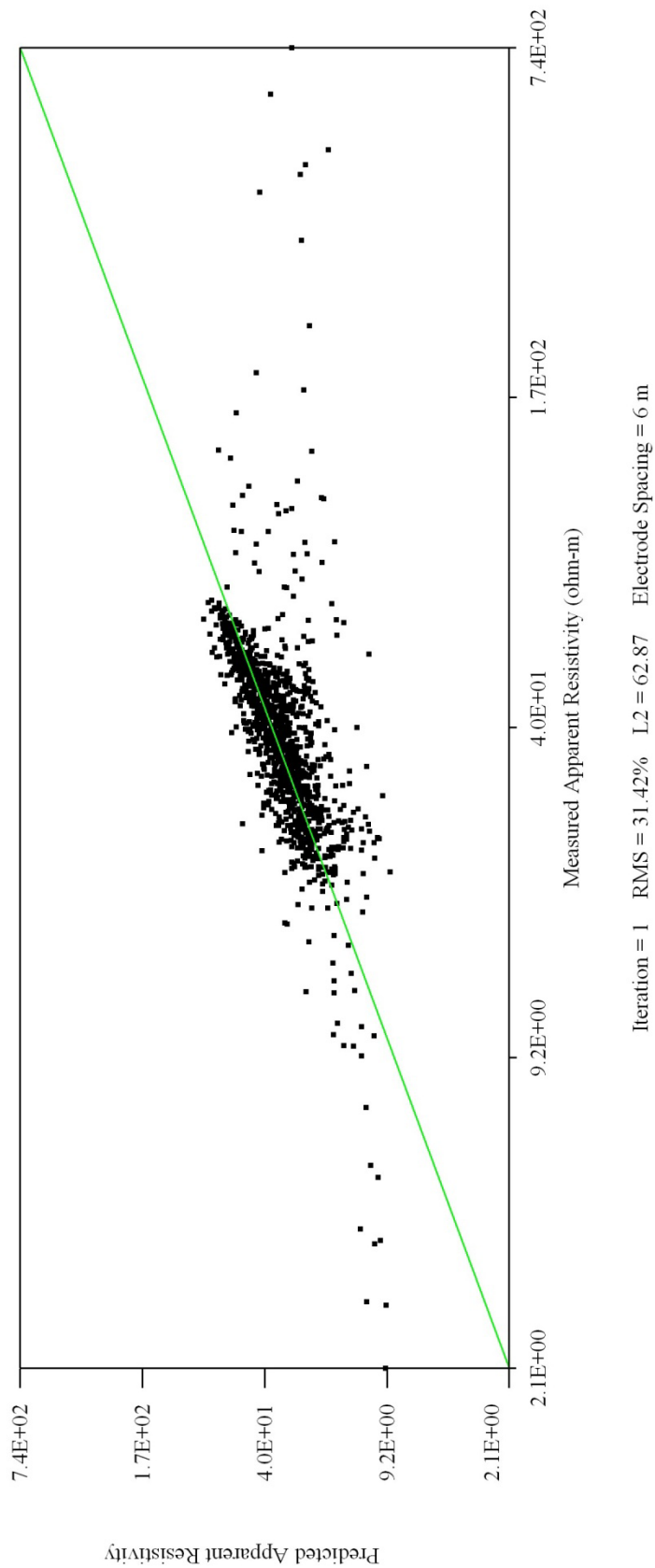
LINE UK-002

Data with Relative Misfit Above 16.5% Removed

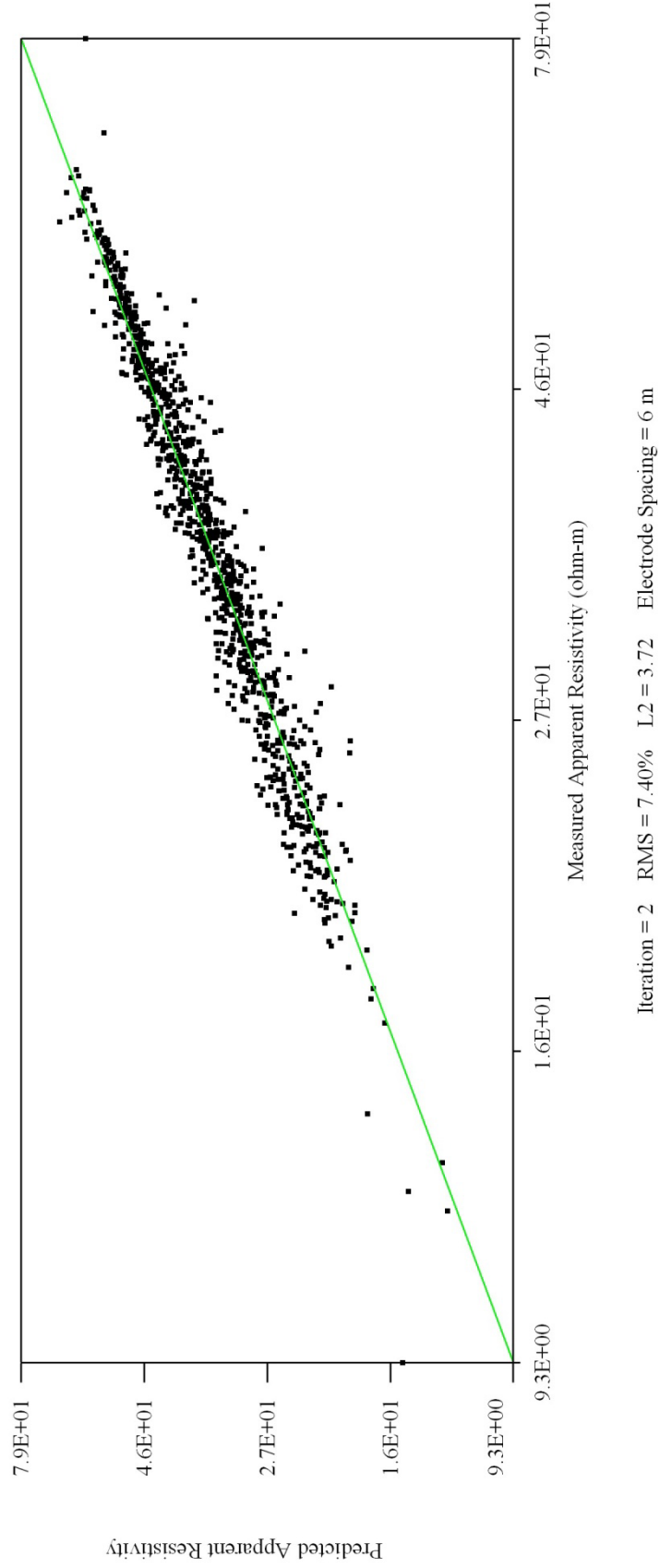


LINE UK-003

No Misfit Data Removed

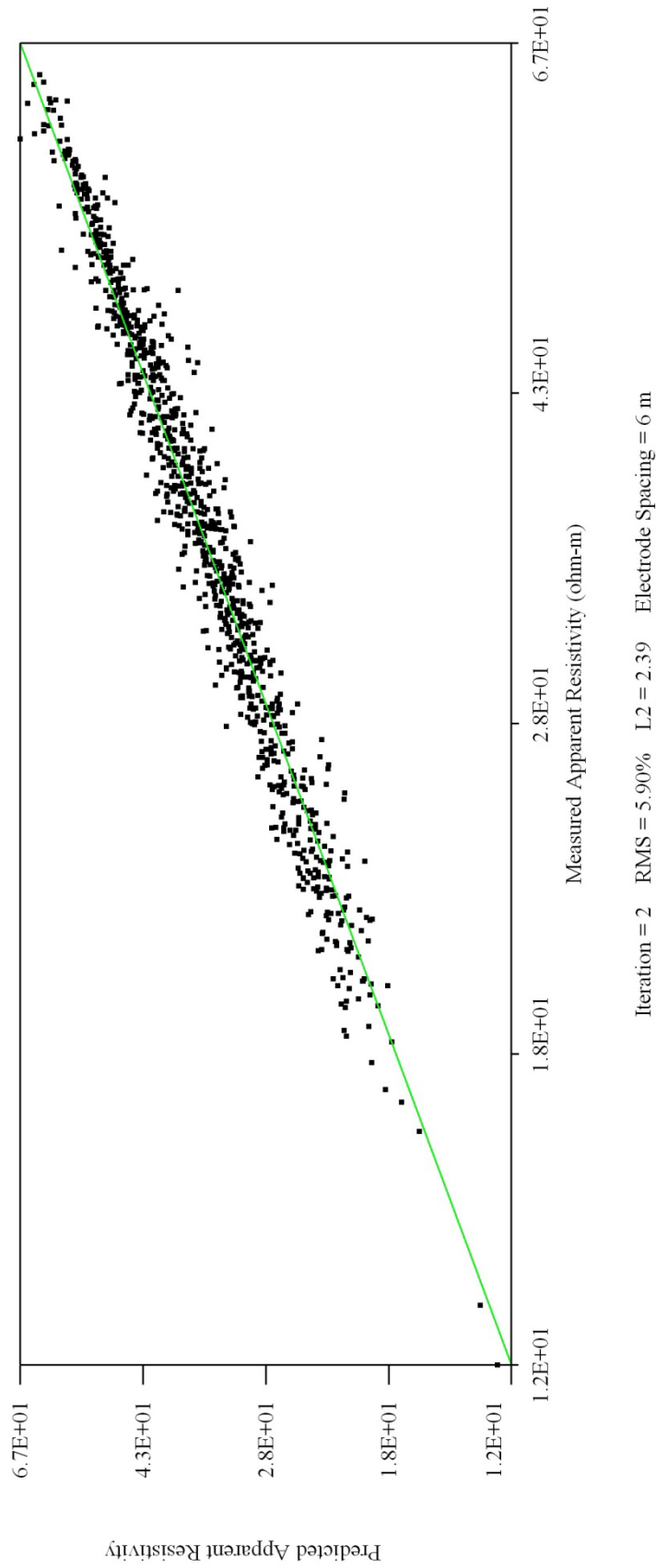


LINE UK-003
Data with Relative Misfit Above 20% Removed



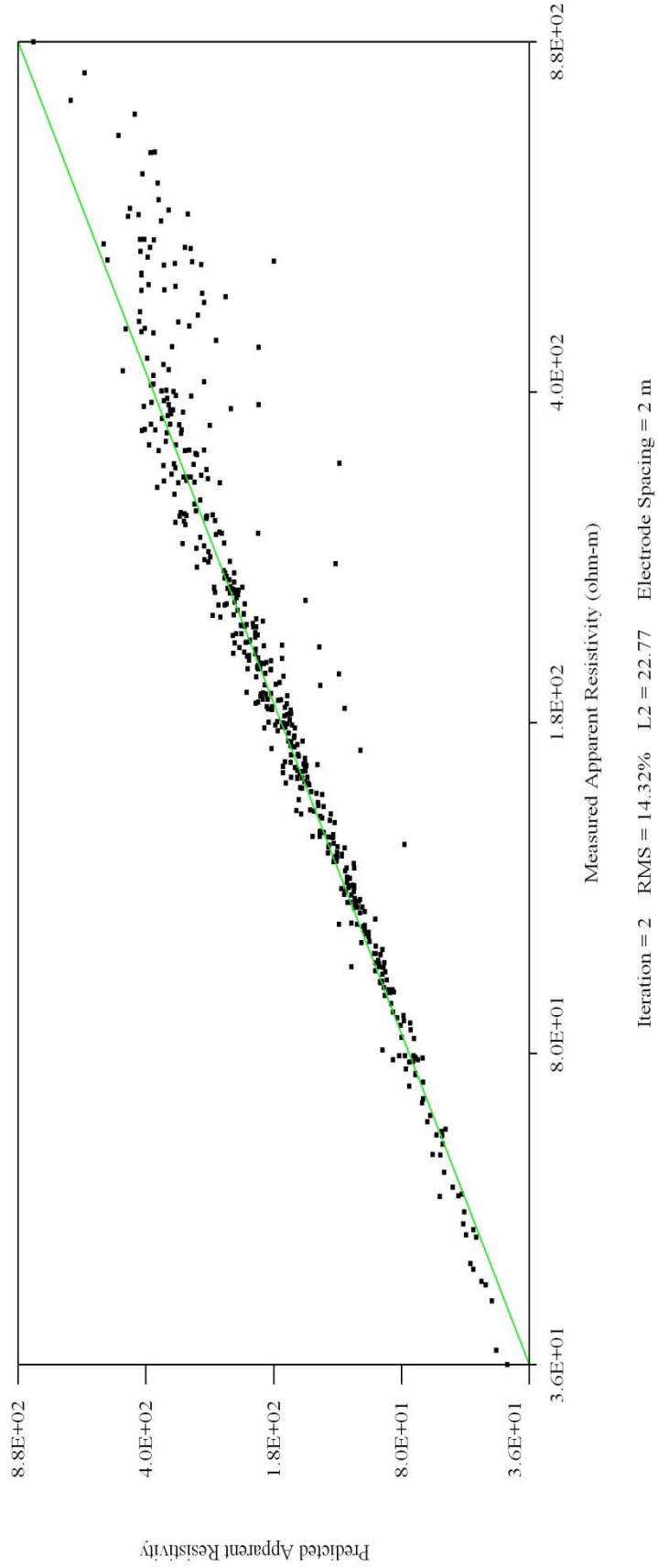
LINE UK-003

Data with Relative Misfit Above 14% Removed



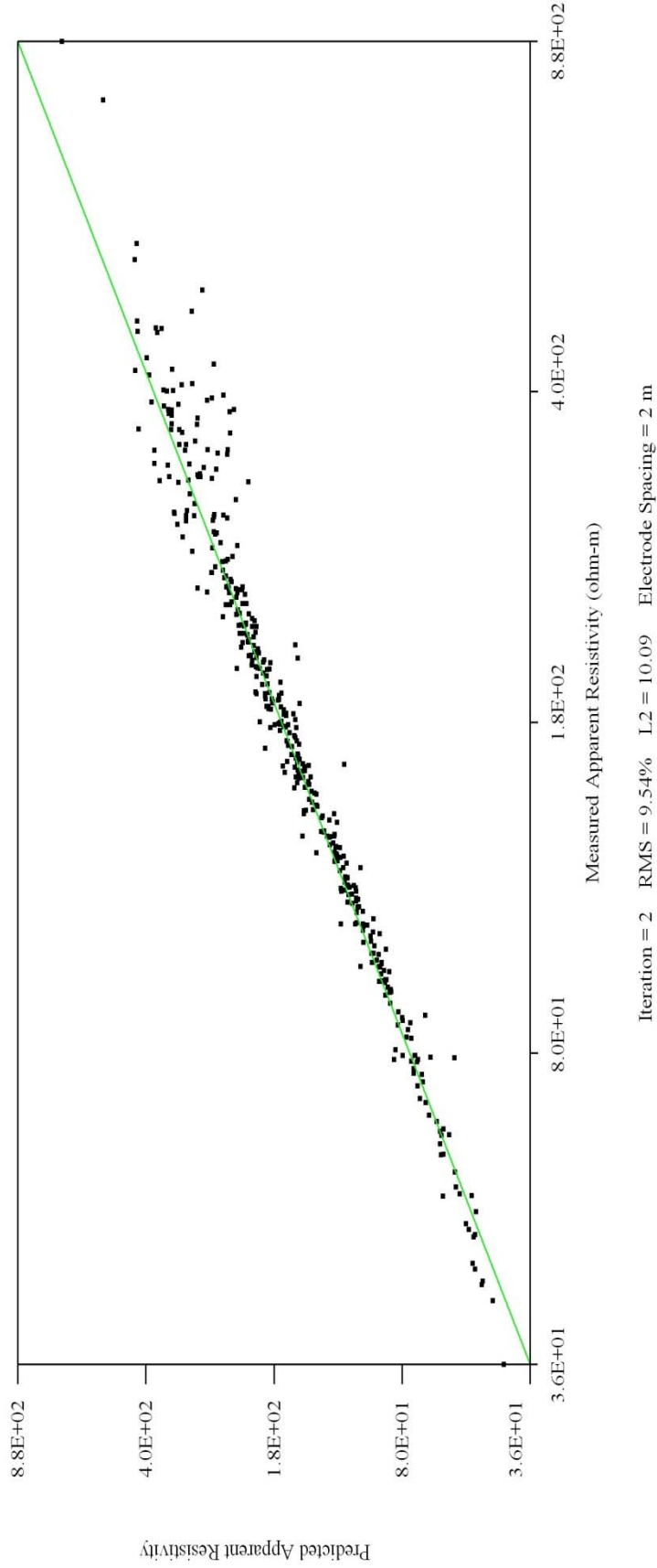
LINE UK-004

No Misfit Data Removed



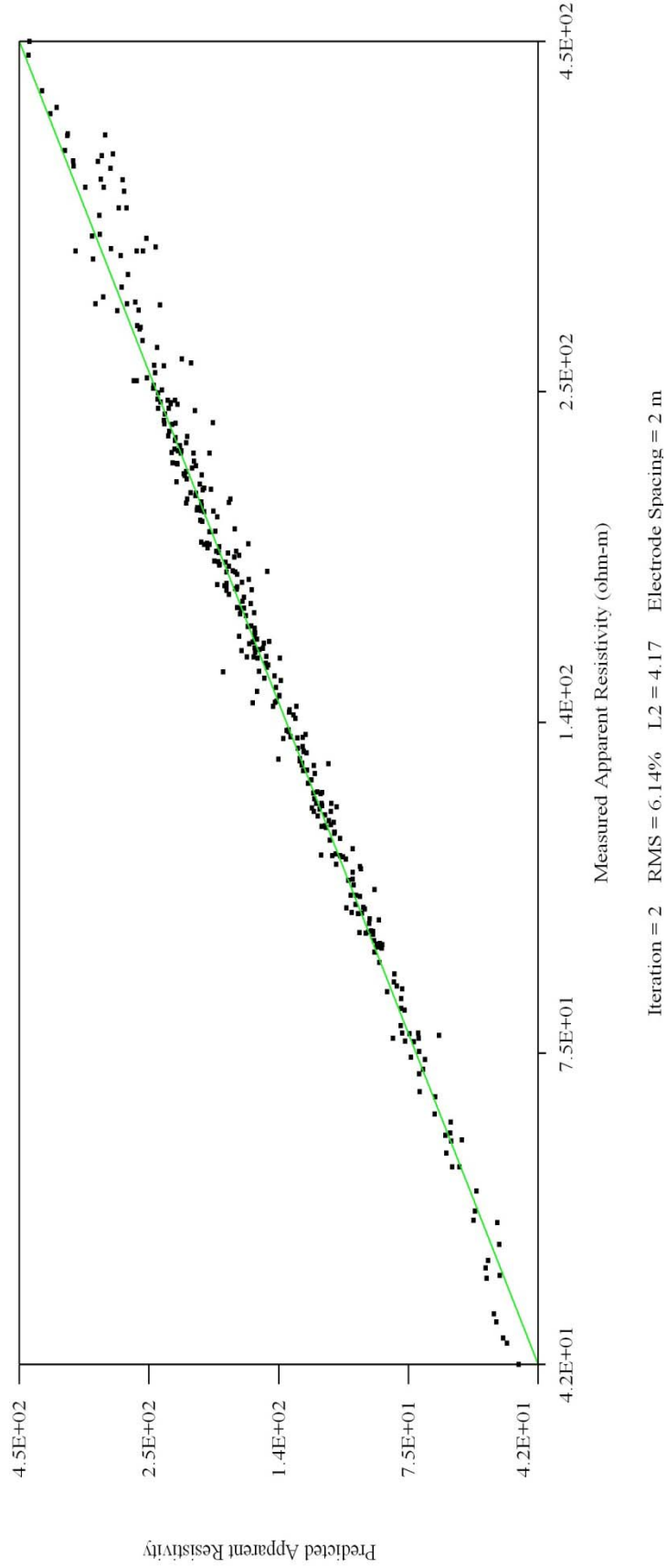
LINE UK-004

Data with Relative Misfit Above 17.5% Removed



LINE UK-004

Data with Relative Misfit Above 12.5% Removed



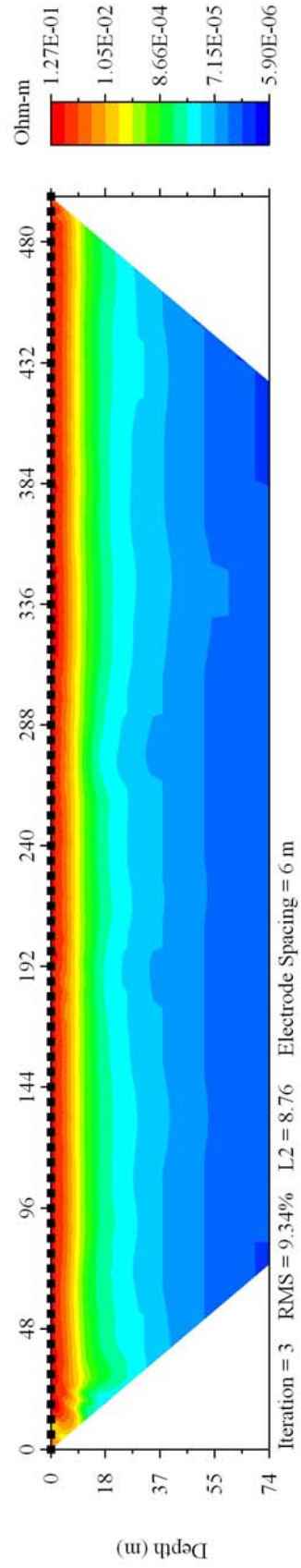
Appendix B

Section 4

Relative model sensitivity sections. Model sensitivity is equivalent to the magnitude of the model vector. Model blocks closer to electrodes have higher sensitivities and generally yield higher model resolutions through the inversion process.

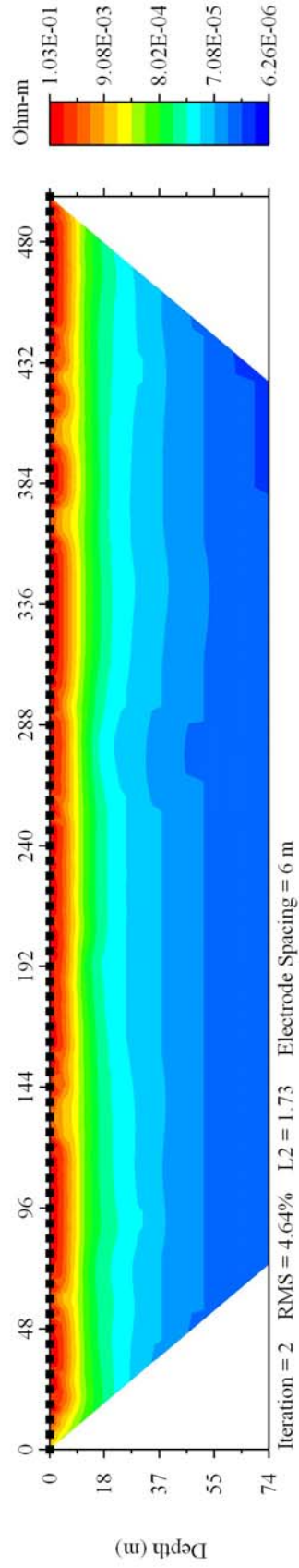
LINE UK-001

No Misfit Data Removed



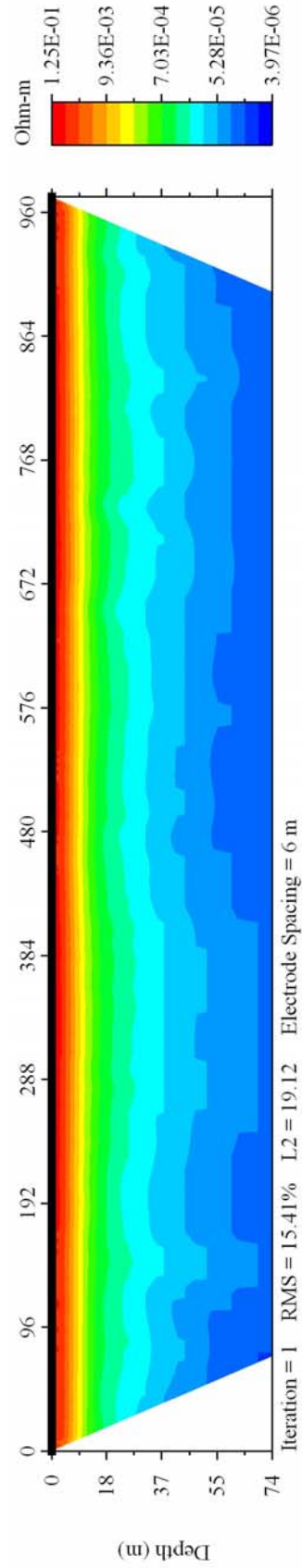
LINE UK-001

Data with Relative Misfit Above 10% Removed



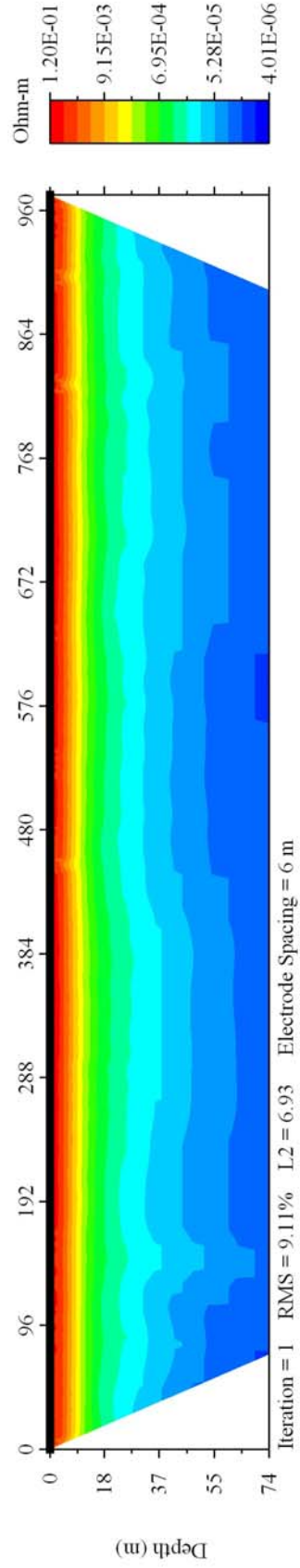
LINE UK-002

No Misfit Data Removed



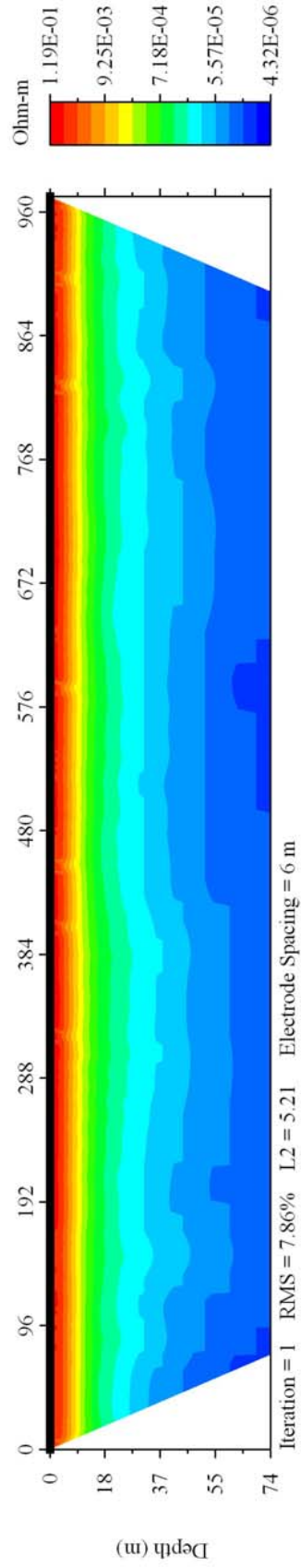
LINE UK-002

Data with Relative Misfit Above 21% Removed



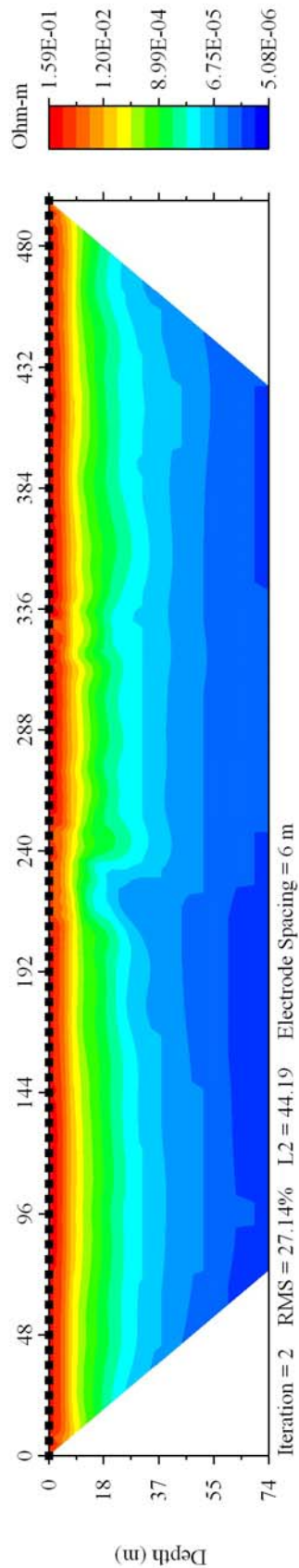
LINE UK-002

Data with Relative Misfit Above 16.5% Removed



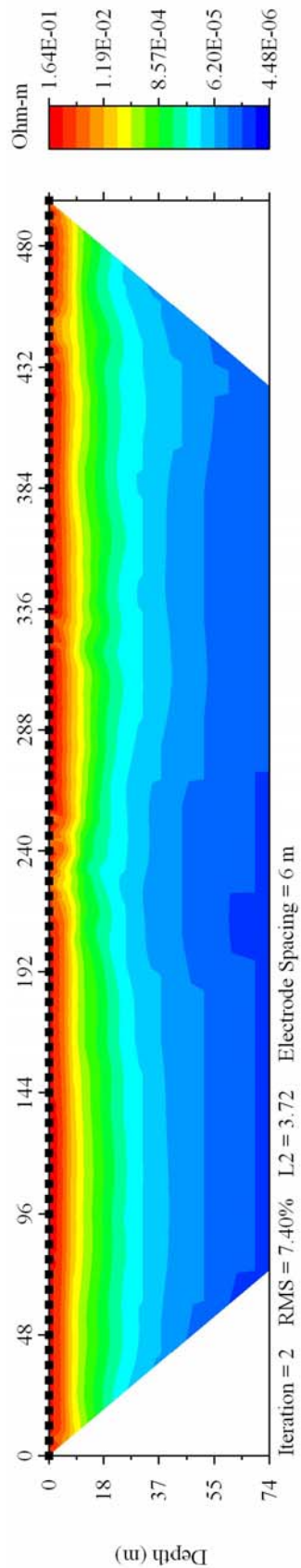
LINE UK-003

No Misfit Data Removed



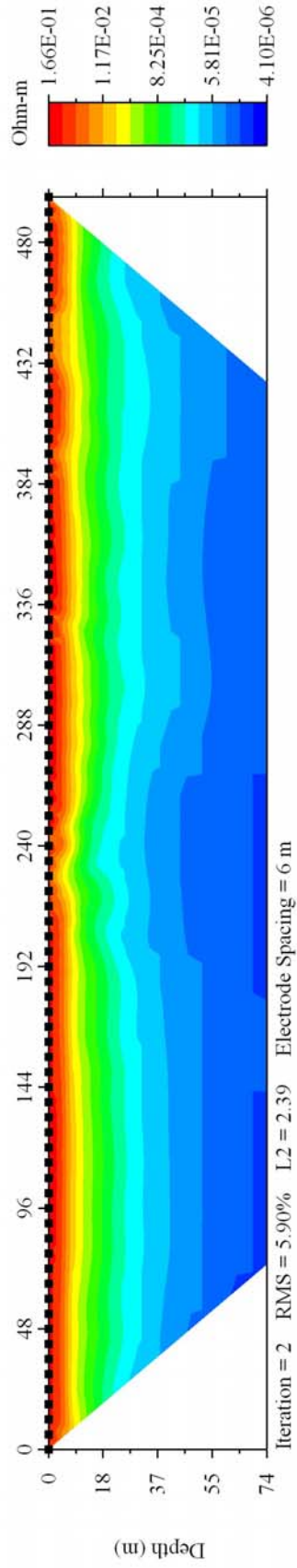
LINE UK-003

Data with Relative Misfit Above 20% Removed



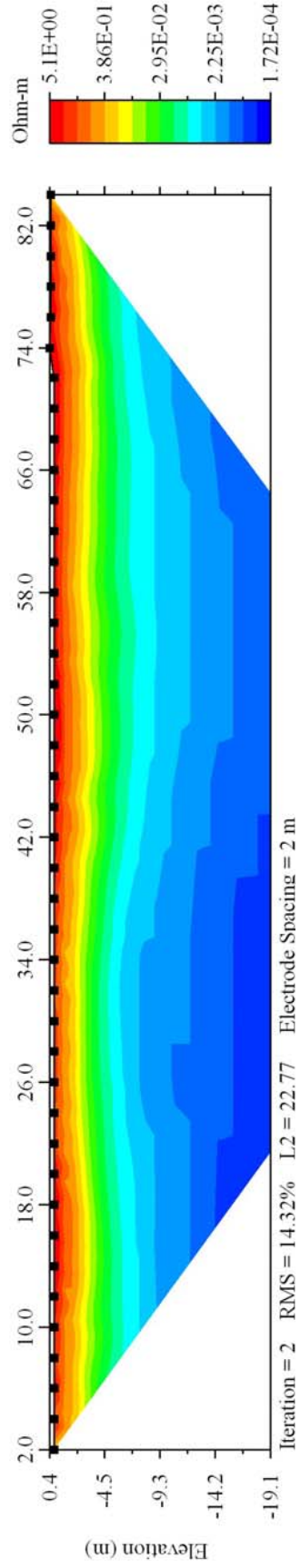
LINE UK-003

Data with Relative Misfit Above 14% Removed



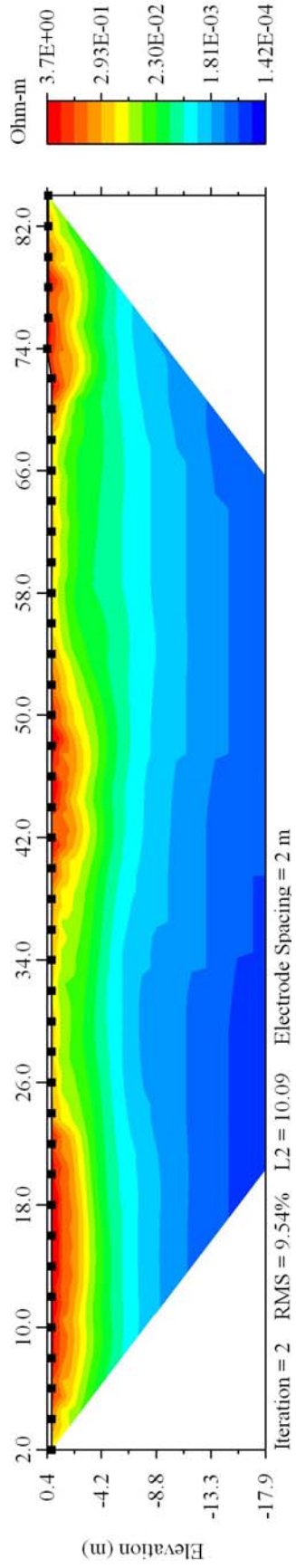
LINE UK-004

No Misfit Data Removed



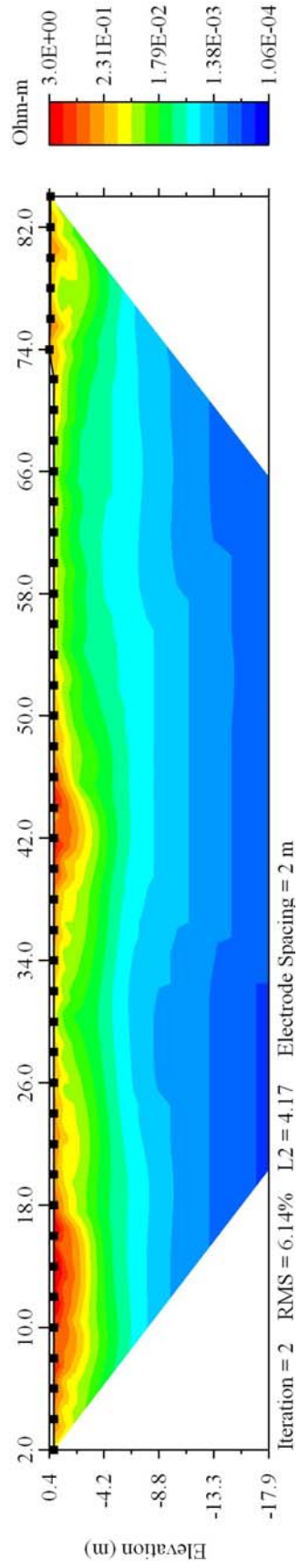
LINE UK-004

Data with Relative Misfit Above 17.5% Removed



LINE UK-004

Data with Relative Misfit Above 12.5% Removed



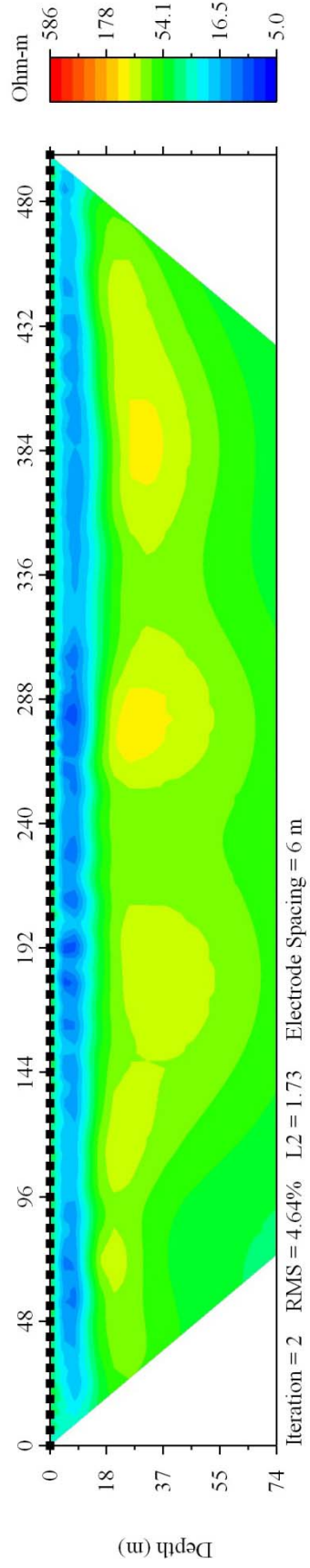
Appendix B

Section 5

Representative inverted resistivity profiles normalized to a common resistivity scale. These normalized sections allow for the comparison of resistivity values obtained throughout the study area.

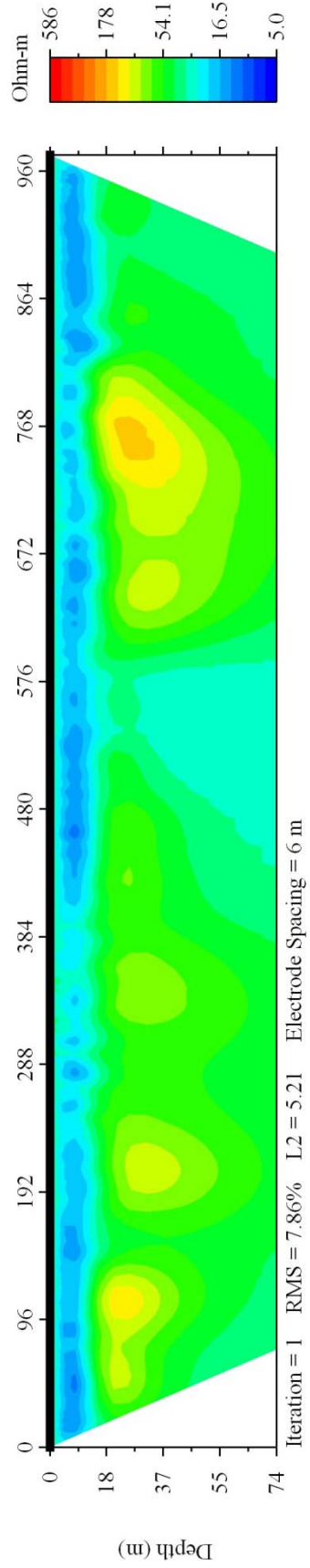
LINE UK-001

Data with Relative Misfit Above 10% Removed



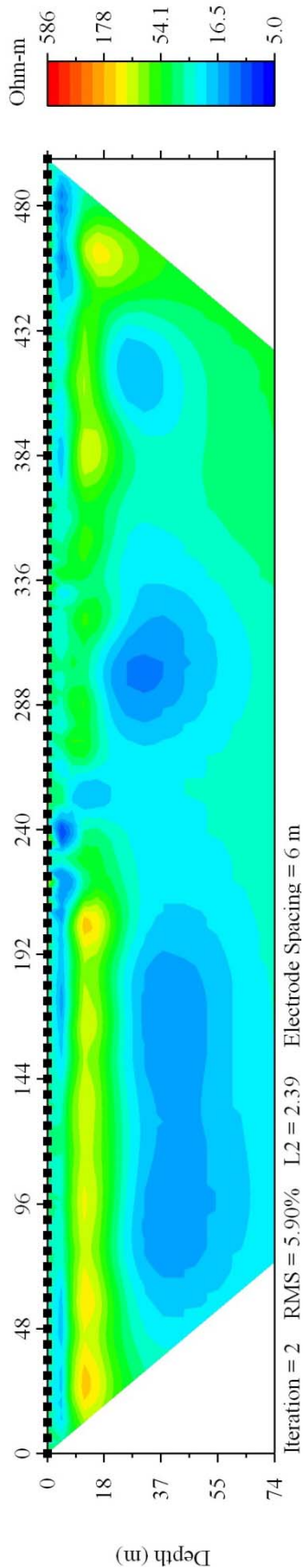
LINE UK-002

Data with Relative Misfit Above 16.5% Removed



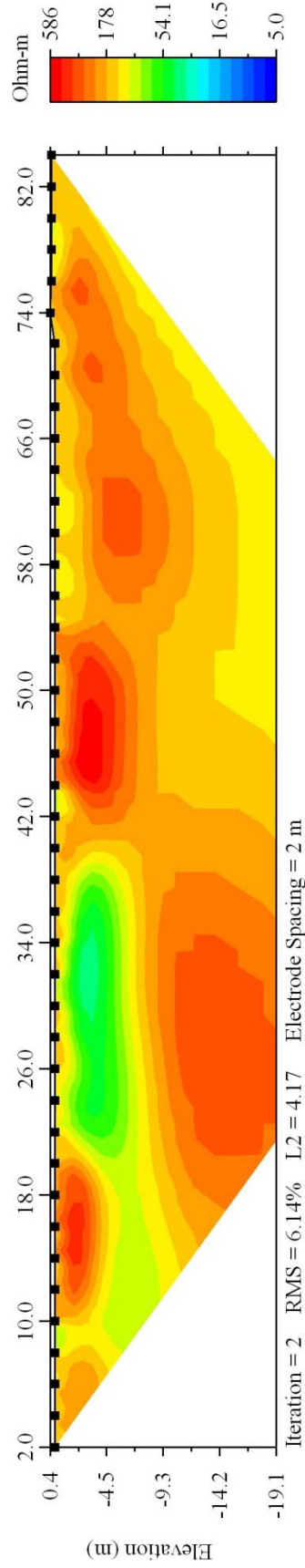
LINE UK-003

Data with Relative Misfit Above 14% Removed



LINE UK-004

Data with Relative Misfit Above 12.5% Removed



Appendix B

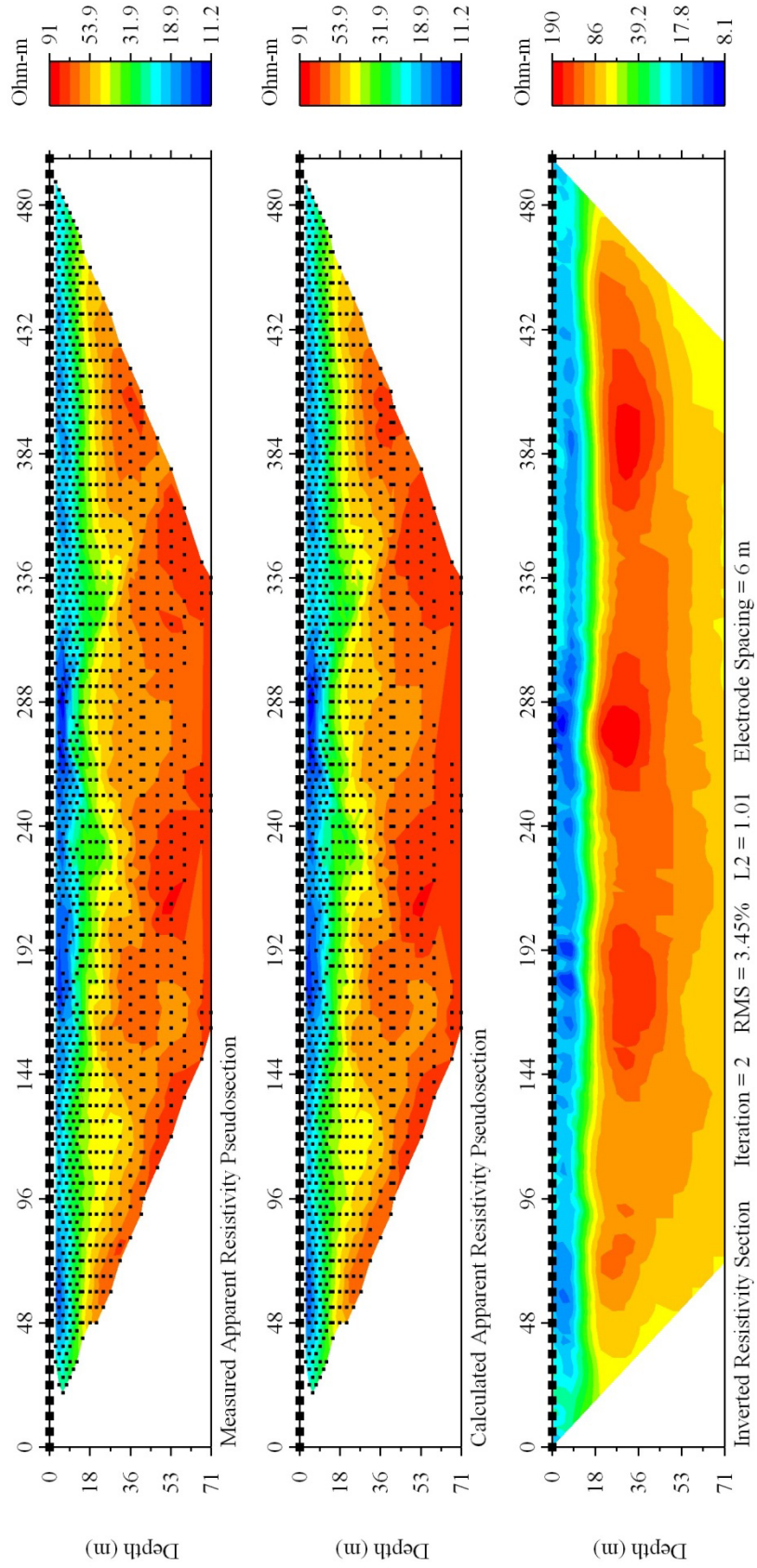
Section 6

Selected resistivity profiles processed using alternate techniques. Settings that varied between trials are given in the table below. In trials 56 (Line UK-001), 17 (UK-002), 22 (UK-003) and 18 (UK-004) all data were retained with the importance of noisy points suppressed relative to other points. This approach yields very large RMS errors, and therefore L2-norm values are considered when selecting the most appropriate iteration.

Selected Processing Parameters									
Line Name	Trial	Inversion Method	Horiz/Vert Roughness Ratio	% Relative Data Misfit	% Data Removed	Inversion Strating Model	Depth Factor	RMS Error	L2-norm
UK-001	58	Robust	1.2	8.0	6.9	Pseudo section	1.0	3.45	1.01
	54		1.2	9.0	8.0	Avg. App. Res.	1.7	3.85	1.20
	38	Smooth	1.2	14.0	3.0	Pseudo section	2.0	3.65	1.15
	14		1.2	NONE	NONE	Avg. App. Res.	1.0	9.98	0.73
UK-002	44	Robust	1.2	19.5	25.9	Pseudo section	1.0	6.87	3.73
	11		1.2	13.5	29.5	Avg. App. Res.	1.1	5.14	2.12
	14	Smooth	1.5	14	28.1	Pseudo section	1.1	5.45	2.37
	17		1.5	NONE	NONE	Avg. App. Res.	1.1	116.59	0.90
UK-003	53	Robust	1.0	20	21.5	Pseudo section	1.0	6.98	2.94
	9		1.0	15.2	25.6	Avg. App. Res.	1.1	4.54	1.27
	51	Smooth	1.0	30	23.5	Pseudo section	1.0	6.74	2.38
	22		1.0	NONE	NONE	Avg. App. Res.	1.1	109.76	1.21
UK-004	13	Robust	0.5	7.5	13.6	Pseudo section	1.0	4.84	2.59
	15		0.5	7.5	19.9	Avg. App. Res.	1.0	5.46	3.29
	17	Smooth	0.5	6	19.9	Pseudo section	1.0	3.40	1.27
	18		0.5	NONE	NONE	Avg. App. Res.	1.0	9.08	0.88

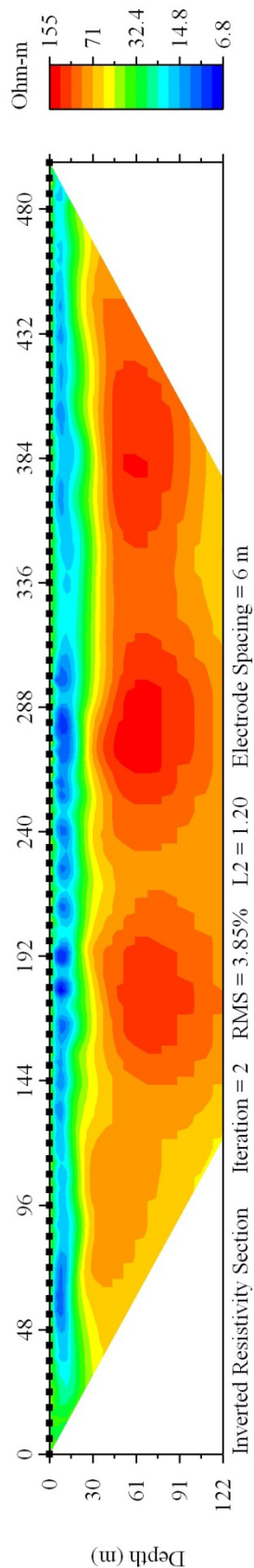
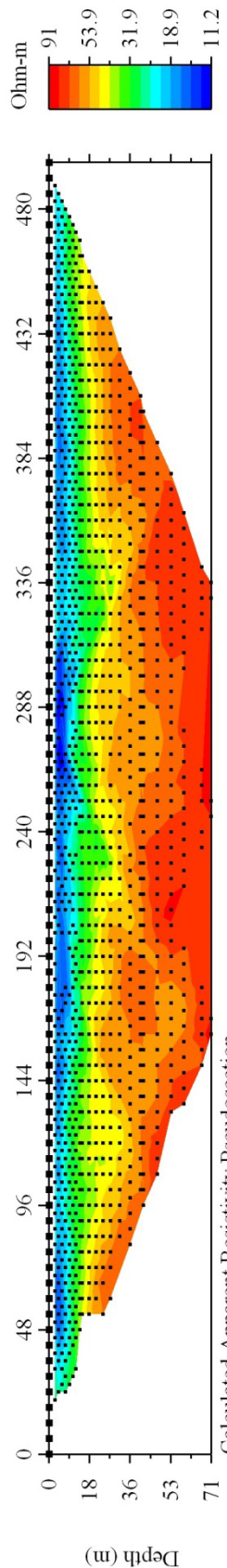
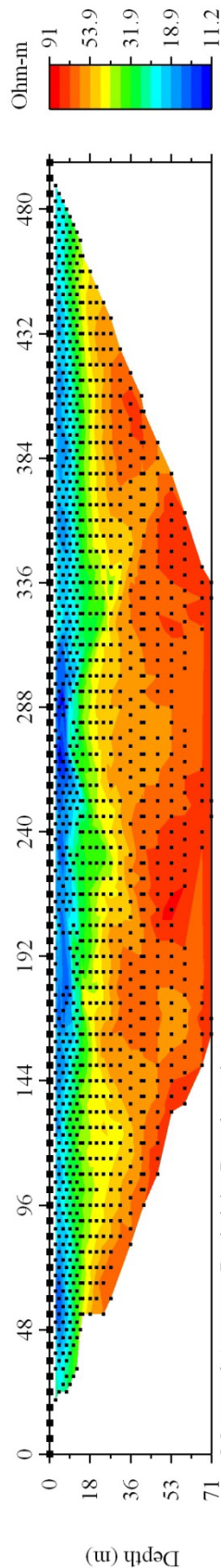
LINE UK-001

Trial 58



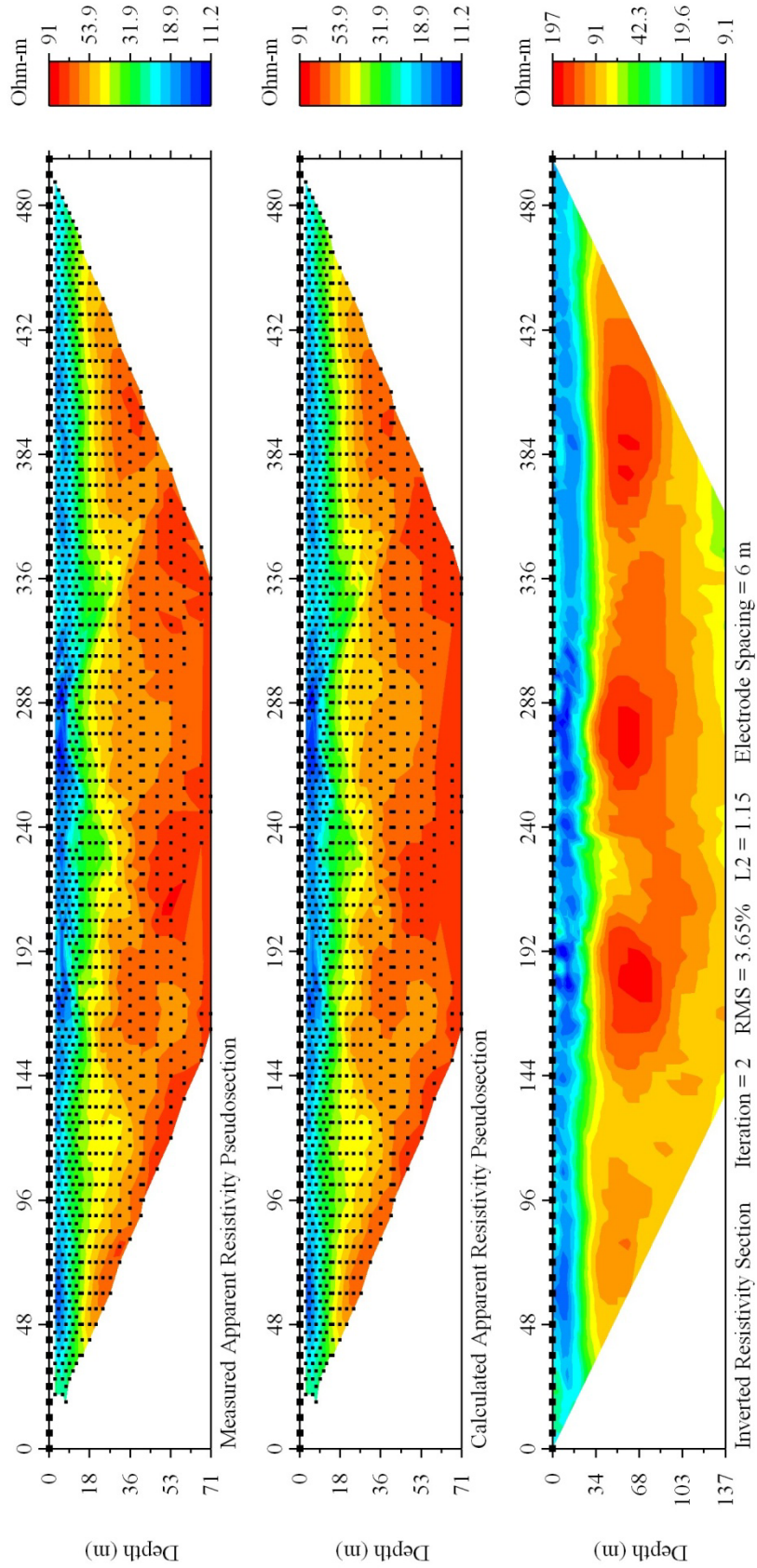
LINE UK-001

Trial 54



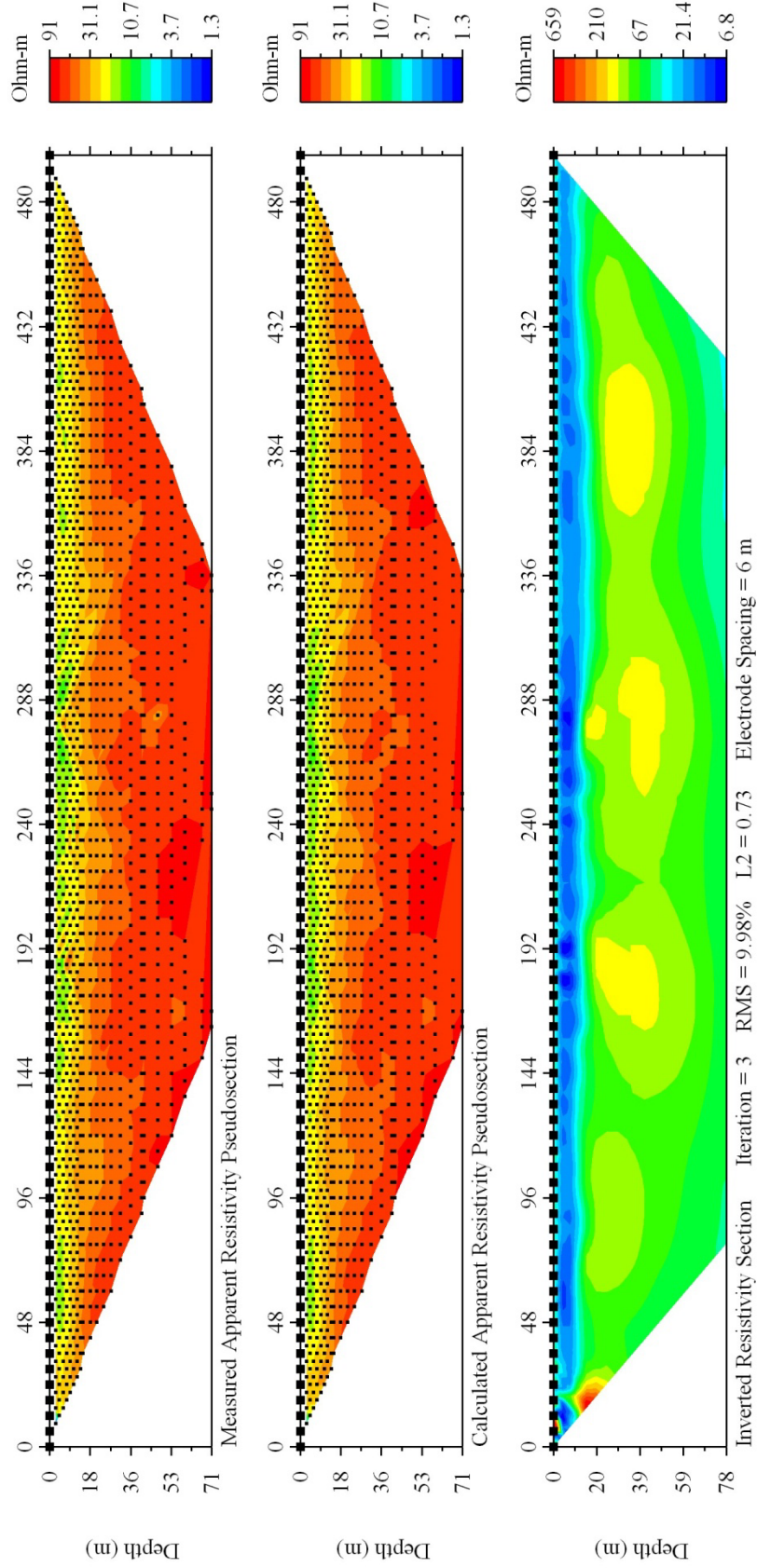
LINE UK-001

Trial 38



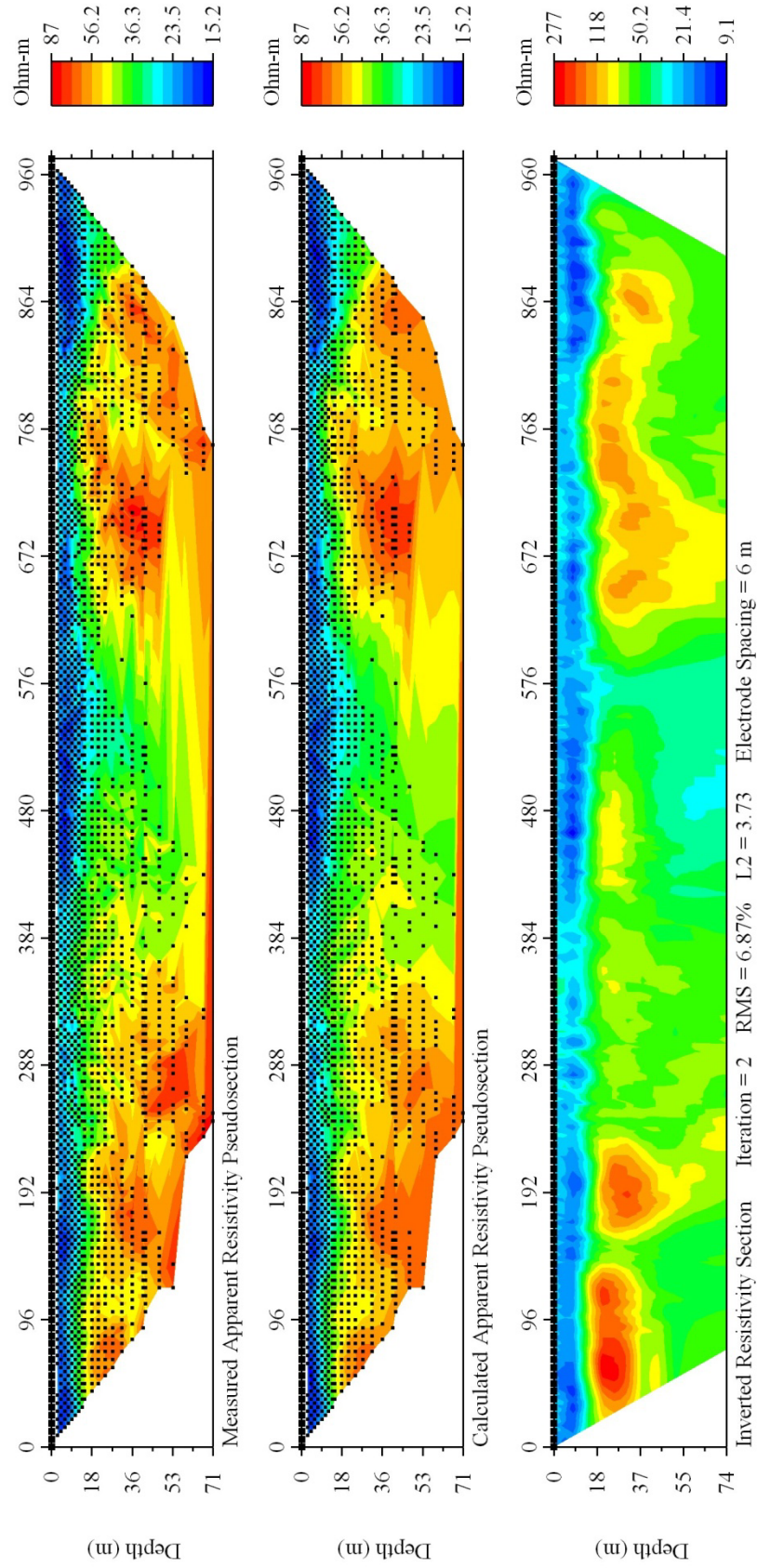
LINE UK-001

Trial 14



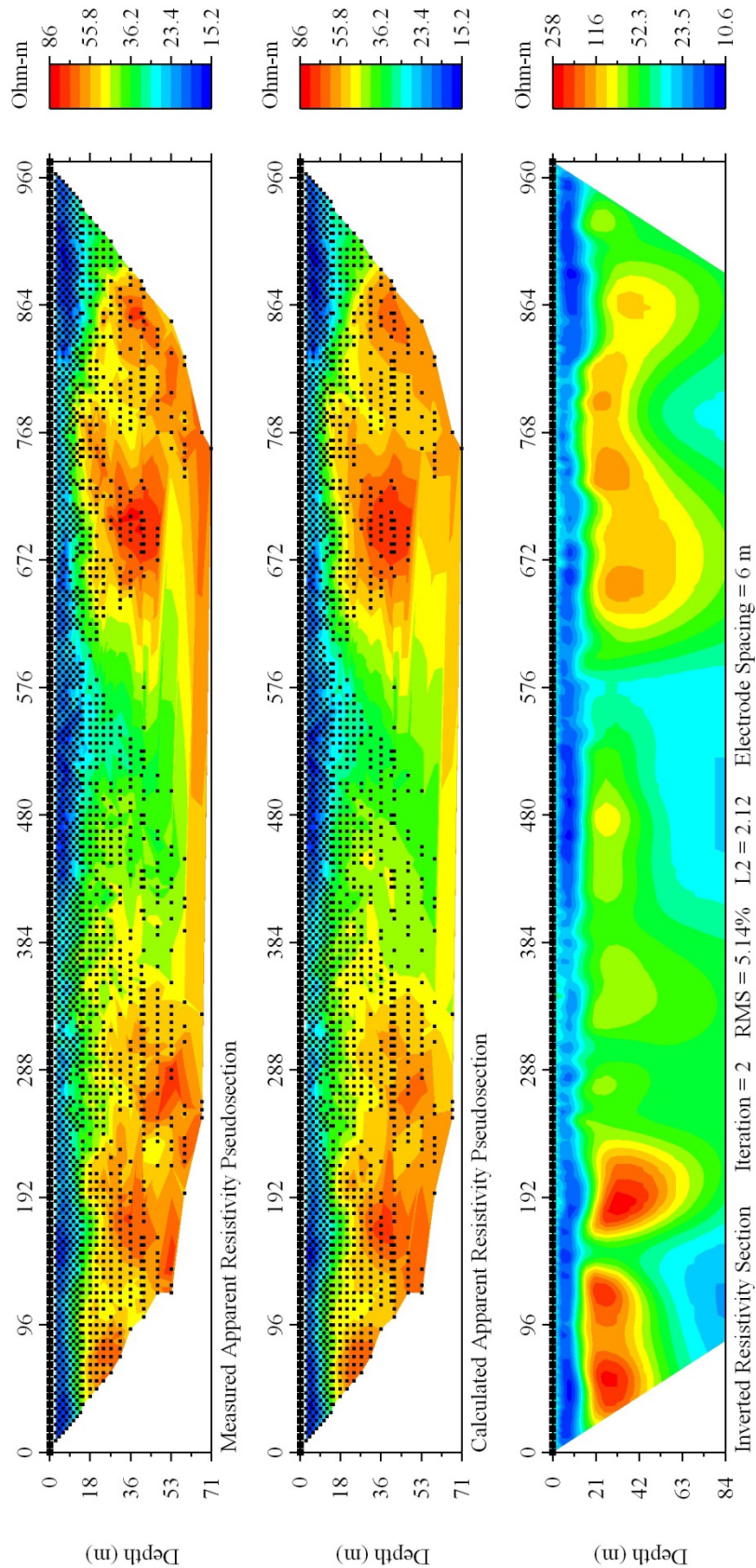
LINE UK-002

Trial 44



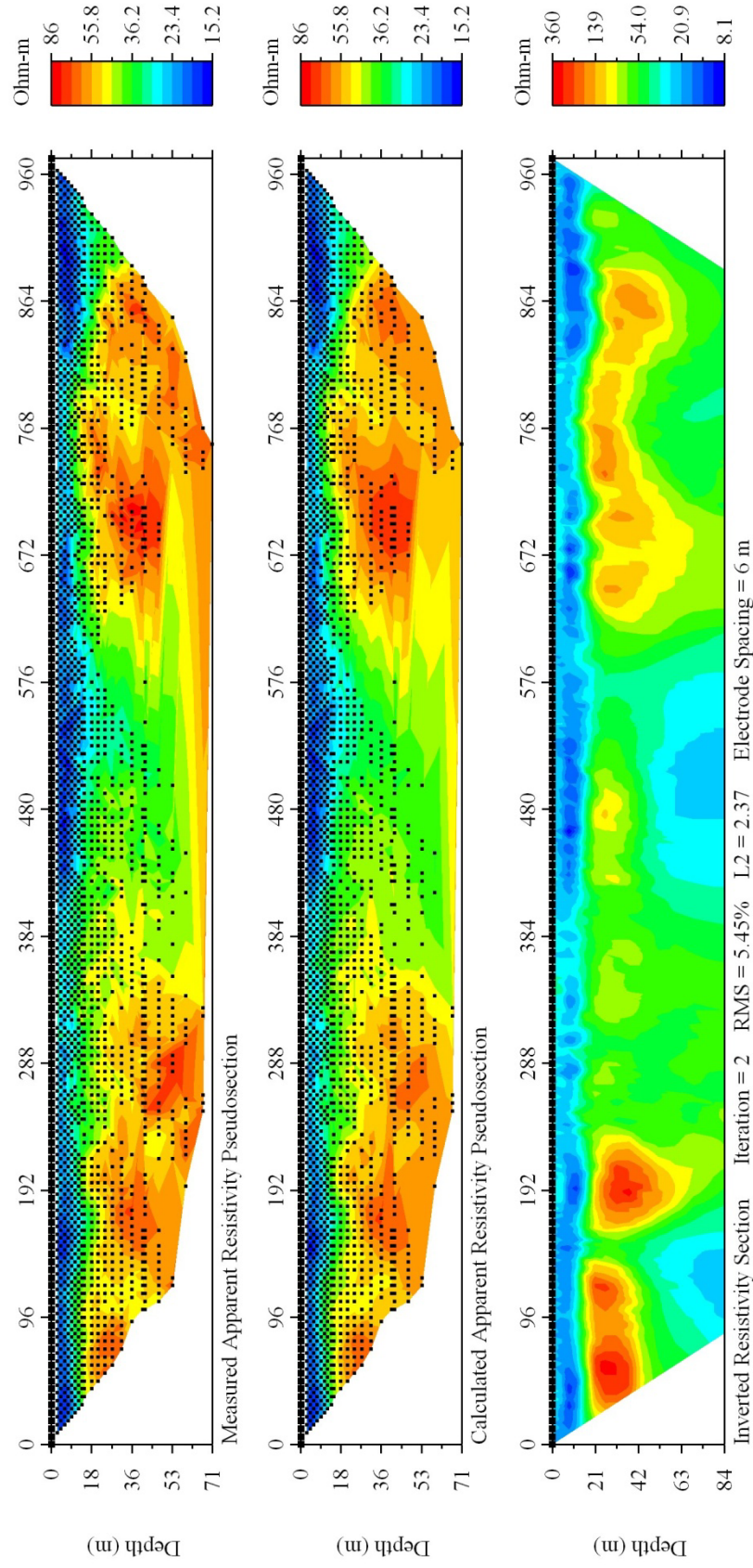
LINE UK-002

Trial 11



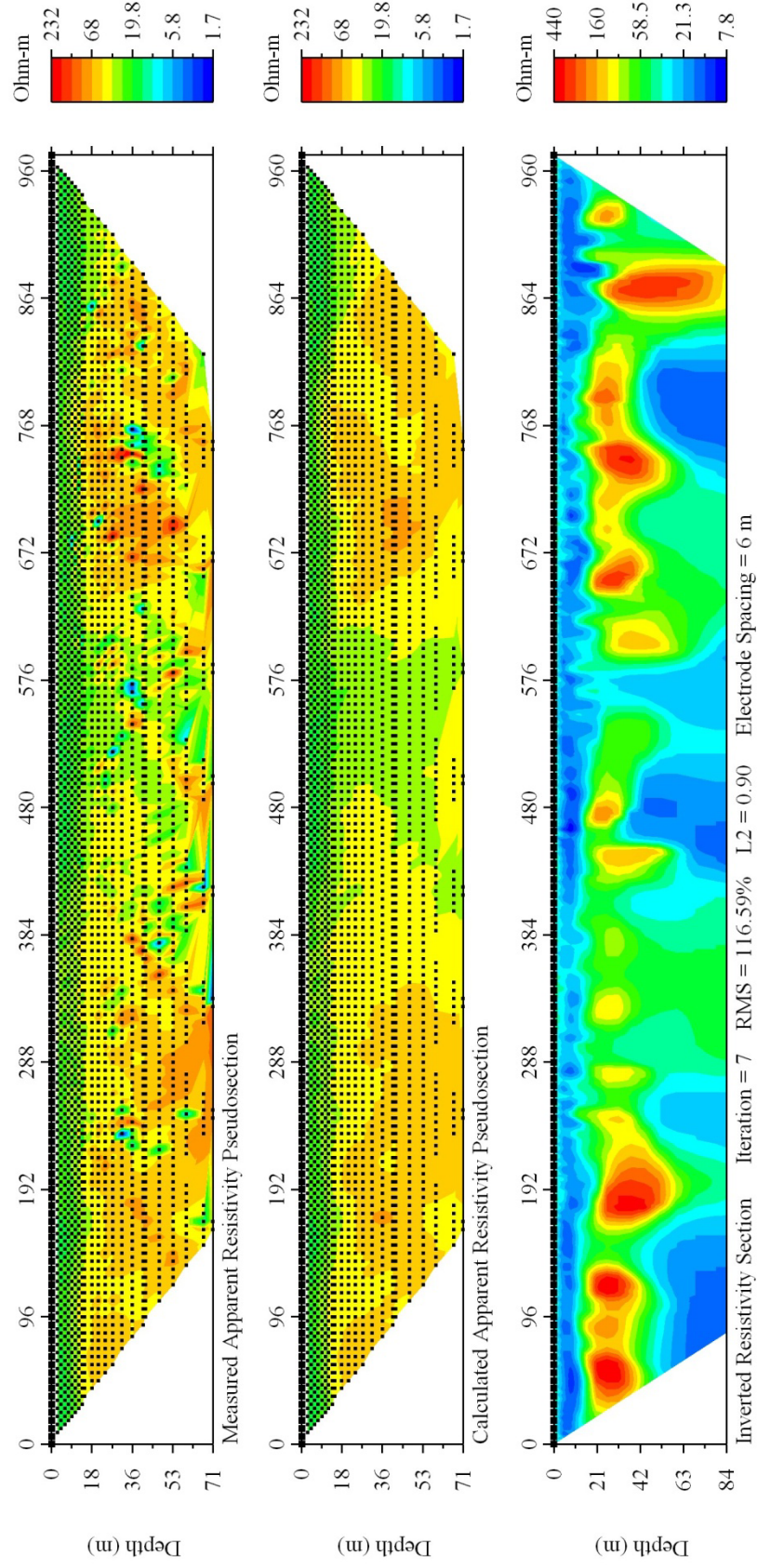
LINE UK-002

Trial 14



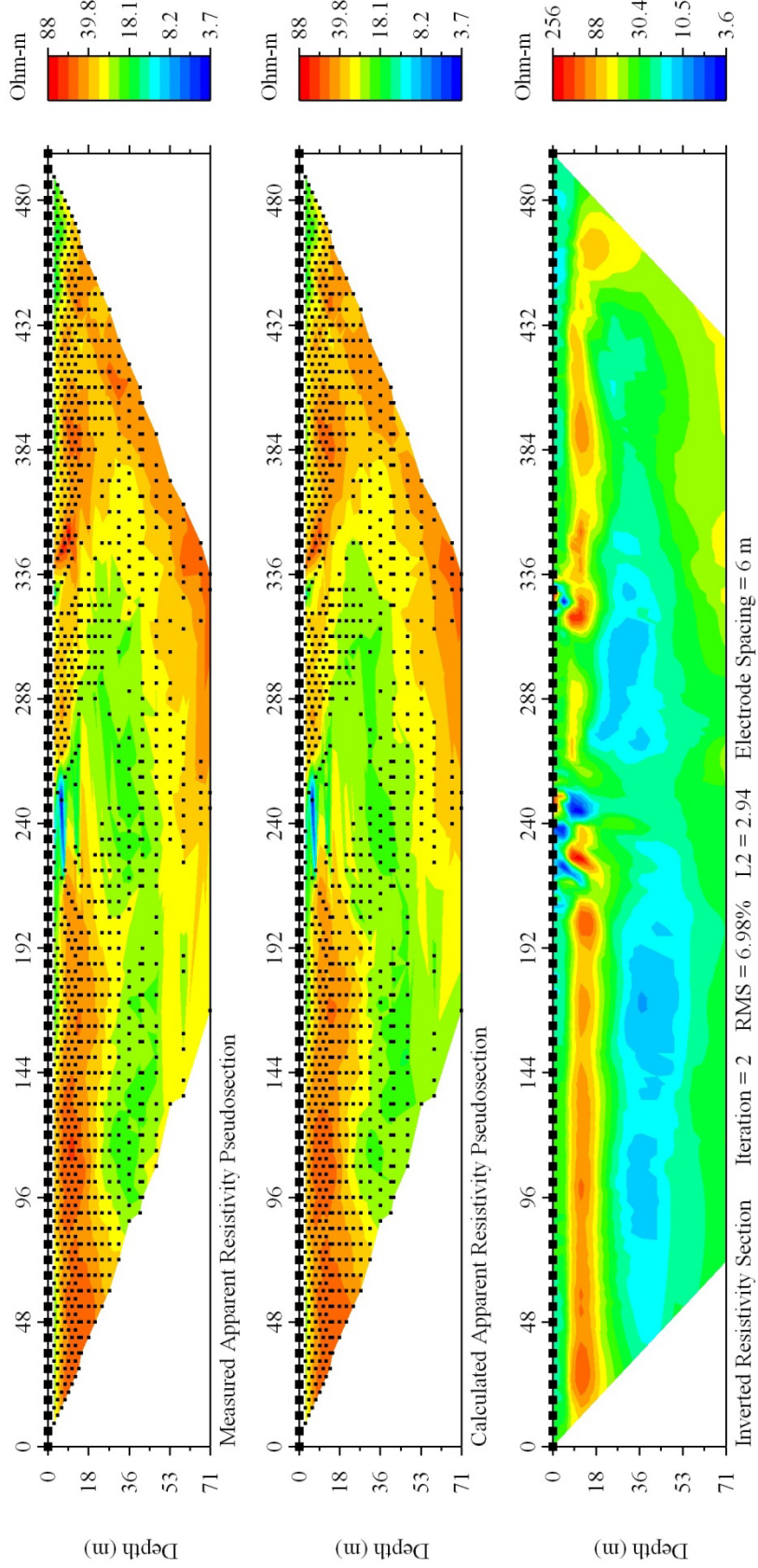
LINE UK-002

Trial 17



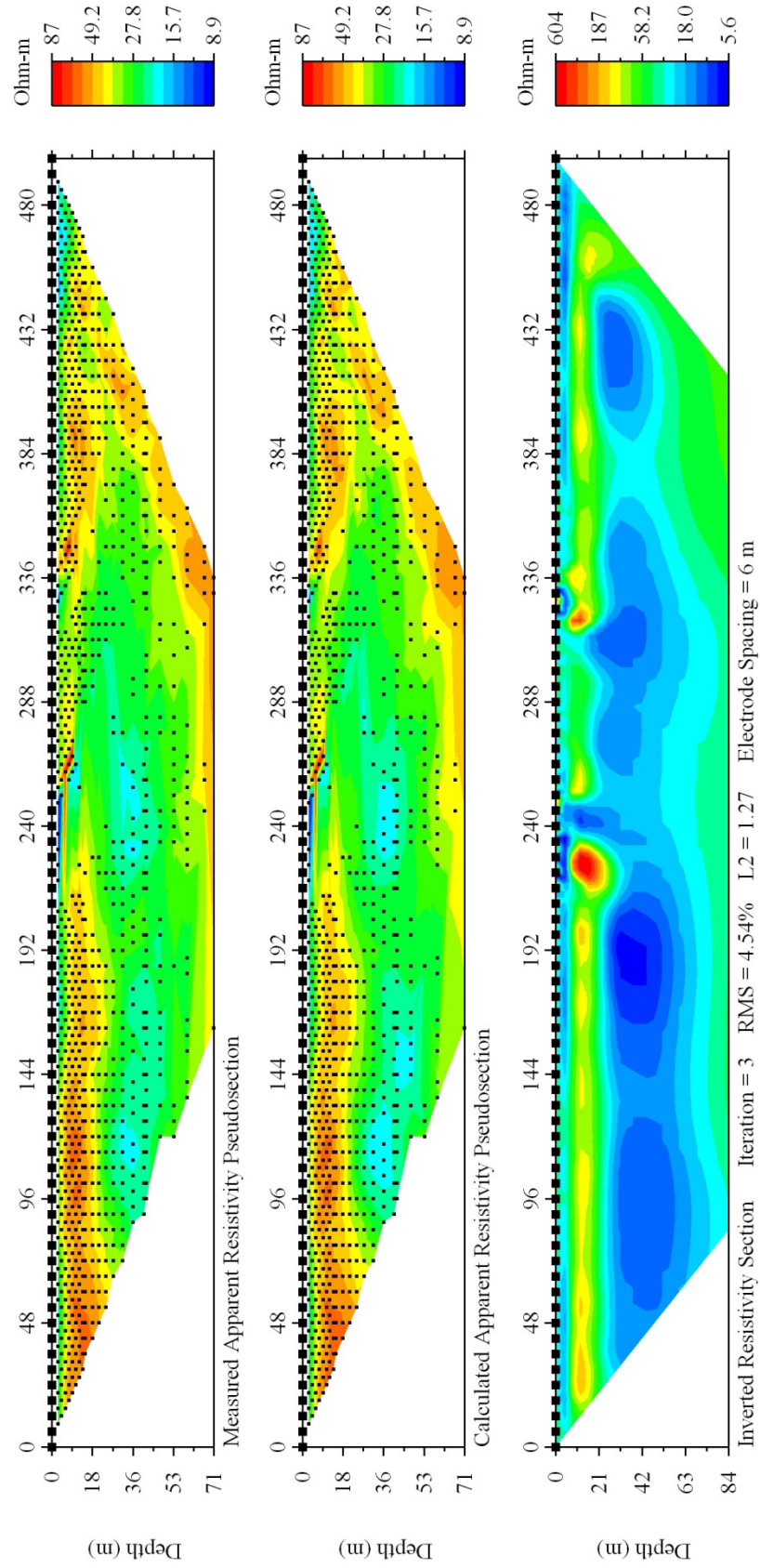
LINE UK-003

Trial 53



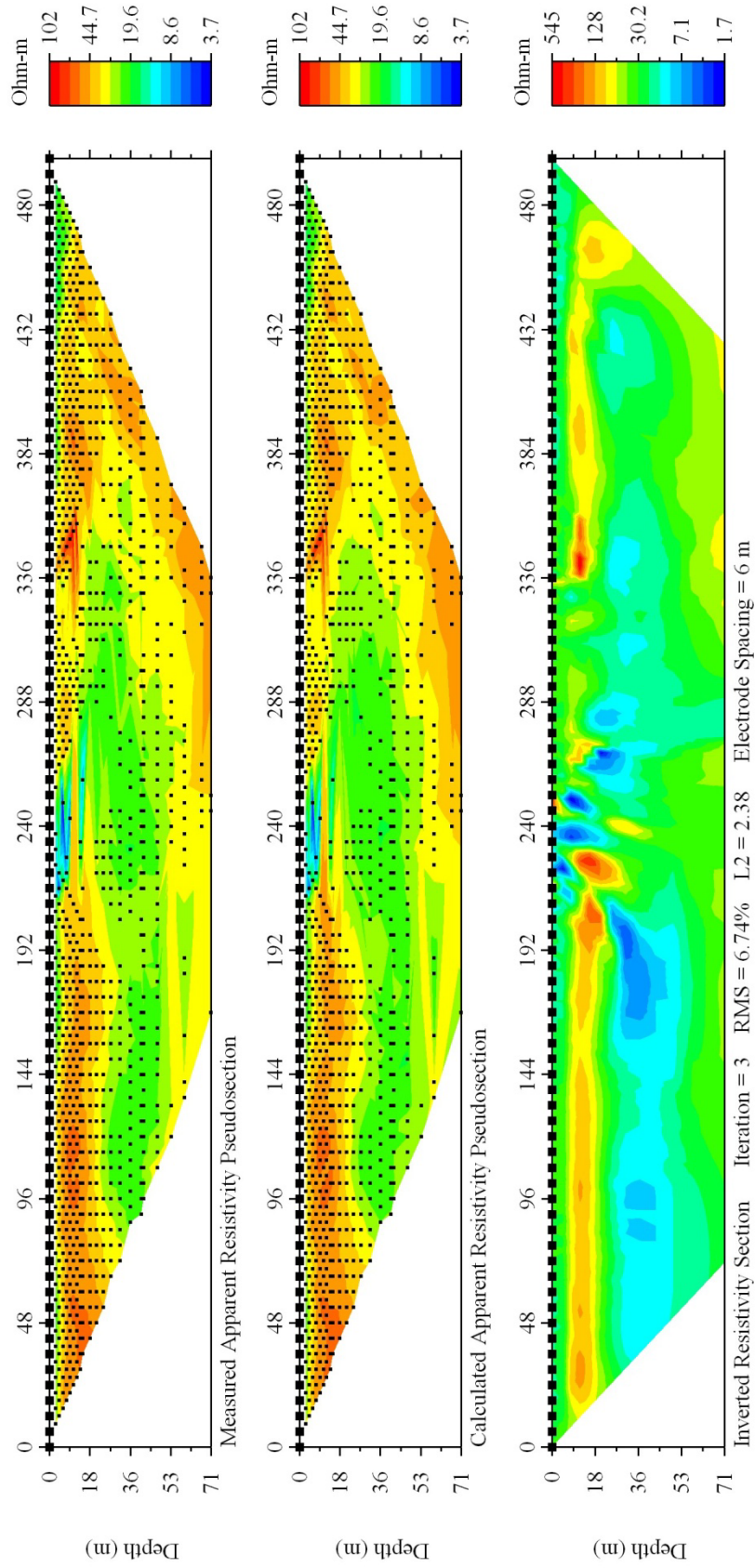
LINE UK-003

Trial 9



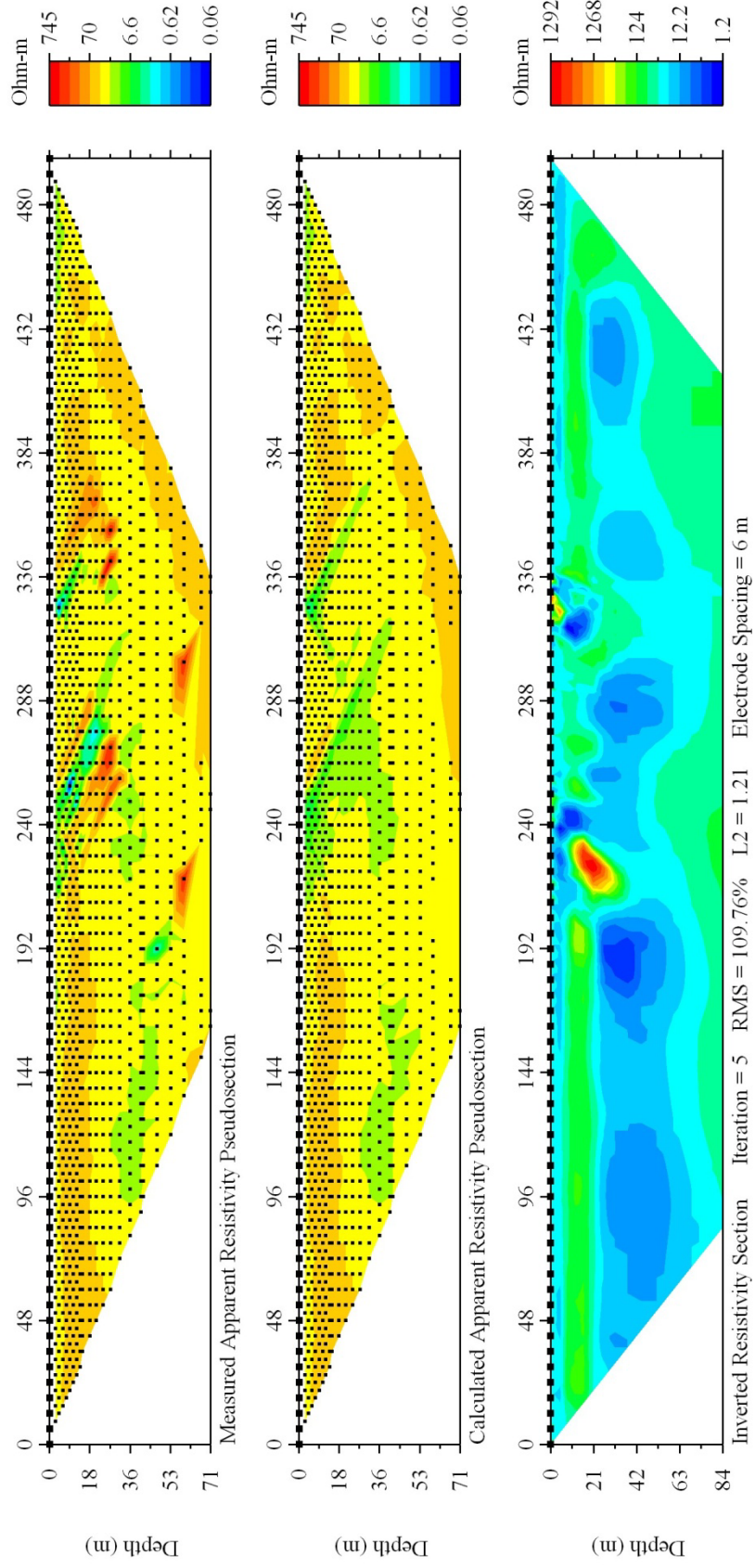
LINE UK-003

Trial 51



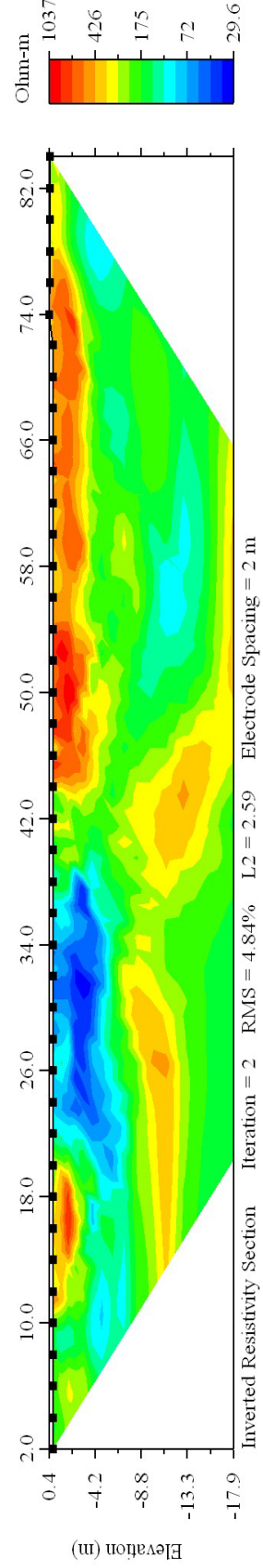
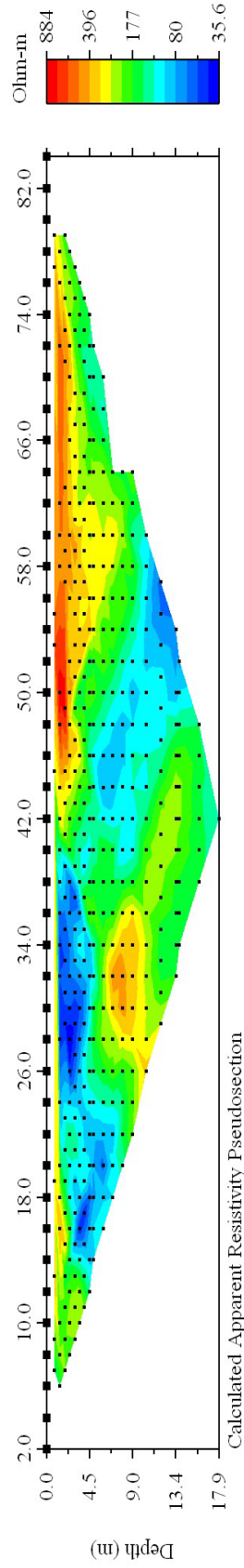
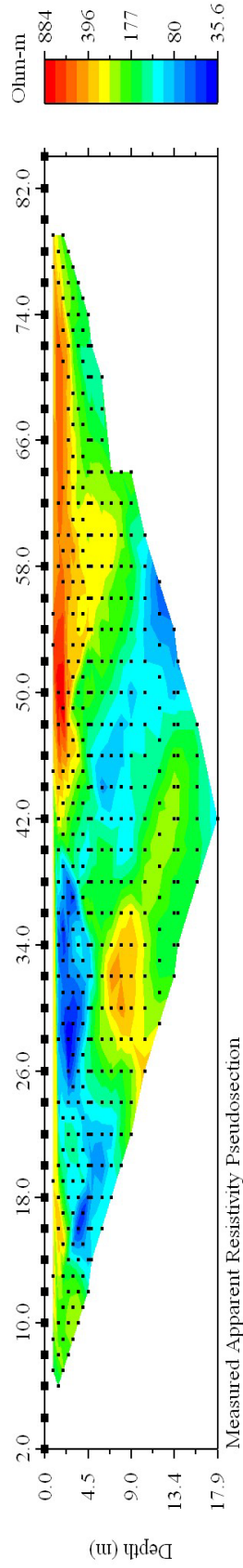
LINE UK-003

Trial 22



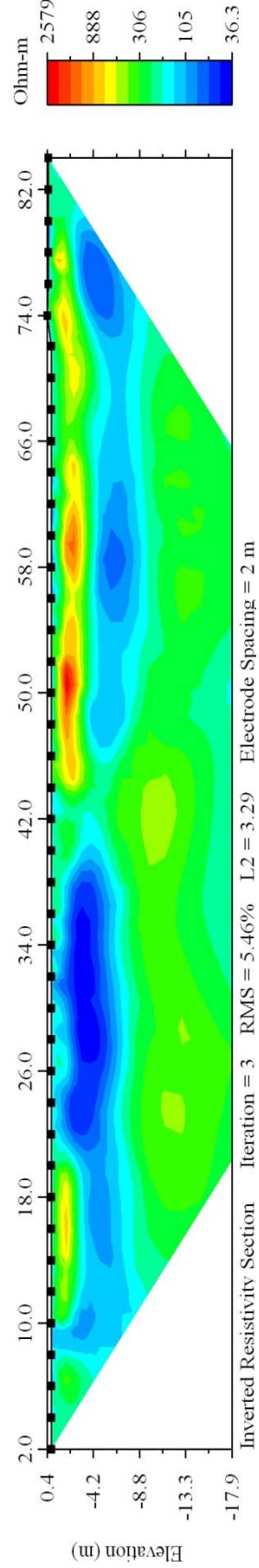
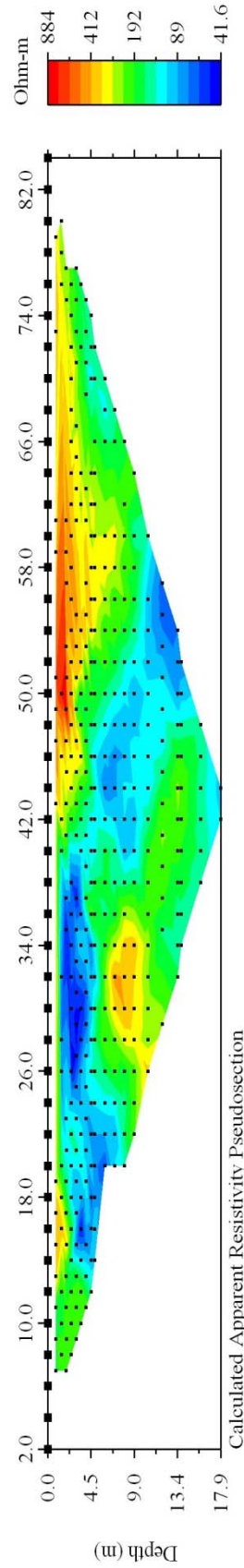
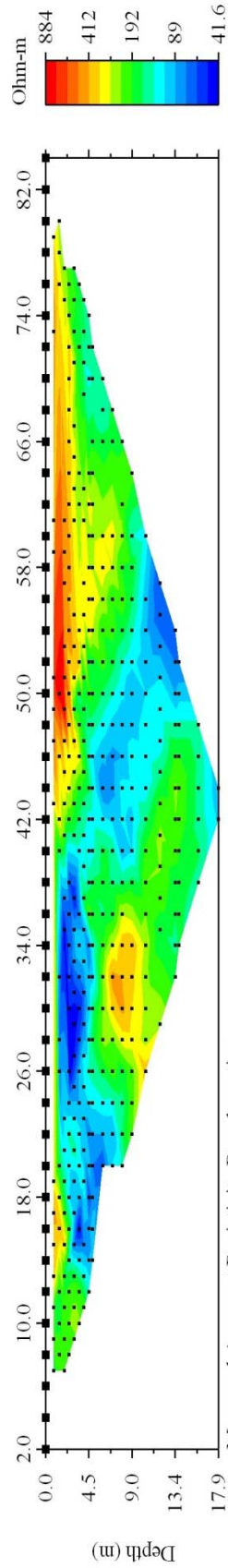
LINE UK-004

Trial 13



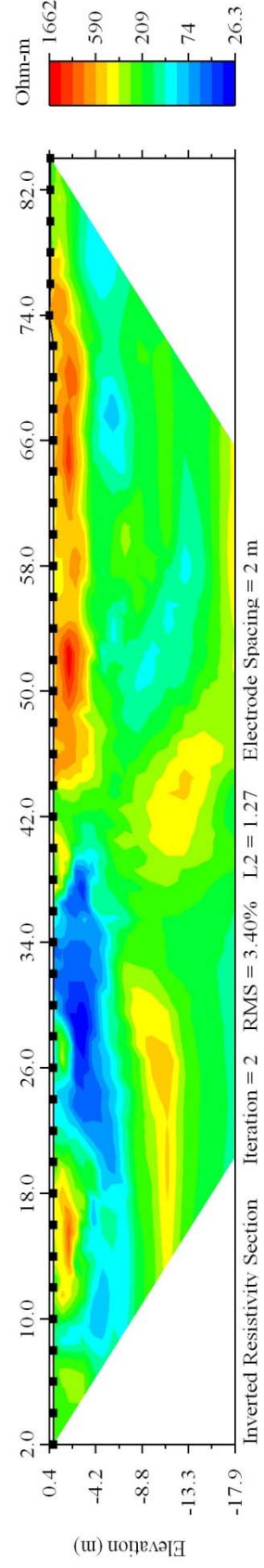
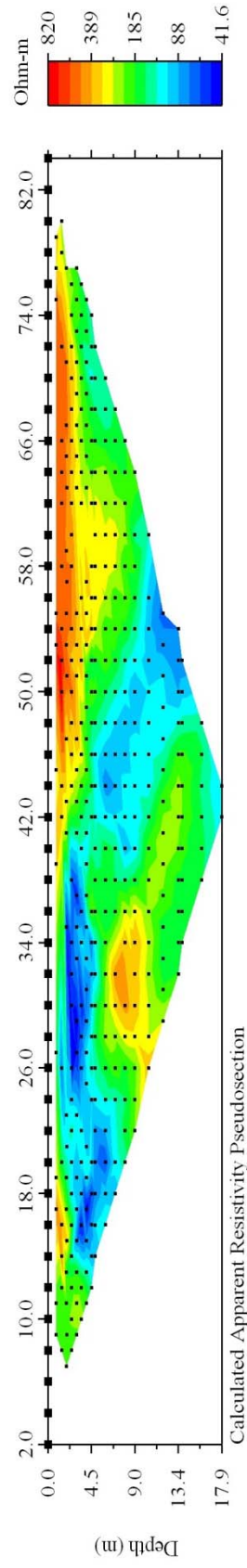
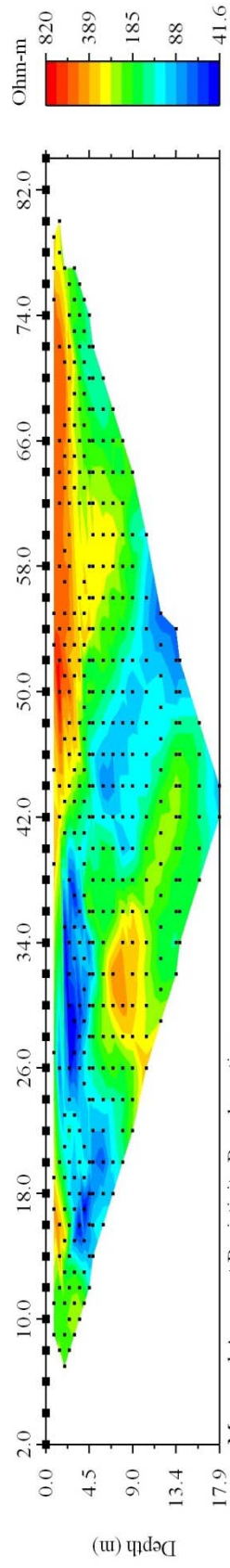
LINE UK-004

Trial 15



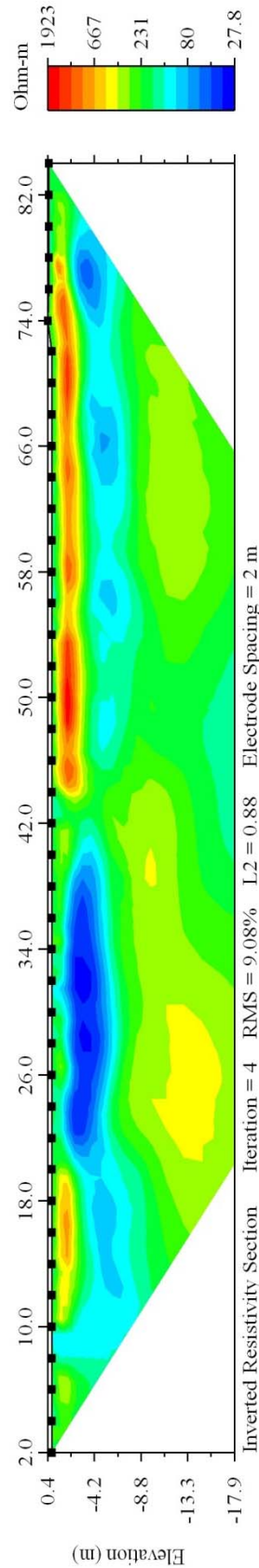
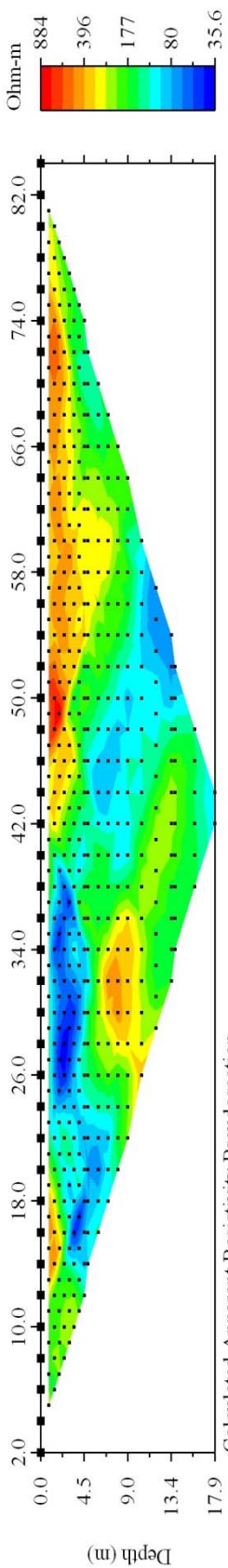
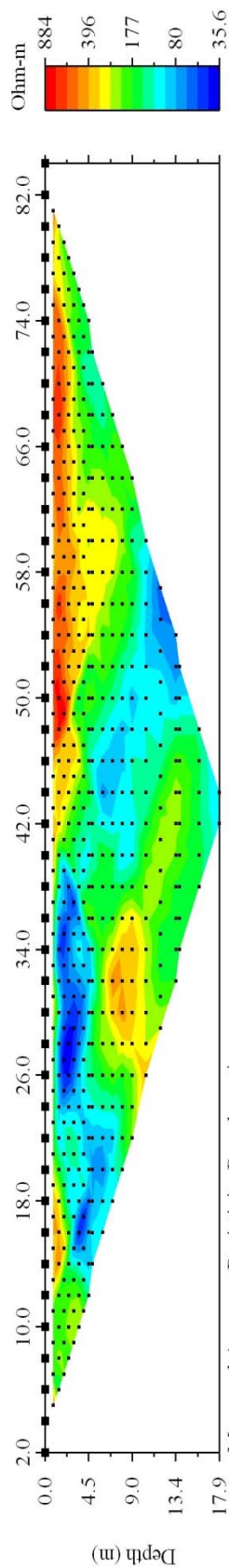
LINE UK-004

Trial 17



LINE UK-004

Trial 18



Appendix C

Depths to lithologic units within the study area based on bore logs. All values are provided by S. Hampson, 2007 except entries for stations MW201 and MW202 interpreted by C. Blits, 2008.

Depths to Soil Horizons from Wells and Borings						
Station Name	X	Y	Elevation	SoilID	HorizonID	Depth
22	-13147.173	245.548	116.1	0	7	0.0
22	-13147.173	245.548	100.9	2	6	15.2
22	-13147.173	245.548	91.1	3	5	25.0
22	-13147.173	245.548	88.1	3	0	28.0
23	-13401.712	3870.152	110.0	0	7	0.0
23	-13401.712	3870.152	97.8	2	6	12.2
23	-13401.712	3870.152	87.2	3	5	22.9
23	-13401.712	3870.152	83.5	3	0	26.5
25	-10312.644	5807.970	109.4	0	7	0.0
25	-10312.644	5807.970	95.7	2	6	13.7
25	-10312.644	5807.970	86.6	3	5	22.9
25	-10312.644	5807.970	82.9	3	0	26.5
26	-5471.341	3210.491	112.5	0	7	0.0
26	-5471.341	3210.491	96.3	2	6	16.2
26	-5471.341	3210.491	90.2	3	5	22.3
26	-5471.341	3210.491	86.6	3	0	25.9
34	-3936.174	7984.749	108.2	0	7	0.0
34	-3936.174	7984.749	95.4	2	6	12.8
34	-3936.174	7984.749	83.2	3	5	25.0
34	-3936.174	7984.749	83.2	3	0	25.0
36	-2871.058	11603.893	105.6	0	7	0.0
36	-2871.058	11603.893	94.6	2	6	11.0
36	-2871.058	11603.893	90.4	3	5	15.2
36	-2871.058	11603.893	86.7	3	0	18.9
37	-7403.254	10139.494	111.6	0	7	0.0
37	-7403.254	10139.494	93.3	2	6	18.3
37	-7403.254	10139.494	84.7	3	5	26.8
37	-7403.254	10139.494	84.7	3	0	26.9
D-14	-6090.000	6930.000	107.3	0	7	0.0
D-14	-6090.000	6930.000	92.0	2	6	15.2
D-14	-6090.000	6930.000	89.0	2	0	18.3
J-3	-5262.000	5986.000	113.9	0	7	0.0
J-3	-5262.000	5986.000	95.7	2	6	18.2
J-3	-5262.000	5986.000	86.9	3	5	27.1
J-3	-5262.000	5986.000	86.6	3	0	27.4
J-12	-6163.000	4546.000	112.8	0	7	0.0
J-12	-6163.000	4546.000	94.8	2	6	18.0
J-12	-6163.000	4546.000	86.9	3	5	25.9
J-12	-6163.000	4546.000	86.6	3	0	26.2

Station Name	X	Y	Elevation	SoilID	HorizonID	Depth
J-13	-6510.000	4771.000	110.6	0	7	0.0
J-13	-6510.000	4771.000	95.1	2	6	15.5
J-13	-6510.000	4771.000	85.3	3	5	25.2
J-13	-6510.000	4771.000	85.0	3	0	25.5
J-15	-7444.000	5142.000	109.8	0	7	0.0
J-15	-7444.000	5142.000	91.4	2	6	18.4
J-15	-7444.000	5142.000	85.0	3	5	24.8
J-15	-7444.000	5142.000	84.7	3	0	25.1
J-16	-7954.000	5317.000	110.2	0	7	0.0
J-16	-7954.000	5317.000	91.4	2	6	18.7
J-16	-7954.000	5317.000	88.7	3	5	21.5
J-16	-7954.000	5317.000	88.4	3	0	21.8
J-19	-5305.000	3195.000	113.8	0	7	0.0
J-19	-5305.000	3195.000	92.4	2	6	21.4
J-19	-5305.000	3195.000	86.3	3	5	27.5
J-19	-5305.000	3195.000	86.0	3	0	27.8
J-22	-6608.000	3112.000	111.6	0	7	0.0
J-22	-6608.000	3112.000	91.7	2	6	19.8
J-22	-6608.000	3112.000	87.2	3	5	24.4
J-22	-6608.000	3112.000	86.9	3	0	24.7
J-24	-7490.000	3112.000	110.6	0	7	0.0
J-24	-7490.000	3112.000	93.0	2	6	17.6
J-24	-7490.000	3112.000	86.6	3	5	24.0
J-24	-7490.000	3112.000	86.3	3	0	24.3
J-33	-7349.000	1464.000	112.4	0	7	0.0
J-33	-7349.000	1464.000	94.8	2	6	17.6
J-33	-7349.000	1464.000	82.6	3	5	29.8
J-33	-7349.000	1464.000	82.3	3	0	30.1
J-34	-7497.000	1465.000	111.9	0	7	0.0
J-34	-7497.000	1465.000	93.6	2	6	18.3
J-34	-7497.000	1465.000	86.3	3	5	25.7
J-34	-7497.000	1465.000	86.0	3	0	26.0
J-38	-7847.000	1414.000	111.2	0	7	0.0
J-38	-7847.000	1414.000	93.6	2	6	17.6
J-38	-7847.000	1414.000	84.7	3	5	26.4
J-38	-7847.000	1414.000	84.4	3	0	26.7
MLS-31	-3056.352	12842.772	103.8	0	7	0.0
MLS-31	-3056.352	12842.772	89.9	2	6	13.8
MLS-31	-3056.352	12842.772	75.7	3	5	28.0
MLS-31	-3056.352	12842.772	72.8	3	0	30.9

Station Name	X	Y	Elevation	SoilID	HorizonID	Depth
MW121	-5678.000	6162.000	113.5	0	7	0.0
MW121	-5678.000	6162.000	97.7	2	6	15.9
MW121	-5678.000	6162.000	89.7	3	5	23.8
MW121	-5678.000	6162.000	61.7	4	4	51.8
MW121	-5678.000	6162.000	52.4	5	3	61.1
MW121	-5678.000	6162.000	49.1	5	0	64.5
MW194	-10178.000	1866.000	107.7	0	7	0.0
MW194	-10178.000	1866.000	93.6	2	6	14.2
MW194	-10178.000	1866.000	91.1	2	0	16.6
MW200	-4824.000	4443.000	114.9	0	7	0.0
MW200	-4824.000	4443.000	94.5	2	6	20.4
MW200	-4824.000	4443.000	90.5	2	0	24.4
MW201			111.1	0	7	0.0
MW201			96.9	2	6	14.2
MW201			91.4	3	5	19.7
MW201			91.4	3	0	19.7
MW202			112.8	0	7	0.0
MW202			97.1	2	6	15.7
MW202			91.4	3	5	21.3
MW202			91.3	3	0	21.5
S-22	-8438.000	981.000	111.7	0	7	0.0
S-22	-8438.000	981.000	93.3	2	6	18.4
S-22	-8438.000	981.000	87.2	3	5	24.5
S-22	-8438.000	981.000	85.0	3	0	26.6
SB-38	-7353.000	1449.000	112.2	0	7	0.0
SB-38	-7353.000	1449.000	94.5	2	6	17.7
SB-38	-7353.000	1449.000	83.5	3	5	28.7
SB-38	-7353.000	1449.000	83.2	3	0	29.0
TVAD-14	-2790.000	12825.000	107.3	0	7	0.0
TVAD-14	-2790.000	12825.000	92.7	2	6	14.6
TVAD-14	-2790.000	12825.000	92.0	2	0	15.2
Z-12	-2980.580	12044.520	107.0	0	7	0.0
Z-12	-2980.580	12044.520	84.2	2	6	22.9
Z-12	-2980.580	12044.520	73.5	3	5	33.5
Z-12	-2980.580	12044.520	64.3	4	4	42.7
Z-12	-2980.580	12044.520	37.2	5	3	69.8
Z-12	-2980.580	12044.520	5.5	6	2	101.5
Z-12	-2980.580	12044.520	5.5	7	1	101.5
Z-12	-2980.580	12044.520	3.4	7	0	103.7

Station	X	Y	Elevation	SoilID	HorizonID	Depth
Z-16	-8436.660	385.150	113.1	0	7	0.0
Z-16	-8436.660	385.150	94.2	2	6	18.9
Z-16	-8436.660	385.150	82.3	3	5	30.8
Z-16	-8436.660	385.150	63.7	4	4	49.4
Z-16	-8436.660	385.150	44.8	5	3	68.3
Z-16	-8436.660	385.150	14.9	6	2	98.1
Z-16	-8436.660	385.150	14.9	7	1	98.2
Z-16	-8436.660	385.150	4.4	7	0	108.7

REFERENCES

- Advanced Geosciences, Inc. (2006). Instruction Manual for EarthImager 2D version 2.2.0 Resistivity and IP Inversion Software: Austin, TX, Advanced Geosciences Inc., 134p.
- Advanced Geosciences, Inc. (2007a). Seminar on resistivity imaging, *AGI Resistivity Imaging Seminar*, Sept. 11-12, Austin, TX.
- Advanced Geosciences, Inc. (2007b). Advanced resistivity imaging, *AGI Advanced Resistivity Imaging Seminar*, Sept. 13-14, Austin, TX.
- Baines, D., D. G. Smith, D. G. Froese, P. Bauman, and G. Nimeck (2002). Electrical resistivity ground imaging (ERGI): a new tool for mapping the lithology and geometry of channel-belts and valley-fills, *Sedimentology* **49**, 441-449.
- Braile, L. W., W. J. Hinze, and G. R. Keller (1997). New Madrid seismicity, gravity anomalies and interpreted ancient rift structures, *Seismological Research Letters* **68**, 599-610.
- Braile, L. W., W. J. Hinze, G. R. Keller, E. G. Lidiak, and J. L. Sexton (1986). Tectonic development of the New Madrid rift complex, Mississippi embayment, North America, *Tectonophysics* **131**, 1-21.
- Burke, K. and J. F. Dewey (1973). Plume-generated triple junctions: key indicators in applying plate tectonics in old rocks, *Journal of Geology* **81**, 406-433.
- CH2M Hill (1989). *Phase I Site Investigation Work Plan Vol. 1*. prepared for the U. S. Department of Energy under contract no. DE-AC05-84OR21400, Paducah, KY, Martin Marietta Energy Systems, Inc.
- Chambers, J. E., O. Kuras, P. I. Meldrum, R. D. Ogilvy, and J. Hollands (2006). Case history: electrical resistivity tomography applied to geologic, hydrogeologic, and engineering investigations at a former waste-disposal site, *Geophysics* **71**, B231-B239
- Clausen, J. L., J. W. Douthitt, K. R. Davis, and N. E. Phillips (1992). *Report of the Paducah Gaseous Diffusion Plant groundwater investigation phase III*. Report KY/E-150, prepared for the U. S. Department of Energy under contract no. DE-AC05-76OR00001, Paducah, KY, Martin Marietta Energy Systems, Inc..
- Clement, W. P., S. Cardimona, A. L. Endres, K. Kadinsky-Cade (1997). Site characterization at the Groundwater Remediation Field Laboratory, *The Leading Edge* **16**, 1617-1621.
- Dahlin, T. and Z. Bing (2003). A numerical comparison of 2D resistivity imaging with ten electrode arrays, *Dept. of Engineering Geology, Lund University and Dept. of Geology and Geophysics, School of Earth and Environmental Sciences, Adelaide University*
- Demant, D., F. Renardy, K. Vanneste, D. Jongmans, T. Camelbeeck, and M. Meghraoui (2001). The use of geophysical prospecting for imaging active faults in the Roer Graben, Belgium, *Geophysics* **66**, 78-89.
- Drahovzal, J. A. and R. T. Hendricks (1997). Geologic features relevant to ground-water flow in the vicinity of the Paducah Gaseous Diffusion Plant: Kentucky Geological Survey Open Report OF-97-02, 33 pp.
- Edwards, L. S. (1977). A modified pseudosection for resistivity and IP, *Geophysics* **42**, 1020-1036.

- Ervin, C. P. and L. D. McGinnis (1975). Reelfoot rift: reactivated precursor to the Mississippi embayment, *Geological Society of America Bulletin* **86**, 1287-1295.
- Garner, L. K., E. E. Morti, and D. R. Smuin (1995). *Northeast plume characterization summary report*. Report KY/ER-65, prepared for the U. S. Department of Energy under contract no. DE-AC05-76OR00001, Paducah, KY, Martin Marietta Energy Systems.
- Geldart, L. P. and R. E. Sheriff (2004). Geophysical Reference Series Vol. 14: Problems in Exploration Seismology and their Solutions: Tulsa, Society of Exploration Geophysicists, 514 p.
- Goldhaber, M. B., C. J. Potter, and C. D. Taylor (1992). Constraints on Reelfoot rift evolution from a reflection seismic profile in the northern rift, *Seismological Research Letters* **63**, 233-241.
- Griffiths, D. H. and R. D. Barker (1993). Two-dimensional resistivity imaging and modelling in areas of complex geology, *Journal of Applied Geophysics* **29**, 211-226.
- Harris, J. B. (1996). Shear-wave splitting in Quaternary sediments: neotectonic implications in the central New Madrid seismic zone, *Geophysics* **61**, 1871-1882.
- Harris, J. B., S. A. Berman, W. C. Beard, R. L. Street, and R. T. Cox (1998). Shallow seismic reflection investigations of neotectonic activity in the Lower Mississippi Valley, *Expanded Abstracts, 68th International Meeting of the Society of Exploration Geophysicists*, Sept. 13-18, New Orleans, LA.
- Harris, J. B. and R. L. Street (1997). Seismic investigation of near-surface geological structure in the Paducah, Kentucky, area: application to earthquake hazard evaluation, *Engineering Geology* **46**, 369-383.
- Hawley, P. F. (1943). Fault location by electrical prospecting – an example, *Geophysics* **8**, 391-403
- Hildenbrand, T. G., M. F. Kane, and J. D. Hendricks (1982). Magnetic basement in the upper Mississippi embayment region – a preliminary report, in F. A. McKeown and L. C. Pakiser, eds., *Investigations of the New Madrid, Missouri, earthquake region*: U. S. Geological Survey Professional Paper 1236E, 14 pp.
- Hildenbrand, T. G. and J. D. Hendricks (1995). Geophysical setting of the Reelfoot rift and relations between rift structures and the New Madrid seismic zone, in K. M. Shedlock and A. C. Johnston, eds., *Investigations of the New Madrid, Missouri, earthquake region*: U. S. Geological Survey Professional Paper 1538-E, 30 pp.
- Jacobs (1997). *Ground-water conceptual model for the Paducah Gaseous Diffusion Plant, Paducah, Kentucky*. prepared for the U. S. Department of Energy under contract no. DE-AC05-93OR22028, Paducah, KY, Jacobs EM Team.
- Johnston, A. C. and K. M. Shedlock (1992). Overview of research in the New Madrid seismic zone, *Seismological Research Letters* **63**, 193-208.
- Kane, M. F., T. G. Hildenbrand, and J. D. Hendricks (1981). Model for the tectonic evolution of the Mississippi embayment and its contemporary seismicity, *Geology* **9**, 563-568.
- Kolata, D. R. and T. G. Hildenbrand (1997). Structural underpinnings and neotectonics of the southern Illinois Basin: an overview, *Seismological Research Letters* **68**, 499-510.
- Kolata, D. R. and W. J. Nelson (1997). Role of the Reelfoot Rift/Rough Creek Graben in

- the evolution of the Illinois Basin, in R. W. Ojakangas, A. B. Dickas, and J. C. Green, eds. Middle Proterozoic to Cambrian rifting, central North America: *Geological Society of America Special Paper*, 287-298.
- Kolata, D. R. and W. J. Nelson (1991). Tectonic history of the Illinois basin, in W. M. Leighton, D. R. Kolata, D. F. Oltz, and J. J. Eidel, eds., *American Association of Petroleum Geologists Memoir* **51**, 263-292.
- Langston, C., J. McIntyre, R. Street and J. Harris (1998). Investigation of the shallow subsurface near the Paducah Gaseous Diffusion Plant using SH-wave seismic methods, *Expanded Abstracts, 62nd International Meeting of the Society of Exploration Geophysicists*, Sept. 13-18, New Orleans, LA.
- Langston, C. and R. Street (1998). Acquisition of SH-wave seismic reflection and refraction data in the area of the northeastward trending contaminant plume at PGDP, *Dept. of Geological Sciences, University of Kentucky*
- Lettis and Associates, Inc. (2006). *Investigation of Holocene faulting, Proposed C-746-U landfill expansion, Paducah Gaseous Diffusion Plant, Paducah, Kentucky.*
- Matias, M. S., M. M. da Silva, P. Ferreira, E. Ramalho (1994). A geophysical and hydrogeological study of aquifers contaminated by a landfill, *Journal of Applied Geophysics* **32**, 155-162.
- McBride, J. H., D. R. Kolata, and T. G. Hildenbrand (2003). Geophysical constraints on understanding the origin of the Illinois basin and its underlying crust, *Tectonophysics* **363**, 45-78.
- McBride, J. H. and W. J. Nelson (2001). Seismic reflection images of shallow faulting, northernmost Mississippi embayment, north of the New Madrid seismic zone, *Bulletin of the Seismological Society of America* **91**, 128-139.
- McBride, J. H., W. J. Nelson, and W. J. Stephenson (2002). Integrated geophysical and geological study of Neogene and Quaternary-age deformation in the northern Mississippi embayment, *Seismological Research Letters* **73**, 597-627.
- Mooney, W. D., M. C. Andrews, A. Ginzburg, D. A. Peters, and R. M. Hamilton (1983). Crustal structure of the northern Mississippi embayment and a comparison with other continental rift zones, *Tectonophysics* **94**, 327-348.
- Nelson, W. J., F. B. Denny, J. A. Devera, L. R. Follmer, and J. M. Masters (1997). Tertiary and Quaternary tectonic faulting in southernmost Illinois, *Engineering Geology* **46**, 235-258.
- Nelson, W. J., F. B. Denny, L. R. Follmer, and J. M. Masters (1999). Quaternary grabens in southernmost Illinois: deformation near an active intraplate seismic zone, *Tectonophysics* **305**, 381-397.
- Odum, J. K., W. J. Stephenson, R. A. Williams, J. A. Devera, and J. R. Staub (2002). Near-surface faulting and deformation overlying the Commerce geophysical lineament in southern Illinois, *Seismological Research Letters* **73**, 687-697.
- Olive, W. W. (1980). *Geologic Maps of the Jackson Purchase Region, Kentucky*, U. S. Geological Survey Miscellaneous Invest. I-1217, 1 sheet, 11 pp.
- Potter, C. J., J. A. Drahovzal, M. L. Sargent, and J. H. McBride (1997). Proterozoic structure, Cambrian rifting, and younger faulting as revealed by a regional seismic reflection network in the southern Illinois Basin, *Seismological Research Letters* **68**, 537-552.
- Rayner, S. F., L. R. Bentley, and D. M. Allen (2007). Constraining aquifer architecture

- with electrical resistivity imaging in a fractured hydrogeological setting, *Journal of Environmental and Engineering Geophysics* **12**, 323-335
- SAIC Engineering, Inc. (2002). *Seismic investigation report for siting a potential on-site CERCLA waste disposal facility at the Paducah Gaseous Diffusion Plant, Paducah, Kentucky*. DOE/OR.07-2038&D1, prepared for the U. S. Department of Energy under contract no. DE-AC05-98OR22700, Paducah, KY, Bechtel Jacobs Company, Inc.
- Schweig, E. S., F. Shen, L. R. Kanter, E. A. Luziatti, R. B. VanArsdale, K. M. Shedlock and K. W. King (1992). Shallow seismic reflection survey of the Bootheel lineament area, southeastern Missouri. *Seismological Research Letters* **63**, 285-297.
- Sexton, J. L. (1988). Seismic reflection expression of reactivated structures in the New Madrid rift complex, *Seismological Research Letters* **59**, 141-150.
- Sexton, J. L., H. Henson, P. Dial, and K. Shedlock (1992). Mini-Sosie high resolution seismic reflection profiles along the Bootheel lineament in the New Madrid seismic zone, *Seismological Research Letters* **63**, 297-307.
- Sexton, J. L. and P. B. Jones (1986). Evidence for recurrent faulting in the New Madrid seismic zone from Mini-Sosie high-resolution reflection data, *Geophysics* **51**, 1760-1788.
- Sheriff, R. E. and L. P. Geldart (1989). *Exploration Seismology Vol. 1: History, Theory, and Data Acquisition*: Cambridge, Cambridge University Press, 244 p.
- Stummer, P., H. Maurer, and A. G. Green (1994). Experimental design: electrical resistivity data sets that provide optimum subsurface information, *Geophysics* **69**, 120-139.
- U. S. Environmental Protection Agency. Technetium-99. 15 Nov. 2007. 15 Jan. 2008. <<http://www.epa.gov/radiation/radionuclides/technetium.html>>.
- U. S. Environmental Protection Agency (2000). *Trichloroethylene hazard summary*. EPA79-01-06, Office of Research and Development, Washington, D. C.
- VanArsdale, R. B., E. S. Schweig, L. R. Kanter, R. A. Williams, K. M. Shedlock, and K. W. King (1992). Preliminary shallow seismic reflection survey of Crowley's Ridge, northeast Arkansas, *Seismological Research Letters* **63**, 309-320.
- VanArsdale, R. B. and R. K. TenBrink (2000). Late Cretaceous and Cenozoic geology of the New Madrid seismic zone, *Bulletin of the Seismological Society of America* **90**, 345-356.
- Ward, S. H. (1990) Resistivity and induced polarization methods in S. H. Ward, ed., *Geotechnical and environmental geophysics: Society of Exploration Geophysicists, Investigations in Geophysics* **5**, 147-189.
- Wheeler, R. L. (1997). Boundary separating the seismically active Reelfoot rift from the sparsely seismic Rough Creek graben, Kentucky and Illinois, *Seismological Research Letters* **68**, 586- 598.
- Williams, R. A., E. A. Luziatti, and D. L. Carver (1995). High-resolution seismic imaging of Quaternary faulting on the Crittenden County fault zone, New Madrid seismic zone, northeastern Arkansas, *Seismological Research Letters* **66**, 42-57.
- Woolery, E. W. and R. Street (2002). Quaternary fault reactivation in the Fluorspar Area fault complex in western Kentucky: evidence from shallow SH-wave reflection profiles, *Seismological Research Letters* **73**, 628-639.

- Woolery, E. W., R. L. Street, and Z. Wang (1993). Near-surface deformation in the New Madrid seismic zone as imaged by high resolution SH-wave seismic methods, *Geophysical Research Letters* **20**, 1615-1618.
- Woolery, E. W., Z. Wang, R. L. Street, and J. B. Harris (1996). A P- and SH-wave seismic reflection investigation of the Kentucky Bend scarp in the New Madrid seismic zone, *Seismological Research Letters* **67**, 67-74.

VITA

Cora Elizabeth Anderson Blits was born in Lexington, Kentucky on June 16, 1982. She graduated summa cum laude from the University of Kentucky in May of 2006, receiving a Bachelors of Science degree in Geology. She held the position of Research Assistant in the Department of Earth and Environmental Sciences from 2007 to 2008.

Publications:

- Blits, C. A., E. W. Woolery, K. A. Macpherson, and S. Hampson. Integrated geophysical imaging techniques for detecting neotectonic deformation in the Fluorspar Area fault complex of western Kentucky, 42nd Annual Meeting of the North-Central Section of the Geological Society of America, April 24-25, 2008, Evansville, IN.
- Anderson, C., Z. Wang, and E. W. Woolery. Observed Seismicity in the Jackson Purchase Region of Western Kentucky Between January 2003 and June 2005, USA, 77th Annual Meeting of the Eastern Section of the Seismological Society of America, October 3-4, 2005, Memphis, TN.

Cora Blits

November 14, 2008